

Methods and explanatory notes¹

Kelemen, P.B., Matter, J.M., Teagle, D.A.H., Coggon, J.A., and the Oman Drilling Project Science Team²

Chapter contents

Introduction	1
Operations	8
Igneous petrology	10
Alteration petrology	18
Structural geology	23
Metamorphic rock description, Site BT1 ...	29
Geochemistry	37
Microbiology	53
Paleomagnetism	64
Physical properties	67
Imaging spectroscopy	74
Downhole logging/hydrogeological testing	78
References	84
Figures	90
Tables	165
Appendix A	169
Appendix B	169
Appendix C	170
Appendix D	171
Appendix E	172
Appendix F	172

Introduction

This chapter documents the procedures, methods, and databases employed at the drill sites and in the various shipboard and shore-based laboratories during Phases 1 and 2 of the Oman Drilling Project (OmanDP), which took place from November 2016 to September 2018. This information applies only to operations and research described in this *Proceedings of the Oman Drilling Project* volume. Also described are the relationships between curatorial information from (1) the International Continental Scientific Drilling Program (ICDP) Drilling Information System (DIS), (2) the shipboard scientific data management system used aboard DV *Chikyu* (Center for Deep Earth Exploration [CDEX] J-Cores), and (3) the core description spreadsheets used to populate the *JOIDES Resolution* Science Operator (JRSO) Laboratory Information Management System (LIMS) database to which the published reports refer. Methods for wireline logging, hydrogeological testing, and preliminary analyses (microbiology and X-ray fluorescence [XRF] major and trace elements) undertaken before the “ChikyuOman” shipboard core logging phase are also described. Methods for post-core description analysis of the OmanDP Phase 1 and 2 samples and data will be described in the individual scientific contributions to be published in the research results section of this *Proceedings* volume and in international peer-reviewed literature.

On-site teams and authorships

All scientists of the OmanDP Science Team contributed to this volume. However, certain operations were undertaken by specific members, and sections were written by discipline-based groups of scientists as listed below (group leaders and then alphabetically):

- OmanDP summary: OmanDP Science Team
- Preliminary site operations and permitting: Matter, Coggon, Kelemen, France, Harris, Koepke, Lissenberg, MacLeod, Müller, Teagle, Zihlmann
- Coring and drilling operations: Coggon, Matter, Harris, Kelemen, Teagle

Drill site teams

Phase 1

- Site GT1: Ildefonse, Harris, Früh-Green, Bompard, Coggon, Jesus, Matter, Müller, Noël
- Site GT2: Harris, Teagle, Ildefonse, Bompard, Coggon, Garbe-Schönberg, Kelemen, Koepke, Matter, Mock, Müller

¹ Kelemen, P.B., Matter, J.M., Teagle, D.A.H., Coggon, J.A., and the Oman Drilling Project Science Team, 2020. Methods and explanatory notes. In Kelemen, P.B., Matter, J.M., Teagle, D.A.H., Coggon, J.A., et al., *Proceedings of the Oman Drilling Project*: College Station, TX (International Ocean Discovery Program. <https://doi.org/OmanDP.proc.2020>

² OmanDP Science Team affiliations.

- Site GT3: Teagle, Harris, Früh-Green, Coggon, Bennett, Boulanger, Bompard, France, Kelemen, Koepke, Koornneef, Lissenberg, Matter, Morris, MacLeod, Nothaft, Zeko
- Site BT1: Kelemen, Coggon, Manning, Bompard, de Obeso, Lafay, Nothaft, Perez, Zeko
- Hole BA1A: Matter, Bompard, Coggon
- Hole BA2A: Bompard, Kelemen

Phase 2

- Hole CM1A: Matter, Teagle, Coggon, Takazawa, Michibayashi, Tamura, Sato, Ishii, Mori, Ceuleneer, Koepke, Kourim, Okazaki, Guotana, Benoit, Becker, Rospabé, Morishita
- Hole CM2B: Matter, Coggon, Guotana, Benoit, Becker, Rospabé, Morishita, Yao, Hatekayama, Senda, Michibayashi, Payot, Chatterjee, A. Evans, Andrews
- Hole BA3A: Matter, Coggon, Kelemen, A. Evans, Andrews, Picazo, de Obeso, Crispini, Notini, Mariani, Giampouras, Ternieten, Eslami, Noël, Templeton, Ellison, Rempfert
- Hole BA1B: Matter, Coggon, Kelemen, Teagle, Crispini, Notini, Mariani, Giampouras, Ternieten, Eslami, Noël, Ulven, Aupart, Früh-Green, Cordonnier, Godard, Jamtveit, Jouselin, Reisberg, Klaessens, Templeton, Ellison, Rempfert, Cardace, Sousa, Fones, Nothaft, Boyd, Glombitza
- Hole BA4A: Coggon, Kelemen, Aupart, Cordonnier, Jamtveit, Jouselin, Reisberg, Klaessens, Jansen, Hörner, Bach, Auzende, Dygert, Xing, Zhu, Nothaft, Boyd, Glombitza, Spear, Kraus, Rasmussen
- Hole CM1B: Matter, Coggon, Kyaw, A. Evans
- Hole CM2A: Matter, Coggon, Kyaw, Takazawa, Okazaki
- Hole BA1C: Teagle, Matter, Coggon, Kelemen, Cordonnier, Ternieten, Aupart
- Hole BA1D: Coggon, Matter, Kelemen, Jansen

Wireline geophysical logging and hydrogeological testing

- Phase 1: Pezard, Brun, Henry, Célérier, Robert, Matter, Lods, Benchikh, Kyaw
- Phase 2: Pezard, Brun, Henry, Paris, Matter, Lods, Célérier, Benchikh, Kyaw, Yamada

Methods and site chapters

- Introduction: Teagle, Coggon, Kelemen, Takazawa, Michibayashi, Harris, Godard, Matter
- Operations: Coggon, Kelemen, Matter, Teagle
- Igneous petrology/Background rock
 - GT1/GT2: Umino, Boulanger, Faak, Ishii, Hoshide, Kondo, Kusano, Nguyen

- BT1/GT3: Koepke, Morishita, Johnson, Jesus
- BA1/BA2: Matter, Bompard
- CM1: Koepke, Python, Payot, Guotana, Johnson, Grambling
- CM2: Koepke, Python, Payot, Guotana, Dygert, Park
- BA1B: Harms, Valera, Kularatne, Aupart, Cocomazzi, Ternieten
- BA3A: Harms, Valera, Kularatne, Aupart, Cocomazzi, Ternieten, K. Evans, Tutolo
- BA4A: Aupart, Cocomazzi, Ternieten, K. Evans, Tutolo
- Alteration and metamorphism/Veins
 - GT1 and GT2: Harris, Akitou, Mock, Zihlmann, Kondo
 - BT1: Manning, De Obeso, Beinlich, Lafay, Zeko, Leong
 - GT-3: Manning, D'Andres (formerly Ducommun), Beinlich, Lafay, Zeko, Leong, Nozaka
 - BA1/BA2: Matter, Bompard
 - CM1: Früh-Green, Kimura, Oyanagi, Grabowska, Klein, Okamoto, Morishita
 - CM2: Früh-Green, Kimura, Oyanagi, Grabowska, Tamura, Warsi
 - BA1B: Kahl, Farough, Hamada, Ichiyama, Eslami
 - BA3A: Kahl, Farough, Hamada, Ichiyama, Eslami, Bach, Malvoisin
 - BA4A: Bach, Hamada, Ichiyama, Eslami, Malvoisin
- Structural geology
 - GT1/GT2: Crispini, Cheadle, Deans, Al Shahri
 - BT1: Ketterman, Kotowski, Harigane, Deamer, Urai
 - GT3: MacLeod, Ketterman, Kotowski, Deamer
 - CM1: Cheadle, Basch, Jansen, A. Evans
 - CM2: Cheadle, Basch, Jansen, A. Evans, Kaczmarek, Hirth
 - BA1B: Crispini, Kakiyama, Aslin, Barbier, Menzel
 - BA3A: Crispini, Jamtveit, Kakiyama, Aslin, Barbier, Menzel
 - BA4A: Jamtveit, Kakiyama, Aslin, Barbier, Menzel
- Geochemistry
 - GT1/GT2: Menzies, Cooper, Perez, Senda
 - BT1/GT3: Godard, Kourim, Bennett, Carter
 - CM1: Kourim, Rospabé, Chatterjee, Giampouras
 - CM2: Kourim, Rospabé, Chatterjee, Ishii
 - BA1B: Senda, Sousa, Klaessens, Zaloumis, Zhang
 - BA3A: Senda, Sousa, Klaessens, Zaloumis, Zhang, Carter
 - BA4A: Senda, Sousa, Klaessens, Zaloumis, Carter
- Paleomagnetism
 - GT1/GT2: Till, Koornneef, Morris, Usui
 - BT1/GT3: Horst, Koornneef
 - CM1: Greve
 - CM2, BA1B, BA3, BA4: Till (on shore only), Leal (on shore only)

- Physical properties
 - GT1/GT2: Abe, Ildefonse, Okazaki
 - BT1/GT3: Abe, Okazaki, Hatekayama
 - CM1: Abe, Okazaki, Hatekayama
 - CM2: Abe, Okazaki, Hatekayama, Akamatsu
 - BA1B: Katayama, Zhu, Hong, Ulven
 - BA3A: Katayama, Zhu, Hong, Ulven, Cordonnier
 - BA4A: Katayama, Hong, Cordonnier
- Near-visible infrared scanning
 - GT1, GT2, BT1, GT3: Greenberger
 - CM1, CM2, BA1B, BA3, BA4: Greenberger, Ehlmann, Amador
- Microbiology: Templeton, Ellison, Glombitza, Rempfert, Kraus, Spear
- Wireline geophysical logging and hydrogeological testing, all sites: Matter, Pezard, Brun, Paris, Henry, Robert, Benchikh, Celerier, Gouze, Roubinet, Leprovost, Lods, Kyaw, Yamada

Core curation procedures during drilling operations

The OmanDP drilling campaign has the overarching ICDP expedition number “5057” in the ICDP Drilling Information System (DIS; Table T1). Six sites were drilled during Phase 1, and five sites were drilled during Phase 2. The codes for each target follow those designated in the ICDP Oman Drilling Project proposal (Kelemen et al., 2014), with individual sites referred to by numbers (e.g., GT1, BA2). At a site, multiple holes are often drilled. Each OmanDP drill hole at a particular site is distinguished by a letter suffix. The first hole drilled is assigned the site number modified by the suffix “A,” the second hole takes the site number and the suffix “B,” and so forth (e.g., BT1A and BT1B).

Diamond drill cores

During diamond coring the cored interval is measured in meters below the ground surface and advances are gauged relative to the driller’s mark on the drill rig. Each core is numbered sequentially and the suffix “Z” is used to designate an ICDP diamond drill core. For the diamond coring operations of OmanDP, each cored interval is either 3 m or 3.05 m (10 ft), the lengths of the two core barrel types used (e.g., Table T1 in the Site GT1 chapter). At the top of holes, following casing, and in areas of hole instability, shorter cores were sometimes pulled. The ICDP suffix “M” is used to designate miscellaneous cores or redrilled intervals, for example where the hole deviated and was then realigned following insertion of casing, such as the upper sections of Hole GT1A (Fig. F9 in the Site GT1 chapter). Two industry standard core diameters were cored: HQ (core diameter = 63.5 mm) and NQ (diameter = 47.8 mm); the larger diameter HQ cores were recovered in the upper parts of

the hole before stepping down to NQ cores following insertion of a temporary NW casing string (Table T2 in the Site GT1 chapter).

Each core recovered is divided into <1 m sections that are numbered serially from the top. Where perfect core recovery was achieved, the sections are numbered sequentially as recovered, starting with 1 at the top of the core (Fig. F1). Where possible, we avoided sawing cores into <1 m sections and instead used natural breaks in the cores to separate sections. Consequently, most cores have more than 3 sections. High recovery, irregular core breakage, sloping fractures, and the avoidance of too snug a fit of sections into the core box slots also resulted in most cores occupying more than 3 sections. The top depth of a core is equated with the top depth of the cored interval (in meters) to achieve consistency in handling analytical data derived from cores (Fig. F2). All pieces recovered are placed immediately adjacent to each other in the core boxes. Each new core was placed at the top of a new core box slot. Core boxes were labeled sequentially. HQ core boxes contain 4 section slots, whereas NQ boxes have 5 slots.

Samples and descriptions of cores are designated by distance measured in centimeters from the top of the section to the top and bottom of each sample or interval (Fig. F2). A full identifier for a sample consists of the following information: ICDP expedition number, site, hole, core number, core type, section number, section half identifier (if applicable), top and bottom offsets in centimeters measured from the top of section (half), and additional subsample names if applicable (Fig. F3). For example, the designation “Sample 5057-GT1A-26Z-1W, 74–79 cm (Thin Section),” represents the thin section made from a billet removed from the interval between 74 and 79 cm from the top of working-half Section 1W of Core 26Z of Hole GT1A of the OmanDP. In addition, core pieces are numbered sequentially from the top of each section, and if a fractured core piece can be re-assembled the subpieces are annotated with the suffix “a, b,” and so forth, from the top of the piece downwards.

Drill site handling

“Core-on-deck” was defined as the time the core barrel was lowered onto the drilling platform following retrieval by wireline. The diamond drill cores were liberated from the wireline core barrel onto a >3 m long plastic split pipe tube supported by a steel core trestle adjacent to the drill rig (Fig. F4). The lowermost piece of core was persuasively freed from the core catcher and reunited with the main core. The bottom of each piece was marked with a red wax pencil as the core was being extracted. The core pieces were washed and scrubbed with local groundwater (see Operations) and plastic brushes to remove drilling fluids, grease, and fine cuttings. The

split pipe holding the core was then slid onto a steel core rack and carried to the OmanDP mobile canvas core curation facility (M3CF). To minimize contamination of the core with gold, platinum group elements, and other trace elements, all personnel handling and describing the cores or other sample material removed jewelry from their hands and wrists before handling. This good practice continued on board *Chikyu* during the core preparation, description, and sampling activities.

Core pieces were reconstructed, subpieces fitted back together, and the recovered length (RL) measured and recorded (Fig. F2). A series of overlapping digital photographs were taken of the whole recovered core using a tablet computer as a precaution against accidents during prelabeling handling of whole-round pieces (see [Supplementary material > K6_On-site tablet photos](#)). Small subpieces were taped together using clear plastic tape. Cores were inspected to locate the appropriate splitting line—generally perpendicular to the dominant igneous fabric (e.g., magmatic layering or foliation, chilled margins) and a blue-red way-up line was drawn along the whole length of the core (Fig. F5) ~90° around core from the optimal splitting line. The blue-red double line is drawn so that the red line is on the right of the blue line when a core is held vertically the correct way up. Generally, core recovery and quality were such that the bottom piece of the overlying core could be fitted together with the top of the next core, and the blue-red way-up line was continued down the next core. Cores or section breaks that could be fitted together were recorded as “continuous” in the DIS and marked on a core spacer inserted into the core box. If pieces were >95 cm, they were sawn using a table saw, recorded in the DIS, and marked on a core box spacer. Core or section pieces that could not be fitted together were recorded as “Discontinuous,” and a new blue-red way-up double line was marked following the convention described above. Pebble-sized and smaller core pieces that could not be reconstructed or reoriented were placed in plastic bags and recorded as “rubble” in the DIS. Cores were then loaded into the core boxes section by section and the core box slots labeled with the section identifiers. Section lengths were measured and recorded in the DIS. These drill site measurements are referred to as Oman curated section lengths (OCSLs). The sum of all OCSLs within a core is known as the Oman curated length (OCL) (Fig. F2).

All core pieces that could be uniformly rotated about their cylindrical downhole axis were imaged using the ICDP DMT CoreScan portable core imaging instrument to record a 360° image of the external surface of the drill core (Fig. F6; see also [Supplementary material > K4_Onsite 360 DMT core scans](#)). Sections were imaged dry. The instrument was operated following standard procedures using the integrated cold blue light. The instrument was posi-

tioned in the rear of the M3CF in order to reduce interference from the changeable natural light conditions in the field laboratory. A white balance calibration was performed at the start of each day. All images were generated in both DMT and BMP formats at 10 pixel/mm (127–1008 dpi). Cores were imaged section by section, and images were labeled in the format 5057_Site-Hole_Core_Section.bmp or .dmt. For example, “5057_1_23_3.bmp” is the whole-round core scan of Section 23Z-3 from Hole GT1A. The BMP files were imported into the DIS and converted to the following formats: high-resolution JPG (without compression), low-resolution JPG (without compression), and a small thumbnail image.

Following 360° imaging, pieces and subpieces in each section were labeled with their ICDP-OmanDP identifiers (Fig. F2). Pieces were labeled sequentially from the top of each section, beginning with number 1; reconstructed groups of piece halves were assigned the same number but were lettered consecutively. Pieces were labeled only on the outer cylindrical surfaces of the core. If the piece was oriented with respect to the way up, an arrow was added to the label pointing to the top of the section. Curatorial data were entered into the DIS including information on the continuity of the cores and sections. Section pieces were then sketched using a tablet computer, subpieces were identified, and prominent features were drawn (see [Supplementary material > K3_On-site core-section sketches](#), e.g., CoreBoxSketch_4_B_Box_73.pdf).

The core sections were then described using the DIS template set up for the OmanDP on the basis of section units, where each different rock type in a specific section is described as a separate unit (Figs. F1, F3). Note that this is a different approach to that used by the igneous petrology core description teams on board *Chikyu*, where igneous intervals of petrographically similar rocks can continue across cores and sections (see [Igneous petrology](#)). These drill site descriptions are available in the DIS for OmanDP, summary tables of curation data, and section-unit rock descriptions in [Supplementary material. > K1_Onsite curation and description and K2_On-site igneous unit summaries](#).

Core sampling generally did not take place on site in Oman except that a 5 cm long half-round core sample of uniform, indistinctive, background rock was taken every ~20 m during Phase 1 and every ~10 m during Phase 2 to provide preliminary observations for the ChikyuOman core description campaign. The DIS assigned these samples International Geo Sample Number (IGSN) identifiers (Figs. F3D, F7). Polished thin sections were made and samples crushed and ground for geochemical whole-rock analyses at the University of Southampton (see [Geochemistry](#)).

Following core description, a flat scan image was taken of each filled core box using the DMT Core-Scan instrument (Fig. F6C; see also [Supplementary material > K5_Onsite DMT box scans](#)). The instrument was refocused every time the scanner was moved from site to site or core box sizes were changed (e.g., from HQ to NQ). Image resolution and format were as described above and images were labeled in the format 5057_Site-Hole_Corebox.bmp or .dmt. A standard photographic color chart was included in all core box scans to facilitate future color correction of images. Each core box was labeled, empty space was packed with foam, and the core boxes and lids were closed with plastic straps and metal clips.

During Phase 1, core boxes were stacked on plastic mats in a designated storage area at each drill site. Stack height was restricted to 5 boxes high for HQ size and 6 boxes high for NQ size boxes. The core boxes were covered with plastic sheeting to keep them dry and shaded to prevent windblown dust contamination. During demobilization from each drill site the core boxes were loaded onto wooden pallets on a flat-bed truck and the stacks were secured using ratchet straps. During Phase 2, boxes were stacked directly onto wooden pallets for storage on site to minimize handling of boxes later during transport. The core boxes were transported to the Ministry of Regional Municipalities and Water Resources (MRMWR) storage facility in Mubaila, where they were offloaded on the pallets using a forklift truck and stored outside on a raised concrete floor, covered in plastic sheeting and under shade. Upon completion of drilling at the first two sites (GT2 and GT1) the core boxes from these sites were loaded into a 40 ft temperature-controlled shipping container and secured using a Thermocoil system. The container was shipped from Muscat, Oman, to Shimizu, Japan, and the cores were loaded onto *Chikyu* upon arrival. Cores from Sites GT3 and BT1 were shipped in the same way after completion of Phase 1 drilling. The second shipment (Sites GT3 and BT1) was stored in the shipping container at Shimizu Port for 2 weeks before loading the cores onto *Chikyu*.

During Phase 2, cores were loaded into containers (not climate controlled) on pallets and shipped to Shimizu. The first shipment (Sites CM1, CM2, and BA3) arrived in early April 2018, and the second shipment (Sites BA1 and BA4) arrived in late June 2018 before being loaded directly onto *Chikyu* for storage in the climate-controlled laboratories on board.

Drill site handling for microbiology sampling

During Phase 2, microbiology sampling was added into core flow for wireline diamond coring. For Holes CM1A and CM2B, a small number (4 and 3, respectively) of whole-round core samples measuring ~20–40 cm were taken at the end of core flow. Gloves

were worn throughout the handling of these pieces, and once sampled, they were wrapped in clean aluminum foil then sealed in plastic bags and stored in a domestic freezer, ready for transport by the microbiology team. Two 5 cm samples of working-half core were also taken from Hole CM1A for thin sections to accompany the two lowermost microbiology samples from this hole.

From Holes BA3A, BA1B, and BA4A, a more comprehensive microbiology sampling strategy was implemented, with ~50 cm of whole-round core sampled every ~10 m downhole. For most cores, core handling continued as described above, but for cores from which a microbiology sample was taken the core handling routine was modified to reduce contamination of these samples, as follows. The number of people who handled the core as it was delivered to the core deck and liberated it from the core barrel was minimized, and all who handled the core wore nitrile gloves. Each core was washed with reverse-osmosis water and a steel wool ball by members of the microbiology team, and a sample interval was selected at the core deck. During reconstruction of the core at the core tables, the chosen sample interval was handled as little as possible and the red-blue way-up lines and bottom marks were not added to the sample interval to avoid contamination from the wax pencils. After reconstruction and measurement of the recovered length, the sample interval was removed from regular core flow by microbiology team members and taken directly to the DMT core scanner, the rollers of which were washed with disinfectant prior to scanning the section. Once a whole-round scan had been acquired, the microbiology sample was taken (cut using the rock saw if necessary) for further processing by the microbiology team as described in [Microbiology](#). A foam spacer was inserted into the sampled section to indicate the position of the sample in the core box.

Rotary drilling holes

During rotary drilling, the drilled depth was measured in meters below the ground surface and advances gauged relative to the driller's mark on the drill rig. During each 1 m advance a composite sample of drill cuttings was collected into a bucket from a diverted stream of cuttings-laden drilling fluid flowing from the borehole. An aliquot of the cuttings sample was taken from the bucket and placed into a rack with individual compartments indicating the sample interval (Fig. F8). A subsample of the cuttings sample was laid out on a large table for preliminary visual examination of rock type and mineralogy.

Drill site handling of drill cuttings

Rock type(s) and/or mineralogy of each cuttings sample were established by visual examination with a hand lens and recorded in the ICDP DIS. Drill cut-

tings sampling took place on site in Oman. An aliquot of ~100 cm³ was taken every 5 m by the drill site scientist. The sample was put into a stack of sieves with mesh sizes of 4.5 mm, 1 mm, and 250 µm and washed with local groundwater and a plastic brush. The 1.0–4.5 mm and the 250 µm–1 mm fractions of the washed cuttings were collected, put into canvas bags, and air-dried. Each sample was recorded in the ICDP DIS with the full identifier for a sample consisting of the following information: ICDP expedition number, site, hole, depth interval, and size fraction (e.g., 5057-5A, 209–210 m, >1 mm). These cuttings samples were shipped to Southampton by air freight for further analysis. An additional subset of cuttings samples was collected at specific depth intervals for microbiological analyses (see [Microbiology](#)).

Core handling, curation, and core splitting procedures

Before the cores were loaded on board *Chikyu* the on-site curation data (cores, sections, depths) from the DIS were entered into the J-Cores laboratory management system. Once loaded aboard *Chikyu*, core boxes were checked for damage, each section was carefully reconstructed and shrink-wrapped, and foam spacers were inserted to separate any discontinuous pieces. Every section was imaged using the whole-round X-ray computed tomography (XCT) scanner and run through the shipboard whole-round multisensor core logger (MSCL-W), which measures whole-round magnetic susceptibility (MS) and logs natural gamma radiation (NGR) (Fig. F9; also see [Physical properties](#)). Data were uploaded to J-Cores database section by section. The XCT scanner and the MSCL-W both generate their own section lengths that may be subtly different from the curated lengths measured at the drill site and recorded in the DIS, due to the adjustment of the cores during transport and handling. The section length generated for each section during its first shipboard whole-round scan is referred to as the *Chikyu* curated section length (CCSL) and is applied to subsequent shipboard measurements and processing (Fig. F2). If there is a difference in length between the archive and working halves after splitting, a foam spacer is inserted into the section (Fig. F10). The sum of all CCSLs within a core is referred to as the *Chikyu* curated length (CCL).

A black splitting line was marked on each shrink-wrapped section so that the sections were split into representative working and archive halves. Ideally, the splitting line is oriented to maximize the expression of dipping structures on the cut face of the core while maintaining representative features in both archive and working halves. Initially there was no set protocol for orientation of the splitting line with respect to the blue-red double line that indicates both

the way-up and the continuity of the sections and cores. Unfortunately, the process of trying to identify the optimum splitting line on a section-by-section basis led to rotation of the blue-red double line with respect to the cut surface with consequent loss of continuity between the sections and cores. From Section GT1A-60Z-3 (OmanDP Core box GT1A-51) on, we adopted the protocol that sections were split perpendicular to the blue-red double line with the half hosting the blue-red line assigned to the archive half. As many core pieces fit together from section to section and core to core and all cores had been imaged using the DMT 360 scanner on which the blue-red double line is visible, this approach provides additional information for the relative orientation of each section and should assist the eventual reorientation of cores back into the geographic reference frame. Although this protocol may not ensure a perfect split perpendicular to the dominant primary fabric of the core (e.g., magmatic layering or fabric), it preserves the impressive continuity of the cores, ensures continuity of the archive and working halves, and benefits from the whole-core observations that were only possible at the drill site. This protocol could be overridden by the presence of special features, such as fault zones, mineralized patches, and dike margins, which should be divided between the archive and working halves to ensure preservation and/or allow shipboard or postcruise sampling. However, because of the requirement of rapid core flow and the huge task of splitting the cores, this was not possible.

The shrink-wrapped sections were cut using the automated bandsaw on board *Chikyu*. Cutting rates were adjusted to avoid saw burn marks or scalloping of the cut surface. The optimum cutting rate for gabbro cores was ~40 mm/min. Because of the vast number of cores to be split and described, some shorter sections (<60 cm) were cut using a circular saw to speed up the core splitting process. To further increase the rate of core splitting, some batches of core were offloaded from *Chikyu* and sent to the Kochi Core Centre (KCC), where they were split using a circular saw before being returned to *Chikyu* for description.

Following core splitting, piece and subpiece labels were attached with epoxy glue to the working and archive halves as required. Digital images of the dry, cut faces of archive halves were captured with the imaging split core multisensor core logger (MSCL-I), and color reflectance and contact probe magnetic susceptibility (MSP) were measured using the MSCL-C (see [Physical properties](#)).

Depth computations

Bit depth in the hole during drilling and coring is based on the length of drill pipe added at and deployed beneath the rig. These depths are expressed

as drilling depth in meters below the ground surface at the drill rig, known as driller's depth (DD). The bit depth at which a coring advance begins and ends defines the cored or drilled interval (DI) (Fig. F2).

Once the recovered core is subjected to curatorial procedures, the top depth of a core, referred to as core top (CT) depth, is used for assigning depths to samples and measurements. The CT is equal to the top of the DI in DD meters. However, the lowermost depth of the core samples and the depths of samples and measurements within the core are based on the curatorial and core processing procedures and have no defined relation to the bottom depth of the cored interval on the DD scale. Depths of samples and associated measurements were calculated by adding the offset (interval, INT) of the sample or measurement from the top of its section and the OCSLs (for samples taken in Oman) or CCSLs (for samples and measurements onboard *Chikyu*) of all higher sections in the core to the top depth of the cored interval (Fig. F2). This calculation produces an Oman curated depth (OCD, in m) or Chikyu curated depth (CCD, in m). This computation assumes that the recovered material represents a contiguous interval starting at the top depth of the cored interval, even if core pieces are separated by nonrecovered stratigraphic intervals. If a core is shorter than core barrel advance and/or consists of more than one piece, the true depth of a sample or measurement in the core is unknown and should be considered a sample depth uncertainty when analyzing data associated with the core material.

During OmanDP, core recovery rates were very high and there was a tendency for sections to expand during curatorial or description processes. In order to remove artificial overlaps between cores and sections related to natural, drilling, instrumental, or curatorial processes, a *Chikyu* adjusted depth (CAD) framework was constructed. A simple, single depth offset was defined for each interval in a core section, calculated following Figure F2. The transformation from the DD scale to the CAD scale for each section interval is defined in an Excel look-up table and presented in meters adjusted depth (mad). In cores where the DI is greater than the CCL, the CAD calculation was not applied, as this would artificially inflate sections; instead, CCD is reported for intervals in these cores.

Additional depth scales are defined for downhole logging operations because those measurements are based on the length of the logging cable deployed beneath the rig floor, with their specific sources of uncertainty and correction procedures.

In summary, the depth scales used are as follows:

- Drilling and coring depth scales:
 - Drillers depth (DD): meters below ground surface (m)
 - Oman curated depth (OCD): meters curated depth (mcd)
 - *Chikyu* curated depth (CCD): meters curated depth (mad)
 - *Chikyu* adjusted depth (CAD): meters adjusted depth (mad)
- Wireline logging depth scales:
 - Wireline log depth below ground surface/rig floor (WRF): m
 - Wireline log speed-corrected depth (WSD): m
 - Wireline log-matched depth (WMD): m

Core reference frame for sample orientation

Each core piece that has a length exceeding that of the wireline core barrel diameter (HQ ~ 65 mm; NQ ~ 50 mm), and hence cannot have tumbled, is associated with its own core reference frame (CRF) (Fig. F5). The primary reference is the axial orientation (i.e., the top and bottom of the piece) based on the piece's orientation when extracted from the core barrel. The core axis defines the z-direction, where positive is downcore. The secondary reference is an arbitrarily marked axis-parallel line on the whole-round surface of the piece. This is the cut line, which marks the plane through the cut line and the core axis where the piece will be split. The cut line is traditionally selected by scientists to maximize the dip angle of planar features on the split surface, which facilitates accurate structural measurements. However, starting from Section GT1A-60Z-3, the cut line was defined as perpendicular to the blue-red double line (see above). The x-axis of the CRF is defined orthogonally to the cut plane, positive (000) into the working half, negative (180) into the archive half. The y-axis is orthogonal to the x-z plane and, using the right-hand cork-screw rule, is positive (090) to the left and negative (270) to the right when looking up-core onto the archive half.

Cube samples taken from the working half were marked with a red wax pencil arrow in the upcore direction (–z-direction) on the working half surface (y-z plane). This defines the cube's orientation unequivocally within the CRF. Thin section billets and thin sections made from billets were also marked with blue arrows showing +y and +z (downcore) in the most common case where the thin section was cut from the y-z plane of the working-half sample. If thin sections were cut in the x-y or x-z plane, these directions were marked on the thin sections (Fig. F5).

Following sample curation, whole-round and section-half measurement and imaging, and splitting (Fig. F9), the archive section halves of each core were described by teams of OmanDP scientists. Observations were recorded using Excel spreadsheets and paper notes. The spreadsheets were designed to be compatible with the JRSO DESClogik interface with

the aim that these data can be loaded into the LIMS (for details, see individual disciplinary sections in this chapter).

Digital color close-up images were taken by individual scientists of particular features for illustrations in the summary of each site. Working section halves of cores were sampled for both shipboard characterization of cores and shore-based studies. Samples were routinely taken for physical properties (8 cm³ cube), paleomagnetic (8 cm³ cube), thin section (billet or slab), geochemical (billet, slab, or quarter round), and X-ray diffraction (XRD) analyses by the ChikyuOman science teams, as described in the sections below. Each extracted sample was logged into J-Cores, including the sample type and the onboard analysis (test) conducted on the sample. Records of all samples taken from the cores were stored in J-Cores and are accessible online. Following description of the cores for each site, cores were sampled by individual scientists or collaborative teams for further analysis and research. Extracted samples were sealed in labeled plastic vials, cubes, or bags. Personal research samples were also recorded in J-Cores. Records of all ChikyuOman and individual scientist samples were uploaded into the ICDP DIS, where they were assigned IGSN codes. There is a specific structure for the extended IGSN assignments for ICDP sample material (see Fig. F7). ICDP is the registered IGSN name space, and the unique ICDP expedition number used in the code (5057 for OmanDP). “E” is used as a default report prefix, and the object tag indicates the sample hierarchy (H = hole; C = core, S = section, X = sample interval), with sample material identified with a unique 5-character code (Table T2).

Following completion of ChikyuOman scientific observations, measurements, and sampling, both core halves were individually shrink-wrapped in plastic to prevent rock pieces from moving out of sequence during transit. Working and archive halves were put in separate core boxes, sealed, and transferred to cold-storage space aboard the drilling vessel. At the end of the ChikyuOman campaign, both the archive and working halves of the core were transferred from the ship for temporary, accessible storage at American Museum of Natural History in New York (USA) for the moratorium period.

Core section graphic visual core description summaries

For each core section from the diamond drilled holes, the most pertinent instrument measurement parameters and core description observables were plotted on a section-by-section graphic summary. These documents are traditionally referred to as visual core descriptions (VCDs). Existing templates from previous scientific ocean drilling expeditions

were reviewed and adapted by the ChikyuOman science teams, and JRSO personnel implemented modifications as needed during the course of the core description campaign to arrive at the final template (Fig. F11). JRSO personnel plotted all graphic summaries using the final template and data retrieved from core describing spreadsheets and J-Cores databases employing symbols, patterns, and line plots with depth, using the commercial plotting program Strater. A key to symbols used on the graphic summaries is given in Figure F12.

The section graphic summary forms are arranged in landscape format and summarize the shipboard observations for the section starting each igneous unit, with a text summary from each description team (igneous petrology, metamorphic petrology, and structural geology) down the right-hand side of the page. All other information is plotted by depth in the main report area, starting with an image of the archive section half and followed by the identification of pieces recovered, lithologic units defined, shipboard samples analyzed, MS measurements, and the most significant observed igneous, metamorphic, and structural parameters (Fig. F6).

Operations

Site selection and permitting

Discussions at the International Continental Scientific Drilling Program/Deep Carbon Observatory (ICDP-DCO) sponsored workshop on scientific drilling in the Samail ophiolite (Palisades, New York, 2010) considered and refined the science goals for investigation of Oman ophiolite-hosted processes from the ancient seafloor to modern hydrogeological systems and developed a drilling strategy. Almost 80 scientists, including many with decades of experience in ophiolite, Oman, and ocean floor research (see Kelemen et al., 2013, 2014), reached consensus on two important strategies: (1) that the first campaign of scientific drilling of Oman would not attempt a single deep well to sample the crust and upper mantle but take an offset drilling approach, in which specific geological targets were sampled in relatively short holes (300–600 m) drilled with mobile mineral exploration drill rigs available in Oman, and (2) that the initial drilling should focus on the simpler southern massifs, reserving the interesting challenges of the more complex, polygenetic northern massifs of the Oman ophiolite for future generations.

For the Oman Drilling Project ICDP proposal, initially submitted in 2013 and successfully revised in 2014 (Kelemen et al., 2014), descriptions were provided for 6 borehole sites based on the geological knowledge of the large proponent groups (Fig. F13). Three sites in the Gabbro Traverse series from the lower cumulate gabbros (Site GT1), through the mid-

dle crustal transition from layered to cumulate gabbros (Site GT2), and the transition from gabbros to sheeted dikes (Site GT3) were initially placed in a southward traverse down Wadi Gideah (near Ibra) building on classic studies by Pallister and Hopson (1981), Nicolas et al. (1996), and others, supplemented by recent mapping and sampling by Koepke, Garbe-Schönberg, and colleagues. Site GT3 was relocated to Wadi Abdah prior to permit applications, due to concerns about the geological suitability of the original location, as described in [Introduction](#) in the [Site GT3A](#) chapter. The Maqсад diapir (e.g., Jousset et al., 1998; Abily and Ceuleneer, 2013) was proposed for sampling the interface between the lower crust and upper mantle (Site MD1) and to complement the Gabbro Traverse drilling and peridotite-hosted aquifer drilling. We were not able to drill at the Maqсад diapir drill site because the proposed drill sites were all within the 3.5 km protection radius of a registered “falaj” irrigation system. We identified two alternative sites (CM1 and CM2) in Wadi Zeeb in the Wadi Tayin massif after extensive mapping of this area by Takazawa and colleagues.

The MOD (Ministry of Defense) Mountain site was identified as the optimum location to investigate the quantitative carbonation of mantle peridotites to form listvenite, rare magnesite quartz rocks that probably form in the mantle wedge above subducting plates. At the proposed MOD Mountain locality on the north side of the wide gravel plain of Wadi Mansah, the most extensive outcrops of listvenites in Oman occur, and the site is just above the basal thrust of the ophiolite, juxtaposing mantle peridotite in the hanging wall with underlying metasediments and metabasalts of the metamorphic sole and the Hawasina Group (Falk and Kelemen, 2015; Streit et al., 2012).

The OmanDP “Batin alteration” (BA) drill sites in Wadi Dima were chosen to create a multiborehole observatory. However, we were not able to find suitable drill sites outside the 3.5 km falaj protection zone, and thus the alternative sites for which we attained permits were Wadi Lawayni (~20 km north-east of the village Batin) for Sites BA1, BA3, and BA4, and the headwaters of Wadi Mehlah along the Batin-Dima road for Site BA2. Both these sites lie along major NW-SE-trending fault systems that cut the Wadi Tayin massif. Observation boreholes maintained by the Ministry of Regional Municipalities and Water Resources exist at or close to these alternative sites.

Drilling permit applications for OmanDP in the Ash Sharqiyah North and the Ad Dakhiliyah Governorate were submitted to the Ministry of Regional Municipalities and Water Resources (MRMWR) in June 2016 and 2017 for Phase 1 and 2, respectively. In addition, an environmental impact report was submitted to the Ministry of Environment and Climate Af-

fairs (MECA). Following a review period, including an inspection of each proposed drill site and required amendments to the drill site locations to respect the falaj protection zones (as described above), permits were granted by the MRMWR. The location of each OmanDP borehole drilled is shown in [Table T3](#) and [Figure F13](#). Phase 1 comprises Holes GT1A, GT2A, GT3A, BA1A, BA2A, and BT1B; Phase 2 comprises Holes CM1A, CM1B, CM2A, CM2B, BA3A, BA4A, BA1B, BA1C, and BA1D.

Wireline diamond coring

Phase 1

For OmanDP Phase 1, Lalbuksh Voltas was contracted to perform wireline diamond coring; Lalbuksh Voltas subcontracted the coring to GeoSolutions Engineering.

Drill pads were prepared by Lalbuksh Voltas by clearing wadi gravels and small boulders using a JCB to build a level pad at each site. Where necessary, extensions of gravel access roads were built using a bulldozer and grader to facilitate transport of the rig and drilling equipment to each site.

Wireline diamond coring was carried out by GeoSolutions Engineering using a custom-made GSC-03 rig. Impregnated diamond HQ and NQ core bits were used. HQ and NQ core barrel length was 3.0 m, and the total bottom-hole assembly length was 4.1 m. Lengths of HQ drill rods (also used as NW casing rods) were 3.00 m (× 50 rods) and 3.05 m (all other rods). NQ drill rods were 3.05 m long. The drilling circulating fluid used was local groundwater, delivered by tanker from local pumping stations during each day of operations, mixed with EZ-Mud (Type 1: EZ-Mud DP Halliburton: clay/shale stabilizer, PHPA co-polymer for hard but fractured formations; Type 2: EZ-Mud polymer emulsion: PHPA—partially hydrolyzed polyacrylamide/polyacrylate co-polymer for formations with fewer fractures) at a concentration of ~500 g/1000 L of water.

Phase 2

Following a tender process, the contract for OmanDP Phase 2 wireline diamond coring was held by GeoSolutions Engineering.

Drill pads were prepared by GeoSolutions Engineering by clearing wadi gravels and small boulders using a JCB to build a level pad at each site and in some cases backfilling with wadi gravel to reduce dust and create a roughly level surface. Where necessary, extensions of gravel access roads were built using a bulldozer and grader to facilitate transport of the rig and drilling equipment to each site.

As in Phase 1, wireline diamond coring was carried out by GeoSolutions Engineering using a custom-made GSC-03 rig. Impregnated diamond HQ and NQ

core bits were used. HQ and NQ core barrel length was 3.0 m and the total bottom-hole assembly length was 4.1 m. HQ drill rods (also used as NW casing rods) and NQ rods used were all 3.00 m long. The drilling circulating fluid used was local groundwater, delivered by tanker from local pumping stations during each day of operations, mixed with EZ-Mud (Type 1 and Type 2 (see [Phase 1 in Wireline diamond coring](#)) at a concentration of ~500 g/1000 L of water.

Rotary drilling

Phase 1

For Phase 1, Hamood Al-Rashidi & Bros. Trad. Co. LLC (HRB) was contracted to perform rotary drilling of two pilot exploration boreholes (BA1A and BA2A).

Drill pads were prepared by HRB by clearing wadi gravels and small boulders using a JCB to build a level pad at each site. An Ingersoll-Rand RD-20 top head drive rig was used for air foam rotary drilling using tricone bits (17½, 12¼, 8, and 6 inches). Air and Tricom TDF-100 drilling foam were used as circulating fluid. Airlift testing borehole development was performed after drilling was completed.

Phase 2

Following a tender process for Phase 2, the contract for rotary drilling was held by Lalbuksh Voltas.

Drill pads were already prepared at Sites CM1 and CM2 for wireline diamond coring. At Site BA1 minimal preparation was necessary; clearance of boulders and leveling was performed by Lalbuksh Voltas using a JCB. An Ingersoll-Rand RD-20 top head drive rig was used for air foam rotary drilling using tricone bits (12¼, 8, and 6 inches). Air and Tricom TDF-100 drilling foam were used as circulating fluid. Airlift testing borehole development was performed after drilling was completed.

Remediation and wellhead installation

After completion of drilling in each borehole, the drillers installed a wellhead comprising a lidded steel casing extending above the surface by ~60–100 cm, set in concrete. All sites were cleared of waste by the drillers and science teams, and mud pits and channels dug at coring sites were backfilled.

Downhole logging

Downhole logging operations were funded by OmanDP operational funds. Slimline downhole logging services were contracted from the Université de Montpellier (France). Oilfield-type wireline logging of the crust–mantle Holes CM1B and CM2A were contracted from Schlumberger Oil Services and man-

aged by the Japan Agency for Marine-Science and Technology (JAMSTEC). The slimline downhole logging service for Phase 1 was conducted 1 month after completion of Phase 1 drilling operations, whereas the Phase 2 slimline and oil-field type services overlapped with Phase 2 drilling operations in order to acquire wireline logs shortly after drilling was completed. All wireline logs were conducted in open borehole conditions. The selection of downhole geophysical tools used for OmanDP was determined in accordance to scientific objectives and hole conditions.

Downhole logs are used to determine physical, chemical, and structural properties of the formations penetrated by the borehole and of the borehole fluids. The data are continuously collected as a function of depth, and measurements are taken at closely spaced depth intervals and measured in situ. Subsequently, these data can be interpreted in terms of stratigraphy, lithology, porosity, fluid content, fluid composition, geochemical composition, and structure of the formation. Where core recovery is incomplete, log data may provide the only way to characterize the geological formation. Where core recovery is high, log and core data are complementary and may be interpreted jointly. Downhole logs measure formation properties on intermediate scale that is between laboratory measurements on core samples and surface geophysical surveys. They are useful in calibrating the interpretation of geophysical survey data (e.g., synthetic seismograms) and provide a necessary link for the integrated understanding of physical properties on all scales.

In addition to wireline logging, specific hydraulic tests were conducted at the BA multiborehole test site (Holes BA1A and BA1D) in May 2017 and March 2018. These tests, which were conducted in collaboration with the Université de Montpellier (France), included flowmeter logging at ambient and pumped borehole conditions using an impeller (spinner) and/or heat-pulse flowmeter (HFM). Borehole flow logging was used to identify the producing intervals intersecting the boreholes and to determine permeability and storage. An overview of the logging program including the flowmeter logging is given in [Downhole logging and hydrogeological testing](#).

Igneous petrology

Rock description procedures closely followed those used during IODP Expeditions 304/305 (Blackman et al., 2006), 309/312 and 335 (Teagle et al., 2006, 2012), 345 (Gillis et al., 2014), and 360 (MacLeod et al., 2017a). These, in turn, were based on Ocean Drilling Program ODP Leg 209 and earlier “gabbro” legs (ODP Legs 118, 147, 153, and 176) to maintain a relatively high degree of uniformity. As during Legs 176, 206, and 209 and Expeditions 304/305, 309/

312, 335, 345, and 360, core descriptions were performed by the entire igneous petrology team working together. Each member was responsible for joint description of one or more aspects (principal lithology and units, igneous contacts, textures, mineral modes, alteration features, and habits) to ensure consistency of recorded observations throughout the core, but commonly the entire team would work together, particularly when defining lithology, units, contacts, mineral content estimates, and so forth, to ensure continuity.

Visual core descriptions

Recovered core was described macroscopically and microscopically, and characteristics were entered into Microsoft Excel worksheets for eventual import into an integrated database such as IODP LIMS. This information was used to produce graphical section summaries (also known as visual core descriptions, VCDs), which summarize the description and instrumental logs of each section of core (see [Visual core descriptions](#)). A key to symbols used on the VCDs is given in Figure F12. The VCDs for Holes GT1A, GT2A, GT3A, CM1A, and CM2B are designed to be as similar as possible, and the VCDs for Holes BA1B, BA3A, and BA4A are based on Phase 1 VCDs to ensure comparability between the three gabbro transect holes and the two crust–mantle transition zone holes. Differences in the VCDs reflect variation in the rocks.

Phase 1

Holes GT1A and GT2A

VCDs for Holes GT1A and GT2A use the same template, and from left to right display the following:

- Depth (mCCD)
- Core/section length (cm)
- Shipboard samples taken
- Scanned image of the archive half
- XCT image of the archive half
- Magnetic susceptibility (MS and MSP)
- Unit
- Subunit
- Lithology (displaying subunit boundaries)
- Primary mineralogy (% abundance)
- Grain size
- Magmatic fabric intensity (rank scale; Hole GT1A only)
- Brittle fabric intensity (rank scale)
- Fault zone locations
- Apparent offset of brittle features
- Structures
- Hydrothermal halos around veins
- Crosscutting veins
- Vein density per meter
- Alteration intensity (rank scale)
- Dip angle and dip azimuth for magmatic and brittle structures

- Description of unit/subunit

Hole GT3A

Hole GT3A VCDs display the following (left to right):

- Depth (mCCD)
- Core/section length (cm)
- Shipboard samples taken
- Scanned image of the archive half
- XCT image of the archive half
- Magnetic susceptibility (MS and MSP)
- Group
- Unit/subunit
- Lithology (displaying subunit boundaries)
- Total phenocryst abundance
- Primary mineralogy (% abundance)
- Grain size
- Brittle fabric intensity (rank scale)
- Fault zone locations
- Structures
- Hydrothermal halos around veins
- Crosscutting veins
- Vein density per meter
- Alteration intensity (rank scale)
- Location of discontinuities
- Dip angle and dip azimuth for contacts and brittle structures (corrected to CRF)
- Description of unit/subunit

Phase 2

Holes CM1A and CM2B

VCDs for Holes CM1A and CM2B display, from left to right, the following:

- Depth (mCCD)
- Core/section length (cm)
- Shipboard samples
- Scanned image of the archive half
- XCT image of the archive half
- Magnetic susceptibility (MS and MSP)
- GRA bulk density
- Sequence
- Unit/subunit
- Lithology (including lithology modifier)
- Primary mineralogy (% abundance)
- Grain size
- Magmatic layering intensity (rank scale; Hole CM1A only)
- Crystal-plastic fabric intensity (rank scale)
- Brittle fabric intensity (rank scale)
- Fracture density
- Fault zone locations
- Apparent offset
- Structures
- Hydrothermal halos around veins
- Crosscutting veins
- Vein density per meter
- Alteration intensity (rank scale)

- Dip angle: magmatic foliation, brittle, crystal-plastic, and veins
- Description of unit/subunit

Holes BA1B, BA3A, and BA4A

VCDs for Holes BA1B, BA3A, and BA4A display the following from left to right:

- Depth (mCCD)
- Core/section length (cm)
- Shipboard samples taken
- Scanned image of the archive half
- XCT image of the archive half
- Magnetic susceptibility (MS and MSP)
- Unit
- Subunit
- Lithology (displaying subunit boundaries)
- Primary mineralogy (% abundance)
- Grain size
- Magmatic fabric intensity (rank scale)
- Brittle fabric intensity (rank scale)
- Fault zone locations
- Apparent offset of brittle features
- Structures
- Hydrothermal halos around veins
- Crosscutting veins
- Vein density per meter
- Alteration intensity (rank scale)
- Dip angle and dip azimuth for magmatic and brittle structures
- Description of unit/subunit

Igneous intervals, units, and contact logs

Phase 1

Holes GT1A and GT2A

The first step in describing core was identification of interval boundaries on the basis of the presence of contacts, chilled margins, changes in primary mineralogy, color, grain size, and structural or textural variations. Within a range of characteristic lithology, an igneous interval may have variations in texture, grain size, and modal amount of constituent minerals. Igneous intervals in Holes GT1A and GT2A were numbered continuously from top to bottom. Lithologically and texturally similar pieces from consecutive core sections were curated as belonging to the same igneous interval. To preserve important information about igneous stratigraphy without defining an unreasonable number of intervals within a single core, subintervals were designated in cases where there were marked changes in texture without accompanying changes in mineralogy, or vice versa. In addition, crosscutting magmatic veins and thin dikes were designated as intervals or subintervals. Where contacts deviated from horizontal within the CRF, their depth was logged at their midpoint. In the uppermost ~100 m of Hole GT1A, distinctive layers

were described as separate subintervals (marked with letters) to allow for more accurate descriptions of the different mineral modes and grain sizes between different layers within a single section. However, this approach was not continued after Igneous Interval GT1A-51. Below this interval, the differences between different layers were described qualitatively in the VCD comments.

After logging of each hole was completed, the igneous intervals were grouped into larger igneous units based on major trends and distinct changes in mineral modes and/or the appearance or disappearance of particular rock types. The descriptions of these major igneous units and nature of the boundaries or transitions between units are presented in summary tables for each hole (e.g., Table T2 in the Site GT1 chapter). These igneous unit, interval, and contact logs provide information about igneous unit, interval, and subinterval boundaries and a brief description of each (sub)interval, including the following:

- Unit number
- (Sub)interval number
- Depth of top (mCCD)
- Core-section-interval of the top
- (Sub)interval thickness
- Lithology
- Description of the upper and lower boundaries
- (Sub)interval description

Hole GT3A

The first step in describing core was identification of units on the basis of the presence of contacts, chilled margins, changes in primary mineralogy, color, grain size, and structural or textural variations. Within a range of characteristic lithology, a unit may have variations in texture, grain size, and modal amounts of constituent minerals. Igneous units in Hole GT3A were numbered continuously from top to bottom. Lithologically and texturally similar pieces from consecutive core sections were curated as belonging to the same igneous unit. New unit numbers were allocated even if units appeared similar but were separated by a lithologically distinct unit. To preserve important information about igneous stratigraphy without defining an unreasonable number of units within a single core, subunits were designated in cases where there were marked changes in texture without accompanying changes in mineralogy, or vice versa. In addition, crosscutting magmatic veins and thin dikes were also designated as subunits. Where contacts deviated from horizontal within the CRF, their depth was logged at their midpoint. The same approach was used to define top and bottom depth of chilled margins where practical.

Basis for the descriptions are recorded in Excel description sheets designed for capturing both quantitative and qualitative variations downhole and gen-

erating information for the VCDs. For each section, the following data were recorded:

- Core
- Section
- Top and bottom depth (mCCD)
- Unit
- Subunit
- Pieces in unit
- Unit lithology name
- Lithology modifier
- Lithology comment
- Top and lower contact of unit
- Nature of top contact
- Top contact geometry
- Chilled margin top
- Chilled margin bottom
- Chilled margin comment
- Intrusive contact relations comments
- General grain size of unit
- Grain size distribution
- Texture
- Texture comment

For dike rocks the following data concerning phenocrysts was also recorded (for plagioclase, clinopyroxene, and olivine):

- Phenocryst abundance
- Minimum, maximum, and average size
- Total phenocryst and vesicle abundance

For gabbros, the following mineralogical data were recorded (for olivine, plagioclase, clino- and orthopyroxene, amphibole, oxide, quartz, and sulfide):

- Mode
- Minimum, maximum, average grain size
- Habit
- Shape

For each unit in a section, a summary was included (VCD summary). Small-scale features such as grain size variations or presence of microxenoliths within a given section were recorded as comments in the corresponding VCD summary. All these data are included in Table T2 and the units are characterized in Table T3, both in the Site GT3 chapter. For each unit, the table lists the following:

- Unit number
- Involved sections
- Depth (mCCD) of its top
- Core-section-interval of the top of the unit
- Unit thickness
- Lithology
- Description of the upper and lower boundaries
- Unit description
- Subunits

Units and subunits were grouped into igneous groups based on major trends and distinct changes in mineral modes and/or the appearance or disappearance of particular rock types or igneous structures. The descriptions of these igneous groups and

nature of the boundaries or transitions between them are presented in a summary table for Hole GT3A (Table T2 in the Site GT3 chapter). For each igneous group, the table lists the following:

- Numbers of the involved units
- Depth (mCCD)
- Top and lower contacts
- Description of the upper and lower boundaries
- Description of the lithology

Phase 2

Holes CM1A and CM2B

The first step in describing core was identification of igneous unit boundaries on the basis of the presence of contacts, chilled margins, intrusive contacts, changes in primary mineralogy, color, grain size, and structural or textural variations. Within a range of characteristic lithology, a single unit may have variations in texture, grain size, and modal amount of constituent minerals. Units in Holes CM1A and CM2B were numbered sequentially from top to bottom. Lithologically and texturally similar pieces from consecutive core sections were curated as belonging to the same igneous unit. To preserve important information about igneous stratigraphy without defining an unreasonable number of units within a single core, subunits were designated in cases where there were smaller sized (centimeter to decimeter level) changes in texture, mineralogy, or both (marked with letters). Crosscutting magmatic veins or peculiar layers of interest (e.g., anorthositic, dunitic, or wehrlitic zones) were also designated as subunits. Where contacts deviated from horizontal within the CRF, depth was logged at their midpoint.

After logging of each hole was completed, the igneous units were grouped into larger sequences based on major trends and distinct changes in mineral modes and/or the appearance or disappearance of particular rock types. The descriptions of these major sequences and nature of the boundaries or transitions between the sequences, are presented in summary tables for each hole. All information about units and subunit boundaries and a brief description of each (sub)unit are summarized in Table CM1A_C_T1 in the Site CM1 chapter and Table CM2B_C_T1 in the Site CM2 chapter. For each (sub)unit, the table lists the following:

- Sequence number
- (Sub)unit number
- Depth (mCCD) of its top
- Core-section-interval of the top of the (sub)unit
- (Sub)unit thickness
- Lithology
- Description of the upper and lower boundaries
- (Sub)unit description

Holes BA1B, BA3A, and BA4A

The first step in describing core was identification of units (apparent thickness of a meter or more on the basis of the presence of contacts, changes in primary mineralogy, grain size, structural or textural variations, or color, often in conjunction with style of alteration and vein types). Within a range of characteristic lithology, a unit may have variations in texture, grain size, and modal amount of constituent minerals. Units in Holes BA1B, BA3A, and BA4A were numbered continuously from top to bottom. Lithologically and texturally similar pieces from consecutive core sections were curated as belonging to the same igneous interval. In order to preserve important information about igneous stratigraphy without defining an unreasonable number of units within a single core, subunits (minimum of ~10 cm size) were designated in cases where minor changes in texture and/or mineralogy, dike intrusions, or deformation features occurred. Magmatic intrusion-like features usually with sharp tectonic-like contacts to the ultrabasic host rocks are called dikes, whereas all typically meandering postmagmatic late features were defined as veins. Dikes or sets of joint dikes of size >10 cm were also designated as subunits. All dikes with an apparent size >5 mm were logged. Where contacts, faults, and mineralogical changes deviated from horizontal within the CRF, their depth was logged at their midpoint.

Macroscopic core description

Macroscopic descriptions are divided by lithology, mineralogy, contacts, texture, and alteration/secondary mineral assemblages.

Lithology

Plutonic rocks

Plutonic rocks were classified on the basis of abundance, grain size, and texture of their primary minerals (as inferred prior to alteration), based on the International Union of Geological Sciences (IUGS) system (Streckeisen, 1974; Le Maitre, 1989; Le Maitre et al., 2002). This classification defines the following rocks (Figs. F14, F15):

- Troctolite: olivine + plagioclase > 95% and both olivine < 90% and plagioclase < 90%.
- Olivine gabbro: olivine + plagioclase + clinopyroxene, none of which is <5%.
- Gabbro or diorite: plagioclase + clinopyroxene > 95%, 90% > plagioclase > 10%, and quartz < 5%.
- Gabbronorite: plagioclase + clinopyroxene + orthopyroxene, none of which is <5%.
- Quartz diorite: quartz 5%–20% of quartz + alkali feldspar + plagioclase (QAP), with alkali feldspar < 10% of alkali feldspar + plagioclase (AP).
- Tonalite: quartz 20%–60% of QAP, with alkali feldspar < 10% of AP.
- Trondhjemite: tonalite with total mafic mineral content < 10%.
- Dunite: olivine > 90%.
- Wehrlite: olivine + clinopyroxene > 95% and 90% > olivine > 40%.
- Anorthosite: plagioclase > 90%.
- Harzburgite: olivine + orthopyroxene > 95% and clinopyroxene < 5%.

In the IUGS classification, diorite is distinguished from gabbro by the anorthite content of plagioclase; diorites have plagioclase containing <50 mol% An, and gabbros have plagioclase containing >50 mol% An. Because this cannot be characterized during macroscopic description, we used the following convention:

- Diorite: gabbroic rock contains <5% quartz or primary amphibole, indicating a relatively high degree of fractionation.
- Gabbro: no quartz or primary amphibole was observed.

Minor modifications to the IUGS system were made to divide the rock types more accurately on the basis of significant differences rather than arbitrary cutoffs based on the abundance of a single mineral. We have attempted to follow as closely as possible the descriptions from Leg 209 (Kelemen et al., 2004) and Expeditions 304/305 (Blackman et al., 2006) and 309/312 and 335 (Teagle et al., 2006, 2012) to facilitate intersite comparison.

For gabbroic rocks, the following modifiers based on modal mineralogy are used:

- Disseminated oxide: 1%–2% Fe-Ti oxide.
- Oxide: >2% Fe-Ti oxide.
- Olivine-bearing: 1%–5% olivine.
- Orthopyroxene-bearing: 1%–5% orthopyroxene.
- Troctolitic: 5%–15% clinopyroxene and >20% olivine.
- Olivine-rich: >70% olivine.
- Anorthositic: >80% plagioclase.
- Hornblende-bearing: 1%–5% orthopyroxene (magmatic hornblende).
- Clinopyroxene-bearing: 1%–5% clinopyroxene.
- Plagioclase-bearing: 1%–5% plagioclase.
- Poikilitic clinopyroxene-bearing: >5% poikilitic clinopyroxene.
- Poikilitic plagioclase-bearing: >5% of poikilitic plagioclase.

Additional descriptive modifiers are defined as follows:

- Leucocratic: light colored, high proportions of plagioclase.
- Mela: prefix for rocks with color index > 65%.
- Micro: prefix for rocks with dominant grain size < 1 mm.

- Doleritic: fine- or medium-grained gabbroic rocks with dominant ophitic or subophitic texture.

In addition to the above list, the following definition and name was used for thin section descriptions.

- Hornblende gabbro: olivine + plagioclase + magmatic hornblende, none of which is <5%.
- Rodingitized = gabbroic or ultramafic rock that underwent Ca metasomatism due to hydrothermal alteration; describes whitish to yellowish rocks from various protoliths that contain at least one of the minerals diopside, clinozoisite, grossular or hydrogrossular (hydrogarnet), prehnite, or zonotlite, and those in which there has been pervasive destruction of primary minerals.

Volcanic rocks

For volcanic and hypabyssal rocks, we used the following definitions:

- Basalt: all igneous rocks of basaltic composition in the grain size range glassy to fine grained.
- Dolerite: holocrystalline, fine- to medium-grained rocks of basaltic composition with well-developed subophitic or ophitic textures.
- Diabase vs. dolerite: in English language usage the term “dolerite” is European in origin and functionally equivalent to the North American usage of diabase, which is the IODP standard term. However, in Japanese, the term diabase has a distinctly different meaning, referring to strongly altered (green) basaltic rocks and is expressed differently in Kanji script. This usage of diabase is also prevalent in Europe. We use the IODP standard term “diabase” for this project.

Basalt and diabase were divided according phenocryst content, using the following convention:

- Aphyric: <1% phenocrysts.
- Sparsely phyr: 1%–5% phenocrysts.
- Moderately phyr: >5%–10% phenocrysts.
- Highly phyr: >10% phenocrysts.

If present, phenocryst phases were placed as modifiers in front of the rock name with a hyphen in between. If <1% phenocrysts are present the rock is given the modifier “aphyr.”

Volcanic rocks are absent from Holes BA1B, BA3A, and BA4A except for a single small basaltic dike (grain size: glassy to fine grained).

Mineralogy

Plutonic rocks

In oceanic plutonic rocks, the primary rock-forming minerals are olivine, plagioclase, clinopyroxene, orthopyroxene, amphibole, Cr-spinel, Fe-Ti oxide, sulfide, and quartz. The following data are recorded in the igneous tab for each primary silicate:

- Modal percent (visually estimated): in fresh rocks—modal mineralogy as observed; in (partially) altered rocks—estimated igneous modes prior to alteration. When initial estimates of modal abundances include minerals in low (<10%) and moderate–high (>10%) modal abundances, the modal% of the more abundant phase is adjusted to make the sum 100%. Where a mineral occurs in trace quantities (i.e., too low to assign a meaningful modal percentage), <1% is recorded and eliminated from the total. Accessory phases are also noted where observed. Modal estimates were made independently by the same group of team members.
- Grain size: maximum and mean grain sizes of each of the major constituent minerals (olivine, plagioclase, clinopyroxene, orthopyroxene, and amphibole) measured in hand specimen along the long axis of each mineral.
- Mineral shape:
 - Euhedral
 - Subhedral
 - Anhedral
- Mineral habit:
 - Equant: aspect ratio < 1:2.
 - Subequant: aspect ratio 1:2 to 1:3.
 - Tabular: aspect ratio >1:3 to 1:5.
 - Elongate: aspect ratio > 1:5.
 - Interstitial.
 - Poikilitic.

The first four terms apply predominantly to subhedral or euhedral grains and the latter two generally to anhedral grains.

Volcanic rocks

In volcanic and hypabyssal rocks, the groundmass, phenocrysts (if any), and vesicles were described. For the groundmass, grain size was recorded using the following definitions:

- Glassy.
- Cryptocrystalline: <0.1 mm.
- Microcrystalline: 0.1–0.2 mm.
- Fine grained: >0.2–1 mm.
- Medium grained: >1–5 mm.
- Coarse grained: >5–30 mm.

For phenocrysts, the abundance (in percent); maximum, minimum, and median grain size (in millimeters) along the long axis; and shape were recorded for each phase. For vesicles, the abundance (in percent) was recorded.

Contacts

For contacts between units, the type, definition, geometry, and interpretation were described. Where the contact was not recovered this was noted. Contact types are as follows:

- Grain size: units on either side have markedly different grain sizes.
- Modal: units on either side have markedly different mineral proportions.
- Color: units on either side have markedly different primary (i.e., not alteration-related) color.

Where contacts are obscured by deformation and metamorphism, they are designated as follows:

- Sheared: interval with deformation fabric in contact with an undeformed interval.
- Foliated: both intervals have deformation fabrics.
- Tectonic: contact appears to be the result of faulting.
- Intrusive: one unit intrudes into another unit.
- Continuous: lithology continues after the bottom section.

Where an intrusive contact shows marked grain size reduction at contact with another unit, descriptions of “chilled margins” are included with top and bottom intervals recorded along with comments about the intrusive relations.

Contact definitions describe how well defined a contact is, using the terms

- Sharp
- Gradational
- Sutured (individual mineral grains interlock across the contact)

Contact geometry can be

- Planar
- Curved
- Irregular
- Anastomosing

Following description, contacts are interpreted as extrusive, intrusive, or igneous. The latter term is used for contacts in plutonic rocks where the units on either side of the contact were interpreted to form part of the same igneous package (e.g., a modal contact between cumulate layers or a grain size contact in a graded sequence).

The term “dike” refers to any sharp, well-defined, and relatively thick (>1 cm) crosscutting feature formed by injection of magma. This contrasts with “igneous vein,” which describes a thin (<1 cm) crosscutting feature formed by injection of magma with generally less well defined contacts.

Texture

Textures are defined on the basis of three categories: grain size, grain size distribution, and the relationships between different grains.

Grain sizes were defined as follows:

- Glassy.
- Cryptocrystalline: <0.1 mm.
- Microcrystalline: 0.1–0.2 mm.
- Fine grained: >0.2–1 mm.
- Medium grained: >1–5 mm.

- Coarse grained: >5–30 mm.
- Pegmatitic: >30 mm.

For plutonic rocks, grain size distributions were classed as follows:

- Equigranular: all minerals are of similar size.
- Seriate: continuous range of crystal sizes.
- Varitextured: domains with contrasting grain size.

For volcanic rocks, grain size distribution applies to phenocrysts only, using the following terms:

- Unimodal: all phenocrysts are of similar size.
- Bimodal: phenocrysts define 2 size populations.
- Seriate: phenocrysts form a continuous range of sizes.

The following terms were used to describe the textural relationships between different silicate grains (Fig. F16):

- Poikilitic: relatively large oikocrysts enclosing smaller crystals, termed chadacrysts, of one or more other minerals.
- Granular: aggregation of grains of approximately equal size.
- Intergranular: coarser grains (typically plagioclase) form a touching framework of the rock; interstices filled with crystalline material.
- Intersertal: coarser touching grains form a framework; interstices filled with glass.
- Subophitic: partial inclusion of plagioclase in clinopyroxene.
- Ophitic: total inclusion of plagioclase in clinopyroxene.
- Porphyritic: large grains in a finer-grained matrix.
- Comb structure: comb-like arrangement of crystals growing inward from a contact.
- Skeletal: either hopper crystals or with hour-glass shape.
- Dendritic: branching arrangement of elongate crystals.
- Porphyroclastic: characteristic mantle texture with porphyroclasts and neoblasts; visible foliation.

Similar to silicate minerals, the textures of oxide and sulfide minerals are described in terms of grain size and their relationship to adjacent minerals. In plutonic rocks, oxides commonly occur as aggregates; for grain size determination an aggregate is counted as a single grain.

Layering, where present, is divided into modal layering and grain size layering or combination of both; when neither term describes the observations well, the term “layering (other)” is used and the nature of layering is described in the comments. In all cases, the geometry of layering is described as follows:

- Sharp
- Gradational
- Irregular

- Anastomosing

Layering intensity is denoted by a number as follows, together with thickness of layering:

- 1 = weak (succession of <2 cm thick layers).
- 2 = moderate (succession of 2–10 cm thick layers).
- 3 = strong (layer thickness >10 cm or <3 layers in a single unit).

In Holes GT1A and GT2A, the confidence of the layering observation was ranked as follows:

- 0 = uncertain.
- 1 = likely.
- 2 = certain.

For Hole CM1A the gabbros are clearly layered and this confidence ranking was not recorded.

Magmatic textures in mantle peridotites are commonly strongly overprinted by high-temperature crystal-plastic creep processes. Consequently, primary igneous textures in mantle peridotites are extremely rare. Typical textures observed in mantle peridotites from Holes CM1A and CM2B and BA1B, BA3A, and BA4A (mostly characterized as porphyroclastic) are defined in [Structural geology](#) (see also Fig. [F16](#)).

Alteration/secondary mineral assemblages

For each Leg 4 unit and subunit, a macroscopic description of the alteration was captured including the following:

- Background alteration color
- Alteration percentage
- Textures (massive, fibrous, pseudomorphs)
- Background comments

In Holes BA1B and BA3A, individual alteration minerals were registered if recognizable by the naked eye. Thin section observations and XRD measurements provided additional information on the nature of alteration (see [Supplementary material > F3_XRD data](#)).

Halos accompanying dikes were categorized according to the following:

- Type of halo (vein vs. litho-contact).
- Apparent thickness of halo around dike.
- Halo alteration color.

Crosscutting relationships between dikes and veins were also observed, and a summary of alteration comment and vein summary was included in the VCD.

Thin section descriptions

Thin sections were described by members of the igneous, metamorphic, and structure teams and entered into a common Excel template. Observations made on thin sections were used to inform core descriptions and integrated into the igneous, metamorphic, and structural sections at each site. Estimates

were made of modes of primary and alteration minerals based on visual observation. Alteration and structural observations were entered in the comments section, and a list of photomicrographs with brief comments was added. The thin section description spreadsheets made during this description are available in [Supplementary material > B_Thin section descriptions](#).

Each whole thin section was digitally photographed in both plane-polarized light (PPL) and cross-polarized light (XPL) (see [Supplementary material > D1_Whole thin section images](#)). During Leg 2, images in reflected light (RL) were also taken when relevant for observations of opaque mineral phases. Thin section descriptions closely follow the procedure for macroscopic core descriptions. Where a thin section contained areas with different primary (i.e., not alteration-related) lithology, mineralogy, and/or texture, these were defined as domains (e.g., Domain 1, Domain 2, and so on). For thin sections with multiple igneous domains, a map of the domains is shown in the full thin section photomicrograph (see Fig. [F17](#) for an example). Domains were described separately, and their relative abundance was noted.

The following data were recorded in an Excel workbook for each thin section.

Lithology and texture

- Rock name (based on thin section observations), using the same definitions as those for macroscopic descriptions.
- Number of igneous domains.
- Nature of igneous domains, if any:
 - Contact between two units
 - Mix of two lithologies in one section
 - Presence of texturally different regions
- Igneous domain relative abundance (percent).
- Igneous domain number within thin section (igneous Domain 1, igneous Domain 2, igneous Domain 3, and so on); this parameter identifies each domain described in the mineralogy tab.
- Igneous domain lithology name; if only one domain is present, this is identical to rock name.
- Igneous domain grain size modal name:
 - Glassy
 - Cryptocrystalline
 - Microcrystalline
 - Fine grained
 - Medium grained
 - Coarse grained
 - Pegmatitic
- Igneous domain grain size distribution:
 - Equigranular
 - Seriate
 - Varitextured
 - Poikilitic

- Igneous domain texture:
 - Granular
 - Subophitic
 - Ophitic
 - Granophyric
 - Porphyritic
 - Intergranular
 - Intersertal
 - Granoblastic

The latter refers to a fine-grained granular metamorphic texture describing a high-grade metamorphic overprint, as defined during Expeditions 312 and 335 [Teagle et al., 2006, 2012]).

Mineralogy

- Igneous domain number: igneous domains defined in the lithologic/textural description.
- Igneous domain mineralogy:
 - Abundance (percent) of primary minerals preserved.
 - Estimated abundance (percent) of primary minerals prior to alteration.
 - Estimated proportions of mineral replacement by alteration (percent).
 - Maximum and median size, shape, habit, and special features of primary minerals, using the same conventions as macroscopic descriptions.
 - Individual comments for primary minerals.
 - Absorption colors and/or pleochroism for clinopyroxene, orthopyroxene, and amphibole.

For plagioclase, a qualifier for zoning was recorded using the following convention:

- 0 = none.
- 1 = zoning is rare and weakly developed.
- 2 = abundant zoning ranging weak–strong.
- 3 = nearly ubiquitous, generally strong zoning.

Characteristic colors, exsolutions, and other special features of constituent minerals are also described.

Alteration petrology

Phase 1

The description of alteration in the cores builds on practices developed during recent hard rock IODP expeditions including Expeditions 335, 345, 357, and 360 (Teagle et al., 2012; Gillis et al., 2014; Früh-Green et al., 2017; MacLeod et al., 2017b). The terms “alteration” and “metamorphism” in this report are used interchangeably without implication as to spatial scale or open- vs. closed-system processes. The characteristics of hydrothermal alteration or metamorphism of rocks recovered from Holes GT1A, GT2A, and GT3A were observed macroscopically aided by hand lens and in thin sections under a microscope. Macroscopic identification of minerals

was confirmed by microscopic observations of thin sections of representative intervals and by XRD analyses. Shipboard macroscopic and microscopic observations were recorded using alteration worksheets in the shipboard core logging spreadsheets, which are based on templates similar to those developed for core description using the JRSO application DESClogik. These data were then used to produce graphic section summaries (VCDs) that report alteration descriptions of each section and present down-hole variation of alteration characteristics. Microscopic observations were summarized in thin section form reports. The terminology and mineral abbreviations used for alteration descriptions are summarized in Tables T4 and T5 (Expedition 304/305 Scientists, 2006; Whitney and Evans, 2010; Früh-Green et al., 2017; MacLeod et al., 2017b). Core descriptions were completed in a collaborative fashion in which the team viewed the cores together, and then for continuity each member of the alteration team was responsible for one or more aspects of observation and description throughout each hole.

Macroscopic core description

Alteration log

All macroscopic observations were carried out on the archive section halves of the cores and logged as description intervals. Alteration was characterized into the following four distinct types (Fig. F18):

1. Background hydrothermal alteration,
2. Localized patchy alteration without apparent relationship to veins,
3. Alteration in halos with or without apparent relationships to veining, or
4. Alteration associated with deformation.

The relative proportion of each of these types was estimated for each alteration interval.

Alteration intensity, color of altered rock, shape, size, and texture of alteration styles, and abundance of secondary minerals were recorded in the “Alteration” worksheet (Fig. F19). The overall abundance of secondary minerals within each type of alteration present was estimated visually. Preliminary associations between secondary and primary minerals were made during macroscopic core description; secondary minerals and their relationships to the original igneous phases were ground-truthed using thin section observations, and identifications were verified with XRD analysis.

The variation of alteration intensity plotted on the graphic section summaries corresponds to the total alteration intensity. The graphic section summaries also contain a summary statement of the alteration characteristics for each section of core.

The procedures adopted for macroscopic observation and description of cores using the alteration Excel worksheets are summarized as follows:

1. Determine the number of alteration intervals in each section and assign each interval to a row in the worksheet. Log each individual interval (row) following Steps 2–10.
2. Estimate the proportion by area of the 4 alteration groups (background, patch, halo, and deformation).
3. Assign a color to each of the 4 alteration groups.
4. Estimate alteration intensity in surface-area percentage of each of the 4 groups to automatically generate a rank scale from the look-up table:
 - 0 = fresh (<3%).
 - 1 = slight (3%–10%).
 - 2 = moderate (>10%–30%).
 - 3 = substantial (>30%–60%).
 - 4 = extensive (>60%–90%).
 - 5 = complete (>90%).
5. Characterize the style of background alteration:
 - Patchy
 - Pervasive
 - Recrystallized
 - Banded
6. For patches of alteration, characterize patch shape and size:
 - Shape: round, irregular, elongate, network.
 - Size: <3 cm, 3–6 cm, >6 cm.
7. Identify the secondary minerals present in each of the 4 alteration groups and the mineral abundance in area percentage.
8. Record additional characteristic features of each alteration group in Comments.
9. Total alteration intensity is calculated automatically, and intensity rank is assigned to each interval.
10. Create a section summary description of total alteration to appear with the VCD for each igneous unit.

Vein and halo log

Veins are defined as linear cracks partially or completely filled with secondary minerals. Fractures are defined as linear cracks with no mineral fill. The term “halo” is used to describe alteration in the original rock spatially related to veins and fractures.

Veins and halos were described collaboratively by representatives from the alteration and structural geology teams, and data were recorded in the Veins worksheet of the shipboard core logging spreadsheets (Fig. F20). The alteration team was responsible for identifying each individual vein and recorded the following properties (Figs. F21, F22, F23):

- Vein type:
 - Vein net
 - Vein
- Secondary mineral percentage (vein nets only).
- Vein interval: section interval (cm) of the upper and lower intersections with the margin of the split face of the archive half of the core, or the greatest upper and lower extent of a vein. This approach allows the area percent (modal%) of specific veins and their mineral fills to be calculated. However, it is a different approach from that used in aspects of the structural team measurements, where only the crossing point of the core center-line was measured.
- Vein width: mean perpendicular width (mm).
- Vein attitude:
 - Vertical: vein extends across <50% of core width.
 - Inclined: vein extends across >50% of core width.
- Vein texture:
 - Massive
 - Cross-fiber
 - Slip-fiber
 - Vuggy
 - Polycrystalline
 - Crack-seal
 - Sheared
 - Patchy
 - Overgrowth
 - Brecciated
- Vein connectivity
 - Isolated
 - Single
 - Branched
 - Network
 - En echelon
 - Crosscutting
 - Ribbon
 - Parallel
 - Anastomosing
 - Overlapping
- Vein morphology
 - Planar
 - Curved
 - Irregular
 - Pull-apart
 - Fault vein
- Vein color.
- Crosscutting relationships: recorded as “x” if the vein is part of a crosscutting set.
- Vein generation: V1, V2, V3, etc., where V1 = earliest vein.
- Secondary minerals: estimated abundance (percent).
- Vein comments.
- Alteration halo half-width (mm).
- Alteration halo comments.

The structural geology team recorded the vein orientation; detailed methods can be found in [Structural geology](#). Veins were identified on the archive half, but vein orientations were measured by the structure team on the working half.

The above method was used for all of vein logging of Hole GT1A. However, for Hole GT2A, the vein log was refined to accelerate core description. Although all vein mineral assemblages continued to be identified and recorded, only veins >1 mm in width were fully recorded using the above list. Veins <1 mm in width within a section were considered to be a vein net. The total percent area within each section represented by veins <1 mm was estimated, and the overall secondary mineral composition estimated. In addition, the total number of veins within a section was counted in order to allow the vein intensity to be calculated in a comparable way to Hole GT1A.

Phase 2

Crust–mantle transition zone

The description of alteration in the cores from the crust–mantle transition zone Holes CM1A and CM2B (Leg 3) follows a modified version of the protocols set for logging Phase 1 Holes GT1A, GT2A, and GT3A, albeit with extra emphasis on alteration of ultramafic rocks.

During Hole CM1A and CM2B core description, the terms “metamorphism,” “alteration,” and “hydration” continue to be used loosely and interchangeably without implications about open- vs. closed-system behavior. The terms “serpentinization,” “rodingitization,” and “oxidation” are used to describe the predominant alteration types and imply a chemical change in the composition of the primary ultramafic or mafic rocks. As we were not able to macroscopically evaluate changes in bulk or mineral composition, we considered these reactions as primarily corresponding to addition of H₂O; addition or loss of calcium, silica, or other elements; or oxidation of ferrous to ferric iron.

Macroscopic core description

Alteration and vein logs. Macroscopic observations of the alteration and vein characteristics were carried out on the archive section halves of the cores and logged in Excel worksheets as description intervals for each section or subunit defined by the igneous team (see [Supplementary material](#) > E_Tabulated VCD data).

Alteration was characterized as follows, following Phase 1 convention:

1. Background hydrothermal alteration;

2. Localized patch alteration without apparent relationship to veins;
3. Alteration in halos with or without apparent relationships to veining; and
4. Alteration associated with deformation.

Secondary mineral identifications were confirmed by XRD, and the associations between secondary alteration and primary minerals were determined by polished thin section microscopy.

As for Phase 1, in Phase 2 veins are defined as linear cracks partially or completely filled with secondary minerals. Fractures are linear cracks with no mineral fill. The term “halo” describes alteration in the surrounding host rock, spatially related to veins and fractures.

Veins and halos were described collaboratively by the alteration and structural geology teams, and data were recorded in the Veins worksheet of the shipboard core logging workbooks. The variation of alteration intensity plotted on the graphic section summaries (VCDs) corresponds to the total alteration intensity. The graphic section summaries also contain a summary statement of the alteration and vein characteristics as well as vein densities for each section of core.

Individual and networks of veins and vein sets were recorded downsection in the Veins worksheet. Vein-free intervals were recorded in the Alteration worksheet. Where several vein types were present in an interval, these were recorded on separate rows. Similar to Phase 1, the following vein features were recorded as defined for the Gabbro Traverse sites (see [Vein and halo log](#), above) and guided by Figure [F22](#):

- Type (vein or vein net)
- Texture
- Structure
- Connectivity
- Morphology
- Color

Also recorded were

- Crosscutting relationships
- Vein generation
- Vein fill mineralogy
- Alteration halo characteristics

The structural geology team added vein orientations and vein densities to the Veins worksheet.

For the Hole CM1A and CM2B descriptions, a vein interval was defined as the section interval (in centimeters) of the upper and lower intersections with the margin of the split face of the archive half of the core, or the greatest upper and lower extent of a vein (Fig. [F21](#)). This approach allows the area percent (modal%) of specific veins and their mineral fills to be calculated. However, it is a different approach

from that used for the structural team measurements, where only the crossing point of the core centerline is measured (see F24). Vein width in millimeters is defined as the mean perpendicular width.

Alteration textures. Alteration textures and their relationships to the primary phases in mafic and ultramafic rocks are generally related to hydration of olivine, pyroxene, and plagioclase, where present. During ChikyuOman Phase 2 description of Hole CM1A and CM2B intervals, the following textures related to serpentinization, metasomatism, and oxidation were documented:

- Serpentinization: hydration textures after olivine and pyroxene; serpentine recrystallization textures and serpentine veins.
- Metasomatic: rodingitization and amphibole-chlorite-talc metasomatism.
- Oxidation: typically indicated by a change in color to more red/orange, occurring pervasively or locally. The color change is considered to be primarily related to iron oxidation.

Serpentine alteration textures. Harzburgitic rocks in the cores from Holes CM1A and CM2B are interpreted to be mantle rocks that experienced (1) high-temperature, dynamic metamorphic recrystallization during upwelling and melting in the mantle, in some instances creating macroscopically identifiable protogranular or porphyroclastic textures, followed by (2) a stage of lower temperature static replacement and/or dynamic recrystallization under lower temperature, hydrous conditions during emplacement and alteration near the seafloor or during obduction.

Rock names were assigned by the igneous group based on the primary phases that existed prior to hydration, serpentinization, or metasomatism. The altered ultramafic rocks show varying degrees of alteration, fracturing (some drilling-induced), and crystal-plastic deformation. Alteration in the ultramafic sequences is dominated by serpentinization reactions and serpentine-bearing mineral assemblages that progressively replace primary olivine and orthopyroxene. The main alteration products of olivine are serpentine, brucite, and magnetite. In altered peridotites, serpentine can be found as 5 different types with different crystallographic properties: lizardite, chrysotile, and rarely antigorite, as well as polygonal and polyhedral serpentines. Lizardite and chrysotile are the most common serpentine phases. Antigorite is not strictly a polymorph because of its slightly higher Si/Mg ratio compared to stoichiometric serpentine.

Textures of serpentines include three types: (1) textures after olivine and pyroxene hydration, (2) recrystallization textures, and (3) veins. We adopted the following definitions for the most common ser-

pentine occurrences (following Früh-Green et al., 2017):

- Mesh texture: serpentine texture after olivine that resembles a fisherman's net. It can be identified at the macroscopic scale but more easily at the microscopic scale. It develops along olivine grain boundaries and intragranular microfractures that define the mesh cells composed of mesh rims, generally of pseudocolumnar lizardite growing orthogonally to the hydration front and towards the mesh center, and mesh cores composed of olivine relics or isotropic serpentine. Mesh textures include the following:
 - Equant: contains mesh cells with rims of similar width.
 - Ribbon-shaped: has rims of different widths resulting from spatially heterogeneous serpentinization. This highlights a preferential orientation of hydration.
 - Hourglass: shows mesh rims reaching the cell center, and mesh cores do not exist.
- Bastite: serpentine texture after pyroxene (generally orthopyroxene). Serpentinization progresses from the pyroxene grain boundary, cleavage plane, and intragranular microfracture towards the center of the grain. This commonly results in a pseudomorphic texture mimicking the primary pyroxene shape and preserving important features of the protolith such as cleavages and plastic deformation.
- Interlocking texture: microscopically, this texture is composed of equant to spherulitic serpentine grains. It develops by recrystallization of a mesh texture or less commonly from a bastite texture.
- Interpenetrative texture: microscopically, this texture is composed of elongated serpentine grains that form blades with orientation that varies from random to preferential. It develops by recrystallization of a mesh texture or less commonly from a bastite texture.
- Fibrous serpentine veins: commonly lens-shaped in which continuous chrysotile fibers link the two walls of the vein. The fibers are commonly visible at the macroscopic scale.
- Serpentine banded veins: continuous veins presenting an infill composed of thin bands parallel to the vein walls. At the macroscopic scale the infill looks homogeneous.
- Lamellar granular isotropic serpentine veins: generally presenting irregular, nonmatching walls and homogeneous infill. At the microscopic scale they are filled with the following:
 - Serpentine lamellae growing from each wall of the veins towards its center.
 - Triangular-shaped serpentine sectors producing black cross-extinction under XPL.
 - Isotropic serpentine.

Magnetite is commonly present in the serpentinized peridotites, observed as tiny grains that concentrate along microfractures in the mesh or in serpentine veins. It forms after olivine hydration incorporating part of its iron under reduced and oxidized forms.

Brucite also forms during serpentinization of olivine and is potentially present in the mesh texture, along microfracture planes, or as veins. Further definitions are provided in the glossary in Table T6.

Rodingitization. The term “rodingite” is used for Si-poor, Ca-rich metasomatized mafic and ultramafic rocks associated with serpentinites and chlorite-rich zones (blackwall alteration) that are characterized by bulk loss of silica, enrichment in Ca, and a consequent increase of the Ca/Si ratio. Macroscopically, rodingites commonly appear as a dense white and pink to pinkish brown rock surrounding smaller, darker remnants of the ultramafic host rock or protolith. Typical calcium silicates formed during rodingitization reactions include clinozoisite, diopside, prehnite, vesuvianite, tremolite, and garnet or hydrogarnet (typically Ca-, Fe-garnets including grossular/hydrogrossular, hibschite, and andradite).

Oxidation. Here we use the term “oxidation” to imply that the Fe^{2+} in Fe-bearing silicate minerals in the ultramafic or mafic rock has been partly to completely oxidized to Fe^{3+} , which is reflected by a change in color to red or orange. This is due to low-temperature aqueous alteration (weathering) of the basement rocks and is well known along slow spreading ridges or in subaerial exposures. It produces minor to dramatic textural and compositional modifications, depending on the extent of reaction. Fe oxyhydroxides, clay minerals, and calcium carbonate fill multiple generations of brittle fractures. Oxidation, with formation of goethite and hematite, is one of the first steps of the weathering process. Oxidation of serpentinites commonly affects veins, mesh texture, and bastites. Strong weathering of mafic or ultramafic rocks typically includes precipitation of secondary low-temperature (phyllo)silicate minerals such as palygorskite, smectite, saponite, nontronite, and Fe-rich montmorillonite.

Mantle alteration zone vein petrology

Vein description in the Leg 4 cores from the mantle alteration Holes BA1B, BA3A, and BA4A follows modified versions of the protocols set up for Phase 1 OmanDP Chikyu core logging, which in turn builds on conventions adopted during recent hard rock IODP expeditions including Expeditions 335, 345, 357, and 360 (Teagle et al., 2012; Gillis et al., 2014; Früh-Green et al., 2017; and MacLeod et al., 2017b). Mineral abbreviations are given in Table T7. The names of minerals not listed in the table are given in full in the text.

Macroscopic core description

Vein logs. Macroscopic observations of vein characteristics were carried out on the archive section halves of the cores and logged in Excel worksheets using depth and vein types defined by the igneous team. Secondary minerals were ground-truthed using XRD, and the association between secondary alteration and primary mineralogy was determined by microscopy on thin sections. Veins were defined as cracks partially or completely filled with secondary minerals. The term “halo” was used to describe alteration in the original rock, flanking veins. Veins and halos were described collaboratively by the vein and structural geology teams, and data were recorded in the Veins worksheet of the shipboard core logging workbooks. The variation of vein density plotted on the graphic section summaries (VCDs) corresponds to the density of different vein types. In the Vein section of the reports for each hole, running averages of vein density as a function of depth are illustrated, weighted in various combinations by vein width and the presence of overlapping vein sets, as described in figure captions. The graphic section summaries also contain a summary description of vein characteristics.

Individual and networks of veins and vein sets were also recorded downsection in the Veins worksheet. Where several vein types were present in an interval, these were recorded on separate rows. Vein textures were recorded in terms of vein type (vein or vein net), texture, structure, connectivity, morphology, and vein color, as defined above in Phase 1 **Vein and halo log** and guided by Figure F22. Crosscutting relationships, vein fill mineralogy, and alteration halo characteristics were also recorded. The structural geology team added vein orientations and vein densities to the Veins worksheet.

Vein interval was defined as illustrated in Figure F21. For Hole BT1B, where possible (inclined or horizontal, individual veins crossing the core section), interval for individual veins corresponds to the upper and lower intersections of the vein contacts with the center line of the core. For vein sets and where individual veins are nearly vertical and coincide with the centerline of the core for a distance more $>3\text{--}5\times$ larger than the perpendicular width of the vein, the vein interval corresponds to the upper and lower intersections of the vein contacts with the edge of the core. Similarly, where nearly vertical veins do not cross the centerline of the core, the vein interval corresponds to the upper and lower intersections of the vein contacts with the edge of the core (Fig. F23). Vein width in millimeters is defined as the mean perpendicular width (Fig. F21).

For Holes BA3A and BA4A, the intervals for all veins and vein sets correspond to the upper and lower in-

tersections of the vein contacts with the edge of the core.

Vein density estimates were logged as in Legs 1, 2, and 3. In addition, for Holes BA3A and BA4A, an added column records estimates of the percent area occupied by a given vein or vein set within its depth interval.

Structural geology

The OmanDP structure team characterized and described the spatial orientation and intensity of a variety of structures ranging from magmatic layering, crystal-plastic fabric, veins, fractures, shear zones, and fault zones related to lower crust accretion, mantle deformation, serpentinization, hydrothermal alteration, and weathering of the ultramafic lithologies within the Samail ophiolite. The methods described here are organized following the down-temperature pattern of the deformation.

Conventions for structural studies established during previous hard rock drilling projects (e.g., ODP Legs 118, 131, 140, 147, 153, 176, 179, 206, and 209, Integrated Ocean Drilling Program Expeditions 304/305, 309/312, 335, and 345, and International Ocean Discovery Program [IODP] Expeditions 357 and 360 [Shipboard Scientific Party, 1989, 1991, 1992a, 1992b, 1992c, 1993a, 1993b, 1995, 1999, 2003, 2004; Expedition 304/305 Scientists, 2006; Expedition 309/312 Scientists, 2006; Expedition 335 Scientists, 2012b; Gillis et al., 2014; Fröh-Green et al., 2017; MacLeod et al., 2017b) were generally followed with minor adjustments during ChikyuOman Phase 1 and Phase 2 core description campaigns. Microsoft Excel worksheets were used to enter all observations and measurements made on the core and thin sections.

Structural orientations

Measurements

Structural features categorized as magmatic, crystal-plastic, or brittle, together with magmatic veins and igneous contacts, were logged by interval in centimeters from the top of each section in the archive half. Depth intervals of structures were recorded as the distance from the top of the section to the top and bottom of the feature, where the feature intersects the center of the section half surface (Fig. F24). This convention is different from the conventions used by the alteration team for mineral veins (see [Igneous petrology](#)).

Structures were measured on the working half relative to the standard IODP core reference frame (Fig. F5). The plane normal to the axis of the borehole is referred to as the horizontal plane, whether or not the borehole is vertical. On this plane, a 360 net is used with pseudosouth (180; $-x$ -direction) pointing

into the archive half and pseudonorth (000; x -direction) pointing from the split surface out of the archive half. The cut surface of the section half, therefore, is a vertical plane striking 090–270.

Apparent dip angles of planar features were measured on the split face of the working half of the core. To obtain a true dip value, a second apparent dip was measured, where possible, in a section perpendicular to the split face (second apparent orientation in Fig. F25). The two apparent dips and dip azimuths (or one apparent direction combined with the strike) measured for each planar feature were used to calculate the dip (0° – 90°) and dip azimuth (000–360) (i.e., the bearing of maximum dip in the CRF). If the feature intersected the upper or lower surface of the core piece, measurements of the strike could be made directly in the CRF, recorded as the trend of a line with zero dip angle, and combined with an apparent dip measurement, measured on the cut surface of the core, to calculate the true dip and dip azimuth in the CRF (Fig. F25). If a feature was exposed on the surface of the core (i.e., a fracture defining the top or bottom of a piece), the true dip and dip azimuth were measured directly on the feature with no need for additional measurement or calculation. All structural measurements made on the core were reported in the worksheets. True dip and dip azimuth in the CRF were calculated using a macro in Excel.

Where linear structural elements such as slickenlines on a fault surface were observed, the trend and plunge of the lineation were measured directly relative to the CRF. The sense of shear on fault surfaces is determined by features such as groove marks or steps in the slickensides. Senses of shear for magmatic fabrics and crystal-plastic fabrics (CPFs) were determined using the asymmetry of rotated crystals, porphyroclast-tail systems, or foliation deflection morphologies (e.g., Ramsay and Huber, 1987).

In many instances it was not possible to reconstruct the full shear sense on an individual structure or to make a complete lineation measurement but only to document the apparent offset of a feature on one surface of the core. During logging of Hole GT3A the structure team chose nevertheless to record such information even though it does not fully constrain the kinematics of the feature. In such cases they logged apparent offsets as dextral or sinistral displacements on the cut surface of the archive half of the core. In those cases where the true sense of shear could be determined, the appropriate terms were used. This applies for all structures but especially brittle structures and veins.

Core splitting and orientation

During the ChikyuOman Phase 1 and Phase 2 campaigns, core descriptions were made on the archive halves and structural measurements were made on the working halves unless otherwise noted. Initially

when the Site GT1 cores were described, cores were split to maximize the dip of planar structures so that the dominant magmatic fabric dips toward 090 in the CRF (see Fig. F25). However, it became evident that it was more valuable to preserve azimuthal continuity of the core by ensuring that the blue-red way-up line was consistently preserved in the archive half; hence from Section GT1A-60Z-3 downhole and for Holes GT2A, GT3A, BT1B, BM1A, CM2B, BA1B, BA3A, and BA4A, cores were cut perpendicular to the blue-red double line, which corresponds to pseudo-south (180; -x-direction) in the CRF.

The blue-red double line was drawn during on-site operations to identify the correct way up for the core and to ensure continuity of orientation relative to the vertical axis when the core pieces could be fitted back together. Drill site personnel were rigorous in determining whether adjacent cores were vertically contiguous, documenting every discontinuity in relative azimuthal core orientation. For example, in Sections GT3A-21Z-3 to 33Z-3 (22.92–56.88 mCAD), >30 m of core could be fitted together without any breaks, and in 13 more instances in Hole GT3A intervals of >10 m of contiguous core were recovered. In Sections BT3A-54Z-2 through 89Z-1 (113.35–216.07 mCAD), >100 m of core could be fitted together. In this way the OmanDP cores contrast with those recovered by offshore drilling (e.g., IODP), which are always much more discontinuous. Although the cores from Holes GT1A, GT2A, and GT3A and BA1B, BA3A, and BA4A are not azimuthally oriented, relative spatial information of high scientific value is preserved within each contiguous interval.

During core logging of Hole GT3A, a log of the discontinuities was made to supplement the on-site record of discontinuities in the DIS. This is particularly useful for within-section discontinuities that were only recorded on site by the definition of a new piece number and with no depth constraint.

In some instances, drill site personnel redrew the blue-red way-up line even when the core pieces were contiguous if it was evident that the existing line would result in a significant feature lying entirely in one half of the core or the other or if the orientation of the magmatic fabric changed substantially. In such cases the on-site team recorded the instances where a “way-up rotation” had been made; however, they did not note the magnitude of this rotation.

During Hole GT3A core logging the structural team attempted to retrieve this information by fitting the (now split) cores together; however, results were equivocal and these discrete points are therefore presented herein as additional discontinuities on the VCDs and in the Hole GT3A structural analysis.

Statistical analysis of true-dip vein and fracture data

Statistical analysis of the true dip of discrete planar features with small lengths compared to the length of the borehole, such as veins and fractures, requires an understanding of two geometrical effects classified as follows and defined below:

- The length-scale or spherical effect, which leads to over-representation of planar structures that are near-parallel to the borehole.
- The so-called borehole effect, which leads to preferential sampling of planar structures that are near-perpendicular to the borehole.

Length-scale or spherical effect

A purely random distribution of planes represented by poles within any given area on a unit hemisphere will, on average, contain the same number of poles, irrespective of the position on the unit sphere. Within any given dip interval, the number of poles is a function of the number of poles intercepting the corresponding arc on the unit sphere. By integration it can be shown that the number of planes (n) with a given dip (α) is obtained by

$$n = C \sin(\alpha), \quad (1)$$

where C is a constant. The resultant distribution for a theoretical random data set is shown in Figure F26. The dip data are biased such that there is over-representation of planar structures that are near-parallel to the borehole as a result of the spherical geometry effect on the true dip data.

Borehole effect

A further consideration is the effect of sampling bias introduced by orientation of the borehole (see Newmark et al., 1985). If we consider an equally spaced set of planes near-perpendicular to the borehole, then the number (n) encountered within a unit borehole length (l) is given by

$$n = l/s, \quad (2)$$

where s is the spacing of the planes. For planes near-parallel to the borehole, either 1 or 0 planes are encountered within the borehole. Thus, for the general case of dipping planes:

$$n = l \cos(\alpha)/s. \quad (3)$$

This effect tends to bias the data in favor of planes near-perpendicular to the borehole (Fig. F26).

Length-scale and borehole effects combined

Combining the two aforementioned effects results in the following relationship:

$$n = K \sin(\alpha) \cos(\alpha), \quad (4)$$

where K is a constant (i.e., scaling factor) and the distribution derived from Equation 4 results in a frequency maximum at 45° inclination to the borehole (Fig. F26).

If a set of planes has a maximum frequency of dips 45° to the borehole, then they are considered to have a random distribution. Consequently, we present a random distribution curve derived from Equation 4 on all appropriate frequency distribution plots for fracture and vein dips to help assess whether dip distributions are random or nonrandom.

If the length scale of structures such as magmatic contacts, layering, or CPFs considerably exceeds the width of the core, then the length scale or spherical effect does not apply. However, these features are still subject to the borehole effect, so structures near-parallel to the borehole will be undersampled relative to structures that are near-perpendicular to the borehole.

To correct for the aforementioned effects we follow the methodology proposed in Shipboard Scientific Party (1992c). For a more in-depth discussion the reader is referred to Martel (1999). Moreover, to allow a first-order comparison between different dip distributions for different data sets, such as amphibole and carbonate vein dips, we also calculated the Gaussian mean, standard deviation, and skewness for each distribution. In particular, we used the Gaussian standard deviation to quantify the range or width of any dip distribution and not as an estimate on the uncertainty of the mean dip.

Macroscopic description and terminology

Workflow organization

During the ChikyuOman core description campaigns (2017, 2018), the structural geologists worked together on the same shift, and each member of the team was responsible for making observations on a specific set of structure throughout the entire expedition (e.g., magmatic fabric, crystal-plastic fabrics).

Each core section was described and logged with detailed structural information and entered into Excel worksheets. The worksheets, listed below, contain data on the interval, type of structure, intensity, orientation, certainty of observation, crosscutting relationships, and comments.

- Magmatic fabric worksheet: magmatic contact characterization in conjunction with the igneous petrology team:

- Contact nature and geometry
- Compositional or grain size layering and fabrics
- Vein geometry, morphology, and composition
- Crystal-plastic fabrics/fabrics in peridotite worksheet:
 - Solid-state foliation morphologies
 - CPF intensity
 - Shear sense
- Veins worksheet: alteration vein data in conjunction with the alteration team:
 - Morphology
 - Width
 - Connectivity
 - Texture
 - Structure
 - Vein crosscutting relationships
- Brittle deformation worksheet:
 - Type of structure
 - Fault rock type
 - Intensity of brittle deformation
 - Apparent fault offset
 - Fracture morphology

A parameter about the “certainty” of the observed feature was included to qualify the degree of confidence related to identification of the logged structure, as follows:

- Uncertain: weakly characterized features.
- Likely: moderately defined structures.
- Certain: well-defined structures.

The most representative and/or prominent structural features in the cores from OmanDP are plotted on the VCD graphic reports (e.g., Fig. F11). Prominent structural features include intensity of magmatic fabric and CPF alignment, brittle deformation intensity, vein intensity, and precise locations of observed prominent structures, such as igneous contacts, magmatic layering and magmatic veins/dikes, alteration veins, vein networks, hydrothermal breccia, fault rocks, and shear veins. The dip and dip azimuth of the magmatic contacts, magmatic fabrics, and CPFs are also plotted on the VCDs. For Hole GT3A, continuity of the core was also plotted on the VCDs.

Short explanations for terms and abbreviations used in the respective structural categories are given below, based on definitions given in Ramsay and Huber (1987), Twiss and Moores (1992), Passchier and Trouw (2005), Fossen (2010), and Davis et al. (2011).

Magmatic structures

Intrusive and structural contacts

Intrusive and structural contacts were measured and described in accordance with the igneous petrology worksheet (plutonic) (see [Igneous petrology](#)). Structural descriptions and measurements refer to the top contact of the lower unit and include the following:

- Top contact type:
 - Grain size

- Modal
- Color
- Sheared
- Foliated
- Tectonic
- Continuous
- Top contact relationship:
 - Sharp
 - Gradational
 - Sutured (contacts where individual mineral grains interlock across the contact)
- Top contact geometry:
 - Planar
 - Curved
 - Irregular
- Orientation in CRF:
 - Dip
 - Dip azimuth

Magmatic layering

Magmatic layering, where present, was measured and described in accordance with the plutonic worksheet in the macroscopic workbook. Descriptions include the following:

- Nature of layering:
 - Grain size layering
 - Modal layering
 - Grain size and modal boundary or contact
 - When none of these terms describes the observations well, the nature of layering is described in the comments.
- Nature of layering boundary:
 - Sharp
 - Gradational
- Geometry of layering:
 - Irregular
 - Planar
 - Curved
 - Anastomosing
- Layering intensity rank:
 - 0 = not applicable; no layering observed.
 - 1 = weak.
 - 2 = moderate.
 - 3 = strong.
- Certainty of the observed feature:
 - 0 = uncertain.
 - 1 = likely.
 - 2 = certain.
- Perpendicular thickness of the layers.
- Orientation where measurable in the CRF:
 - Dip
 - Dip azimuth

Magmatic fabric

Magmatic fabrics were defined by the presence and intensity of any shape-preferred orientation (SPO) of

magmatic phases. A magmatic fabric intensity of 0 was attributed to intervals characterized by isotropic texture and/or where no igneous textures are preserved due to crystal-plastic overprint. Descriptions of magmatic fabric were captured in the Magmatic fabric worksheet and include the following:

- Geometry of magmatic fabric:
 - Linear
 - Planar
 - Planar-linear
 - Anastomosing/irregular.
- Magmatic fabric intensity accompanied by intensity rank (Fig. F27):
 - 0 = isotropic.
 - 1 = weak.
 - 2 = moderate.
 - 3 = strong.
- Certainty of the observed feature:
 - 0 = uncertain.
 - 1 = likely.
 - 2 = certain.
- Sense of shear:
 - Normal (n)
 - Reversed (r)
 - Dextral (d)
 - Sinistral (s)
 - Combination (nd, ns, rd, or rs)
 - Unknown
- Magmatic phase(s) defining the SPO:
 - 1 = olivine.
 - 2 = plagioclase.
 - 3 = pyroxene.
 - 4 = oxide.
 - Combinations (e.g., plagioclase-pyroxene).
- Orientation of the magmatic fabric where measurable in the CRF:
 - Dip
 - Dip azimuth
 - Trend of lineation
 - Plunge of lineation

Magmatic veins

Magmatic veins and thin dikes were measured, and described in accordance with the following:

- Magmatic vein type:
 - Anorthosite
 - Basalt
 - Gabbro
 - Diorite
 - Tonalite
 - Trondhjemite
 - Other
- Contact nature:
 - Sharp
 - Gradational

- Sutured (individual mineral grains interlock across the contact)
- Contact geometry:
 - Planar
 - Curved
 - Irregular
- History and crosscutting relationships of the veins and dikes as a comment.
- Orientation (dip azimuth and dip angle of contact dike or vein).

Crystal-plastic fabrics

CPF's include planar or linear fabrics defined by crystals exhibiting plastic deformation. Descriptions for CPF's were captured in the crystal-plastic fabrics worksheet and include the following:

- CPF geometry:
 - L = linear.
 - S = planar.
 - L-S = planar-linear.
 - Gradational.
 - Anastomosing/irregular.
- Deformation intensity, after petrographic thin section inspection, when possible (Fig. F27):
 - 0 = undeformed (0).
 - 1–2 = two stages of foliation development.
 - 3 = protomylonitic.
 - 4 = mylonitic.
 - 5 = ultramylonitic.
- CPF boundary sharpness:
 - Sharp
 - Diffuse
- Sense of shear (apparent):
 - Normal (n)
 - Reversed (r)
 - Dextral (d)
 - Sinistral (s)
 - Combination (nd, ns, rd, or rs)
 - Unknown
- CPF perpendicular thickness (cm).
- Orientation of the CPF (dip and dip azimuth, where measurable in the CRF; in practice, almost exclusively foliation planes).
- Certainty of the observed feature (CPF intensity or sense of shear):
 - 0 = uncertain.
 - 1 = likely.
 - 2 = certain.

Fabrics in peridotites

Mantle peridotites represent a special problem for grading crystal-plastic deformation because they commonly show high-temperature crystal-plastic creep processes and therefore lack a primary igneous texture. They generally have either protogranular or porphyroclastic textures when unmodified by late

deformation processes. Protogranular textures are generally the earliest fabric and are characterized by smoothly curved grain boundaries with complex cusps and lobes (Fig. F27). However, alteration has commonly entirely obscured olivine grain size and shape in hand specimens in the peridotites, and visual core description is almost entirely based on pyroxene and spinel textures. Crystal-plastic deformation grades (Fig. F28), therefore, are as follows:

- 0 = purely protogranular texture; earliest formed texture, may or may not have a preferred crystallographic mineral fabric or shape fabric. Porphyroclastic textures are generally superimposed on protogranular textures, and frequently elements of both are present; we used the name of the predominant texture. Intensity grade 0.5 indicates that elements of both textures are prominent.
- 1 = porphyroclastic texture defined by relict orthopyroxene if there is only weak or no pyroxene shape fabric developed.
- 2 = porphyroclastic pyroxene exhibits a significant shape fabric, noting that only a few protogranular textural elements are present; these intervals are still referred to as porphyroclastic.
- 3 = protomylonite; shape fabric is strong with well-developed foliation accompanied by significant grain size reduction. Protogranular peridotites generally have a pyroxene grain size ~3–6 mm. At this grade, there are generally no relict protogranular textural elements.
- 4 = mylonite peridotite has significant grain size reduction and consists of a fine-grained mass of olivine with embedded pyroxene porphyroclasts and prominent foliation.
- 5 = ultramylonite; no foliation is visible because of extreme grain size reduction.

This deformation scale closely parallels that used for gabbro here and during previous legs/expeditions and represents very similar or the same intensities of deformation at each grade.

Brittle structures

Brittle structures described during the ChikyuOman core description campaigns include faults, defined as fractures with shear displacement, and joints, defined as fractures with no shear displacement and no mineral fill. We use “fracture” as a general term indicating a brittle failure with or without displacement. Crack/fracture density per 10 cm was recorded. Also the most prominent shear veins (e.g., Passchier and Trow, 1996), hydraulic (or hydrothermal) breccia veins, and cataclastic zones were recorded.

Descriptions captured in the brittle deformation worksheet include the following:

- Type of fracture, e.g.:
 - Slickenside

- Fault zone
- Cataclastic zone
- Hydrothermal breccia vein
- Shear vein
- Shear zones (brittle-ductile)
- Fault rock type (in the core of the fault), e.g.:
 - Fault gouge
 - Fault breccia
 - Cataclasite
 - Foliated cataclasite
 - Hydrothermal breccia
 - Pseudotachylite
- Fault rock cohesion:
 - 1 = incohesive.
 - 2 = semicohesive.
 - 3 = cohesive.
- Damage zone thickness (cm).
- Apparent fault offset (cm), where measurable.
- Sense of shear (apparent):
 - Normal (n)
 - Reversed (r)
 - Dextral (d)
 - Sinistral (s)
 - Combination (nd, ns, rd, or rs)
 - Unknown
- Crack/fracture density (Holes CM1A and CM2B):
 - 0 = no fractures.
 - 1 = <1/10 cm.
 - 2 = 1–5/10 cm.
 - 3 = >5/10 cm.
- Fracture and vein density (Holes BA1B, BA3B, BA4A):
 - 0 = no main fractures/veins (networks of serpentinite veinlets are widespread downhole are not counted in the density value).
 - 1 = 1/10 cm.
 - 2 = 2–5/10 cm.
 - 3 = 5–15/10 cm.
 - 4 = 15–20/10 cm.
 - 5 = >20/10 cm.
- Brittle deformation intensity for fabrics, based on the density of fracturing or percentage of matrix vs. clasts present in each fault rock (Fig. F27); thin section descriptions, wherever available, aided this categorization:
 - 0 = mostly undeformed.
 - 1 = minor fracturing.
 - 2 = moderate fracturing.
 - 3 = fracturing with incipient grain size reduction and clast rotation.
 - 4 = well-developed cataclasis (with evident grain size reduction and clast rotation).
 - 5 = ultracataclasite (or fault gouge).
- Certainty of the observed fault rock:
 - 0 = uncertain.
 - 1 = likely.
 - 2 = certain.

- Damage zone/fracture perpendicular thickness (cm).
- Clast in fault rock (percent).
- Matrix in fault rock (percent).
- Average size of clast in fault rock (mm).
- Fracture morphology (Fig. F29):
 - Planar
 - Curved
 - Irregular
 - No open fractures if none were recorded
- Fracture network morphology (Fig. F29):
 - Stepped
 - Splayed
 - Anastomosing
- Orientation (dip and dip azimuth) of fracture and trend and plunge of associated lineation (e.g., slickenlines/slickenfibrs).

Fault rock characterization refers to the core of the fault/cataclastic zone or is a general estimation of the overall damage zone.

In the brittle deformation worksheet we reported as a note where brittle fabrics overprint CPFs or the structure can be considered as brittle-plastic (semibrittle).

For Site GT2, a semiquantitative scale of the general fracturing and veining intensity per each section (intensity per ~1 m of core) was used during core description.

We assigned specific values to visual intensity estimates according to spacing of veins, volumetric occurrence of veins, percentage of matrix in cataclastic zones, and partitioning of deformation structures:

- Slight (1 = 5%–10%).
- Moderate (2 = 10%–40%).
- High (3 = 40%–70%).
- Complete (4).
- Evenly distributed (E).
- Heterogeneously distributed (H).
- Localized (L).

Alteration veins

Alteration vein descriptions during ChikyuOman Phases 1 and 2 were captured in the veins worksheet (see **Igneous petrology**). Much of the vein information was characterized and recorded by the alteration petrology team including vein type, width, texture, structure, mineralogy, and vein halo. The structure team was responsible for observing and recording vein sense of shear, offset, true thickness, orientation, and vein density. Structural descriptions of veins include the following:

- Sense of shear:
 - Normal (n)
 - Reversed (r)
 - Dextral (d)
 - Sinistral (s)

- Oblique (o)
- Combination (e.g., nd, ns, rd...)
- Unknown
- Vein offset (mm), if present/measurable.
- Orientation of the vein where measurable, of associated lineation in the CRF:
 - Dip
 - Dip azimuth
 - Trend
 - Plunge
- Vein density: number of veins per core (Fig. F27):
 - 0 = no veins.
 - 1 = <1/10 cm.
 - 2 = 1–5/10 cm.
 - 3 = 5–10/10 cm.
 - 4 10–20/10 cm.
 - 5 = >20/10 cm.

Microstructure description and terminology

Workflow organization

To better characterize different types of deformation, we studied the microstructural features of interesting and/or prominent mesoscopic structures. Thin sections were examined to determine the following:

- Characterize the microstructure of the rocks,
- Confirm macroscopic descriptions of structures,
- Document crystal-plastic and brittle overprinting of magmatic fabrics,
- Provide information on the kinematics of deformation,
- Identify crosscutting relationships between magmatic and crystal-plastic deformation and alteration processes, and
- Document downhole strain variations.

Shipboard thin sections were systematically oriented relative to the CRF, as marked on each thin section (see Fig. F5). Marking two directions is necessary to achieve unambiguous orientation of the thin sections cut parallel to the cut surface of the core. Digital photomicrographs were taken to document microstructures that best illustrate deformation styles, crosscutting relationships, and intensity. Microstructural notes were entered into the shipboard thin section worksheets for each thin section.

Microstructure terminology

We followed, with minor changes, the terminology used during Legs 153, 176, and 209 and Expeditions 304/305, 345, and 360 (Expedition 304/305 Scientists, 2006; Gillis et al., 2014; MacLeod et al., 2017b).

In the worksheet we described the following microstructural features for each thin section:

- Intensity of magmatic fabric and rank:
 - 0 = isotropic.
 - 1 = weak.
 - 2 = moderate.
 - 3 = strong.
- Intensity rank of overall CPF (Fig. F27):
 - 0 = undeformed.
 - 1 = weakly foliated/lineated.
 - 2 = moderately foliated/lineated.
 - 3 = porphyroclastic/protomylonitic.
 - 4 = mylonitic/blastomylonitic.
 - 5 = ultramylonitic.
- Brittle deformation intensity:
 - 0 = undeformed.
 - 1 = minor fracturing.
 - 2 = moderate fracturing.
 - 3 = fracturing with incipient grain size reduction and rotation.
 - 4 = well-developed cataclasis (with evident grain size reduction and clast rotation).
 - 5 = ultracataclastic.
- Comments: specific notes including any particular feature or special minerals, textures, sense of shear, or shape-preferred orientation.

Metamorphic rock description, Site BT1

Hole BT1B is unique in the Oman Drilling Program, and in the annals of ODP and IODP because the core was exclusively composed of metamorphic rocks. Although many of these lithologies had igneous protoliths, most are so fully recrystallized and, in many cases, so completely chemically modified that they contain no relict minerals from the protolith. More than half of the core is composed of listvenites, which are fully carbonated mantle peridotites composed of quartz + magnesite and/or dolomite + Fe oxides and oxyhydroxides ± chrome spinel ± fuchsite. Even among specialists in metamorphic petrology, studies of listvenites are unusual and not well known. For these reasons, special rock description procedures were adopted for the core from Hole BT1B.

Host rock

Banding vs. veins

Given that much of the core contains mineral banding, also known as mineral segregations, in which some bands are anastomosing or crosscutting, it was important to establish a distinction between banding and veins. In this report, banding is considered to be a set of many subparallel segregations with spacing dimensions approximately equivalent to their true width extending over tens of centimeters

perpendicular to banding and commonly folded or undulating with irregular band contacts. In contrast, veins cut the banding and foliation of the host rock as well as massive portions of the host rock. Veins typically are tabular with sharp contacts and are commonly monomineralic or bimineralic. Similarly, fractures are tabular crosscutting features with sharp contacts. Fractures are narrower than 100 μm and/or have no evident minerals within them. The term “halo” is used to describe host rock alteration that is spatially related to veins and fractures, the intensity of which gradually decreases with distance from the corresponding vein or fracture.

Shear zones and breccias are common in the listvenite sections of the core. In some cases, they extend for tens of centimeters along the core and host smaller veins, fractures, and shear zones. We used an arbitrary cutoff of 20 cm “true thickness” (perpendicular to planar contacts) to distinguish larger shear zones and breccia intervals, which are part of the host rock, from localized deformation features.

Core description teams

Core descriptions were performed by three teams working together. One team focused on host rock petrology, a second focused on vein petrology, and a third focused on structural geology. The structure group worked closely with both petrology groups to measure and tabulate the geometry of banding and foliation in the host rock and the geometry of veins cutting the host rock. The structure team also was tasked with observing and quantifying zones of localized deformation including ductile and cataclastic shear zones and fractures, joints, and microcracks. The methods used by the three teams are described in order below.

Each member of a team was responsible for one or more aspects of the description to ensure consistency of recorded observations throughout the core, but the entire team met and coordinated on a daily basis.

In addition to logging macroscopic observations of the core, all three teams described thin sections taken from representative core units. Each whole thin section was digitally photographed in PPL, XPL, and cross-polarized reflected light (XPRL) (see [Supplementary material > D1_Whole Thin Section Images](#)). Note that routinely obtaining reflected light photomicrographs for every whole thin section differs from the methods for Sites GT1, GT2, and GT3.

Host rock petrology

The host rock petrology team’s role was to identify and describe the host rock of the cores—the host material for veins, shear zones, and vugs. The team was charged with identifying and logging the overall

host rock lithology of a section, the nature of the banding in the section, the host rock grain size, and contacts between distinct host rock units, as well as recording in as much detail as possible the major and minor mineral phases present in each section. As logging progressed, the host rock petrology team identified major host rock unit contacts separating units containing common textural and/or mineralogical characteristics spanning many meters to tens of meters. Host rock units in Hole BT1B were numbered continuously from top to bottom. Where contacts between distinct host rock units deviated from horizontal within the core reference frame, their depth was logged at their midpoints.

When major lithologic changes occurred and after logging each hole was completed, the host rock units were grouped into larger host rock groups based on major trends and distinct changes in texture and/or mineral proportions. The descriptions of these major host rock groups and the nature of the boundaries or transitions between units and groups are presented in the “Host rock” section of the chapter for each site.

Macroscopic core description of host rock petrology

Macroscopic descriptions were divided into the following categories of host rock lithologies based on abundance, grain size, and texture of their minerals. Note that some categories are partially redundant because it is not always possible to assign highly specific lithologic names. Thus, choices include dunite, harzburgite, lherzolite, and peridotite. The latter refers to any of the previous three lithologies in cases in which it is not possible to make a more specific determination of mineralogy during macroscopic core description.

- **Dunite:** relict mantle minerals or clearly identifiable pseudomorphs are present, and it is apparent that the host rock was composed of >90% olivine prior to alteration.
- **Harzburgite:** relict mantle minerals or clearly identifiable pseudomorphs are present, and it is apparent that the host rock contained 40%–90% olivine, 10%–60% orthopyroxene (enstatite-hedenbergite), <10% plagioclase, and <5% clinopyroxene (diopside-augite) prior to alteration.
- **Lherzolite:** relict mantle minerals or clearly identifiable pseudomorphs are present, and it is apparent that the host rock contained 40%–90% olivine, 5%–55% orthopyroxene, 5%–50% clinopyroxene, and <10% plagioclase prior to alteration.
- **Peridotite:** relict mantle minerals or clearly identifiable pseudomorphs are present, and it is apparent that the host rock contained >40% olivine and <10% plagioclase prior to alteration.

- **Listvenite:** >90% of the host rock volume is composed of magnesite and/or dolomite + quartz (\pm chalcedony \pm opal) + <10% Fe oxides and oxyhydroxides, with <10% ferromagnesian silicate minerals. Listvenites in Site BT1 core commonly contain relict chromian spinel and/or chromian mica (fuchsite and chromian muscovite), but this is not a requirement for rocks to be classified as listvenite in this report. When the rock clearly contains >70% quartz, the modifier “silicified” is used. When the rock clearly contains <30% quartz, the modifier “silica poor” is used. We recognize that if this lithologic name is taken out of context, it could be erroneously applied to a variety of sedimentary rocks. However, at Site BT1 all host rock lithologies with this composition are inferred to have formed through alteration of peridotite.
- **Magnesite listvenite:** listvenite as above in which the carbonate minerals are >75% magnesite.
- **Dolomite listvenite:** listvenite as above in which the carbonate minerals are >75% dolomite.
- **Serpentinite:** >80% of the host rock volume is composed of serpentine phases, and there are <5% relict mantle minerals or identifiable pseudomorphs.
- **Ophicalcite:** >80% of the host rock volume is composed of serpentine + carbonate phases, >20% of which is composed of carbonate minerals.
- **Alluvium:** present in the top of the core.
- **Chromitite:** >40% of the host rock volume is composed of relict chromian spinel.
- **Metabasalt:** identifiable mafic metamorphosed volcanic host rock.
- **Metavolcanic:** identifiable metamorphosed volcanic host rock.
- **Greenstone:** massive actinolite-pumpellyite, (sub)greenschist, or amphibolite facies metamorphic host rock; unclear if the host rock is metasedimentary or metavolcanic.
- **Shale:** very fine grained metasedimentary host rock. Slates or mudstones are not identified.
- **Phyllite:** foliated fine-grained metasedimentary host rock.
- **Schist:** strongly foliated metasedimentary host rock with macroscopic chlorite and/or micas and/or amphiboles.
- **Amphibolite:** metamorphic host rock with >40% amphibole.
- **Chromite bearing.**
- **Silicified:** host rock with higher SiO₂ concentration than the inferred protolith, caused by the addition of SiO₂ or removal of other components during fluid-rock reaction. For listvenites, host rock with >70% quartz.
- **Low silica:** host rock with lower SiO₂ concentration than the inferred protolith, caused by the removal of SiO₂ or addition of other components during fluid-rock reaction. For listvenites, host rock with <30% quartz.
- **Leucocratic:** >70% light-colored minerals as viewed on the cut surface of the core (quartz, feldspars, carbonates, etc.). In some cases, very fresh plagioclase is dark on the cut surface, but plagioclase-rich rocks are still be classified as leucocratic.
- **For estimation of colors,** we used the Munsell Standard Soil Color Charts. Often used color names include reddish orange, dark red, dark reddish brown, greyish olive.
- **Melanocratic:** >70% dark-colored minerals as viewed on the cut surface of the core (amphibole, oxides, serpentine, etc.).
- **Partially serpentinized:** modifier for peridotite, dunite, harzburgite, and lherzolite with 30%–95% serpentine minerals in the host rock.
- **Fuchsite bearing.**
- **Carbonate bearing.**
- **Quartz bearing.**
- **Quartz + carbonate bearing.**
- **Brucite bearing.**
- **Psammitic:** silty to sandy metasedimentary bulk composition.
- **Pelitic:** peraluminous (formerly “clay rich”) metasedimentary bulk composition.
- **Mafic:** inferred bulk composition with <55 wt% SiO₂.
- **Volcanoclastic:** (meta)sediment formed from volcanoclastic rocks (pyroclastic rocks, volcanic ash, mudflows, pumice, etc.).
- **Amygdule bearing:** containing vesicles (gas bubbles) filled with secondary minerals.
- **Vesicular:** containing unfilled vesicles.
- **Pillow structured:** containing recognizable pillow basalt texture.

The following modifiers based on modal mineralogy were used:

- Graphite bearing.
- Fe oxide bearing.
- Hematite bearing.

Mineralogy of the host rock

Four main rock types form the host rock in the Site BT1 core: listvenite, serpentinite (and perhaps lesser amounts of serpentinized peridotite), metasediment, and metavolcanic lithologies. Minerals in each of these lithologies are listed here and in Table T8, with abbreviations in brackets. Abbreviations are from Whitney and Evans (2010) where possible. Some

mineral names are redundant, which allowed teams to choose names of mineral groups (e.g., serpentine, Fe oxide) where identification of specific minerals (e.g., chrysotile and magnetite) was not possible.

The primary rock-forming minerals in listvenite are

- Carbonates (Carb): magnesite (Mgs), dolomite (Dol), calcite (Cal).
- Quartz (Qz): including chalcedony and perhaps opal.
- Fe oxides and Fe oxyhydroxides (FeOx): magnetite (Mag), hematite (Hem), goethite and all other Fe oxyhydroxides (Gth).

Important and ubiquitous minor phases include chromian spinel (Chr) and chromian mica (Fuc).

Serpentinites are mainly composed of

- Serpentine group minerals (Serp): antigorite (Atg), chrysotile (Ctl), lizardite (Lz), and proto-serpentine.
- FeOx: locally with relict olivine (Ol), pyroxene (Pyrx), orthopyroxene (Opx), clinopyroxene (Cpx).
- Chromian spinel (Chr).
- Gold (Au).
- Ni-As-S.

The primary rock-forming minerals in metasediment and metavolcanic lithologies are

- Quartz (Qz).
- Plagioclase (Pl).
- Calcite (Cal).
- Amphibole (Amph): actinolite (Act) and perhaps riebeckite (Rbk).
- Epidote (Ep).
- Clinozoisite (Czo).
- Pumpellyite (Pmp).
- Chlorite (Chl).
- Muscovite (Ms).
- Clay (Clay): smectite (Sme), illite (Ilt), montmorillonite (Mnt), saponite (Sap), etc.

Additional minor phases in listvenite and Serp may include

- Graphite (Gr).
- Talc (Tlc).
- Apatite (Ap).
- Sulfides (Slfd): pyrite (Py), chalcopyrite (Ccp), pentlandite (Pn).
- Sulfates (Slft): gypsum (Gp), anhydrite (Anh), barite (Brt).
- Brucite (Brc).

Minor phases in metasediment and metavolcanic lithologies may include

- Crossite (Crt).
- Stilpnomelane (Stp).
- Prehnite (Prh).
- Lawsonite (Lws).
- Dolomite (Dol).
- Titanite (Ttn): also known as sphene.

- Ilmenite (Ilm).
- Apatite (Ap).
- Graphite (Gr).
- Au.
- Sulfides.
- Sulfates.

Visually estimated modes of minerals are recorded in the host rock petrology worksheets. Because the main minerals in listvenite are often smaller than 100 μm (with the exception of chromite, which can reach 1 mm), it was not possible to accurately quantify the mode in vol%. Instead, we used rank numbers, with 1 for the most abundant mineral, 2 for the second most abundant mineral, and 3 for the third most abundant mineral. The modal estimates were checked by microscopy. Where a mineral occurs in trace quantities (i.e., too low to assign a meaningful modal percentage), 0.5% is recorded. Modal estimates were made independently by the same group of team members.

Texture of the host rock

The following textural characteristics of the host rock are recorded in the host rock petrology worksheets:

- Volume proportion of host rock, veins, localized deformation features (breccia, ductile shear zones, cataclastic shear zones), and vugs in a given section or lithologic unit. For veins we used two categories: > 1 mm and < 1 mm (vol%).
- Grain size: mean grain size and the nature of grain size variability of the host rock were recorded. Grain size is ranked as follows:
 1. Glassy/amorphous (isotropic in thin section).
 2. Cryptocrystalline: visible grains are <100 μm .
 3. Microcrystalline: grains are 100–200 μm .
 4. Fine grained: grains are 200–1000 μm .
 5. Medium grained: grains are 1–5 mm.
 6. Coarse grained: grains are 5–30 mm.
 7. Grains > 30 mm.
 8. Undeterminable.
- Grain size variability of the host rock is classified as follows:
 - Equigranular: standard deviation of grain size measurements <33% relative, or for very fine grained rocks, not measurable.
 - Seriate: somewhat uniform grain size variation over a range >33% of the mean value.
 - Porphyroblastic/porphyroclastic: bimodal or trimodal grain size distribution with clearly distinct classes having different grain sizes.
- Contacts between mineralogically distinct bands and segregations in banded matrices and contacts between lithologic units are recorded. Both types of contacts are classified based on contrasts in the following:
 - None (lithologic units with no banding),

- Mineral proportions.
- Grain size.
- Grain shape.
- Grain orientation.
- Color.
- Vein type.
- Host rock banding or foliation intensity was ranked using the semiquantitative rankings illustrated in Figure F30 as follows:
 - Not present
 - Weak
 - Moderate
 - Strong
 - Variable, using the semiquantitative rankings illustrated in Figure F30
- Spinel grain size was recorded.

Thin section descriptions of host rock petrology

Thin section descriptions of host rock petrology closely follow the procedure for macroscopic core descriptions. Where a thin section contained areas with different lithologies, mineralogy, and/or texture, these were defined as domains (e.g., Domain 1, Domain 2, etc.). For thin sections with multiple igneous domains, a map of the domains is shown in the full thin section photomicrograph (Fig. F17). Domains were described separately, and their relative abundance was noted.

The following data were recorded in an Excel workbook for each thin section. Thin section data are available in [Supplementary material](#).

Lithology and texture

- Host rock lithology name (based on thin section observations) using the same definitions as those for macroscopic descriptions.
- Number of lithologic domains within the thin section.
- Nature of lithologic domains, if any (e.g., contact between two units, mix of two lithologies in one section, or presence of texturally different regions within one thin section).
- Relative abundance of lithologic domains (percent).
- Lithologic domain number within the thin section (lithologic Domain 1, lithologic Domain 2, lithologic Domain 3, etc.). This parameter identifies each domain described in the Mineralogy tab.
- Lithologic domain lithology name. If only one domain is present, this is identical to the host rock lithology name given to the entire thin section.
- Lithologic domain grain size:
 - Glassy
 - Cryptocrystalline
 - Microcrystalline
 - Fine grained

- Medium grained
- Coarse grained
- >30 cm
- Lithologic domain grain size distribution:
 - Equigranular
 - Seriate
 - Porphyroblastic

Mineralogy

- Lithologic domain number: lithologic domains defined in the lithologic-textural description.
- Lithologic domain mineralogy: abundance (percent) of minerals.
- Maximum size, median size, shape, and special features of minerals, using the same conventions as during macroscopic description; absorption colors/pleochroism for micas, amphibole, and epidote-clinozoisite; and color (opaque, translucent brown, reddish, green, etc.) for spinels and relict spinels.
- Characteristic colors, exsolutions, zoning, and other special features of constituent minerals are also described.

Vein structure and petrology

The vein petrology team described the veins cutting the host rock as well as irregular vugs (voids in the core that were once filled with fluid, lined, and partially filled with minerals). Vein structure overview and vein types were identified and logged in each section, the grain size of vein minerals, and the nature of contacts between veins and host rock as well as recording in as much possible detail the mineral phases present in veins.

Vein structure overview

The large number and pervasive nature of small (<1 mm) veins encountered in the Hole BT1B drill core made it impractical to identify every vein using visual techniques. Considering this, veins were categorized into two groups: (1) higher density smaller veins <1 mm in diameter and (2) lower density larger veins >1 mm in diameter. Veins in both categories were counted and density per 10 cm was calculated. Results were recorded in the following 5 density categories:

- <1 vein/10 cm
- 1–5 veins/10 cm
- 5–10 veins/10 cm
- 10–20 veins/10 cm
- >20 veins/10 cm (the practical upper limit used)

The general orientation of veins <1 mm in diameter and >1 mm in diameter were evaluated using the following the qualitative categories illustrated in “Schistose and network fabrics” in Figure F31:

- Isotropic

- Weakly oriented
- Moderately oriented
- Strongly oriented

Fractures, faults, and cataclasites, defined following Sibson (1977, see Fig. F32), were individually counted. Faults and cataclasite counts were recorded as density per meter. Characteristics of prominent veins and structures, such as width, depth, and color, were recorded in the VCD comment section of the BT1B StructureOverview worksheet.

Other features of vein structure, including offsets, crosscutting relations, and so on, were recorded as part of the description of the structure of localized features (see below).

Macroscopic core description of vein petrology

Macroscopic descriptions characterized entire vein sets or individual veins based on texture and mineralogy. Veins and vein sets were assigned a vein type on the basis of textures and the minerals present using the categories listed below. As for the host rock lithologies, some vein type categories are partially redundant because it is not always possible to assign highly specific lithologic names. Thus, choices include calcite, dolomite, magnesite, and carbonate. The latter refers to any of the previous three minerals in cases in which it is not possible to make a more specific determination of mineralogy during macroscopic core description. Vein types used in this report are

- quartz
- calcite
- magnesite
- dolomite
- carbonate
- carbonate-quartz
- magnesite-dolomite
- calcite-dolomite
- hematite
- Fe oxyhydroxides
- Fe oxides + quartz
- Fe oxides + carbonate
- graphite
- graphite + hematite
- graphite + Fe oxyhydroxides
- serpentine
- Fe oxides + serpentine
- carbonate + serpentine
- prehnite
- zeolite
- amphibole
- albite
- chlorite
- smectite
- illite
- gypsum
- anhydrite
- barite

- fuchsite
- fuchsite + quartz
- polymineralic
- other

The minerals in the veins are expected to be similar to those in the host rock but with simpler mineral assemblages in each vein. Vein minerals, in addition to the host rock minerals listed above, are zeolites (Zeol), laumontite (Lmt), and stilbite (Stb).

Visually estimated modal percent of each of these minerals in veins was recorded in the vein petrology worksheets. Where a mineral occurs in trace quantities (i.e., too low to assign a meaningful modal percentage), “<1%” was recorded and eliminated from the total.

Adjectives recording vein textural characteristics include

- Cross-fiber
- Blocky
- Laminated/foliated
- Massive
- Slip-fiber
- Vuggy
- Crack-seal
- Sheared
- Patchy
- Overgrowth/replacement
- Brecciated
- Syntaxial
- Antitaxial
- Epitaxial
- Pull-apart
- Zoned

Veins and vein sets were measured; for vein sets the maximum width was usually recorded.

Vein contact types were described based on contrast in the following:

- Modal/mineral
- Grain size
- Grain shape
- Grain orientation
- Color

The contact geometry of veins and vein sets was assigned one of the following descriptors:

- Irregular
- Planar
- Curved
- Anastomosing
- Sutured
- En echelon
- Splaying
- Sheared contact
- Foliated contact

The following textural characteristics of the vein-fill minerals are recorded in the vein petrology worksheets.

- Grain size: mean grain size and the nature of grain size variability of the veins were recorded. Grain size is ranked as
 1. Glassy/amorphous/isotropic in thin section.
 2. Cryptocrystalline: visible grains are <100 μm .
 3. Microcrystalline: grains are 100–200 μm .
 4. Fine grained: grains are 200–1000 μm .
 5. Medium grained: 1–5 mm.
 6. Coarse grained: 5–30 mm.
 7. Greater than 3 cm.
- Grain size variability of the host rock is classified as follows:
 - Equigranular: standard deviation of grain size measurements <33% relative, or, for very fine grained rocks, not measurable.
 - Seriate: somewhat uniform grain size variation over a range >33% of the mean value.
 - Porphyroblastic/porphyroclastic: multimodal grain size distribution with clearly distinct classes having different grain sizes.

Visually estimated modal percent of vein-filling minerals was recorded in the vein petrology worksheets. Where a mineral occurs in trace quantities (i.e., too low to assign a meaningful modal percentage), “<1%” was recorded and eliminated from the total.

Also noted where present were the characteristics of vein selvages (sharply bounded zones flanking veins, in which the host rock has been replaced by another mineral or group of minerals) and vein halos (diffuse alteration zones flanking veins, commonly grading into the host rock laterally away from veins).

The presence of vugs and the textures and identities of minerals that (partly) fill them were noted

Thin section descriptions of vein petrology

Thin section descriptions of vein petrology closely follow the procedures for macroscopic core descriptions of veins. Where a thin section contained several different veins, these were numbered (e.g., Vein 1, Vein 2, etc.). For thin sections with multiple veins, a map of the veins is shown in the full thin section photomicrographs (Fig. F17). Different vein types were described separately, and their relative abundance was noted.

The following data were recorded in an Excel workbook for each thin section:

- Vein texture
- Vein continuity
- Vein width
- Relative age (where discernible)
- Vein-filling minerals and grain sizes
- Vein halo features, if any.

Thin section data are available in [Supplementary material](#).

Lithology and texture

- Number of veins within the thin section.
- Nature of vein contacts.
- Relative abundance of vein types (percent).
- Vein number within the thin section (Vein 1, Vein 2, etc.) for each vein described in the Mineralogy tab.
- Vein type.
- Vein grain size.
- Vein grain size distribution:
 - Equigranular
 - Seriate
 - Porphyroblastic/porphyroclastic

Mineralogy

- Vein number: the veins defined in the lithological-textural description.
- Vein mineralogy: abundance (percent) of minerals.
- Maximum size, median size, shape, and special features of minerals, using the same conventions as during macroscopic description; absorption colors/pleochroism for micas, amphibole, and epidote-clinozoisite.
- Any characteristic colors, exsolutions, and other special features of constituent minerals were also described.

Structural geology

The structure team measured the orientation, intensity, textural characteristics, and overprinting relations of ductile and brittle deformation features (veins, fractures, faults, cataclasites) cutting the host rock and the orientation of host rock banding and/or foliation.

Conventions for structural studies established during previous “hard rock” drilling projects such as ODP Legs 118, 131, 140, 147, 153, 176, 179, 206, and 209; Integrated Ocean Drilling Program Expeditions 304/305, 309/312, 335, and 345; and IODP Expedition 360 were generally followed with minor adjustments. Excel worksheets were used to enter all observations and measurements made on the core and thin sections. General procedures for structural measurements were similar to those used for the other sites during Oman Drilling Program Phase 1 and are described in [Structural geology](#). Measurements were taken in the core reference frame (Fig. F5).

Each core section was described and logged with detailed structural information. This information was then entered into the worksheets. The worksheets, listed below, contain data on the unit, type of structure, intensity, orientation, certainty of observation, crosscutting relationships, and comments.

This was accompanied by annotated core scans of selected areas illustrating the main structural elements and their overprinting relations.

The structure worksheets are formatted in much the same way as those for Sites GT1, GT2, and GT3, with the exceptions noted below.

The structural worksheets are oriented toward quantitative measurements of planar features and lineations in the CRF. Overall estimates of feature frequency in core sections (volume percent host rock, veins, localized shear zones, and vugs and spatial frequency of veins, shear zones, and fractures) are in the host rock petrology logs, but the structural team had primary responsibility for making and recording these observations.

We note here the importance of the scale of observation, as many of the structures appear self-similar and are also present when observed at higher magnification. In these descriptions, we aimed for a practical solution of scale at which it was possible to complete the description in the given time. Orientations were measured of structures large enough to outcrop on the outside of the core more than several centimeters.

Host rock structural features

The focus of the host rock structure worksheet is on characterizing the geometry and nature of banding and foliation in the host rock, together with the overall frequency of veins cutting the host rock in a given section. Description protocol followed that for igneous layering/banding and contacts at Sites GT1, GT2, and GT3 but with a simplified set of observations. Banding and foliations are evident in Site BT1 core, and there was no need to rank the “certainty of observed features,” for example.

Overall host rock structural feature types are defined as follows:

- Host rock (unspecified)
- Banding
- Foliation
- Schistosity
- Lineation
- Breccia
- Cataclasite
- Ultracataclasite
- Pseudotachylite
- Mylonite
- Ultramylonite
- Fold

These types are modified by adjectives for the structural features and described in terms of adjectives as follows:

- Granoblastic
- Porphyroclastic

- Polymict
- Breccia clasts in breccia
- Banded
- Foliated
- Lineated
- Brecciated
- Cataclastic
- Mylonitic
- Ultramylonitic
- Folded

Where breccias or cataclasites are present, the lithology of clasts was identified. These terms are defined elsewhere in the methods section of this volume. Microstructural deformation intensity and shape-preferred orientation (foliation) intensity are ranked as for structural observations at Sites GT1, GT2, and GT3 using the semiquantitative ranking scheme illustrated in Figure F30. The minerals defining the banding or shape-preferred orientation (foliation) were identified, and the sense of shear (if any) constrained by the host rock texture was tabulated. These observations were followed in the host rock structure worksheet by quantitative data on the orientation of structural features in the core reference frame.

Structure of localized features

Logs of the structure of localized features, including ductile and cataclastic shear zones, veins, and fractures, are organized in a very similar manner to the logs of host rock structural features.

Feature types include

- Vein
- Fault
- Joint
- Crack
- Shear zone
- Fold
- Breccia
- Cataclasite
- Ultracataclasite
- Pseudotachylite
- Mylonite
- Ultramylonite

Characteristics used to describe localized structural features are

- Granoblastic
- Schistose
- Foliated
- Banded
- Lineated
- Mylonitic
- Ultramylonitic
- Cataclastic
- Ultracataclastic
- Brecciated

- Folded
- Slickensides
- Cohesive gouge
- Incohesive gouge
- Polymict
- “Containing clasts of breccia”

Microstructural deformation intensity and shape-preferred orientation (foliation) intensity were ranked as for structural observations at Sites GT1, GT2, and GT3 using the semiquantitative ranking scheme illustrated in Figure F30. The minerals defining the banding or shape-preferred orientation (foliation) were identified. The sense of shear (if any) within veins, faults and shear zones was tabulated.

For sense of displacement, sinistral or dextral is used for confirmed displacement on the core cut surface (with clearly correlated markers). Normal or reverse is more difficult to confirm when no slickensides are observed.

Commonly it was possible to identify overprinting relationships between different generations of veins, small faults, and fractures. Therefore, we added columns to the worksheets to differentiate between generations. Vein morphology was observed to vary from planar to variable thickness, so we added a descriptor accordingly.

Contact types for the features were identified, and the geometry of contacts were described. The true width and grain size distribution (mean and variability) within features were tabulated. The localized structural feature worksheet identifies up to two types of features crosscut by the feature of interest and up to two features that cut the feature of interest within the section.

Older generations of veins were deformed by younger structures in different ways, so we added terms to describe this: sheared veins are offset by younger structures with visible drag, as opposed to faulted veins offset along sharp contacts. Fragmented veins were logged when fragments (distant more than several centimeters) could be correlated to belong to the same vein.

These observations are followed in the localized structural feature worksheet by quantitative data on the orientation of structural features in the core reference frame.

Geochemistry

Phase 1

This section describes the sample preparation procedures and analytical approaches used to determine elemental concentrations of whole-rock and mineral samples collected during Phase 1 of OmanDP. This includes samples taken in the field (on site) during

Phase 1 drilling as well as samples taken during the ChikyuOman core description phase. Whole-rock sample powders were analyzed for major and trace element concentrations by X-ray fluorescence (XRF) and mixed acid/alkali-fusion digestion (AFAD) inductively coupled plasma–mass spectrometry (ICP-MS), loss on ignition (LOI), and volatile element (H, C, N, S) concentrations by elemental analyzer (EA).

On site whole-rock powder preparation

A selection of whole-rock samples was taken at the drill sites during Phase 1 coring operations. Relatively fresh background gabbro samples were selected every 20 m downhole to provide an initial supply of polished thin sections and preliminary whole-rock geochemical data for the ChikyuOman core description teams. Half-cores, 5 cm long, were cut from the cores in the field, and blue-red double lines were drawn on the working and archive halves. Unoriented polished thin section billets were cut from the half-rounds, and most of the remainder of the core was crushed and ground into a fine homogeneous powder for whole-rock geochemical analysis. Saw marks and alteration blemishes were removed from the samples by precision sawing or grinding on a diamond-impregnated belt or with carborundum powder. Samples were then ultrasonicated in Milli-Q deionized water (18.2 MΩ·cm) for consecutive rounds until the Milli-Q water was clear with no turbidity. The cleaned pieces were dried for 12 h at 60°C before they were placed in Ziplock plastic bags and crushed to <5 mm grit between plastic plates using a fly press. These pieces were then ground in chrome-steel ring mills using a Rocklabs bench-top mill for ~3 min or until the powder was fine enough such that it felt smooth when rubbed between gloved fingers. The chrome-steel ring mills were cleaned with Milli-Q water and isopropanol after each run and cleaned with pure quartz sand after changes in sample type or if powdery rock residue was noted in the mills after cleaning in Milli-Q and isopropanol. After milling, sample powders were homogenized and split into three portions: 10 g was sent to the University of St. Andrews for major and trace element XRF analyses, 10 g was stored at the University of Southampton in case of losses during transit, and the remainder was transported to *Chikyu* for shipboard analysis, cross-calibration, and personal sampling by the OmanDP Phase 1 Science Party.

XRF analyses at University of St. Andrews

At the University of St. Andrews the samples were analyzed on a Spectro XEPOS_HE energy dispersive polarized XRF (EDP-XRF) analyzer using a tungsten anode and a silicon drift detector. The targets used are adjusted depending on the elements being analyzed to optimize the measurement conditions. For

major elements, Mo, Al_2O_3 , Al, Co, and Pd targets are used, and for trace elements, Mo, Al_2O_3 , Co, and Pd targets are used. Calibration is carried out using international rock standard reference materials (SRM).

Loss on ignition. For LOI, 1–2 g of dried powdered sample was weighed into a porcelain crucible and then ignited at 1020°C for at least 2 h before cooling and reweighing.

Major elements: preparation/analysis of glass beads.

For major element analysis, the samples were dried at 105°C before 0.5000 g was accurately weighed and mixed with a fixed weight (5.000 g) of lithium metaborate. A releasing agent (5 mg of NH_4I) was then added. The mixture was fused at 1080°C for 15 min in a Pt crucible and then cast into a 32 mm diameter glass bead.

Major elements analyzed on the glass beads were SiO_2 , TiO_2 , Al_2O_3 , Fe_2O_3 , MnO, MgO, CaO, Na_2O , K_2O , P_2O_5 , and SO_3 . Analysis time per sample was 15–20 min. Accuracy and precision of the analyses were assessed by replicate analyses of two Japan Geological Survey geological SRMs (JB-1b and JGb-1). The gabbro JGb-1 was chosen to represent the types of material analyzed during ChikyuOman Leg 1. Calibration curves are shown in Figure F33, and results are shown in Table T9 along with calculated levels of detection (LoD). The results show that the precision of the analyses are generally better than 4.5%; however, as the signal approaches the detection limit this deteriorates. For example, the precision of P_2O_5 in the JGb-1 analyses decreases to 15.5%. The accuracy of the measurements is better than 6% for all elements except for P_2O_5 and SO_3 in JGb-1, where the results are higher than the recommended values by 27% and 16%, respectively, due to small signal size.

Trace elements: preparation/analysis of powder pellets.

To prepare pressed powder pellets, ~8 g of dried powdered sample was mixed with polyvinyl alcohol binder (Movial 1%) and pressed at 20 T using WC anvils to produce a 32 mm diameter pellet.

The suite of elements analyzed on the pressed pellet samples included V, Cr, Co, Ni, Cu, Zn, Ga, Ge, As, Se, Br, Rb, Sr, Y, Zr, Nb, Mo, Ag, Cd, In, Sn, Sb, Ba, La, Ce, Pb, Th, and U; the analysis time for this was ~30–40 min per sample. Accuracy and precision of the analyses were assessed by replicate analyses of the same two SRMs as for the major elements (JB-1b and JGb-1). Calibration curves are shown in Figure F34, and results are shown in Table T10 along with calculated LoDs for elements above the detection limit.

Elements with a precision better than 5% for both standards are V, Cr, Ni, Cu, Zn, Sr, Zr, and Ba. A number of other elements, Co, Rb, Y, and Nb, have slightly worse precisions (<7%), particularly in SRM JGb-1, which is a consequence of the low concentrations of these elements in this gabbro standard and should be considered as the appropriate assessment

of error for the gabbro samples analyzed for ChikyuOman Leg 1.

The accuracy of the results is generally better than 10% for the elements with precisions better than 7%, noted above, apart from Co, Rb, and Nb in the JGb-1 standard. The poor accuracy of Rb and Nb is probably a result of the low concentrations in that standard. Cr, which despite showing good accuracy (3.3%) for JB-1b, has very poor accuracy in JGb-1 (27% low). This is probably due to problems with the correction for the interference of the $\text{FeK}\beta$ line on the $\text{CoK}\alpha$ line. This correction will be more important for JGb-1, as it has ~2× the Fe concentration of JB-1b.

Whole-rock analyses aboard Chikyu

Sample preparation

Geochemical samples were selected during the daily ChikyuOman sampling meetings in consultation with the core description teams. For Sites GT1, GT2, and GT3, an oriented thin section was taken adjacent to each whole-rock geochemical sample. When possible, Hole BT1B whole-rock geochemical samples were selected as close as possible (same lithologies) to the thin sections of the core description teams. Additionally, systematic XRD analysis were carried out on Site BT1 whole-rock sample powders to 200 m depth.

Generally, shipboard samples were cut from the working half of the core as 5 cm (HQ) to 8 cm (NQ) long quarter-round core sections (HQ core: ~100 g; NQ core: 60 g). A diamond rock saw was used to carefully cut rock samples from the working half of cores and to remove altered rinds resulting from drilling and sawing. The samples were cut into thin slices to facilitate crushing to a ~2 mm grit. Samples were then ground with 220 μm carborundum powder on a grinding disk or sand paper with a grit size of 220 μm to remove saw marks.

Samples were ultrasonicated for 10 min in ethyl alcohol, which was then decanted, and then samples were ultrasonicated in Milli-Q water 3 times for 10 min or until there was no turbidity in the water. Hole GT3A samples from deeper than 199 m were ultrasonicated only in Milli-Q deionized water according to the method implemented at the University of Southampton. The cleaned samples were placed in an oven at 105°C to dry for at least 6 h. Dried samples were precrushed to <5 mm and then placed in plastic bags, put in a large tungsten carbide (WC) mortar, and pounded with a heavy WC-tipped pestle. Grinding actions with the WC pestle were avoided to reduce potential contamination by WC. Samples were then quantitatively crushed to <2 mm using the Spex SamplePrep 3630 X-Press with samples enclosed in plastic bags and squeezed between plastic sleeves and upper and lower plastic sheets. Sample powders for XRF and other geochemical

analyses were produced from the sample using a Fritsch Pulverisette 5 planetary mill with agate grinding bowls (500 mL) and agate balls (13 mm × 20 mm and 5 mm × 30 mm diameter). Grit samples were run at 200 rpm for 10 min and allowed to cool for 5 min 4 times, after which contents of the jars were sieved through 160 µm, 500 µm, and 250 µm sieves. Large pieces (>3 mm) were hand crushed with the WC mortar and pestle before resieving and returning to grinding bowls for a further 10 min. Once the whole sample was powdered, all sample material was powdered and then all sample was returned to the grinding bowl and milled for 5 min to homogenize. The final powders were stored in ethyl alcohol-cleaned, 100 mL screw-top polystyrene bottles.

Because of the fragility of Site BT1 samples, their preparation differed from that outlined above regarding sample cleaning. Site BT1 samples were not sonicated in either ethyl alcohol or Milli-Q water; instead, they were rinsed 4–5 times in Milli-Q water until the water was clear.

The first steps of the crushing procedure were also modified for samples from Sites BT1 and GT3 compared to Sites GT1 and GT2. Following sample drying, samples were wrapped in plastic bags and placed atop a steel hammer. A smaller hammer was then used to crush the sample by hand. The resulting sample material was passed through a 4 mm sieve, and any material retained in the sieve returned to a plastic bag and crushed again by hand. As for Site GT1 and GT2 samples, persistent large pieces (≥4 mm) were hand crushed with the WC mortar and pestle. The resulting <4 mm sample material was powdered using the Fritsch planetary mill. Samples were milled at 200 rpm for 10 min intervals (shortened to 5 min when Hole BT1B listvenite samples showed signs of welding to the agate) separated by 5 min resting time using 2–6 repetitions, as necessary, until the entire sample passed through a 250 µm sieve and felt smooth between gloved fingers. The samples were then homogenized and stored as above.

Loss on ignition

To determine LOI, an aliquot of sample powder was weighed using the OHTI (Ocean High Technology Institute, Inc., Tokyo, Japan) motion-compensated balance system into a preweighed ceramic crucible using a spatula (that has never been in contact with lithium metaborate flux; 5 g for Site GT1 and GT2 samples and 2–3 g for Site BT1 and GT3 samples). The OHTI balance was calibrated at the start of the ChikyUOman Phase 1 core description campaign using 7 calibration points for each mass range of interest (~20 g and ~1 g), and the balance calibration was checked every 12 h by running equal weights on the master and measure balances. If the measured

weight was off by >0.0005 g, the first step was to tare the standards and repeat the check. If this second check failed, the balance was recalibrated. Weighing errors are conservatively estimated to be ±0.02 mg.

Before LOI measurement, sample powders were dried in an oven for 2 h at 105°C to remove absorbed water, allowed to cool to room temperature in a desiccator, and reweighed. This dried powder was then ignited at 1000°C for 3 h to determine LOI. The crucibles were allowed to cool before being removed from the furnace, placed in a glass desiccator until at room temperature, and then reweighed. These data were recorded in the Glassbead log sheet on the geochemistry laboratory computer with “user” and “date” recorded in the comments column and saved to the temporary geochemistry folder on the ship-board network before being uploaded to J-Cores with the XRF data. The ignited sample was then ground using an agate mortar and pestle and transferred to a new labeled and cleaned sample bottle.

XRF analysis

Calibration and operation. The RIGAKU Supermini wavelength dispersive XRF spectrometer equipped with a 200 W Pd anode tube at 50 kV and 4 mA on *ChikyU* was used to measure major oxide and trace element abundances in powdered rock samples during OmanDP Phase 1. Processed data were uploaded into J-Cores as a comma-delimited data file. Data are reported as total counts on the peak and also as oxide weight percent or parts per million.

The instrument was calibrated using either pre-prepared glass beads for the major elements or pressed pellets for the trace elements made from Geological Survey Japan geological SRMs. Rock standards JA-1, JA-2, JB-2, JB-3, JF-1, JF-2, JG-1a, JG-2, JGb-1, JGb-2, JH-1, JP-1, JR-2, JR-3, and JSy-1 were common to both calibrations, with the addition of JG-1 for the major elements and a 3:1 mix of JGb-2 and JP-1 for the pressed pellets. This mixture was made to provide a high-concentration standard to improve the standard range for Cr and Ni, which for the samples are expected to fall within a large (>2000 ppm) gap in the calibration using the same standards as for major elements. The calibration curves are shown for the major elements in Figure F35 and for the trace elements in Figure F36.

Following calibration prior to an analysis run, SRM JB-1b was run 10 times as an instrument check standard. The average values ±3σ were then used to define limits on instrument performance. The instrument check standard routine automatically compares the result of this run to these limits and flags if the results are anomalous. Variations may be due to factors including changes in the performance of the X-ray tube. If a repeat run of the check routine also

fails for a number of elements, then a drift routine is performed. The drift routine uses a limited number of standards to calculate a factor to apply to the calibration curves to correct for this drift in X-ray intensity with time. The drift was also evaluated when changing from measuring glass beads to pellets.

The LoD of the instrument was determined from 3× the standard deviation of the JB-1b standard used during the check standard routine together with an independent SRM JB-1b bead prepared during ChikyuOman Leg 1 run as an unknown. This standard had the largest number of replicate data available, as it was analyzed each time the instrument was run and on initial calibration. Any runs where a significant number of elements fell out of range indicating a drift correction was needed were ignored. Accuracy and precision of the analysis were determined from repeated analyses of SRM JGb-2, and precision was further assessed by repeat runs of a sample to provide an estimate of the precision in samples that matched the samples being analyzed.

Major elements: preparation/analysis of glass beads.

Between 0.8950 and 0.9040 g of ignited dried sample powder was weighed and mixed with predried and preweighed lithium metaborate flux (4.5 g) in an agate mortar and pestle. This mixture was transferred to a clean platinum crucible using weighing paper, and ~4–5 drops of LiI (20 wt%) releasing agent was added. The crucible was then placed into the TK-4100 (Tokyo-Kagaku) automated beadmaker and heated using the standard *Chikyu* procedure of a 2-step heating ramp, initially to 800°C over 1.6 min, and then to 1150°C over 1.5 min and held at this temperature for 4.3 min before the cup is automatically rotated and tilted for a further 4.25 min to mix the sample and reduce air bubbles. At the end of this time, further manual agitation of the sample was required to ensure all the bubbles were removed. Once melting was complete, the crucible was removed from the furnace cup using tongs and placed on the cooling stand. Once cooled, the bead was removed from the Pt crucible by inverting the crucible onto weighing paper, labeled on the reverse edge in marker pen, and stored in a weighing paper envelope in a Ziplock bag in a desiccator prior to analysis. This procedure is documented in [Appendix D](#).

The XRF is routinely used for quantitative measurement of the 10 major rock-forming elements (represented as oxides: SiO₂, TiO₂, Al₂O₃, Fe₂O₃, MnO, MgO, CaO, Na₂O, K₂O, and P₂O₅). Precision and accuracy were better than 3% (P₂O₅ = 3.8%) and 2.5%, respectively, for all oxides apart from K₂O, which had accuracy better than 5% during Leg 1 and Leg 2 (Table T9). As beads were prepared from ignited powders, we assume all of the Fe has been oxidized and hence total ferric iron oxide (Fe₂O₃^{Total}) is measured and FeO^{Total} is calculated from Fe₂O₃. Major element

analyses were determined to be acceptable if the sum of the anhydrous oxide concentrations totaled to 99–101 wt%. Analyses reported during Leg 1 are recalculated to totals including LOI and as anhydrous. The measured analyses are reported directly for Leg 2, including some samples that were outside of the 99–101 wt% range. Low and high totals were measured mainly in Hole BT1B samples from the upper listvenite-dominated units, which have SiO₂ compositions significantly out of the calibration range (Fig. F37). We calculated a linear correction on the basis of SRMs and internal standards measured as unknowns during the XRF runs (DTS-2b, JP-1, JGb-1, JGb-2, JB-1b, and C5701A-66Z-3, 6–11 cm; also see [Appendix A](#)). The correction was applied to all Hole BT1B samples.

Trace elements: preparation/analysis of powder pellets.

Unignited whole-rock sample powders were pressed into powder pellets for trace element analyses by XRF using a Spex SamplePrep 3630 X-Press. Powder (4 g) was weighed and carefully placed into a 5 mm high sample holder cut from a 38 mm (OD) diameter polypropylene pipe. The powder was separated from the metal plates that apply the load by Prolene film (CHEMPLEX, Florida, USA). Because of the fragility of some early Site BT1 pellets, 5 g instead of 4 g of powder was used. The press was set to ramp up to 25 ton and held there for 20 s. The pressure was then gradually released over 66 s, after which the sample in the sample holder was removed from the press, labeled, and placed into a weighing paper envelope, sealed in a labeled Ziplock bag, and stored in a desiccator until analysis.

ChikyuOman core processing was one of the first times the XRF had been used for trace element analyses. The initial suite of elements of interest was Sc, V, Cr, Co, Ni, Cu, Zn, Ga, Rb, Sr, Y, Zr, Nb, Ba, La, Ce, Pb, Th, and U. However, despite doubling the count time, the calibrations obtained for some of these elements was poor, particularly Sc, Co, Y, Zr, Nb, and Ba, which had low signal intensities during Leg 1 (Fig. F35). The elements that were considered to be satisfactory during Leg 1 were V, Cr, Ni, Cu, Zn, Rb, and Sr. These had precision better than 5% and accuracy better than 10%, though for V there is a large discrepancy between the accuracy for SRM JB-1b (+23.9%) and JGb-2 (−0.7%). Although SRM JGb-2 is more representative of the samples analyzed, this suggests the accuracy is satisfactory for this work (see Table T10). During Leg 2, the measured suite of elements was Sc, V, Cr, Co, Ni, Cu, Zn, Ga, Rb, Sr, Y, Zr, Nb, and Ba. Ga concentrations were systematically below LoD in samples from Holes GT3A and BT1B, and therefore this element was not included in the result tables (Table T9; Fig. F38).

As ICP-MS was also used to quantify trace element concentrations, results from both methods were compared during Leg 1 to assess the best method for

each element (see **ICP-MS analysis**). As the major elements were also analyzed as part of the trace element routine to allow for interference correction, we used the pressed pellet K_2O analysis (measured and reported as K_2O) because the concentrations of potassium in samples was near the detection limit for analysis on glass beads.

XRF data comparison: University of St. Andrews and Chikyu

Some samples taken on site during coring operations were analyzed at the University of St. Andrews and onboard *Chikyu* as part of an interlaboratory comparison. Major element data compare well between laboratories for all oxides ($R^2 > 0.9$ when regression is forced through (0,0); Fig. **F39**; Table **T11**) apart from K_2O during Leg 1 (due to limits of detection being higher on the *Chikyu* and therefore near detection on glass beads).

Trace element data comparisons between the laboratories at University of St. Andrews and on board *Chikyu* are generally good, with $R^2 > 0.9$ for V, Ca, Ni, Cu, and Sr (Table **T12**). Agreement between laboratories for Zn is not as good, with $R^2 = 0.5$ and scattered data during Leg 1. During Leg 1, we measured K_2O on powder pellets as trace elements because of low concentrations. When comparing these measurements to those on beads made at University of St. Andrews, R^2 is 0.7, but *Chikyu* measurements are one-third lower than those made at the University of St. Andrews, likely due to the analyses on beads being near detection limits at the University of St. Andrews (Fig. **F40**).

During Leg 2, trace element data comparisons between the laboratories at the University of St. Andrews and *Chikyu* are also good, with $R^2 > 0.9$ except for Co ($R^2 = 0.3$) (Fig. **F41**; Table **T13**). The data collected during Leg 2 are also clearly affected by an issue of interlaboratory repeatability for V, which appears to be overestimated in some *Chikyu* analyses relative to measurements made at St. Andrews (Fig. **F42**). Similar problems with V analyses were noted during Leg 1. For Leg 2, this issue only appears to affect samples from the metamorphic sole of Hole BT1B, whereas samples from Hole GT3A and the Hole BT1B listvenites agree well with the St. Andrews analyses (Fig. **F40**). Repeat analyses of standards run as unknowns show similar overestimation of V for SRM BHVO-2 and, to a lesser extent, SRM JB-1b (Table **T10**). Whereas both SRMs have high concentrations of V, they are still well within the calibration range of the instrument, as are the metamorphic sole samples (Fig. **F38**). For this reason, a calibration range problem is not the suspected cause. The overall elemental abundances in standards BHVO-2 and JB-1b closely match the mean composition of the metamorphic sole samples for both major and trace elements. This strongly suggests a matrix (Table **T14**)

effect is the cause of the poor reproducibility of V. The exact cause of this is unknown but may relate either to the higher Na_2O , TiO_2 , K_2O , and P_2O_5 contents of basaltic and metamorphic rocks or to spectral interference from a minor or trace species.

ICP-MS analysis

Trace element analyses were performed aboard *Chikyu* using the Agilent7500ce quadrupole ICP-MS. All samples from Holes GT1A and GT2A were prepared for ICP-MS, and most of them were analyzed during Leg 1. Only a subset of Site GT3 samples were prepared for ICP-MS analyses during Leg 2; for safety, it was decided to stop rock digestion when *Chikyu* left port on 3 September 2017. As anticipated from tests carried out during Leg 1 on peridotite SRM JP-1, digestion of the ultramafic samples recovered from Hole BT1B was challenging. A subset was finally digested and analyzed on the ICP-MS, together with a subset of Hole GT3A samples and the remaining Leg 1 solutions.

Sample preparation: alkali fusion/acid digestion.

Whole-rock powders were digested using the AFAD method of Senda et al. (2014) (see **Appendix B**). Samples and standards were weighed on the OHTI microbalance. Aliquots ($100.0 \text{ mg} \pm 0.1 \text{ mg}$ during Leg 1 or $\pm 1 \text{ mg}$ during Leg 2) of the ignited whole-rock powders were weighed into clean 30 mL Pt crucibles, and 1 mL of 70% $HClO_4$ (TAMAPURE AA-100, TAMA Chemicals) and 1 mL of 38% HF (TAMAPURE AA-100, TAMA Chemicals) were added in a scrubbed fume hood. The samples were heated to 80°C on a hot plate in the fume hood, and the temperature was gradually increased to 200°C over 3 h during Leg 1. The temperature was increased to 250°C during Leg 2. During Leg 2, complete acid evaporation commonly required 6 h. After acid evaporation, the remaining sample was mixed with $500.0 (\pm 0.5 \text{ mg})$ during Leg 1 or $\pm 1 \text{ mg}$ during Leg 2) of preweighed sodium carbonate (Na_2CO_3 ; JIS special grade, Wako Pure Chemical Industries, Japan) flux added to the Pt crucible. The mixture in the Pt crucible was then fused in a furnace at $\sim 1000^\circ\text{C}$ for 10 min, after which the crucible was moved into the fume cupboard and allowed to cool. Aliquots of 5 mL of 68% HNO_3 (TAMAPURE AA-100, TAMA Chemicals) and 60 μL of HF with 10 mL of Milli-Q water was carefully added to the crucible and put on a hot plate at 120°C for 30 min. Then the acid solution was pipetted into a preweighed, labeled 60 mL low-density polyethylene or high-density polyethylene bottle. The crucible was washed with 3 mL Milli-Q water more than 3 times, and each washout solution was added to the sample bottle. Aliquots of 10 mL of HCl (TAMAPURE AA-100, TAMA Chemicals) and 60 μL of HF with 5 mL of Milli-Q water were added to the crucible and heated to 150°C for 30 min in a fume hood. This solution

was added to the sample bottle and again washed with Milli-Q water 3 more times. The bottle was filled to the top (~60 mL) with Milli-Q water and weighed. The reagents used are summarized in Table T15 and the step-by-step procedure is described in Appendix B.

Trace element analysis. For ICP-MS analyses, the sample solution was brought to a final dilution of 30,000 during Leg 1 and to 13,000 during Leg 2 in a 10 mL bottle to reduce the matrix effects from high concentrations of C and Na. The sample solutions were diluted in 2% HNO₃ and 0.1% HF by weight containing 1 ng/mL In, Re, and Bi as internal standards. Following the first tests carried out during Leg 1, it was decided to use 5 ng/mL In, Re, and Bi as internal standards during Leg 2. Calibration solutions for AFAD were prepared by addition of standard solutions to the procedural blank solutions prepared with the samples to achieve a matrix match. During Leg 2, calibration solutions were prepared using an aliquot of the same blank solution used to prepare calibration solutions during Leg 1. The 10 mg/L CLMS-1 (SPEX; containing Y, rare earth elements [REE], and Th), 10 µg/mL XSTC-331 (SPEX; containing Ni, Rb, Se, Cs, Ba, Pb, Th, and U), 1 µg/mL Zr (SCP Science), 1 µg/mL Nb (SCP Science), and 1 µg/mL Hf (SCP Science) solutions were used for calibrations at different dilutions to cover the expected sample concentration range. Standard solution CLMS-1 was diluted to 0.05, 0.5, and 5 ng/mL. Standard solution XSTC-331 was diluted to 1 and 10 ng/mL. Zr, Nb, and Hf solutions were mixed together and diluted to 0.05, 0.5, and 5 ng/mL. Examples of the calibration curves obtained are shown in Figure F43. Although the instrumental conditions were adjusted to maintain the best balance between high sensitivity and low oxide formation, we had to correct for overlaps between the spectra of oxides and hydroxides for some elements (e.g., ⁵³Cr⁴⁰Ar⁺ on ⁹³Nb⁺, ¹³⁷Ba¹⁶O⁺ on ¹⁵³Eu⁺, ¹⁴¹Pr¹⁶O⁺ on ¹⁵⁷Gd⁺, ¹⁴⁷Sm¹⁶O⁺ on ¹⁶³Dy⁺, ¹⁴⁹Sm¹⁶O⁺ on ¹⁶⁵Ho⁺, and ¹⁵³Eu¹⁶O⁺ on ¹⁶⁹Tm⁺) (Dulski, 2001). To calculate the correction factors we measured three separate solutions prepared with 10 ng/mL Cr, 10 ng/mL Ba, Pr, Nd, and Sm, and 10 ng/mL Eu, Gd, Tb, and Dy. The correction factors for the oxides and hydroxides were calculated (correction factor < 1.5%) and applied to all the analyses. For ⁸⁸Sr to reduce the signal intensity to the detector, the instrument was set to analyze in defocused mode. We used the SRM powders to check the precision and accuracy of this methodology, including 2 gabbros (JGb-1 and JGb-2) and 3 basalts (JB-1b, BHVO-2, and Band CR-2). Solutions of JB-1b (or JGb-2) were used as in-house standards and run every 15–20 samples during ICP-MS measurement. Measurement of the sample solutions takes about 5 min/sample, and after each measurement,

5% HNO₃ and 3% HNO₃ + 0.2% HF solutions were aspirated to clean the instrument. Instrument conditions during analysis are summarized in Table T16.

The results of the SRM analyses are shown in Table T17. Because of problems with instrument blanks, despite extensive cleaning of the introduction system and cones, and digestion blanks (Table T18) for Sc, V, and Cr, these elements are not reported. Only Ni, Rb, Sr, Y, Zr, Nb, Cs, Ba, REEs, Hf, Pb, Th, and U were measured by ICP-MS on samples digested by AFAD. Other than those mentioned earlier, the LoD of the elements analyzed were sub-parts per million, and for many sub-parts per billion, the exception being Zr at 1.5 ppm (Table T19). Precision of the analyses varies depending on the standard analyzed. For example, JGb-1 shows better precision than JGb-2 for Sr, Nb, and Zr. As these are multiple digests, this may be related to different digestion efficiencies of the AFAD technique in these rock types; for some elements (e.g., Pb) this may be related to blank issues, as this work was not carried out in a clean lab. Zr shows highly variable accuracy (between 6% high and 36% low depending on the standard (Table T17). The AFAD digest method has shown successful digestion of accessory phases in more felsic rocks (Senda et al., 2014), so unsuccessful digestion of zircons is unlikely to be responsible for this discrepancy. However, the results for JP-1 with low recoveries (>50% low) for a large number of elements suggests that the method may have problems with dissolution of peridotites. For REE, the results from AFAD/ICP-MS show good accuracy (<10% except Dy: 14%) and precision (<6.5%) in JGb-1, but as the concentrations decrease to those present in SRM JGb-2, the precision of the analyses decreases a little (<11%) and the accuracy of the results decreases, particularly for Gd (19% high) and Tb (31% low); the other REEs are better than 12%. For very low concentrations in SRM JP-1, the accuracies are dramatically worse (>50% low for many REEs and other elements). This may be related to the potential problem noted earlier with the use of AFAD with peridotites.

XRF and ICP-MS trace element data comparison

Of the elements measured by ICP-MS on *Chikyu*, two were also measured by XRF on *Chikyu* (Sr and Ni) and four at St. Andrews (Sr, Ni, Zr, and Ba). Here, we compare data produced for these elements using both methods. Concentrations of Ni and Sr correlate well between analyses by ICP-MS and XRF, with $R^2 > 0.9$ for both elements (Fig. F44). XRF measurements give consistently slightly lower values than ICP-MS, 9% lower for Ni and 7% lower for Sr, which are on a similar order of magnitude as the error on these measurements by XRF (<10% and <1%, respectively, for Ni and Sr; Table T10) and ICP-MS (3%–10% for both Sr and Ni; Table T17). Zr and Ba measured by XRF on

Chikyu were not used because of poor calibrations resulting in large errors; however, we compare ICP-MS with results from St. Andrews XRF measurements. Zr shows a weak correlation ($R^2 = 0.7$) between XRF and ICP-MS, but this trend is significantly offset with a non-zero intercept (Fig. F44). Measurement by XRF yields consistently $\sim 3\times$ higher concentrations than ICP-MS, and digestion of SRMs has indicated low and variable recoveries of Zr. Measurement error for Zr by XRF is low ($<2\%$) and LoD is ~ 4 ppm, which approaches the values obtained from ICP-MS for these samples. For ICP-MS, errors in samples with low concentrations may be as high as 11% (Table T17) and LoDs are 1.5 ppm. For Ba, the correlation between concentrations measured by ICP-MS and XRF is also poor ($R^2 = 0.5$) but nearer to the 1:1 line (Fig. F44), and concentrations determined by XRF are higher than those by ICP-MS, particularly at lower concentrations where XRF measurement approaches the LoD (~ 4 ppm). Errors on both XRF and ICP-MS measurements of Ba are low ($<5\%$), but because of the lower LoD by ICP-MS (0.6 ppm) and poor calibrations for Ba by XRF on *Chikyu*, we report ICP-MS data.

We summarize the methods that we prefer to use to quantify major and trace elements in Table T20 and compare the results for the replicate analyses of SRMs JB-1B, JGb-1, and JGb-2 in Tables T21, T22, and T23, respectively.

EA measurements of volatile elements

For analysis of the volatile elements total carbon (C^{Total}), total nitrogen (N^{Total}), and hydrogen, hereafter CHN, and total sulfur (S^{Total}), two separate Thermo Finnigan Flash EA 112 elemental analyzers were used, one for CHN analysis and the other for S^{Total} . The instruments were configured differently to optimize the conditions for analysis. For both analyses the samples were dried at 105°C for 12 h to remove adsorbed water then weighed into a soft tin capsule (ThermoFisher Scientific, Cambridge, UK). For CHN analysis, ~ 40 mg of sample is used compared to ~ 20 mg with an excess of V_2O_5 oxidation enhancer added for S^{Total} . These are introduced by an autosampler and combusted in an O_2 -rich environment within the EA prior to separation by gas chromatography (GC) and detection.

The CHN analysis system uses 2 reaction chambers, a combustion reactor containing copper oxide and silvered cobaltous/cobaltic oxide held at 900°C and a reduction reactor containing reduced Cu. This results in the production of CO_2 , N_2 , and H_2 , which are separated on a 3 m GC column in a flow of He gas and detected using a thermal conductivity detector.

The S^{Total} system uses a single combined combustion and reduction reactor containing tungsten trioxide and reduced Cu held at 1000°C , which produces SO_x ,

followed by a 0.8 m GC column to separate these from other combustion products.

The existing methods on *Chikyu* have been optimized for analysis of sediment samples that routinely contain weight percent levels of carbon, nitrogen, and sulfur, in contrast to the part per million levels expected from the samples from OmanDP Holes GT1A, GT2A, and GT3A. Hydrogen measurements have not been routinely undertaken on board. Historically, calibrations have used sulfanilamide (41.84 wt% C, 16.27 wt% N, 18.62 wt% S, and 4.64 wt% H); however, the expected sample concentrations would fall below the usual lowest standard. To improve the results, a new calibration strategy was devised based on the methods used during IODP Expeditions 345 and 360 (Gillis et al., 2014; MacLeod et al., 2017b) to increase the standard coverage at lower concentrations. The imprecision of weighing the required low levels (sub-milligram) of sulfanilamide onboard *Chikyu* meant that rock standards were used to calibrate the low levels combined with sulfanilamide for the higher concentration end of the calibration. For C^{Total} , N^{Total} , and S^{Total} this used 2 additional sulfanilamide standards; for H, 6 additional sulfanilamide standards were used (Tables T24, T25, T26, T27). Ideally, a range of different standards with varying concentrations would allow the same weight of each standard rock powder as sample to be used to cover the required calibration range, thus minimizing potential variations resulting from the amounts of material combusted. However, the limited range of well-characterized standards on board required that the calibration be carried out with varying masses of single rock standards; SRM JSI-1 was used for CHN (Kubota, 2009) and JGb-1 for S^{Total} (Erdman et al., 2014) (Tables T26, T27). The results were calculated using the blank-corrected peak area with the calibration curve forced through 0. Calibration curves obtained from this method of calibration are good with no offset between standard types (Fig. F45). For both systems the precision and accuracy of the method were determined using replicate analyses of SRM JGb-2 (Imai, 1999) at the same weight as the samples. The LoD for each analyte was determined from $3\times$ standard deviation of replicate analyses of JGb-2.

Following calibration for CHN, the samples were run in batches of 8. Samples were preceded by a blank check and followed by 1 mg sulfanilamide as a reactor column condition check. For S^{Total} , samples were run in batches of 6 and bracketed with blank and reactor condition checks. If the results for the condition checks fall outside $\pm 5\%$ of the known value, the run was terminated.

Leg 2 inorganic carbon/carbonate, CHN, and S calibrations are shown in Tables T28, T29, and T30.

Coulometry determination of carbonate

The carbonate analyzer onboard *Chikyu* (Coulometrics 5012 CO₂ coulometer) has a carbonate decomposition device and a coulometer as a detector. The carbonate decomposition device is composed of two lines with nitrogen gas flow, one for acidification of samples and the other for CO₂ sampling and injection into the coulometer. Sample vials are purged with N₂ gas followed by the addition of 2 M HCl that yields CO₂ gas from the decomposition of carbonate minerals. The liberated CO₂ is then injected into the coulometer with a N₂ gas flow for measurement by coulometric titration.

Oman DP Chikyu Oman Phase 1 initially followed ship protocols: 15–25 mg of powdered rock was weighed into aluminum foil capsules for the analyses; however, in light of the low concentrations in the samples this was increased to 40–50 mg of powder. Calibration was obtained using preweighed CaCO₃ calibration standards (×3) and empty capsules to act as the baseline blanks (following standard *Chikyu* shipboard protocol). For Holes GT1A, GT2A, and GT3A, and for the metasediments and metabasalts sampled in Hole BT1B, the percentage of carbonate minerals present was determined assuming all CO₂ released came from CaCO₃. Total organic carbon contents were calculated by subtracting inorganic C from the total carbon (TC) measured by elemental analysis. Because of the abundance of dolomite and magnesite in the listvenite-dominated domains in the upper part of Hole BT1B, we assumed that all CO₂ released came from dolomite (and/or Mg calcite) but that magnesite was not dissolved. For this reason, TOC was not determined for the samples from the listvenite-dominated domains in the upper part of Hole BT1B.

Precision and accuracy were assessed by measuring SRMs NIST88b and JSd-2, both of which were included in each batch of samples (Table T25). The accuracy for inorganic C was better than 5% with a precision of better than 3% for both standards.

X-ray diffraction

XRD was used to identify secondary minerals and mineral mixtures associated with hydrothermal veins, breccias, alteration halos, fault zones, and other features in the Oman DP cores. For Holes GT1A and GT2A, a limited number of altered whole-rock samples from the margins of veins and fault zones were also investigated to determine the secondary mineral assemblage developed. Samples were generally taken from small pieces that had flaked off the core sections or small samples scraped from the working half; however, some samples were sawn from the cores to liberate features of interest. Hole BT1B whole-rock powders sampled to 200 m depth were analyzed using XRD.

Powders were dried in the oven at 60°C if necessary, lightly ground with an agate mortar and pestle, and the powder stored in a small labeled bottle. Samples were mounted as random bulk powders in a glass or aluminum holder. The holder chosen was based solely on the volume of sample available, with the glass holder having a higher capacity. The depression in the holder was filled with powder and to ensure a flat surface at the correct height it was gently pressed into place with a glass thin section slide. When sample volumes were insufficient, sample powder was mounted in the middle of the holder. The samples were then loaded into the autosampler of the XRD instrument. Before loading, the outside of the sample holders were cleaned with ethyl alcohol and a soft paper cloth to remove any stray powder.

X-ray diffractograms were produced for each sample using the PANalytical CubiX³ PRO (PW3800) diffractometer with associated Panalytical X'Pert HighScore Plus software for data processing. Backgrounds were determined using default values of 0 for the bending factor and 23 for granularity. The instrument and software peak search settings are given in Table T31. When necessary, unrecognized peaks were inserted manually or wrongly identified peaks were deleted. Search match for matching phases to peaks was performed with a restriction to search for minerals only, and chemistry of minerals was restricted to major and most transitional metals excluding rare elements (e.g., Re, Os, REE, actinides). Matching phases were selected by best fit, choosing only well-known mineral phases that were likely to occur.

Phase 1 summary

A summary of the instrumentation used during OmanDP Chikyu Oman Phase 1 is presented in Table T32. Tables T21, T22, and T23 give summaries of the accuracy and precision data for the two laboratories, *Chikyu* and St. Andrews, for the major and trace element analyses of the SRMs JB-1B, JGb-1, and JGb-2.

Phase 2

This section includes samples taken on site during Phase 2 drilling as well as samples taken during the *Chikyu* Oman Phase 2 core description campaign. Whole-rock sample powders were analyzed following near-identical analytical approaches used during Phase 1. Major and trace element concentrations were determined by XRF, LOI was measured by mass, and volatile elements were measured by EA. Whole-rock trace elements were analyzed on pellets using laser ablation-inductively coupled plasma-mass spectrometry (LA-ICP-MS). Trace element analysis by AFAD ICP-MS was not continued because of safety concerns, especially relating to undertaking this method at sea. Consequently, whole-rock and min-

eral samples from Holes CM1A and CM2B were prepared for trace element concentration analyses by LA-ICP-MS. Here we update changes to previous methods and provide analytical precision and accuracy information for each method used during ChikyuOman Phase 2.

XRF analyses at University of Edinburgh

At the University of Edinburgh, the bulk composition of each Phase 2 powdered drill site sample was measured using a Philips PW2404 wavelength dispersive (WD) sequential X-ray spectrometer at the School of GeoSciences. Operation parameters are as follows: rhodium anode end window X-ray tube accelerating voltage = 50kV, tube current = 50 mA. For major element analysis, fused glass discs were prepared as described in Norrish and Hutton (1969): samples were dried at 110°C and fired at 1100°C to establish LOI. Samples were then fused into glass discs using a borate flux (Johnson and Mathey Spectroflux 105: 47% lithium tetraborate [$\text{Li}_2\text{B}_4\text{O}_7$], 37% lithium carbonate [Li_2CO_3], and 16% lanthanum oxide [La_2O_3] as a X-ray heavy absorber) in a ratio of 1:5 (sample:flux). For trace element analysis the samples were mixed with 0.32 mL of a 2% polyvinyl acetate binder solution, then pressed into 48 mm diameter pellets under 8 tonnes for 2 min in an automatic press.

The spectrometer was calibrated using a suite of 12 internationally recognized standards using the data reported in Govindaraju (1994). Raw data were corrected for fluorescence line overlaps and variation in matrix density as described in Norrish and Hutton (1969) and Reynolds (1963).

Rotary drilled cuttings samples

XRF analysis at University of Plymouth

XRF analysis was used to determine major oxides and trace elements in 6 samples from rotary-drilled Holes BA1A and BA2A (3 samples from each hole) on milled drill cuttings samples from different depths.

Major oxides: preparation and analysis. Sample powders were prepared for analysis by fusion, which was undertaken using a PANalytical Egon 2 furnace following laboratory standard operating procedures. Samples and flux (lithium tetra/metaborate, 67:33) were accurately weighed into Pt-Au crucibles using a calibrated balance at a ratio of 9 g flux to 0.9 g sample. Fusion was carried out at 1200°C using the pre-programmed WROXI GEN fusion method. The procedure was validated using a reference material (CNRS BE-N basalt) of similar composition to the unknown samples. Repeatability was assessed by preparing the reference material in triplicate with relative standard deviation across triplicates shown to be <2% for the majority of oxides and <7% for those at lower concentrations. LOI was determined in a separate procedure on subsamples of the material by ig-

niting at 1050°C for 1 h in a muffle furnace. Fused beads were analyzed using a PANalytical Axios Max WD XRF, with concentration data reported as element oxide (%) for each analyte. The oxide form of the element is assumed. The PANalytical Axios Max operates a Rh target X-ray tube at 4 kW power with sequential detection of elements undertaken with Ar gas flow and scintillation detectors. Measurement conditions were optimized using PANalytical SuperQ software and the WROXI analysis application.

Analytical quality control was carried out daily following standard operating procedures using a multi-compound glass melt sample (glass monitor C3, Britlander) to ensure instrument stability. The total summations of oxide concentrations plus the LOI (sum total = oxide% + LOI%) were within the desired limits of 99%–101% for all samples.

Trace elements: preparation and analysis. Milled sample material was mixed with a polypropylene wax binding agent (Clariant Ceridust 60 50M) at a ratio of 1:4 (binder:sample) prior to pressing into sample pellets. Samples were pressed in 40 mm diameter Al sample cups under 150 kN of pressure using a Herzog TP20 manual press. Samples were analyzed using the PANalytical Protrace application with daily instrument quality control carried out following standard procedures as above. Triplicate samples were unable to be prepared owing to sample mass limitations. A sample of reference material (CNRS BE-N basalt) was prepared in the same manner as the unknown samples for measurement validation.

XRD analysis at Southampton University

Mineralogy of OmanDP cuttings from rotary boreholes BA1A and BA2A was analyzed by X-ray diffraction at Southampton University School of Ocean and Earth Science XRD Laboratory. Cuttings samples (size fraction >1 mm to <250 μm) were milled to a fine sifted flour consistency using the same procedure as described above for the core samples. Samples were mounted as bulk powders in a zero-background silicon disc holder.

X-ray diffractograms were produced for each sample using the PANalytical X'Pert PRO diffractometer, with associated Panalytical HighScore software for data processing, using the ICDD 2016 minerals database. The instrument and software peak search settings are given in Table T31. When necessary, unrecognized peaks were inserted manually and wrongly identified peaks were deleted. Matching phases were selected by best fit, choosing only well-known mineral phases that were likely to occur.

Whole-rock analyses aboard Chikyu

Sample preparation

Geochemical samples were selected during the daily ChikyuOman sampling meetings in consultation

with the core description teams. An oriented thin section was taken adjacent to all whole-rock geochemical samples and described by the science teams. In addition, during Phase 2 operations a homogeneous sample of relatively fresh background rock was selected every 10 m downhole (vs. every 20 m in Phase 1) to provide an initial supply of polished thin sections and preliminary whole-rock geochemical data for the Phase 2 core description teams. Powders of the on-site samples were made at the University of Southampton and sent to *Chikyu* for basic analyses. These powders were analyzed by XRF at the University of Edinburgh, and Leg 4 samples were analyzed by XRD at the University of Southampton.

Following identical sampling practices from Phase 1, shipboard samples were cut from the working half of the core as 5–6 cm (HQ) to 8–10 cm long (NQ) quarter-round core sections (HQ core: ~100 g; NQ core: 60 g). A diamond-impregnated continuous-edged lapidary blade saw was used to carefully cut rock samples from the working half of cores and to remove altered rinds resulting from drilling and sawing. The samples were rinsed and ultrasonicated in Milli-Q deionized water multiple times until the Milli-Q water was clean. Clean pieces were dried for 12 h at 60°C before they were cut into thin slices to facilitate crushing to a <1 mm grit. The first steps of the crushing procedure were modified for the Phase 2 samples (Holes CM1A, CM2B, BA1B, BA3A, and BA4A) compared to Phase 1. A new Retsch BB50 jaw crusher purchased by OmanDP for the *Chikyu* geochemistry laboratory was used to crush sawn and cleaned samples to a grit (see [Appendix C](#)). This new jaw crusher is excellent for gently crushing relatively small samples with large feed sizes without loss. For Phase 2, the samples were crushed in 4 steps, starting with a 14 mm jaw gap then decreased in stages to 7 mm, 4 mm, and 1 mm. To avoid contamination, during Leg 4 after the 14 and 7 mm crushing steps, samples were placed in a 250 µm sieve and particles that passed through were discarded. The resulting <1 mm crushed sample was then powdered using the Fritsch Pulverisette 5 planetary mill following the same procedures as used in Phase 1.

During Leg 4, the crushed samples were placed in agate grinding bowls (80 mL) with 5 large (30 mm diameter) and 13 small (10 mm diameter) agate balls. The planetary mill was then run 4 times for 10 min at 200 rpm with some cooling time between runs. Powders were sieved at 500 and 250 µm, and the remains were milled again for an additional 10 min. After powders were sieved and homogenized, they were divided for analysis: ~2 g for elemental analysis (CARB/CNHS analysis using glass bottle and metal spoon to avoid any plastic-derived contamination), ~3 g for LOI and XRF beads (using porcelain crucibles), ~15 g for XRF and LA-ICP-MS pellets (glass dish), and ~0.5 g for XRD (small centrifuge tube).

Loss on ignition

To determine LOI, an aliquot of sample powder was weighed using the OHTI motion-compensated balance system into a preweighed ceramic crucible using a spatula (that has never been in contact with lithium metaborate flux; 3g for sample powders). The balance was calibrated at the start of the Phase 2 core description campaign using 7 calibration points for each mass range of interest (~20 g and ~1 g), and the balance calibration was checked before every batch of 4–8 samples using equal weights on the master and measure balances. If the difference between the master and measured weight was larger than 0.0005 g, the balance system was tared again using the standard weights and the check was repeated. If this second check failed, the balance was recalibrated. Weighing errors are conservatively estimated to be ±0.02 mg.

Before LOI measurements, sample powders were dried in a 105°C oven for 6 h to remove absorbed water. Samples were cooled to room temperature in a desiccator and reweighed. This dried powder was then ignited at 1000°C for 3 h. The crucibles were reweighed after cooling before being removed from the furnace and placed in a glass desiccator until at room temperature. Data were saved in a temporary folder on the chemistry laboratory computer for later upload to J-Cores along with XRF data. Finally, the ignited sample was ground using an agate mortar and pestle and transferred to a new cleaned and labeled sample bottle. Detailed strategy procedures for LOI and the production of glass beads are available in [Appendix D](#).

XRF analysis

Calibration and operation. The RIGAKU Supermini WD XRF spectrometer equipped with a 200 W Pd anode tube (50 kV and 4 mA) on board *Chikyu* measured major oxide and trace element abundances in powdered rock samples during Phase 2. Processed data were uploaded into J-Cores as comma-delimited data files. Data are reported as total peak counts and also as oxide weight percent or parts per million.

The instrument was calibrated using either pre-prepared glass beads for major elements or pressed pellets for trace elements made from Rock SRMs JA-1, JA-2, JB-2, JB-3, JF-1, JF-2, JG-1a, JG-2, JGb-1, JGb-2, JH-1, JP-1, JR-2, JR-3, and JSy-1. JG-1 was added for the major elements, and a 3:1 mix of JGb-2 and JP-1 was added for the pressed pellets. This mixture was made to provide a high-concentration standard to improve the calibration range for Cr and Ni. Expected ranges for Cr and Ni are expected to fall within a large (>2000 ppm) gap in the calibration performed using only the major element standards.

During Leg 4, we added Cr₂O₃ for the major element analysis of beads in anticipation of high concentra-

tions of Cr in ultramafic rocks. We made two calibration curves for bead analysis. The first included JP-1 standard and Cr_2O_3 as analytes; the second was generated to compensate for instability of the instrument at sea. Legs 3 and 4 used the same calibration curves for powdered pellet analysis. Leg 3 calibration curves are shown for major elements in Figure F46 and for trace elements in Figure F47. Precision and accuracy are better than 2.5% for all oxides except TiO_2 for DTS2B-2 and JP-1 (better than +11%) and Na_2O , P_2O_5 , and K_2O for JGb-2 (3.40%, 17.60%, and 7.49% respectively). For Leg 4, the last calibration curves for major elements of bead analysis are shown in Figure F48. Leg 3 and 4 precision and accuracy for bead analyses are presented in Table T9 and in Table T10 for pellet analysis. As beads were prepared from ignited powders, we assume all Fe has been oxidized and hence total ferric iron oxide ($\text{Fe}_2\text{O}_3^{\text{Total}}$) is measured and $\text{FeO}^{\text{Total}}$ is calculated from Fe_2O_3 . Major element analyses were acceptable if the sum of the anhydrous oxide concentrations totaled 99–101 wt%. For Leg 3, low and high totals measured in some samples had SiO_2 compositions slightly out of the calibration range. Therefore, we calculated a linear correction on the basis of CRM and internal standards measured as unknowns during the XRF runs (SRM DTS-2b, JP-1, JGb-1, JGb-2, JB-1b, and C5701A-66Z-3, 6–11 cm). The correction was applied to all samples from Holes CM1A and CM2B.

Trace element analyses of pressed powder pellets.

During ChikyuOman Leg 3, trace elements Sc, V, Cr, Co, Ni, Cu, Zn, Ga, Rb, Sr, Y, Zr, Nb, and Ba were measured by XRF on pressed powder pellets. During Leg 4, the measured suite of elements was Sc, V, Cr, Co, Ni, Cu, Zn, Ga, Rb, Sr, Y, Zr, Nb, and Ba. Major elements were analyzed as part of the trace element routine to allow for interference correction and as an internal standard element for LA-ICP-MS analysis. A 3:1 mix of JGb-2 and JP-1 pressed pellet standard was made to provide a high-concentration standard to improve the standard range for Cr and Ni, which for the samples are expected to fall within a large (>2000 ppm) gap in the calibration using the same standards as for major elements. Precision and accuracy are shown in Table T10. As LA-ICP-MS was also used to quantify trace elements, results from both methods were compared during Leg 3 to assess the best method for each element (see below and Table T33).

Recalibration of shipboard XRF data using shore-based XRF data. Shipboard XRF data were recalibrated using data from the shore-based XRF analyses (University of St. Andrews [Phase 1] and University of Edinburgh [Phase 2]) of drill site samples to create a single, self-consistent data set and remove artifacts of the offset between the *Chikyu*, St. Andrews, and Edinburgh data sets. Recalibration was carried out by plotting *Chikyu* data vs. shore-based data for each element; in cases where the two data sets define a lin-

ear relationship, the gradient and intercept of the line were used to recalibrate the *Chikyu* data, resulting in a relationship close to $y = 1x + 0$ (Fig. F49). This recalibration was performed for SiO_2 , TiO_2 , Al_2O_3 , Fe_2O_3 , MnO , MgO , CaO , Na_2O (not for BA holes), K_2O (not for BA holes), V, Cr, Ni, Cu, Zn, and Sr. Recalibration calculations were applied for the GT holes, BT1, the CM holes, and the BA holes, in these respective groupings (i.e., all GT hole data were subject to the same recalibration factor). Spreadsheets showing recalibration calculations can be found in [Supplementary material > F1_XRF Recalibration](#).

LA-ICP-MS analysis

Leg 3 preparation and analysis of powder pellets.

After the first stage of milling (powder sample grain size < 250 μm , see above), 3 g of sample powder was further milled using the Fritsch planetary mill in 80 mL agate grinding bowls with 4 × 30 mm diameter agate balls. Sample powders were rotated at 400 rpm for 30 min and allowed to cool for 5 min for 4 repeat cycles, after which the contents of the jars were sieved through 100 μm and 60 μm nylon meshes (Clever, Toyohashi, Japan). Material >100 μm was returned to the bowls and ground for a further 30 min. Once the whole sample was powdered to <60 μm , each sample was recombined and returned to the grinding bowl and milled for 5 min to homogenize. The final powders were stored in ethyl alcohol-cleaned polystyrene sample vials. Approximately 1.5 g of whole-rock powders (grain size < 25 μm) were pressed into powder pellets for trace element analyses by LA-ICP-MS using the Spex SamplePrep 3630 X-Press. The 1.5 g of powder was weighed and placed into a 5 mm tall sample holder cut from an 18 mm outer diameter (OD) polypropylene tube (Fig. F50). The powder was isolated from the metal rams that apply the load from the press to the sample powder using Prolene film (CHEMPLEX, Florida, USA). The press was set to ramp up to 15 tons and held there for 20 s. The pressure was then gradually released over 66 s, after which the sample in the sample holder was removed from the press, labeled, and placed into a weighing paper envelope, sealed in a labeled Ziplock bag, and stored in a desiccator until analysis. The method is documented in [Appendix E](#).

This procedure was tested using reference materials JP-1 (peridotite), BIR-1a/1G (basalt), and BHVO-2 (basalt) and then to determine the trace element concentrations for a selection of 8 samples from Hole CM1A (gabbros: 6Z-2, 12–17 cm; 18Z-1, 26–33 cm; 25Z-4, 50–59 cm; 41Z-2, 0–6 cm; 62Z-2, 24–30 cm; dunites: 51Z-1, 31–39 cm; 58Z-2, 1–6 cm; 68Z-1, 19–26 cm) and 6 samples from Hole CM2B (dunites: 11Z-1, 34–39 cm; 15Z-4, 38–43 cm; 18Z-2, 77–83 cm; 27Z-1, 13–18 cm; 35Z-2, 1–5 cm; 35Z-3, 16–23 cm).

The final steps of the pellet preparation procedure were modified for Hole CM2B samples compared to

the process used for Hole CM1A. Approximately 1 g of homogenized powder (<25 μm) was loaded into a 5 mm tall sample holder cut from a 7 mm OD Al pipe (Fig. F50) and pressed into a tablet by applying 10 tons of pressure for 20 s. The pressure was gradually released over 66 s, after which the sample was removed from the sample holder, labeled, and placed into a weighing paper envelope, sealed in a labeled Ziplock bag, and stored in a desiccator until analysis. This adapted procedure was tested using standard reference materials BIR-1a, BHVO, and JP-1 and on 6 samples selected from Hole CM2B (dunites: 11Z-1, 34–40 cm; 15Z-1, 38–43 cm; 18Z-2, 77–83 cm; 27Z-1, 13–18 cm; 35Z-2, 1–5 cm; and 35Z-3, 16–23 cm).

The ICP-MS configuration was adjusted before each analytical sequence to ensure the high sensitivity required to measure the very low concentrations of ultra-trace elements in peridotites. Operating conditions for all analyses are as follows: spot size = 100 μm , pulse rate = 5 Hz, and energy density = 12.0 J/ cm^2 . Instrumental background analyzed before each analysis was subtracted from the following signal obtained during sample ablation. BHVO-2_GP (glass pellet) was analyzed and used as external standard following the recommended concentrations proposed by Barrat et al. (2012). Analytical sequences consisted of one analysis of BHVO-2_GP between the analysis of each natural sample pressed powder pellet to monitor the instrumental drift and possible matrix effects caused by pressed powder ablation. ^{42}Ca was used as an internal standard following major element composition obtained by XRF on beads.

Results obtained by LA-ICP-MS analysis of pressed powder pellets prepared for the 3 reference materials BHVO-2, BIR-1a, and JP-1 are shown in Figure F53 and reported in Table T34. The associated relative standard deviation (%RSD) is given as reflecting the intermediate precision of the averaged composition (i.e., the repeatability over the different analytical sessions). The precision is variable depending on the standard analyzed and the element considered. The standard deviation basically increases with lower concentrations; RSD averaged for all the analyzed elements are lower than 8%, 14%, and 19% for BHVO-2, BIR-1a, and JP-1, respectively. Concentrations for (ultra)trace elements are generally close to reference or certified values (<10% for BHVO-2 and BIR; <20% for JP-1), and REE and multielement normalized patterns are adequate (Fig. F53). Among given elements, Ce and Cs are not systematically reported. Ce was regularly high compared to the preferred SRM value, possibly a result of uncorrected oxide interferences, whereas Cs shows poor reproducibility. In addition, transition elements such as Ni, Co, Cu, and Zn are overestimated by >20% in SRMs BIR-1a and JP-1. In the case of peridotite JP-1, underestimation of Ti and high-field strength elements (HFSE) is associated with underestimation of Cr concentrations. This

possibly reflects the greater difficulty to mill chromite grains relative to olivine even using the 2-stage sample milling process, which is most apparent in this ultra-depleted reference material. A further consequence of this “undersampling” of chromite could be an “oversampling” of olivine that leads to overestimation of minor elements such as Ni and Co.

Although development of this analytical facility has to be improved on other materials in future cruises of the *Chikyu* and considering the previous observations, results obtained for reference materials were generally in good accordance with preferred values (Fig. F53). Following the different steps tested during the whole-rock in situ trace element analysis development both in terms of sample grain size (number and duration of milling) and instrument parameters, it appears that 3 analyses on each sample is the minimum required to account for sample powder heterogeneity so that the averaged compositions are adequately close to reference or preferred SRM values.

Leg 4 preparation and analysis of powder pellets. A method was developed to determine low-abundance trace elements (e.g., REEs) by LA-ICP-MS in powder pellets during Phase 2. The laser ablation system was used for the first time during ChikyuOman Leg 3 to measure trace element concentrations in whole-rock pressed powder pellets (see above) and mineral separates presented in polished epoxy mounts. The LA-ICP-MS system comprises a NewWave Research UP-213 Nd:YAG deep UV (213 nm) laser ablation system coupled to an Agilent 7500ce quadrupole ICP-MS. The elements analyzed were Li, Al, Si, Ca, Sc, Ti, V, Cr, Mn, Fe, Co, Ni, Cu, Zn, Ga, Rb, Sr, Y, Zr, Nb, Cs, Ba, REEs, Hf, Ta, Pb, Th, and U. Spot size was 100 μm for all analyses. Operating conditions: pulse rate = 5–10 Hz, energy density = 12.0 J/ cm^2 . Reference materials and standardization processes were adapted to specific sample types analyzed (whole-rock pellets vs. polished separated minerals, see below).

To prepare samples, residual powder from XRF pellets was ground with agate mortar and pestle for >10 min, carefully placed into a 2.5 mm high sample holder cut from an 18 mm OD polypropylene pipe, and pressed into a small (~1 cm) pellet at 25 tons. These small-diameter pellets were used because of excessive ablation of standard wider diameter XRF pellets (likely due to lower pressure). Pellets were prepared following 2 milling steps to ensure the grain size was <25 μm , which is critical as both the grain size of whole-rock powders following the first stage of milling and the maximum spot size that can be used using the laser ablation system are similar (~100 μm) (Fig. F52; see also Peters and Pettke, 2017). Large grain sizes can result in widely contrasting signals between different analyses in a given sample containing two or more minerals. Two-step milling was undertaken for 14 selected samples of gabbro and dunite from Holes CM1A and CM2B as well as for

SRMs JP-1, BIR-1a, and BHVO-2, analyzed as unknown samples to check the precision and accuracy of the LA-ICP-MS methods on pellet samples.

Trace element analyses for whole-rock composition were performed on pressed powder pellets following the sample preparation and instrumental parametrization as above (Table T35); analysis parameters: laser power = 60% (corresponding to initial fluence of 12 J/cm², which decreased steadily during analysis), repeat rate = 10 Hz, stage speed = 20 µm/s over raster of ~600 µm × 600 µm, line spacing = 150 µm. Blanks were analyzed for 120 s and ablation runs for 60 s for NIST612 glass and 150 s for all other samples. During the first 30 s of ablation, the signal often showed a period of equilibration before settling to a steady count rate. As a result, the first 30 s of ablation analysis was discarded.

Samples were bracketed by analyses of NIST612 glass, and within each bracket pellets of powdered standard materials JP-1 or BHVO-2 were run to check accuracy and reproducibility. All sample data were calibrated to the average sensitivity (in units of [concentration]/[counts per second]) of the two bracketing NIST612 analyses (see Table T36). An internal calibration to known concentrations of Si was applied to correct for differences in the efficiency of ablation between analyses. This results in better reproducibility and accuracy in secondary standards compared to omitting both the correction and Ca internal calibrations (Figs. F54, F55).

Table T36 summarizes the mean elemental concentrations, standard deviations, and percentage deviations from reference values measured in secondary standards across all sessions. Since NIST612 was used to calibrate and correct for instrumental drift, it cannot be reported in the same way. BHVO-2 showed good accuracy and reproducibility, RSD <30% and deviation from reference values <10% for the majority of elements. SRM JP-1 was more analytically challenging; most elements range 10%–60% RSD, and deviate <25%. A few elements show consistent large deviations from reference values. Sn and Pb were consistently significantly overestimated in both JP-1 and BHVO-2 (>844% deviation). In light of this, these elements were discarded. In addition, several low-abundance trace elements (e.g., Tm, Th, Nb, Y) were underestimated in JP-1, likely because of low abundance and consequent signal-to-noise issues. However, since the deviations were <90% it was judged that they should be included. Overall, the data indicate that the method is particularly useful for more trace element-enriched lithologies (e.g., gabbros) but can also be successfully applied to peridotites with the proviso that the least abundant elements may only be accurate to within a factor of 2.

Preparation of polished grain mounts and analysis of trace elements in minerals. A 2 g aliquot of crushed material was separated from whole-rock samples fol-

lowing the final stage of the jaw crushing process (grain size < 1 mm). Clinopyroxene, orthopyroxene, plagioclase, and garnet mineral separates were hand-picked under a binocular microscope, and then the picked minerals were mounted onto a stiff flat surface of an epoxy ring support (2 cm diameter, 5 mm thick; Fig. F51) using two-sided tape. After pouring in epoxy, the mounts were cured for at least 12 h. The mounts were then manually ground to develop a flat surface and then polished in a figure-eight motion to avoid bulging of the mount surface. The polished plug was cleaned using dry alcohol in an ultrasonic bath, dried, labeled, and placed into a weighing paper envelope, sealed in a labeled Ziplock bag, and stored in a desiccator until analysis. The method is documented in [Appendix F](#).

Mineral trace element contents were obtained by LA-ICP-MS on orthopyroxenes and clinopyroxenes separated from gabbros, dunites, and harzburgites from Holes CM1A and CM2B. Operating conditions were spot size 100 µm, 10 Hz pulse rate, and energy density of 12.0 J/cm² for all analyses. SRM612 was used as an external standard following the recommended concentrations proposed by Jochum et al. (2011). Bracketing data reduction was undertaken by including NIST612 every 6–10 pyroxenes analyzed. ²⁹Si was used as an internal standard. Reference material BIR-1G (glass pellet) was analyzed as an unknown sample in each sequence dedicated to pyroxenes analysis. BHVO-2_GP was also investigated in few cases.

The results obtained for BIR-1G and BHVO-2 are given in Figure F56, and concentration, precision, and accuracy for each element determined for these standards are given Table T34. Similar to results obtained by analyses of pressed powder pellets, Cs is not reported because of poor determination. The intermediate precision averaged for all elements is lower, better than 9% and 16% for BHVO-2 and BIR-1G, respectively. Results obtained on glass plots are very close to reference or preferred values and yield similar REE and multielement patterns. The intermediate precision for REE ranges 3.2%–9.8% (except Eu; RSD = 14.7%) in BHVO-2 and 7.7%–14.8% in BIR-1G. Elements with higher standard deviations are Zn (22%–24%), Th (10%–26%), and U (16%–41%) in both standards, as well as Ta in BIR-1G (28%).

XRF and LA-ICP-MS data comparison

Most of the (ultra)trace elements determined in samples from Holes CM1A and CM2B during ChikyuOman Leg 3 were acquired only by LA-ICP-MS (Table T34). XRF detection limits (~5 ppm) are far too high for low-abundance trace elements. Minor to trace element (Cr, Co, Ni, Cu, Zn and Sr) concentrations analyzed by XRF and LA-ICP-MS are compared in Figure F57. The correlation factor is ~80% for Ni and Cr, with overestimation in the LA method in comparison to XRF. The Cr value ob-

tained by LA-ICP-MS was preferred, as it has been well determined for two reference materials (BHVO-2 and BIR-1a) and only slightly underestimated for one other (JP-1). Because of the overestimation in Ni discussed earlier, regarding the reference or preferred values in SRMs, XRF results are preferred. Concerning Co, Cu, and Zn, the correlation factor between the LA and XRF procedures is poor (27%–39%). Although values obtained by LA-ICP-MS seem slightly overestimated compared to the results obtained for the three investigated SRMs, they are preferred, as these elements are clearly much more underestimated using the XRF method. Sr content obtained by LA-ICP-MS was preferred primarily because values are close to reference or preferred values but also because of the relatively high detection limits of this element when determined by XRF (see Table T34).

EA measurements of volatile elements

For analysis of the volatile elements CHN and S^{Total} , two separate Thermo Finnigan Flash EA 112 elemental analyzers were used, one for CHN and the other for S^{Total} . The instruments were configured differently to optimize the conditions for analysis.

Leg 3. For both analyses the samples were dried at 105°C for 12 h to remove adsorbed water then weighed into a soft tin capsule. The same analytical procedures and conditions used during OmanDP Phase 1 were used for analysis. Calibration curves are shown in Figure F58 and precision and accuracy data are presented in Tables T37, T38, T39, and T40.

Leg 4. Sample powder (42.5 ± 2.5 mg for CHN analysis and 22.5 ± 2.5 mg with same amount of V_2O_5 for S analysis) was weighed into a soft tin capsule. During these analyses the analytical procedures and conditions of OmanDP Phase 1 were closely followed. Sulfanilamide standards (0.5, 1, 2, 3, and 5 mg) weighed on land were used to generate calibration curves with high CNH content. For samples of relatively low C and N concentrations, NCS soil standards (0.5, 1, 2, 3, and 5 mg) were used for calibration. Sulfanilamide (10 and 25 mg) and SRM JGb-2 (0.5 and 1 mg) were used to calibrate sulfur analysis. The concentrations of the standard material of each measurement is shown in Tables T41 and T42.

Coulometry determination of carbonate

The carbonate analyzer on board *Chikyu* (Coulometrics 5012 CO₂ coulometer) has a carbonate decomposition device and a coulometer detector. The carbonate decomposition device is composed of two lines with nitrogen gas flow, one for acidification of samples and the other for CO₂ sampling and injection into the coulometer. Sample vials are purged

with N₂ gas followed by addition of 2 M HCl, which yields CO₂ gas from decomposition of carbonate minerals. The liberated CO₂ is injected into the coulometer with N₂ gas flow for measurement by coulometric titration.

As during ChikyuOman Phase 1, 40–50 mg of powdered rock was weighed into an aluminum foil capsule. Calibration was obtained using preweighed CaCO₃ standards (5–15 mg \times 3) and empty capsules to act as the baseline blanks (following standard *Chikyu* shipboard protocol). For ChikyuOman, the percentage of carbonate minerals present was determined assuming all CO₂ released came from CaCO₃. Total organic carbon contents were calculated by subtracting inorganic C from the measured TC. Because of the abundance of dolomite and magnesite in the listvenite-dominated domains in the upper part of Hole BT1B, we assumed that all CO₂ released came from dolomite (and/or Mg calcite) but that magnesite was not dissolved. For this reason, TOC was not determined for the samples from listvenite-dominated domains in the upper part of Hole BT1B.

Precision and accuracy were assessed by measuring SRMs NIST88b and JSd-2, both of which were included in each batch of samples (Table T43). The accuracy for inorganic C was better than 5% and precision was better than 3% for both standards.

X-ray diffraction

X-ray diffraction (XRD) was used to identify minerals and mineral mixtures associated with the unaltered primary composition of peridotitic and gabbroic rocks as well as secondary mineralization features such as serpentinization, hydrothermal veins, alteration halos, and fault zones in the cores. We measured whole-rock powders to determine the secondary mineral assemblage down to 400 m depth.

Preparation and analysis of whole-rock samples.

Whole-rock samples for XRD analysis were taken from the powdered sample after milling. Details of the powdering methods are shown in sections above. Powders were dried in the oven at 60°C if necessary and then stored in a small labeled bottle. Samples were mounted as random bulk powders in glass holders. The choice of holder was based solely on the volume of sample available, with the glass holder having higher capacity. The sample holders were cleaned with ethanol to remove any strays. The depression in the holder was filled with powder, and to ensure a flat surface at the correct height it was gently pressed into place with a glass thin section slide.

Samples were loaded into the XRD autosampler. X-ray diffractograms were produced for each sample using the PANalytical CubiX3 PRO (PW3800) diffrac-

tometer with associated Panalytical X'Pert HighScore Plus software for data processing. Backgrounds were determined using default values of 5 for bending factor and 20 for granularity. The instrument and software peak search settings are given in Figure F59. When necessary, unrecognized peaks were inserted manually or wrongly identified peaks were deleted. Search match for matching phases to peaks was performed with a restriction to search for minerals only and without restriction in chemistry of minerals including transition metals and rare elements. Matching phases were selected by best fit, choosing only well-known mineral phases that were likely to occur.

Phase 2 summary

A summary of the instrumentation used during ChikyuOman Phase 2 is presented in Table T44. Tables T21, T22, and T23 give summaries of the accuracy and precision data for the two laboratories, *Chikyu* and St. Andrews, for major and trace element analyses of the SRMs JB-1b, JGb-1, and JGb-2, respectively. Tables T9 and T10 give summaries of geochemistry laboratory measurement accuracy and precision data through ChikyuOman Legs 1–4 for major and trace element analyses of SRMs JB-1b, JGb-2, DTS-2b, and JP1.

X-ray fluorescence core scanning

X-ray fluorescence core scanning (CS-XRF) is potentially a highly useful semiquantitative technique for near-continuous elemental mapping of drill cores and other samples. A core scanning XRF is available onboard *Chikyu* and at some core repositories and other institutions and is increasingly deployed to measure relative chemical changes in continuous sedimentary sequences. CS-XRF is not yet available on the *JOIDES Resolution* and, consequently, this new technique has not been extensively deployed by scientific ocean drilling to make chemical maps of long continuous sections of igneous rocks. The description of 1500 m of drill core from the Samail ophiolite cored by Phase 1 of the OmanDP aboard *Chikyu* during the ChikyuOman core description campaign provided an opportunity to test the application of continuous, high-spatial resolution CS-XRF elemental mapping for igneous, alteration, and metamorphic petrology and structural geology. This technique provides complementary data to visual core description, discrete sampling for microscope observation, and whole-rock geochemistry and continuous monitoring of physical properties by the multi-sensor track core loggers, the X-ray CT scanner, and visible near-infrared imaging spectrometry (VNIR).

We undertook whole-rock semiquantitative XRF spectrometry analysis for major and trace elements on selected core material (Na, Mg, Al, Si, P, K, Ca, Ti, Cr, Mn, Fe, and Ni). These methods have been

adapted from those described by previous CS-XRF analyses of sedimentary rocks during IODP Expeditions 322 and 343 (see Expedition 322 Scientists, 2010; Expedition 343/343T Scientists, 2013). Semiquantitative element scanning of core sections was undertaken using the onboard JEOL TATSCAN-F2 energy dispersive spectrometry (EDS)-based split-core scanner equipped with a cryogenic Si semiconductor and a 76 mm beryllium window (Sakamoto et al., 2006). The target for X-ray generation is rhodium (Rh) that can generate X-rays with 5× higher intensity compared to the standard EDS-based scanner. The diameter of the collimator produces an X-ray beam that is 0.8 mm in diameter, and the penetration depth into the sample is ~1.1 mm. The distance between the sample surface and detector strongly affects the intensity of X-rays received. Consequently, the TATSCAN-F2 can automatically adjust the position of the X-ray unit to maintain a 1 mm distance between the core surface and the measurement window, thereby reducing this problem.

All the XRF-EDS spectral data for each analytical spot were saved, converted to a CSV file using Element-Station2 software, and uploaded into J-Cores. Depths of sample spots are determined relative to the J-Cores curated section lengths. Semiquantitative oxide weight percentages for selected elements were calculated from background-corrected integrated peak intensities using software provided by the vendor (JEOL) for the TATSCAN-F2. Further theoretical details and operational procedures are outlined in Richter et al. (2006) and Sakamoto et al. (2006).

Prior to the ChikyuOman core description phase and following an extended period not being operated, the JEOL TATSCAN-F2 CS-XRF onboard *Chikyu* was recommissioned using parts from the similar instrument at the Kochi Core Center.

Calibration testing of CS-XRF vs. SRMs

Before analyzing OmanDP split cores, we undertook a number of calibration exercises to ascertain the responses of the instrument to igneous rocks with different compositions, assess the precision and accuracy of the instrument, and establish optimum operating conditions (Table T45). Samples were analyzed for the classic suite of major rock-forming elements (Si, Ti, Al, Fe, Mn, Mg, Ca, Na, K, and P) along with the important compatible elements Cr and Ni.

To identify the optimum balance of operating conditions between analytical quality and the time for core scanning, a series of measurements was made on XRF pressed powder pellets of 4 SRMs: basalt (JB-1b), gabbro (JGb-1), andesite (JA-2), and peridotite (JP-1) that straddle the range of primary igneous rocks recovered from the OmanDP drill cores (Terashima et al., 1998). Spots (7 mm) on each disk were analyzed at two different beam currents (0.17 and

0.04 mA) for a range of measurement times from 15 to 200 s for each analysis (Fig. F60).

Although the higher beam current (0.17 mA) produces higher count rates, these come at the cost of poorly defined light-element peaks for Na, Mg, and Al that sit on the low-energy shoulder of the major Si $K\alpha$ peak (e.g., Fig. F60). The phosphorous peak is also poorly defined. The $K\alpha$ peaks for Na, Mg, and Al are better discerned with a lower 0.04 mA current, but Na and Mg remain barely above background values. Linear regression lines were calculated for whole-rock analyses by CS-XRF vs. established values for the SRMs (Table T46) for the best-fit line, and the best-fit line was forced through a zero intercept. An r^2 is calculated for the best-fit lines. Analytical errors are not accounted for in these best-fit lines.

No usable data were achieved for Na and P in any of the operating conditions tested. Most elements give reasonable correlations, albeit for only 4 points. However, most lines have slopes that are greatly different from 1:1, and many have significant y -axis intercepts (Table T46). Consequently, the raw whole-rock data of the SRMs are poor and not as good as published *Chikyū* CS-XRF analyses (e.g., Expedition 343/343T Scientists for JB-1b; see Table T47). Count times longer than 60 s do not yield significant improvement in the correlations, and the higher beam (0.17 Ma) currents do not lead to better correlations compared to analyses at 0.04 mA. Given the poor distinction of light-element peaks at the higher current, it was decided that core sample analyses would be carried out at 0.04 mA current and 60 s count time. Although not strictly statistically valid, the SRM spot analyses can be recalculated using the 4-point regression lines. The results for JB-1b listed in Table T47 show reasonable agreement with the reference values for most elements, although there are no data for Na_2O or P_2O_5 .

Calibration testing of CS-XRF vs. archive core samples

Coarse-grained igneous rocks such as the OmanDP gabbro cores present interesting challenges for CS-XRF scanning because some of the individual minerals are of the same size or bigger than the analytical spot size. Whole-rock core samples were taken at the rig site approximately every 20 m from homogeneous background gabbro samples for thin sections and major and trace element analysis. Ten cores from the equivalent interval in the archive half were selected, cleaned, and lightly ground to remove saw cuts and ridges and then analyzed by CS-XRF. A total of 49–96 analytical ~7 mm spots were analyzed for each of the archive-half samples and the results averaged and compared to the preliminary XRF whole-

rock analyses undertaken at the University of St. Andrews (Fig. F61).

Linear regression lines were calculated for the averaged values by CS-XRF vs. abundances determined by XRF at the University of St. Andrews (Table T48) for the best-fit lines and calculated r^2 . Regression lines were not calculated for Na, P, and K because the determinations of these elements were poor in most analyses. The regression lines of other major elements plus Cr and Ni fit reasonably well with the data except for SiO_2 , for which the regression line is poor. The intercepts and slopes of the regression lines for 9 elements are used to calculate the compositions of the selected cores of the Oman gabbro and other rock types.

Our calibration method was tested by applying this approach to one of the archive-half core samples. Uncorrected and corrected data are compared to whole-rock XRF data analyzed at University of St. Andrews. The result gives reasonable agreement between the corrected and St. Andrews data. Reproducibility of analytical data was tested by duplicate analyses of 3 archive halves over 5 days. Significant drift in compositional data was not observed for most elements (Table T49).

Our method was then applied to a significant length of archive-half core as a final test before routine analysis. Interval GT1A-38Z-3A, 13–40 cm, was measured by CS-XRF to identify fine-scale downhole variations in elemental compositions. The analytical conditions were the same as for the previous calibrations (60 s analysis, 0.04 mA, 7 mm spot size). Analyses were made every 5 mm with 6 analyses across the core for every depth increment. The 6 analyses at each depth were averaged and the average and individual analyses plotted on a diagram of downhole compositional variation (Fig. F62; Table T50). All elements vary within limited ranges and indicate systematic wavy-like patterns. The geologic meaning of these patterns will be discussed in a later section.

Leg 2 CS-XRF scanning

Selected core intervals were scanned on the XRF-CL to obtain geochemical compositions of core cut surfaces in 2 dimensions. Analyses are collected on 7 mm sized points with 5 mm grid spacing over specified X - Y grids on the cut surface. Element concentration maps were created from the 2-D scan data and were used to create element concentration contour plots to aid in identifying rock compositions, compositional variations, and zones of mineral and rock compositional changes (Fig. F63). These maps guide selection of intervals for thin section study and higher precision chemical analysis by XRD, XRF, and ICP-MS on the ship and complement macroscopic visual and thin section descriptions.

Microbiology

Phase 1

Microbiology and mineralogy samples

Gabbro from Hole GT3A

DNA extraction. ICDP-5057-EX3370, 42–47 cm.

- DNA/RNA: ~0.25–0.5 g crushed rock from inside of core (3 replicates).
- DNA/RNA: ~0.25–0.5 g crushed rock from outside of core (3 replicates).
- DNA/RNA: ~5 mL of water from the rock saw used to cut the core interval (3 replicates).
- An additional 3 replicates of inner and outer core collected in cryovials and frozen for possible future metabolomic or single-cell genomic work.

Lipid extraction. ICDP-5057-EX3370, 37–42 cm.

For future analyses of lipid biomarkers, whole core rounds were wrapped in sterile, ashed aluminum foil and transported in solvent-washed (methanol + dimethylchloride) Teflon bags to prevent contamination during transportation. Upon arrival at University of Colorado-Boulder, samples were immediately frozen at -80°C for preservation of intact lipids. All future sample processing will take place at CU Boulder to both minimize and account for potential contamination during subsectioning of the core and downstream processing.

Serpentine from Hole BT1B

Lipid extractions. BT1B-39-1, 85–92 cm.

For future analyses of lipid biomarkers, whole core rounds were wrapped in sterile, ashed aluminum foil and transported in solvent-washed (methanol + dimethylchloride) Teflon bags to prevent contamination during transportation. Upon arrival at University of Colorado-Boulder, samples were immediately frozen at -80°C for preservation of intact lipids. All future sample processing will take place at CU Boulder to both minimize and account for potential contamination during subsectioning of the core and downstream processing.

DNA extractions. 77–84 cm.

- DNA/RNA: ~0.25–0.5 g crushed rock from inside of core (3 replicates).
- DNA/RNA: ~0.25–0.5 g crushed rock from inside of core (3 replicates).
- Remainder of core: frozen at -80°C for future sampling.

Drill cuttings from Site BA1

DNA analysis (from depth = 54 m).

- DNA/RNA: ~0.25–0.5 g crushed rock from inside of core (3 replicates).
- DNA/RNA: ~20 mL of drilling foam/liquid used on site (3 replicates).
- Inner and outer core collected in cryovials and frozen for possible future metabolomic or single-cell genomic work (3 replicates).

Spectroscopic analysis

- ~15 g of drill cuttings sampled from Site BA1 every 10 m at 10–140 m depth and every 20 m at 150–390 m depth. Additional samples of interest were also collected at 23, 58, 64, 65, 66, 144, 148, and 400 m depths.
- ~15 g of drill cuttings sampled from Site BA2 every 20 m at 3–383 m depth plus 1 sample at 400 m.

All of the above samples were packed into a Mylar bag with a oxygen scrubbing sachet, heat sealed, shipped to the University of Colorado-Boulder, and placed inside an anaerobic chamber (3% H_2 in N_2 , <1 ppm O_2).

Bulk nitrogen analysis

- Sampled from Site BA1 every 20 m at 130–390 m depth.
- 2 g from the wet-sieved, <2 mm, aerobically prepared fraction of the samples collected for spectroscopic analysis above.

Sample preservation

DNA extraction

Core collected from the sites was wrapped in sterile aluminum foil and transported to Muscat. Using a flame-sterilized chisel and mallet, the core was split and the outer material chiseled off. Pieces of the inner core were separated from the outer core, and each was crushed independently in a small flame-sterilizer rock crusher. Drill cuttings were collected on site after they had dried and were also crushed in a small flame-sterilized rock crusher. The powdered rock for each sample was scooped into bead tubes from the ZymoBIOMICS DNA/RNA Mini Prep Kit, shaken by hand for 30 s, and frozen in a liquid nitrogen dewar for preservation and shipping to laboratories in the US.

In the laboratory, samples were stored at -80°C until processing. When thawed, the Zymo bead tubes were bead beat on a MiniBeadBeater (Biospec Products) for 1 min intervals (total of 5 min) to prevent the tubes from heating in a longer bead beat cycle. The extraction protocol in the ZymoBIOMICS DNA/RNA Mini Prep Kit manual was used for parallel purification of DNA and RNA from each sample. Resultant

product DNA was quantified by Qubit HS dsDNA assay. RNA product was not quantified to preserve as much material as possible for future analysis.

Reverse-transcription polymerase chain reaction (RT-PCR) was done for RNA samples to convert to cDNA and amplify SSU rRNA amplicons using primers 515F-Y-M13 and 926R and the qScript XLT One-Step RT-PCR Kit (Quanta BioSciences). PCR was done for DNA samples using the same primers. Cycling conditions were adapted from Parada et al. (2016).

PCR and RT-PCR product was checked with gel electrophoresis and cleaned with Kapa Pure Beads. A 6-cycle barcoding PCR step was done to attach Illumina barcodes with the same cycling conditions as above. Products were again cleaned with Kapa Pure Beads, quantified with Qubit HS dsDNA assays, and normalized by DNA concentration for pooling.

All samples were pooled and sent to Duke Center for Genomic and Computational Biology for sequencing on an Illumina MiSeq. Data from this run are currently being analyzed with QIIME and other programs.

Lipid extraction

Prior to subsampling, we will wash the core with UV-treated, filtered (0.22 μm filter) ultrapure water in an attempt to remove any drilling fluids. We will only sample the interior of cores, removing the exterior of the core and processing separately to assess contamination derived from initial sampling. Prior work has shown that the interiors of rock cores are generally free of contamination (Lever et al., 2006; French et al., 2015). During all stages of laboratory work, samples will be handled as little as possible with appropriate laboratory attire (ethanol-sprayed nitrile gloves and laboratory coat as well as a face-mask if not in an ethanol-wiped fume-hood workspace), and all equipment and tools will be solvent-cleaned or ashed prior to use. Currently, the core samples for lipid extraction are frozen (whole) at -80°C while extraction and core handling methods are optimized. We anticipate processing 2 replicate exterior and interior core samples (each >50 g); however, replicates will be pooled and concentrated if samples are too organic-poor.

Contamination reduction

To account for contamination during the drilling process prior to sample acquisition, a sample of drilling fluid was collected in a sterile bottle to later be concentrated on an ashed glass fiber filter for organic extraction. For future lipids work, we will take additional steps to assess contamination in the laboratory through the use of combusted brick blanks to undergo the entire round of sample preparation including sawing (using solvent-cleaned blade, ceramic tile blanks between samples, and cooled with UV-

treated ultrapure water) and milling. Additionally, combusted sand blanks will be powdered in the puck mill between samples to prevent sample-to-sample contamination, with the final sand blank between samples extracted for analysis.

For all DNA and RNA extractions, general contamination reduction protocols were followed when possible such as wearing nitrile gloves, using sterile foil and tools, and flame-sterilizing the chisel, rock crusher, etc. To account for contamination from drilling fluids and core processing, samples of the outer core rounds were collected as a contamination control for comparison to the inner core microbial community. Samples of water from the rock saw at Site GT3 and drilling foam from Site BA1 were also collected as contamination controls for further comparison. In the laboratory, all hoods used in processing were cleaned prior to use with 20% bleach and treated with UV light for 15 min. The hood, pipettes, and other small equipment were wiped down with RNase Away to limit RNAases. Typical laboratory practices to limit contamination were employed through all molecular processing.

Phase 2

Microbiology and mineralogy samples

Microbiology subsamples were allocated from 50 cm BIO whole-rounds (WR) during Phase 2 as follows (see Table T51):

- DNA extraction/sequencing: 5 cm intact WR.
- Lipid extraction: 15 cm intact WR.
- DNA preservation: 4 cm intact WR.
- Fluorescence microscopy, cell counts, tracer counts: <0.5 cm WR crushed, formaldehyde-fixed.
- Cultivation experiments: <0.5 cm WR crushed, preserved in anoxic site water.
- Carbon compound transformation rates: 5 cm intact WR.
- Raman, electron probe, XANES, C-imaging, XRD, S-isotopes: 4 cm intact WR.
- TOC, TIC, and carbon isotopes: 1 cm intact WR.

Bulk nitrogen isotopic analysis

Without contamination controls for nitrogen, as discussed above in Phase 1, we cannot confidently assess what organics extracted from the rock core are autochthonous. We adapted the Phase 2 protocols for lipid analysis accordingly. Drill cuttings recovered during the rotary drilling of Site BA1 for microscale characterization of mineralogy were also processed for bulk rock nitrogen stable isotopic analysis. Well chips had been wet sieved to remove drilling fluids and to collect the >2 mm fraction. Approximately 2 g from this fraction from each of the depth intervals (130–390 m) were air-dried and crushed to

a fine powder using an agate mortar and pestle. Between 400 and 600 mg of powder per sample was weighed into 9 mm × 10 mm tin capsules, sealed, and then introduced in the autosampler of a Thermo Delta V elemental analyzer for continuous flow analysis of bulk rock nitrogen stable isotopes. Samples contained very little nitrogen, and tin capsule blanks were run after each sample to allow for precise blank corrections. These data are currently being processed to subtract any N contamination from the tin capsules and to calculate precision of measurements.

Whole-rock core and contamination control

Samples for microbiology investigations (“BIO”) were identified once every 10 m downhole during drilling operations at the “BA” sites in January–March 2018. Approximately 50 cm of WR core was allocated in each 10 m interval from Holes BA3A, BA1B, and BA4A. These BIO samples were logged into the ICDP database and given a simple working name using a system tied to site and approximate downhole depth (e.g., “BA3A_10m, BA3A_20m, BA3A_30m...”). For Hole BA1B, additional ~5 cm WR samples were taken at irregular intervals from 0–50 m depth to extract DNA from zones with highly variable alteration and redox states.

For each 50 cm WR sample for BIO, several protocols were followed to ensure the best possible preservation of the core (Figs. F64, F65). These protocols included immediately scrubbing and washing the outside of BIO core with ultraclean deionized water and then placing the core on muffled carbon-free foil inside the core liner during the initial archiving, imaging, and description. No wax was drawn onto the BIO core, and wax residues were removed with bleach and ethanol from the core scanner before each BIO core section was imaged. In addition, the saw water was replenished with freshwater on a regular basis, and all personnel handling the core wore nitrile gloves through all stages of handling. Once the BIO core was appropriately entered into the ICDP database, the ~50 cm sample was brought to the BIO-van and rubbed with ethanol along the full exterior; it was then placed on carbon-free muffled aluminum foil and sectioned into Samples A–J (see Table T51) using an ethanol-washed hammer, chisel, and tweezers. The exterior of each subsample was given a final deionized water wash in a laminar flow hood. Samples A, B, C, F, G, and H were moved into an anaerobic chamber flushed with nitrogen gas; each sample was placed inside a Mylar bag filled with nitrogen and sealed to retain anoxic conditions. Samples A–C were frozen, and Samples D–J were kept at refrigeration temperature (Table T51).

In the BIO-van, we saved some small rock chips generated during subsampling of the 50 cm WR core. These chips are derived primarily from the interior of each core subsample but also include pieces of the

core exterior. The chips were added to an epitube with ethanol-cleaned tweezers and fixed in 1.5 mL of 4% paraformaldehyde (designated as “D” samples). Separately, some of the larger chips were added to 10 mL sterile glass vials. These vials were moved into an anaerobic chamber, filled with groundwater pumped from the rock formation, and sealed under a nitrogen atmosphere. These samples of rock fragments submerged in site fluid were designated as “E” samples and preserved for microbial cultivation efforts.

UV Dayglo paint used as a contamination tracer

Despite extreme care to handle and store core cleanly, surface contamination during the drilling process is unavoidable. Prior work has shown that the interiors of rock cores are generally free of contamination (Lever et al., 2006; French et al., 2015); however, this cannot be assumed for all samples, especially if the rock is highly fractured.

Therefore, all the biological assays require careful assessment of drilling contamination. To efficiently screen the integrity of the interior of the core before sample processing to allow for selection of the most pristine samples, “Invisible Blue” Dayglo fluorescent microsphere tracer was spiked into the EZ Mud drilling fluid during OmanDP Phase 2 for drilling Holes BA3A, BA1B, and BA4A to trace the infiltration of drilling fluid into the core. Measurements of the extent of drilling mud contamination are critical in order to focus microbiology work on samples least impacted by allochthonous carbon and microbial biomass added to the system. Thus during drilling, we added Invisible Blue Dayglo paint (e.g. Friese et al., 2017) into the pit that was loaded with water and EZ Mud. Invisible Blue contains micrometer-sized particles that fluoresce under UV light. We diluted the paint at ~1:10,000 ratio to the volume of drilling mud in an effort to maintain the particle tracer concentration at ~10⁸ particles/mL through the day. More Invisible Blue paint was added to the pit whenever new water was added to restore fluids lost during drilling. We established a UV optical density calibration curve so that we could determine when the tracer particle load was too low and more paint should be added to the mud pit (see Fig. F66).

The “D” sample, derived from small rock chips fixed in paraformaldehyde, was used for fluorescence microscopy to quantify Invisible Blue tracer particles in each depth interval; these “D” samples also will be used to conduct future cell enumeration experiments to determine microbial cell density. Because the particle size of the DayGlo tracer is equivalent to a microbial cell, if microspheres are detected via fluorescent microscopy in the interior of the core, microbial cells have also penetrated into the core during drilling, likely compromising the sample. Subsamples of rock chips were initially screened via fluorescent microscopy. Samples with little to no visible In-

visible Blue particles were selected for downstream biological analysis.

To identify which samples contained high loads of UV paint particles, we homogenized the “D” sample by vortexing the sample tube, dispensed two 50 μ L aliquots of mineral fragments onto a glass slide with coverslip, and examined samples from each depth interval at 400 \times magnification using a Zeiss Axioimager epifluorescence microscope. The semirounded micrometer-scale paint particles glow brightly when excited by a Hg lamp coupled to a UV filter, and they possess distinct shape, brightness, and spectral characteristics compared to microbial cells that were counter-stained with Syto-9 to fluoresce in the green channel (Fig. F67). The UV particles were counted in 10 fields of view (FOV) per sample. Highly contaminated samples contained 20–30 particles per FOV; notably clean samples contained <1 particle summed across all FOVs. The samples considered to be “contaminated” by drilling mud were then considered lower priority for further biological analysis (see Table T52). However, more quantitative tracer measurements will be conducted on fragments from the interior vs. exterior of “B” and “G” samples to determine whether the interior of the cores are cleaner for lipid extractions and biological rate assays.

Building a “contamination control” library for DNA and lipids

Because of the extremely low predicted inventory of biomass stored within ultramafic rock, even in seemingly uncontaminated samples, it is necessary to evaluate any potential sources of exogenous DNA or organic material to the samples during the drilling or core handling process. To recognize when organic contaminants may have penetrated into the interior of the core, we developed a deep library of contamination controls using combusted glass fiber filters (0.3 μ m pore size) to filter fluid contamination sources (e.g., EZ drilling mud from the holding pond, drinking water used to wash the core, recirculation water from the rock saw, air inside the mobile laboratory) or to swab surfaces the core came into contact with (the interior of the core barrel and the core deck tray). A parallel set of contamination controls for DNA contaminants were collected using 0.2 μ m pore size polycarbonate filters and sterile cotton swabs, respectively, with two additional controls: a core-scanner swab and a filter of effluent from the core-washing process. Throughout drilling the active alteration zone, more than 720 of these contamination controls were collected. Contamination controls will be processed downstream with correlated DNA or organic samples (by date, or more specifically, drilling depth) such that statistically relevant

contaminating compounds or sequences can be removed during data processing.

Nucleic acid extraction (A samples)

Rock cores collected in 2018 will be cut and powdered by hand as cleanly as possible to extract nucleic acids for DNA sequencing of small subunit (SSU) rRNA genes (for identification) and metagenomics (whole community functional potential). A modified phenol chloroform isoamyl alcohol extraction with linear acrylamide will be used to isolate DNA from rock powders. The Daly protocol from Colorado State University (CSU), created for use in shale rock, was altered slightly by Emily Kraus at the Colorado School of Mines (CSM) for use in dunite/harzburgite. Any extracted genomic material will be quantified via qPCR using the ZymoBiomix Femto-Bac kit because of the kit’s detection limit sensitivity to low (femtoprogram) levels of DNA input. Quantifiable samples will then undergo PCR amplification using primers to target SSU rRNA for identification of microbial genera (described in Parada et al., 2016). A separate amplification of extracted genomic material using random hexamer primers for metagenomic library generation will be done for functional gene identification to assess community metabolic potential changes.

Rock preparation and DNA extraction

To prepare the A samples for DNA extraction, we will chisel off outer core surfaces and separate from inner pieces. We will then powder the inner core pieces in a laminar flow hood in one of the small handheld rock crushers that has been sterilized twice with ethanol and flaming. The outer core pieces will be powdered in a second rock-crusher, also sterilized twice with ethanol and flame. The rock powders will be placed into labeled clean 50 mL conicals.

The DNA extraction procedure has been adapted from Rebecca Daly at CSU (adapted from Lever et al., 2015). It involves preparing fresh lysis solution; 5 M NaCl; phenol:chloroform:isoamyl alcohol, 25:24:1, pH 8; chloroform:isoamyl alcohol (Ch:laa), 24:1; 100% ethanol; 70% ethanol; elution buffer (warm to 50°C); and linear acrylamide and requires lo-bind tubes and 50 mL centrifuge tubes. All reagents, supplies, and pipettes are placed in the laminar-flow hood, which is UV sterilized for 15 min. The heat block is set to 50°C, and all surfaces are sprayed with DN Away solution.

The procedure involves the following steps:

1. Place ~0.5 g rock powder in 2 mL tubes (nothing in blank tubes).
2. Add 1.0 mL of lysis buffer I solution, vortex to mix, and freeze at –80°C.

3. Thaw sample, then vortex and incubate for 1 h at 50°C, vortexing each 10 min.
4. Centrifuge samples at 10,000 × g for 3 min at room temperature and transfer supernatant from replicates to a 50 mL tube.
5. Place this 50 mL tube on ice and extract again from each tube by adding 1.0 mL of lysis buffer I solution, vortexing to mix.
6. Centrifuge samples at 10,000 × g for 2 min at room temperature and transfer supernatant from replicates to the 50 mL tube in Step 5.
7. Add 1 volume of phenol:chloroform:isoamyl alcohol to the combined samples and mix by inversion.
8. Centrifuge at 10,000 × g for 10 min at room temperature and transfer supernatant to new 50 mL tubes.
9. Add 1 volume of chloroform:isoamyl alcohol to the samples and mix by inversion.
10. Centrifuge at 10,000 × g for 5 min at room temperature and transfer supernatant to 50.0 mL tubes.
11. Repeat Step 10 twice using Ch:Iaa.
12. Precipitate DNA by adding 30 µL of linear acrylamide and 0.2 volumes of 5 M NaCl solution, then 2.5 volumes of 100% ethanol to the new volume.
13. Incubate the sample overnight at 4°C.
14. Centrifuge the sample at 12,000 × g for 30 min at room temperature, washing twice with 70% ethanol, then centrifuge at max speed for 10 min and remove excess ethanol with a pipette.
15. Dry the pellet in the hood for 2–3 min.
16. Resuspend the DNA in ~50 µL of warm elution buffer.

Quantitative polymerase chain reaction

Quantitative polymerase chain reaction (qPCR, also known as real-time PCR) is used to detect and accurately quantify DNA extracted from environmental samples. Absolute quantification against a standard curve gives robust reproducible results of nanograms of DNA in each reaction, which is used to calculate total amounts of DNA recovered per gram rock and gene copy number of the targeted genomic region being amplified. Additionally, accurate DNA quantification is necessary for downstream sequencing applications for high-quality data generation. For this work, DNA quantification will be used first to determine which rock extractions contain enough bacterial/archaeal genomic material to be suitable for successful PCR amplification and sequencing (of SSU rRNA and whole-community metagenomes). Quantification of a 350 bp portion of the 16S rRNA gene will also be used to calculate total amounts of genomic material recovered between rock samples and as a rough proxy for assessing differences in cellular

biomass. Performing qPCR on the 16S rRNA gene allows quantification of the bacterial and archaeal microbial genomic load but does not include or amplify eukaryotic DNA, which is deemed a general contaminant in the Samail ophiolite cores.

qPCR of extracted genomic material from each inner sample will be carried out using the Zymobiomics Femto Bacterial Quantification Kit and bacterial standards because of the kit's high sensitivity for low amounts of input bacterial DNA in the presence of background eukaryotic DNA (human contamination in this case). The included primers target a 350 bp segment of the 16S SSU rRNA gene, and the lower detection limit of this procedure is 20 fg of DNA per microliter (equivalent to 5 copies of *E. coli* genomic DNA), making it ideal for low-biomass environments. Technical replicate reactions will be run for each core sample and standard. Results of this method are in nanograms of DNA, which can be used to backcalculate approximate nanograms of DNA or 16S gene copy number present in the original grams of rock powder. Additional qPCR protocols targeting other functional or marker genes may be done as well if the need arises.

Amplification for SSU rRNA genes and metagenomic sequencing

Little is known about the microbial communities harbored in the rock-hosted biosphere of the Samail ophiolite. In this work, we aim to identify microorganisms residing in the rock cores and their genetic functional potential capabilities for energy generation and growth. DNA sequencing efforts will initially target a 450 bp region of the 16S rRNA genes from genomic material recovered from the Site BA cores. Samples that show positive quantification with the FemtoBac qPCR kit will be amplified using PCR for sequencing. We will use the modified Parada primer set (515Y-M13 and 926R) to amplify a section of the V4/V5 regions of SSU rRNA genes for taxonomic identification, as these primers are considered the least biased when targeting all three domains of life (Parada et al., 2016). PCR cycling and sequencing conditions will be used as described in Krause et al. (2018). In addition to identification and phylogenetic relatedness, metagenomic sequencing will be done to identify and annotate functional protein coding regions of all microorganisms within a sample. This allows examination of possible metabolic differences between microbial communities across boreholes, depths, or geochemical/mineralogical regimes within the ophiolite. A separate amplification procedure will be done with random hexamer primers to randomly target all genomic material present in a sample for metagenomic sequencing. This data set will be assembled and annotated for functional gene coding regions.

Lipid biomarkers (B samples)

We will pare off the exterior ~1 cm from the B core samples at CSU Boulder using a MK Diamond 2002E saw with a 14 inch 62Q wet-cutting diamond blade retrofitted with a Milli-Q water inlet for cooling. The blade will be removed and extensively cleaned with high-performance liquid chromatography (HPLC)-grade methanol after each day of sawing. Between samples, the blade will be rinsed with Milli-Q water and a combusted brick will be sawed to remove contaminating particles from the blade.

Only the interior subcore sample will be utilized for downstream biomarker analysis. However, we will process the exterior 1 cm of the core as well as a combusted brick blank in tandem with the interior such that the biomarker composition of the exterior and interior subsamples can be compared statistically to distinguish exterior contamination from endogenous organic matter; all contamination introduced during sample processing can be subtracted. In the event that the exterior and interior core subsamples cannot be distinguished, the extensive array of contamination controls collected should allow us to determine not only the source of the contamination but to subtract the contamination signal. For a more conservative approach, only compounds that are not present in any of the contamination controls and that are more abundant in the interior will be considered as autochthonous.

Both the interior and exterior subsamples along with brick blanks will be crushed with a chisel and hammer and stainless steel mortar and pestle until <1 cm diameter is achieved. Rock fragments will then powdered and homogenized using a ceramic ball mill. As with the saw blade, the chisel, hammer, mortar and pestle, puck, and sample containers will extensively cleaned between samples using Hellmanex III cleaner and subsequent Milli-Q and solvent rinses.

Microbial cell membrane-derived lipids and lipid degradation products will be extracted from 30 g of powdered core samples using sonication and buffers in a modified Bligh and Dyer protocol to maximize yields (Wormer et al., 2015). We will run 10 μ L of concentrated (10% of total lipid extract) injections for characterization using an untargeted MS approach for identification of intact polar lipid (IPL) compounds representative of the extant biosphere. Hydrophobic interaction liquid chromatography (HILIC) will be utilized to separate lipid classes according to polar headgroup. Analysis of chromatographically separated lipid classes can then be conducted using variable data-independent acquisition mode on a Quadrupole-Orbitrap Thermo Q Exactive Focus MS. IPL surveys will also be compared with core lipid compositions to assess which biomarkers persist in the environment and could act as potential biosignatures for microbial metabolism in ancient systems. Core lipids are the natural breakdown prod-

ucts of IPLs; any core lipids measured represent recalcitrant lipid products that have thus far survived complete degradation. Using the same total lipid extract, 50% of the remaining extract will be saponified, and nonsaponified acids will be derivatized to trimethylsilyl (TMS) derivatives (Welandar et al., 2012; Jahn et al., 2004; Schubotz et al., 2015). Hydrocarbons, alcohols (as TMS ethers), and fatty acids (as methyl esters, e.g., fatty acid methyl esters [FAMES]) will then be analyzed with a Thermo Scientific TSQ 8000 EVO triple quadrupole with a Thermo Trace1310 GC interphase. Untargeted structural identification will be conducted through MS information with a full scan (m/z 540–600).

We will take additional steps to assess contamination in the laboratory during preparation for extraction through the use of combusted brick blanks to undergo the entire round of sample preparation including sawing and sample homogenization. The careful handling of these cores and comprehensive evaluation of contamination should allow for the confident detection of biomarkers in these core samples, even if only present in very low concentrations.

We have tested our ability to subtract contamination signals with controls from a heavily contaminated sample from 37 m depth from Hole BA1B where large quantities of fluorescent tracer were detected via fluorescent microscopy. From a density plot of lipid classes, compound classes identified from liquid chromatographic separation retention time and measured mass were detected in the sample but not in any of the contamination controls. These compounds will need to be identified more comprehensively through targeted collision experiments and measurement of parent and daughter compounds.

Carbon utilization rates (F samples)

The F samples will be used to determine potential rates of carbon utilization by microorganisms inhabiting microfractures within serpentinite rock cores. To accomplish this objective, rock core surfaces will first be treated with ethanol and flame using a protocol optimized in our laboratory to remove viable cells from the sample surface (probable contaminants) without killing cells in the sample interior (Fones and Boyd, unpubl. data). Samples will then be pulverized using a sterilized jaw crusher, transferred to sterile, anoxic vials, and milled to homogenize particle size at optimized settings that maximize both cell viability and signal detection (Fones and Boyd, unpubl. data). Pilot work has determined that evidence of microbial metabolism can be detected in rock samples without introducing significant laboratory contamination (Fones and Boyd, unpubl. data).

Once pulverized, samples will be added to sterile vials containing a defined medium including ^{14}C -acetate or ^{14}C -bicarbonate. Following incubation, rates of acetate and bicarbonate transformation will be

quantified using methods described previously. Rates of bicarbonate assimilation will serve a proxy for autotrophic activity, rates of acetate oxidation/assimilation will serve as proxies for heterotrophic activity, and rates of methanogenesis from both substrates will be determined. Rates of substrate transformation in sample vials will be compared with those measured in abiological control vials containing sterilized, pulverized rock and medium to quantify rates of substrate transformation attributable to biology. Furthermore, rates will be compared with measurements from vials controlling for potential addition of laboratory contaminants at any stage in sample processing.

Potential biological sulfate reduction rates in serpentinizing mantle rocks (G samples)

Twenty-three of the G sample pieces were selected to measure potential sulfate reduction rates. The samples cover a broad variety of mineralogical composition and water chemistry as well as provide a comprehensive downcore profile for Holes BA1B, BA3A, and BA4A. The packed G subsamples were opened inside an anoxic chamber under N_2 atmosphere. To avoid the uncontrolled addition of H_2 to all samples, we avoided the common use of catalytic H_2 reduction of the atmosphere. Instead, oxygen-free conditions were ensured by circulating the gas atmosphere through a $FeCl_2$ solution and controlled by purging the gas through a Resazurin indicator solution.

The G samples were split into 5–10 cm^3 pieces using an ethanol-cleaned chisel. Outer parts of the core material were removed and placed aside, and inner material was collected and powdered with a clean tungsten carbide mortar and pestle (Glombitza et al., 2016). The homogenized powder of each sample was distributed into 10 replicate headspace vials (minimum of 5 cm^3 powder per vial) to be used for differing incubation conditions (i.e., different electron donor additions) with 3 replicates each and 1 replicate to be used as a killed control. The killed control samples were autoclaved for 3×50 min at $134^\circ C$. Additionally, 2 samples were separated for quantification of the fluorescent particle contamination tracer added to the drilling mud, one from the inside of the core that was also used in incubation experiments and a second from the outer 1 cm removed during the sample preparation.

To conduct the radiotracer incubations, 5 mL of anoxic medium resembling the principal interstitial water composition (50:50 mixture of Type 1 and Type 2 fluids (Barnes and O'Neil, 1969; Rempfert et al., 2017) with a sulfate background of 1 mM (see below) was amended to the subsamples to generate slurries. The headspace vials containing the slurries were sealed under N_2 atmosphere. Subsequently, in 3

replicates the headspace gas (N_2) was replaced by H_2 gas, and in 3 other replicates the headspace gas was replaced by CH_4 (see Table T52). The 10 incubation vials of each sample (i.e., no substrate, H_2 and CH_4 treatments, and the killed control) were preincubated with medium and respective headspace at $35^\circ C$ for 3 days to enable adjustment of the microbial communities to the incubation conditions. Following the preincubation, 3 MBq (15 μL) of carrier-free ^{35}S -labeled sulfate was injected into each incubation vial, and the vials were quickly shaken and incubated for 14 days at $35^\circ C$. Following incubation, the vials were opened and the content was transferred into 50 mL Falcon tubes containing 10 mL 20% zinc acetate to fix the generated sulfide and to terminate biological activity. The samples were frozen at $-20^\circ C$ until further treatment.

Carrier-free $Na_2^{35}SO_4$ was purchased from American Radiolabeled Chemicals (ARC) and diluted with sterile filtered Milli-Q water to a final activity of 200 kBq/ μL . Three aliquots of 15 μL (3 MBq) were each fixed in 10 mL of a 20% zinc acetate solution and subjected to the standard work-up procedure to check for a background of reduced ^{35}S -labeled sulfur species in the tracer. The tracer was found to be background-free.

In total, 4 L of the medium was prepared in 2 L glass bottles (Schott) by solving the following salts (amounts per 1 L medium):

- $CaCl_2$: 114 mg
- $Ca(OH)_2$: 50 mg
- $MgSO_4 \cdot 7H_2O$: 90 mg
- KNO_3 : 5.3 mg
- KCl : 7.5 mg
- K_2SO_4 : 2.5 mg
- H_4SiO_4 : 0.5 mg
- $NaBr$: 1.1 mg
- $NaCl$: 275 mg
- NaF : 0.02 mg
- Na_2SO_4 : 88.5 mg

A few drops of a 1 mg/L Resazurin solution was added as redox indicator. The media bottles were autoclaved for 50 min at $134^\circ C$ and cooled under N_2 purging before the pH was adjusted to 9.5 by addition of $NaOH$. The redox potential was lowered by adding a few drops of concentrated $Na_2S_2O_4$ solution until the indicator became colorless. Four 5 mL subsamples were collected and incubated with 3 MBq (15 μL) sulfate tracer for 14 days and subjected to the standard work-up procedure. The small background turnover of the medium was used to correct the sample measurements.

For the work-up procedure, the frozen and fixed slurries were thawed and a 100 μL aliquot was taken to measure the total radioactivity of the sample by scin-

tillation counting. The remaining samples were subjected to the cold-chromium distillation procedure (Kallmeyer et al., 2004; Røy et al., 2014; Glombitza et al., 2016). Subsamples were placed in the distillation aperture (Røy et al., 2014) together with 10 mL of dimethylsulfoxide (DMSO) and 0.2 mL of 0.5 M NaS₂ solution serving as sulfide carrier during the work-up procedure. Subsequently, 8 mL of 6 N HCl and 12 mL of 1 M CrCl₂ solution in 3 N HCl were slowly added via an injection port into the air-tight apparatus. The generated H₂S gas was directed through an acetic acid wash and trapped in a 5% zinc acetate trap where it forms zinc sulfide. N₂ was used as carrier gas for the entire procedure. The content of the zinc sulfide trap was collected and the radioactivity was measured by scintillation counting. The measured radioactivity of this fraction is used together with the measured total activity to calculate the sulfate reduction rates in the rock material.

Microscopic and spectroscopic analysis of active alteration core sample mineralogy (H samples)

The H samples were prepared for detailed mineralogical analysis in order to correlate results from the BIO investigations to the in-depth characterization of the core conducted by the geochemistry teams.

We prepared a set of 52 samples as petrographic thin sections and whole-rock powders (see Table T53). The samples were chosen to adequately sample features of interest that were identified during drilling as well as the background lithologies. Samples were removed from the anaerobic pouch and photographed. A billet, ~1 cm × 2 cm × 4 cm, was cut from the whole-round core using a water-cooled diamond trim saw. In order to save material to be prepared under strictly anaerobic conditions, the billet was then cut into two duplicate, ~5 mm thick billets using a diamond sectioning saw. The rest of the core, plus one of the duplicate thin section billets, was loaded into an anaerobic chamber (~3% H₂ in N₂, <1 ppm O₂) and resealed in the Mylar pouch with an anaerobic sachet. The remaining billet was prepared as a standard petrographic thin section by Spectrum Petrographics (Vancouver, WA).

Trimblings left over from billet preparation were saved for bulk mineral characterization and powdered for quantitative XRD (Table T31). In addition, a split from these powders was prepared for $\delta^{34}\text{S}$ of monosulfides and pyrite.

Petrographic thin sections were optically examined and described using a petrographic microscope. Abundance of mineral phases and textures were estimated. Features identified and estimated optically included olivine, orthopyroxene, clinopyroxene, spinel, serpentine, iron oxide/hydroxides, chlorite, veins (size, morphology, and crosscutting relationships), mesh texture (serpentine, etc., after olivine),

and bastite texture (serpentine, etc., after pyroxene). Photomicrographs of representative and notable features were collected in plane- and cross-polarized transmitted light.

To identify or confirm the optical identification of mineral phases and to detect some phases that are difficult to discern optically, Raman spectroscopy was conducted on the standard petrographic thin sections at the Raman Microspectroscopy Laboratory at the University of Colorado-Boulder. A Horiba LabRAM HR Evolution Raman spectrometer with a 532 nm laser and 600 gr/mm diffraction grating was used. Acquisition parameters including the microscope objective, dwell time, number of accumulations, and laser power were varied to optimize signal-to-noise and avoid heat damage to the sample.

Trimblings left over from sawing the thin section billets were used for quantitative powder XRD using a modified method based on Eberl (2003). An aliquot of 400 mg of crushed and sieved sample was mixed with 100 mg corundum and ground in a McCrone micronizing mill with 4 mL ethanol for 5 min, generating particle sizes on the order of 10–30 μm . After drying at 60°C, the mixture was transferred to a plastic scintillation vial with 3 acrylic balls (~1 cm in diameter) along with 200–800 μL Vertrel solution (DuPont) and shaken for 10 min. The powder was passed through a 250 μm sieve to break up larger aggregates and loaded onto an XRD sample holder. Samples were analyzed using a Siemens D500 X-ray diffractometer from 5° to 65°2 θ using CuK α X-ray radiation with a step size of 0.02°2 θ and a dwell time of 2 s per step. Quantitative mineralogy was calculated using the USGS software, RockJock (Eberl, 2003), which fits XRD intensities of individual mineral standards to the measured diffraction pattern.

Petrographic thin sections were carbon-coated for electron microprobe analysis (EMPA), which was performed at the Electron Microprobe Laboratory, University of Colorado-Boulder with a JEOL-8230. Garnet analyses were conducted with 15 kV accelerating voltage, 20 nA current, 1 μm beam size, 30 s on-peak count time (15 s off-peak above and below), and ZAF matrix correction. Garnet water content was calculated by balancing the excess charge on the A+B sites (Ca + Fe + Al + Cr – Si) with H⁺. Quantitative WDS maps were conducted using 15 kV accelerating voltage, 50 nA current, 2 μm beam size, 2 μm step size, and 150 ms on-peak count time, with mean atomic number matrix correction.

Sulfide $\delta^{34}\text{S}$ measurements

Samples were powdered and then acidified with 6 N HCl under N₂, trapping evolved H₂S as ZnS, to extract any acid-volatile sulfur (AVS; Rickard and Morse, 2005), which includes reduced sulfur mineral phases (e.g., FeS and other metal sulfides). Following this treatment, the remaining residue underwent

chromium-reducible sulfur (CRS) extraction following the method of Canfield et al. (1986) to isolate pyrite and elemental S phases. Briefly, this involves adding 6 N HCl and 1 M reduced chromium chloride solution under a N₂ atmosphere, using the N₂ to pass the evolved H₂S gas into a Zn acetate trap to precipitate ZnS.

Isotopic analysis of the resulting S phases was performed using a Costech ECS 4010 elemental analyzer coupled to a Thermo Finnigan Delta V Plus MS at Washington University. For each analysis, ~100 µg of S was loaded into a tin capsule and combusted at 1000°C. The evolved SO₂ gas was introduced to the MS in continuous flow mode. Sulfur isotope composition was calibrated against NBS-127, IAEA-S1, and IAEA148. Sulfur isotope values are reported in permil (‰) relative to the V-CDT (Vienna Canyon Diablo Troilite) scale. Based on replicate analyses across several days, reproducibility of sulfur isotope measurements was <0.3‰ (1σ).

Inorganic and organic carbon quantification and isotopic composition (J samples)

The J samples will be used for total carbon (TC), total inorganic carbon (TIC), total noncarbonate carbon (TOC) contents, δ¹³C and δ¹⁸O of TIC, and δ¹³C of TC and TOC.

Rock chips will be crushed to collect center pieces, which will then be ground by hand using an agate mortar previously cleaned with dichloromethane (DCM) to obtain a homogeneous powder.

The TOC and δ¹³C isotope composition will be determined using 500 mg aliquots decarbonated with 3 mL of 3 M HCl to remove all acid-soluble carbon. The remaining material will be rinsed several times with Milli-Q water, dried at 70°C overnight, and homogenized by hand using an agate mortar previously cleaned with DCM.

The TC and TOC contents and isotopic compositions are measured on a ThermoFisher Scientific FlashEA 1112 Elemental Analyzer interfaced with a ConFlo IV to a Delta V Plus Isotope Ratio MS (ThermoFisher Scientific, Bremen, Germany). For analyses of TC, TOC, δ¹³C_{TC}, and δ¹³C_{TOC}, 1–60 mg of sample is placed into tin capsules and combusted on the FlashEA. The carbon content will be calculated using two simultaneously measured standards (Bodenstandards No. 5: 0.141% TOC, HEKAtech, Wegberg, Germany, and nicotinamide: 59.01% TOC, ThermoFisher Scientific, Milan, Italy) in each run. Four empty tin capsules are measured every 20 samples for blank correction. Analytical reproducibility of the measurement for δ¹³C_{TC} and δ¹³C_{TOC} is 1σ ± 0.11‰.

TIC contents are measured on a CM 5012 CO₂ coulometer interfaced with a CM 5130 acidification

module. Sample (20–30 mg) is weighed into glass capsules and reacted with 2 M perchloric acid (HClO₄), which converts the carbonates to CO₂. Empty glass capsules are measured at the beginning and the end of each run for blank correction. Precision for the measurement strongly depends on TIC content and was determined from laboratory internal standards and duplicate analyses to account for heterogeneity of the samples. Reproducibility for TIC is better than 2.5% for standards with >1 wt% carbon, and maximum error at <600 ppm carbon is ±30 ppm (see Schwarzenbach et al., 2013).

δ¹³C and δ¹⁸O of TOC are measured on a ThermoFisher GasBench II device connected to a ThermoFisher Delta V MS (ThermoFisher Scientific, Bremen, Germany), as described in detail in Breitenbach and Bernasconi (2011). For analyses, 0.06–8 mg sample is weighed into 4.5 mL Exetainers (Labco, High Wycombe, UK), flushed with pure helium, and subsequently reacted with 3–4 drops of 100% phosphoric acid (H₃PO₄) at 70°C. The average long-term reproducibility based on replicate standards is 1σ ± 0.10‰ for δ¹³C and 0.11‰ for δ¹⁸O. Calibration is based on international standards NBS19 (δ¹³C = 1.95‰; δ¹⁸O = −2.2‰) and NBS18 (δ¹³C = −5.01‰; δ¹⁸O = −23.01‰).

A subset of carbonate veins will be analyzed for clumped isotopes (Δ47) on a Kiel IV carbonate device interfaced with a ThermoFisher Scientific MAT253 isotope ratio MS following the methodology described in detail in Meckler et al. (2014) and Müller et al. (2017). Briefly, 130–160 µg aliquots of the sample are loaded in the Kiel IV carbonate device and reacted with 3 drops of 104% phosphoric acid at 70°C. The purity of the sample is confirmed by previous XRD investigations. The evolved CO₂ is purified on a custom-build Porapak Q trap held at −4°C and measured on a MAT253, where *m/z* 44, 45, 46, 47, 48, and 49 are measured in microvolume mode using the LIDI protocol (Hu et al., 2014; Müller et al., 2017). The results are converted to the carbon dioxide equilibration scale (CDES) using the carbonate standards ETH-1, ETH-2, and ETH-3 as described in Bernasconi et al. (2018). With a reasonable amount of replicate analyses, the margin of error is ±3°–5°C for Earth surface temperature samples at the 95% confidence limit per sample (Fernandez et al., 2017).

Microscopic and mineralogical characterization

We conducted microscopic examinations and mineralogical characterizations on subsamples from WR cores designated for microbiological analyses. These observations provide a crucial context for targeting and identifying mineralogical controls on microbiological distribution and activity in this heterogeneous rock-hosted environment.

Biological sulfate reduction rates

Dissimilatory sulfate reduction (SR) is among the oldest known microbial processes on Earth, and it is the predominant anaerobic microbial process in sulfur-rich marine sediments (Canfield and Raiswell, 1999). Recent measurements revealed that sulfate is available in several of the water-bearing rocky environments now known beyond Earth, making SR a potentially important metabolism in those systems (Vance et al., 2016). The inferred presence of both sulfate and peridotite rocks in ophiolites points toward a potential niche for sulfate reducers and highlights the need to understand how and under which conditions SR occurs in serpentinizing systems on Earth.

We conducted assays to measure the potential rate of biological sulfate reduction in the partially serpentinized and sometimes partially sulfurized WR core subsamples collected by the BIO team. Samples were selected to contrast potential biological activity as a function of depth and mineralogical characteristics.

Site BA1 rotary well chips and drill cuttings

The following mineralogical and isotopic analyses were performed at the University of Colorado-Boulder.

Optical and spectroscopic analysis

Drill cuttings recovered during rotary drilling of Sites BA1 and BA2 were sampled for mineralogical characterization and microscale spectroscopic analysis, with a particular interest in Fe-bearing phases present. Approximately 10 g of drill cuttings from each sampling depth was collected from the organizer box at the drill site. Samples were placed in a Whirlpak bag and closed loosely to allow gas exchange. Because actively altering peridotite is likely to contain reactive Fe-bearing phases and because the valence of Fe is of particular interest for studying geochemical reactions that may produce H_2 at low temperatures, preservation of the in situ Fe speciation and oxidation state is important for these investigations. Thus, sampling and sample preparation were performed to minimize exposure to oxygen prior to chemical analyses. In batches of 10–15, the samples were placed into a Mylar pouch along with an oxygen scrubbing sachet (BD GasPak) for shipment to the University of Colorado-Boulder.

Upon arrival, the anaerobic pouches were transferred into an anaerobic chamber containing ~3% H_2 in N_2 and <1 ppm O_2 . Subsamples of the material collected from Site BA1 from 10 to 390 m depth at 20 m intervals were then taken from the anaerobic chamber and handled without concern for oxidation of reactive species: these samples were wet sieved to remove

drilling fluids and to collect the >2 mm fraction and then air dried. The dried cuttings were submitted for preparation as polished thin sections using standard procedures. A portion of the finer fraction (212 μm –2 mm) was crushed to a powder in an agate mortar and pestle for bulk X-ray absorption near-edge spectroscopy (XANES). The drill cuttings collected from Site BA2 have not yet been prepared.

Following initial examination and Raman spectroscopic analysis of 20 standard thin sections from Site BA1, 5 samples of interest were identified for further investigation. The samples were selected to represent the range of variation observed across all depths. These samples were from depths of 30, 90, 150, 210, and 390 m.

For these depths, a portion of the drill cuttings that remained in the anaerobic chamber were prepared anaerobically to prevent oxidation of reactive Fe phases. These subsamples were wet sieved using anaerobic water to remove residual drilling fluid, and the >2 mm fraction was collected for mounting. This fraction was allowed to dry at ambient temperature in the anaerobic chamber, then cast in a 1 inch diameter epoxy puck. After curing, silicon carbide grinding paper was used to expose the interior of the rock chips. The surface was polished using diamond polishing compound. Initial investigations by Raman spectroscopy were completed on this surface by bringing the mount out of the anaerobic chamber for up to several hours.

To prepare a sectioned sample for further analyses, the polished surface of the epoxy mount was attached to a frosted glass slide with epoxy. This was allowed to cure and then taken out of the anaerobic chamber, and the majority of the epoxy puck was removed with a diamond saw. The portion of the sample still attached to the glass slide was immediately dried with compressed air after sawing and transferred back into the anaerobic chamber. The new sample surface was then ground with silicon carbide grinding paper until the rock chips were partially translucent (several hundred micrometers thickness removed), then polished with diamond and alumina polishing compounds.

Raman spectroscopy. For an initial examination, standard thin sections were examined and photographed on a petrographic microscope. Individual chips or regions within chips were selected for identification of minerals within these regions by performing spot Raman spectroscopic analyses. Raman spectra were collected at selected points using a Horiba LabRam HR Evolution Raman spectrometer. A 532 nm laser was focused through a 50 \times (0.75 NA) or 100 \times (0.90 NA) objective lens, giving either a 2 μm or 1 μm analysis spot size. The maximum power at the sample surface was 29 mW for the 50 \times objective and 15 mW for the 100 \times objective, and this was

decreased further using neutral density filters to prevent heating damage to the sample from the focused laser beam. A 600 lines/mm diffraction grating and a 100 μm confocal pin hole were used to give a spectral resolution of 4.5 cm^{-1} full width at half maximum. The spectrometer was calibrated using the 520.7 cm^{-1} peak of Si. Multiple spectra were averaged to increase the signal-to-noise ratio and to allow cosmic ray “spikes” to be filtered from the data. Spectral data were then corrected for instrumental artifacts and a polynomial baseline was subtracted using LabSpec6 (Horiba Scientific). Spectra were matched to reference Raman spectra in the RRUFF database (La-fuente et al., 2016) for identification.

Wavelength dispersive spectroscopy element mapping.

Areas of interest within particular drill cuttings in the standard petrographic thin sections were further characterized by quantitative elemental mapping on a JEOL JXA-8230 electron microprobe. The areas were mapped in two passes with 5 wavelength dispersive spectrometers (WDS) to quantitatively analyze 10 elements: Fe, Mg, Si, Ca, Al, Cr, Mn, S, Ni, and Cl. A 15 KeV acceleration voltage, 50 nA beam current, and 40 ms dwell time (per pixel, per pass) were used. A full matrix correction was performed to produce the quantitative element maps.

X-ray absorption fluorescence spectroscopy. Powdered drill cuttings handled without special precautions for oxidation were used for bulk Fe K-edge XANES, measured at beamline 4-1 at the Stanford Synchrotron Radiation Lightsource (SSRL). The X-ray beam energy was selected with a Si(220) $\phi = 0^\circ$ double-crystal monochromator. Powders were sealed in Kapton tape, and Fe fluorescence was measured with a passive implanted planar Si (PIPS) detector at a 90° angle from the beam. The XANES spectrum was collected by scanning the incident X-ray energy from 6882 to 7500 eV, with fine sampling (at least every 0.35 eV) between 7092 and 7200 eV. Spectra were calibrated using an Fe foil transmission spectrum collected with every sample by two ion chambers downstream of the sample. The first inflection point of the Fe foil was calibrated to 7112.0 eV. Spectra were background corrected and edge-step normalized.

In order to more intensely characterize the mineral reservoirs of Fe(II) and Fe(III) in the drill cuttings, the anaerobically prepared sections were examined using μ -XAFS (X-ray absorption fine structure) at beamline 2–3 at SSRL. The energy was selected using a Si(111) $\phi = 0^\circ$ double-crystal monochromator, then focused down to approximately a $2\ \mu\text{m} \times 4\ \mu\text{m}$ spot. Fluorescence was detected using a single-element Vortex detector. Maps were generated at individual energies by scanning the sample through the X-ray beam. Maps of element abundance were generated at 11,000 eV in order to select appropriate regions for detailed mapping. The smaller regions were then

mapped at 9 energies across the pre-edge region of the Fe K-edge (7109–7117.2 eV) and at 7200 eV (above the edge for normalization).

Bulk nitrogen isotopic analysis

Well chip samples from each of the depth intervals at 130–390 m were wet sieved to remove drilling fluids and to collect the $>2\ \text{mm}$ fraction. This fraction was then repeatedly rinsed with organic-free water (Hach product 2641549) to remove contamination from drilling. Samples were then air-dried.

To measure dissolved nitrogen species in pore water leachate, $\sim 1\ \text{g}$ of the sieved and washed sample was added to acid-washed polypropylene tubes containing 5 mL of organic-free water. Tubes were incubated at 30°C and shaken at 250 rpm for 1 week. After the incubation period, tubes were centrifuged and supernatant was collected in a clean tube and frozen. The remaining sample was air-dried and then crushed to a fine powder using an agate mortar and pestle. The powdered sample was transferred to a clean tube with 5 mL organic-free water and incubated again at 30°C and shaken at 250 rpm for 1 week to measure dissolved nitrogen species in fluid inclusions. Once again, at the end of the incubation period, supernatant was collected and frozen. To measure exchangeable nitrogen, 5 mL of 1 M potassium chloride was added to the same tube. Samples were incubated overnight and the supernatant from this incubation was collected and frozen. Dissolved nitrate and nitrite from each of the three incubations were measured via spectrophotometry on a Biotek Synergy H1 microplate reader using the protocols described in Garcia-Robledo et al. (2014). Ammonium concentrations were also measured through microplate colorimetry using protocols adapted from Weatherburn (1967). To measure the bulk dissolved nitrogen concentration from pore water leachate and fluid inclusions, 1 mL of supernatant was oxidized with 1 mL of persulfate solution (2 g organic-cleanly reprecipitated potassium persulfate and 2 g Optima grade NaOH in 100 mL Savillex water) during a 120 min autoclave incubation. Oxidized samples (all N converted to dissolved nitrate) were then pH adjusted to neutral and quantified by conversion to NO followed by chemiluminescence detection (Braman and Hendrix, 1989) on an Antek1750 nitrate/nitrite analyzer. A 20 nmol aliquot of measured nitrogen was denitrified by *P. chloraphis* (Weigand et al., 2016) to nitrous oxide for measurement via GC-irMS on a Thermo MAT 253 with an N_2O extraction and purification system at Princeton University.

To measure bulk rock nitrogen, $\sim 2\ \text{g}$ of the sieved and washed sample was crushed to a fine powder using an agate mortar and pestle. A sample of 400–600 mg of powder was weighed into 9 mm \times 10 mm tin capsules, sealed, and then introduced in the autosampler of a Thermo Delta V with elemental ana-

lyzer for continuous-flow analysis of bulk rock nitrogen stable isotopes. Samples contained very little nitrogen, and so tin capsule blanks were run after each sample to allow for precise blank corrections.

Well chip samples were found unsuitable for bulk $\delta^{15}\text{N}$ measurements because of contamination with organic nitrogen from drilling fluid and foam. The measured concentration of total N (after persulfate oxidation) from pore water leach and fluid inclusion protocols was ~7 times greater than the combined concentration of measured nitrate, nitrite, and ammonium, despite washing the well chips prior to the incubation and procedural blanks having nitrogen concentrations below the detection limit of the methods. This high concentration of detected organic N, even in fluid inclusion samples that had previously been subjected to a week-long incubation in organic-free fluid prior to crushing, suggests the drilling foam or fluid must have penetrated the interior of the well chip and attached to mineral surfaces, as it was not completely removed during washing. Accordingly, powdered rock samples for bulk analysis would also be extremely contaminated. Because the signal from this contamination is far greater than the signal from ammonium sourced from the rock itself, we could not reliably subtract the isotopic signal from contamination.

The pervasive contamination of well chip samples with organic material observed during the attempt to quantify bulk nitrogen in well chips necessitates a more comprehensive sampling of potential sources of contamination for lipid analysis. The quantification of lipid and hydrocarbon compounds from drilling mud and water, the core barrel, trays, and saw in contact with the core prior to subsampling, as well as the air on the drill site, should allow for subtraction of these contaminating compounds from those detected in the interior of the rock core. A wash with Milli-Q water on site prior to transportation of these samples should also prevent the penetration of contaminants on the exterior of the core into the pristine interior.

Other microbiology work in progress

- Cell enumeration: quantifying number of cells/gram rock in the interiors of cores from all depths.
- Total carbon and isotopic characteristics as a function of depth, lithology, etc.
- Isotopic variability in mineral sulfide and aqueous sulfate in BA cores/holes.
- Quantifying rates of carbon utilization for various metabolisms and cell growth.
- DNA extraction, amplification, and sequencing in Holes BA3A, BA1B, and BA4A; comparative genomics.
- Extraction, purification, and analysis of intact polar lipids and lipid biomarkers.

- Fe and S redox mapping in zones of active vs. low biological activity.

Current state of samples

All DNA and RNA extractions collected in the field have been processed, and data from the SSU rRNA sequencing run are being processed. Extra core material from Site GT3 was disposed of in Oman. A piece of the Hole BT1B whole core and cryovials containing gram amounts of Site GT3 and BA1 drill cuttings are stored at -80°C in the Spear laboratory at the Colorado School of Mines.

A portion of all drill cuttings samples collected for spectroscopic analysis remain stored in the anaerobic chamber (3% H_2 in N_2 , <1 ppm O_2) in the Templeton Laboratory at the University of Colorado-Boulder. Mounted sections of the >2 mm separates of the 30, 90, 150, 210, and 390 m depth samples from Site BA1, which were prepared under anaerobic conditions to the extent possible, are also kept in this anaerobic chamber. A portion of the samples collected every 20 m from 10–390 m from Site BA1 have been taken out of the anaerobic chamber, wet sieved, and dried. Petrographic thin sections of the >2 mm separate, as well as remaining <2 mm and >2 mm separates, are stored in the Templeton Laboratory at the University of Colorado-Boulder.

Paleomagnetism

Phase 1

During OmanDP Phase 1 operations on the *Chikyu*, routine shipboard paleomagnetic and magnetic anisotropy experiments were carried out within the shipboard shielded room. Unfortunately, remanent magnetization of continuous archive section halves could not be measured because of an unexpected malfunction of the automated pass-through direct-current superconducting quantum interference device (DC-SQUID) cryogenic rock magnetometer (2G Enterprises Model 760R-4K, with a Model 2G 800 sample handler system). Therefore, all remanent magnetization was measured on discrete cube samples taken from the working halves that were subjected to either stepwise alternating field (AF) or thermal demagnetization. Because the azimuthal orientations of core samples recovered by rotary drilling are not constrained, all magnetic data are reported relative to the CRF (Fig. F5). In this system, $+x$ points into the working section half, $+z$ is downcore, and $+y$ is orthogonal to x and z in a right-hand sense. Therefore, $+x$ corresponds to 000 and $+y$ to 090 in the CRF, as also used by the structural geology team. For Hole GT3A, the corrected core reference frame defined by the structural geology group was used where possible. Magnetization directions of samples were determined using principal component analysis

(PCA; Kirschvink, 1980) and analyzed using inclination-only statistics (Arason and Levi, 2010). Sample values are presented as a function of the *Chikyu* adjusted depth, which is measured as the depth to the center of the sample for discrete samples.

Data analysis

The principal components of the remanent magnetization directions were calculated using a modified version of the “MacPaleomag” software (written by J. Gee, Scripps Institution of Oceanography). PCA picks for discrete samples were chosen based on the maximum angular deviation (MAD) for components in different coercivity or temperature windows. All components were processed by selecting coercivity or temperature boundaries without anchoring to the origin. The median destructive field (MDF) and median destructive temperature (MDT) were calculated for each sample. All PCA picks with MAD values $> 10^\circ$ were rejected to ensure statistically acceptable linearity of components, with the highest stability component directed towards the origin and representing a stable remanence direction.

The intensity reported for such PCA directions represents the length of the projection of the lowest and highest treatment vectors used in the PCA calculation onto the best-fit direction. Because the origin is not included in the PCA calculation and the remanence remaining after the highest treatment may potentially be significant, the resulting characteristic natural remanent magnetization (ChRM) intensity values will be systematically lower than those derived from the remanence at the lowest demagnetization step adopted for the PCA calculation.

Archive section half remanent magnetization

The remanent magnetization of archive section halves is routinely measured during IODP expeditions. However, the archive section halves could not be measured during Oman DP Phase 1 operations due to a repeated malfunction of the X SQUID of the superconducting rock magnetometer (SRM). Despite repeated efforts to fix the issue, the SRM was not fully functional to allow measurement and demagnetization of any archive section halves. However, the inline AF demagnetizer attached to the SRM was still functional and used for samples from Hole GT3A, as explained in more detail below (Fig. F68).

Discrete sample remanent magnetization data

All discrete samples taken from working section halves for shipboard magnetic analysis were 8 cm³ cubes with a sampling density of ~ 1 one per core. In some cases, cubes were cut near dike margins or other zones of interest. Although standard 2.5 cm diameter minicores are often used, cubic samples were preferred, as they should have a more precisely deter-

mined vertical reference (based on a saw cut perpendicular to the core length) than minicores, where the arrow on the split-core face must be transferred to the long axis of the sample. Generally, core sections that were visibly affected by extensive alteration, veining, or deformation were omitted from paleomagnetic shipboard sampling, although this was not always possible in some highly altered sections of cores in Holes BT1B and GT3A.

Remanent magnetization of discrete samples was measured exclusively with a Natsuhara Giken SMD-88 fluxgate spinner magnetometer. The magnetometer software subtracts the stored value of the holder magnetization during the calibration procedure of the instrument, which was performed at the onset of discrete sample measurements for Hole GT1A. The empty sample holder (with a volume set to 8 cm³) has an intensity on the order of 4×10^{-5} A/m, representing a noise limit of the system that is insignificant compared to typical intensities of rocks from the Samail ophiolite.

Stepwise AF demagnetization of discrete samples from Holes GT1A and GT2A was performed using a Natsuhara Giken DEM-95C system with a sample tumbling mechanism capable of producing peak fields up to 180 mT. The residual magnetic field at the demagnetizing position in this equipment was < 5 nT. Samples were AF demagnetized at peak fields of 5, 10, 15, 20, 25, 30, 40, 50, 60, 80, and 100 mT. Additional 20 mT steps up to 180 mT were applied as needed. Because of mechanical problems with the sample tumbling mechanism during measuring samples from Hole GT3A, stepwise AF demagnetization of discrete samples was achieved using the integrated inline AF demagnetizer (2G model 600 attached to the SRM). Progressive demagnetization of the samples occurred in 2.5 mT steps up to 10 mT, 5 mT steps up to 30 mT, 10 mT steps up to 70 mT, and a final step at the peak field of 85 mT.

Thermal demagnetization of discrete samples was performed using a Natsuhara Giken TDS-1 thermal demagnetizer capable of demagnetizing samples up to 700°C. The cooling chamber of the oven has an ambient field < 5 nT. Each sample boat for thermal demagnetization included up to 8 samples, and sample orientations were changed between each successive step to allow any magnetic interaction between adjacent samples to be identified. Samples were heated in 50°C steps from 150°C to 450°C, in 25°C steps to 500°C, then in 10°C steps to 600°C. For samples from Hole GT3A, an additional temperature step was added at 100°C. Samples were held at the desired temperature for 30 min prior to cooling. Bulk magnetic susceptibility was measured using an AGICO KLY-3 Kappabridge susceptibility meter or MS2B Bartington susceptibility meter after every heating step to monitor thermal alteration of magnetic minerals during heating.

The Königsberger ratio, Q , was used to indicate the relative contributions of remanent magnetization compared to induced magnetization and is defined as follows:

$$Q = \text{NRM}/(K \cdot H), \quad (5)$$

where

NRM = intensity (A/m),

H = ambient field strength (A/m), and

K = volume (bulk) susceptibility in SI units.

The modern International Geomagnetic Reference Field value at the drilling locality is $\sim 40.0 \mu\text{T}$.

Anisotropy of low-field magnetic susceptibility

In addition to standard paleomagnetic measurements, the anisotropy of low-field magnetic susceptibility (AMS) was determined for all discrete samples using the KLY-3 Kappabridge with the AGICO software “Susar.” The AMS tensor is represented by an ellipsoid with maximum, intermediate, and minimum axis lengths proportional to the principal susceptibilities, termed K_{max} , K_{int} , and K_{min} , respectively. The corrected anisotropy degree, P' , is reported following Jelínek (1981):

$$P' = \exp \sqrt{2 \left[(\eta_1 - \bar{\eta})^2 + (\eta_2 - \bar{\eta})^2 + (\eta_3 - \bar{\eta})^2 \right]} \quad (6)$$

where,

$\eta_1 = \ln(K_{\text{max}})$ [maximum eigenvalue],

$\eta_2 = \ln(K_{\text{int}})$ [intermediate eigenvalue], and

$\eta_3 = \ln(K_{\text{min}})$ [minimum eigenvalue],

$\bar{\eta}$ = mean of η_1 , η_2 , and η_3 ,

and the shape factor, T , is calculated as follows (Jelínek, 1981):

$$T = (2\eta_2 - \eta_1 - \eta_3)/(\eta_1 - \eta_3), \quad (7)$$

where T ranges between +1 (purely oblate) to −1 (purely prolate).

The ChRM directions were used to rotate the AMS fabrics for comparison within the paleomagnetic reference frame. The AMS tensor was rotated around the z-axis of the core reference frame so that the declination of ChRM was 000. Previous outcrop investigations of the Samail Ophiolite reported consistent paleomagnetic directions within each massif (Luyendyk et al., 1982; Luyendyk and Day, 1982; Weiler, 2000; Morris et al., 2016); therefore, the ChRM directions may be used as a reference direction. It should be emphasized that this rotation within the paleomagnetic reference frame does not constitute a geographic reorientation but serves only as an indicator of the angular relationships between the principal susceptibility axes and the stable remanence vector. Further conversion of the paleomagnetic reference

frame into geographic coordinates is thus necessary and awaits core-log integration.

Magnetism of Site BT1 metamorphic rocks

The rocks recovered from Hole BT1B are exceptional in the OmanDP, as described in [Host rock](#) in the [Site BT1](#) chapter. Nonetheless, routine shipboard paleomagnetic and magnetic anisotropy experiments were carried out within the shipboard shielded room aboard *Chikyu* using similar methods as described for Sites GT1, GT2, and GT3. Although similar methods for measuring remanent magnetization on discrete cube samples were continued, the following few adjustments were made to the demagnetization procedure. Remanent magnetization was measured on discrete cube samples subjected to either stepwise AF or thermal demagnetization, though priority was given to thermal demagnetization. Samples were AF demagnetized at peak fields in 5 mT steps at 5–30 mT, 10 mT steps at 40–80 mT, and 20 mT steps to 180 mT. Samples were heated in 50°C steps at 50–450°C, 25° steps to 500°C, 20° steps to 600°C, 20° steps to 680°C, and 5° steps to 690°, with a final step at 700°C. Bulk magnetic susceptibility was measured using a MS2B Bartington susceptibility meter after every heating step to monitor thermal alteration of magnetic minerals during heating.

Thermomagnetic properties

To estimate Curie temperature, magnetic susceptibility was measured as a function of temperature using the KLY-3 Kappabridge with a CS-3 furnace apparatus and the AGICO “SUSTE” software. Powdered samples (250–500 mg) were collected from whole-rock powders prepared for shipboard geochemistry analyses or from powder preparation of on site samples at the University of Southampton (see [Geochemistry](#)). The powder samples were cycled from room temperature to 700°C and back to room temperature in the presence of argon gas to prevent excessive oxidation. Quasi-continuous measurements were made during heating and cooling cycles. AGICO CUREVAL software allows processing and graphical plots of data for analysis and Curie temperature estimates.

Phase 2

Samples for paleomagnetic analysis were collected as part of shipboard core description activities on the *Chikyu* during Phase 2 of OmanDP. Discrete sample cubes were taken from working half cores at an interval of approximately one per core. No measurements were conducted on archive-half cores because of the continued malfunction of the onboard pass-through cryogenic magnetometer. Shipboard measurements were performed on discrete samples from Hole CM1A, including AMS, bulk susceptibility, natural

remanent magnetization, thermal demagnetization, and AF demagnetization. Collection of discrete samples was continued in the same manner for Holes CM2B, BA1B, BA3A, and BA4A; however, shipboard measurements were limited to AMS determinations conducted by members of the physical properties team. Orientation parameters P1, P2, P3, and P4 in the KappaBridge software were 6, 0, 6, and 0, respectively, for AMS measurements. The remaining paleomagnetic analyses were conducted as shore-based measurements at the University of Iceland paleomagnetism laboratory, including natural remanent magnetization and thermal and AF demagnetization sequences. Many of the discrete samples from Phase 2 cores were used for both physical properties measurements and paleomagnetic measurements. For these samples, a suite of physical properties tests was conducted after AMS and bulk susceptibility measurements but prior to demagnetization treatments. Demagnetization and measurement of Phase 2 samples followed the procedures used in Phase 1 as closely as possible.

Shore-based paleomagnetic determinations were performed in a low-field cage containing an AGICO JR-6A spinner magnetometer for remanence measurements, an AGICO LDA-5 AF demagnetizer capable of both tumbling and 3-axis demagnetization modes, and a Magnetic Measurements MMTD80 shielded furnace with field control for thermal demagnetization. The thermal demagnetization furnace is capable of holding up to 80 samples and has a maximum temperature of 800°C.

Data analysis

PuffinPlot software (Lurcock and Wilson, 2012) was used for visualization of shipboard and shore-based paleomagnetic results, as well as PCA to identify ChRM directions.

Physical properties

Phase 1

Shipboard measurements of physical properties were undertaken to characterize recovered core material. These data are used to link the geological observations made on the core to the measurements made by downhole wireline geophysical logging and also the regional geological survey results.

The general procedures section is followed by the description of measurement parameters for each physical property investigated during ChikyuOman Phase 1. These methods closely follow those used during IODP Expeditions 304/305, 309/312, 335, 345, and 360 of *JOIDES Resolution* and IODP *Chikyu* Expeditions 322, 348, and other nonscientific expeditions. A comprehensive discussion of methodologies and calculations used in the *Chikyu* physical properties

laboratory (except for the X-ray computed tomography) is presented in Blum (1997).

Laboratory core flow

All core sections were shrink-wrapped and run through the X-ray computed tomography (X-ray CT) scanner to generate an X-ray CT image, followed by the whole-round multisensor core logger (MSCL-W), which measures natural gamma radiation (NGR) and magnetic susceptibility (MS), for Holes GT1A and GT2A. Additional measurements of gamma ray attenuation (GRA) density, P-wave velocity, and non-contact resistivity (NCR) were taken for Holes BT1A and GT3A with MSCL-W. These instruments also generate the J-Cores *Chikyu* curated section lengths for each core section (Fig. F2). Following whole-round measurements and core splitting, the archive section halves were passed through the split-core multisensor core logger (MSCL-C) for measurements with a contact sensor probe of point magnetic susceptibility (MSP) and determination of color spectroscopy.

Phase 2

The procedures for physical properties measurements during ChikyuOman Phase 2 generally follow those used during Phase 1. The main change is the additional measurement of electrical resistivity (complex impedance). Also, minicube samples were vacuum saturated for 24 hr in salt water (3.5‰ NaCl solution) before moisture and density (MAD), P-wave, and electrical resistivity measurements to better represent conditions. During Leg 4, dry condition of electrical resistivity was measured before water saturation.

Laboratory core flow

All core sections were shrink-wrapped and run through the X-ray CT, followed by NGR, MS, GRA density, and NCR on the MSCL-W. P-wave velocity (Vp) measurement by the MSCL-W was only conducted on Hole CM1A cores. After those whole-round measurements, all sections were split into halves and run through the MSCL-C for color reflectance and MSP. However, because of instrument trouble during ChikyuOman Legs 3 and 4, MSP measurements were completed only for Hole CM1A and part of Hole CM2B cores to Section 37Z-1.

Most discrete sample measurements were undertaken on 20 mm × 20 mm × 20 mm sample cubes cut from the working half of the cores. In addition to compressional wave (P-wave) velocity and MAD measurements (used to determine bulk density, grain density, and porosity), electrical resistivity (complex impedance) measurements were also undertaken. Most of the minicube samples were also used for paleomagnetic measurements, although those for ther-

mal demagnetization were excluded and a separate cube sampled.

X-ray computed tomography

X-ray CT scanning is a routine measurement of the IODP measurement plan onboard *Chikyu*, which enables nondestructive observation of the internal structure of core samples. X-ray CT imaging provides information about chemical compositions and densities of the cores and is useful for assessing sample locations and the quality of the whole-round samples. Our methods follow those in the measurement manual prepared by CDEX (X-ray CT Scanning, version 3.00, 24 March 2015) and used during previous IODP expeditions (e.g., IODP Expeditions 322, 343). The manual is based on GE Healthcare (2013), Mees et al. (2003), and Nakano et al. (2000).

The X-ray CT scanner (Discovery CT 750HD, GE Medical Systems) on *Chikyu* scans and reconstructs the image of a 1.4 m section in 10 min and produces a series of scan images, each 0.625 mm thick (Fig. F69). The X-ray tube (as an X-ray source) and the X-ray detector are installed inside of the gantry at opposing positions to each other. The excitation voltage and current for X-ray tube are 140 kV and 100 mA, respectively. The gantry rotates continuously around the core sample at a rotation speed of 1 revolution/s during scanning. The core sample is scanned in the gantry with the scanning rate of 20 mm/s.

The distribution of attenuation values mapped to an individual slice comprises the raw data that are used for subsequent image processing. Successive 2-D slices of 512×512 pixels yield a representation of attenuation values in 3-D voxels of 512×512 by ~ 1600 in length (Fig. F69).

X-ray intensity varies as a function of X-ray path length and the linear attenuation coefficient (LAC) of the target material as:

$$I = I_0 \times e^{-\mu L}, \quad (8)$$

where

- I = transmitted X-ray intensity,
- I_0 = initial X-ray intensity,
- μ = LAC of the target material, and
- L = X-ray path length through the material.

LAC is a function of the chemical composition and density of the target material. The basic measure of attenuation, or radiodensity, is the CT number given in Hounsfield units (HU) and is defined as follows:

$$\text{CT number} = [(\mu_t - \mu_w)/\mu_w] \times 1000, \quad (9)$$

where

- μ_t = LAC for the target material, and
- μ_w = LAC for water.

Data quality is monitored using a quality control (QC) reference standard (Fig. F70) that comprises three layers: air, water, and an aluminum cylinder that telescopes in diameter from 6 cm to 1 cm in six steps. The QC standard was scanned after air calibration (called “Fast Cal” in the program) and CT numbers of air, water, and aluminum layers were checked that they were within the QC range: $-1008 < \text{CT number} < -1002$ for air; $-2 < \text{CT number} < 7$ for water; and $2416 < \text{CT number} < 2499$ for aluminum.

Data generated for each core consist of core-axis-normal planes (X-Y planes) of X-ray attenuation values with dimensions of 512×512 pixels in $9 \text{ cm} \times 9 \text{ cm}$ cross-section, meaning at the dimensions of a core section, the resolution is 0.176 mm/pixel (Fig. F69). Data for each core were stored as medicine (DICOM) formatted files including a digital image for a whole section (Fig. F71). Using the CT data in a common software such as MATLAB requires modification of the last two extensions in each DICOM file name to four-digit numbers, as shown in Figure F71.

An example X-ray CT image of a section from Hole GT1A (Section 108Z-4) is shown in Figure F72 along with the core photo. An X-ray CT image of a core-section that has the same core-axis longitudinal plane (Y-Z plane) as the archive-half photo of the core (see Fig. F69) was generated and included in the VCD sheets for all cores.

For Phase 2 shipboard logging, we also calculate the average and the median of CT number of the X-Y section in the circle with a radius of 17.6 mm (100 pixels) from the center of the core section with the interval of 0.625 mm along the Z-axis for all core sections.

Whole-round multisensor core logging

Whole-round MS and NGR are measured using the MSCL-W (GEOTEK MSCL, GEOTEK Ltd.) This instrument consists of the main center sensor stand, right/left core tracks, core pusher, and measurement sensors. The system is designed to be operated primarily under computer control. For the OmanDP Phase 1 cores, whole-round (1) magnetic susceptibility and (2) natural gamma ray were measured using this instrument. For Phase 2 cores, (1) whole-round magnetic susceptibility, (2) natural gamma ray, (3) non-contact resistivity, (4) gamma ray attenuation density, and (5) P-wave velocity (only for Hole CM1A because of instrument trouble) were measured using this instrument. OmanDP HQ cores have approximately the same diameter (63.5 mm) as the inner diameter of the IODP core liner, but in contrast, NQ cores have an outer diameter of only 47.6 mm, which requires correction for volume ratio.

Whole-round magnetic susceptibility

MS is a volume-specific measure of the degree to which a material can be magnetized by an external magnetic field. MS varies in response to type and concentration of magnetic grains, making it useful for identification of compositional variations in the cores. MS (K) is defined as follows:

$$K = M/H \text{ (SI)}, \quad (10)$$

where M is the magnetization induced in the material by an external field with strength H (very low field, ≤ 0.5 mT).

Phase 1

A loop sensor with 8 cm diameter was used to measure magnetic susceptibility during Phase 1. An oscillator circuit in the sensor produces a low-intensity (~ 80 A/m RMS), nonsaturating alternating magnetic field (0.565 kHz). When a material is put in the sensor, the oscillator frequency changes and variance is converted into magnetic susceptibility value. The spatial resolution of the loop sensor is 23–27 mm, and it is accurate to within 2%. Magnetic susceptibility data were collected every 4 cm along the core.

Phase 2

Because we first used the 80 mm loop sensor for measurement of strongly magnetic Hole CM1A cores, most of measured values saturated around 7000×10^{-5} SI. Therefore, we remeasured MS on Hole CM1A core using the archive halves after splitting using the 125 mm loop sensor and made a volume correction for the archive halves (core sample volume is half of the whole-round core sample) by multiplying the raw data by a factor of 2. We show this corrected data in [Paleomagnetism](#) in the [Site CM1A](#) chapter. For Hole CM2B, the measurement was conducted with whole-round cores with same procedure as the Phase 1 measurements but with the 125 mm loop sensor rather than the 80 mm loop sensor.

Natural gamma radiation

NGR measurements provide insights into mineral composition and thus can be used to identify some rock types and some interesting geological features. Whole-round cores were monitored for NGR emissions to obtain spatial variability in radioactivity and establish gamma ray logs of cores for correlation to downhole gamma ray logs. A lead-shielded counter, optically coupled to a photomultiplier tube and connected to a bias base that supplies high-voltage power and a signal preamplifier, is used. Two horizontal and two vertical sensors are mounted in a cube-shaped lead housing. The NGR system records radioactive decay of long-period isotopes ^{40}K , ^{232}Th ,

and ^{238}U . NGR has a resolution of 120–170 mm and was measured every 16 cm with a count time of 30 s. Background radiation noise was determined by taking measurements on a water-filled calibration core. NGR counts of the gabbroic cores from Holes GT1A, GT2A, and GT3A mostly returned negative values because their NGR counts are lower than the count value of the background water-filled calibration core. In this case, we ignore the negative values and only use the positive count values. All acquired NGR data including negative values are shown in Supplemental Tables [ST6](#) in the [Site CM1](#) chapter and [ST8](#) in the [Site CM2](#) chapter. Further background tests were conducted with other background materials including air, an air-filled core liner, an aluminum liner, and an acrylic column.

Gamma ray attenuation density

Bulk density can be used to evaluate pore volume in OmanDP cores. GRA density is based on the detection of a gamma ray beam produced by a cesium source. The beam, produced by a ^{137}Cs gamma ray source at a radiation level of 370 MBq within a lead shield with a 5 mm collimator, is directed through whole-round cores. The gamma ray detector includes a scintillator and an integral photomultiplier tube to record the gamma rays that pass through the whole-round core. GRA bulk density (ρ_b) is calculated as follows:

$$\rho_b = (1/\mu d) \times \ln(I_0/I), \quad (11)$$

where

- I_0 = gamma ray source intensity,
- I = measured intensity of gamma rays passing through the sample,
- μ = Compton attenuation coefficient, and
- d = sample diameter.

The Compton attenuation coefficient (μ) and source intensity (I_0) are treated as constants, so ρ_b can be calculated from I . The gamma ray detector is calibrated with a sealed calibration core (a standard core liner filled with pure water [Elix] and aluminum cylinders of various diameters). To establish the calibration curves, gamma ray counts were taken through each aluminum cylinder for 60 s. Each aluminum cylinder has a density of 2.7 g/cm^3 , and $d = 1, 2, 3, 4, 5$, or 6 cm. The relationship between I and μd is

$$\ln(I) = A(\mu d) + B, \quad (12)$$

where A and B are coefficients determined from the calibration experiment. GRA density measurements on core samples are conducted every 4 cm for 4 s. The spatial resolution is 5 mm.

Porosity (ϕ) is calculated from MSCL density assuming a solid grain density (ρ_s) of 2.7 g/cm³ and a pore fluid density (ρ_f) of 1.024 g/cm³:

$$\phi = (\rho_s - \rho)/(\rho_s - \rho_f). \quad (13)$$

P-wave velocity

P-wave data can be used to evaluate small-strain moduli, correlate log and core data, and evaluate pore structure and cementation. P-wave velocity is defined by the time required for a compressional wave to travel a set distance as follows:

$$V_p = d/t_{\text{core}}, \quad (14)$$

where

d = path length of the wave across the core, and
 t_{core} = travelttime through the core.

P-wave velocity transducers on the MSCL-W system measure total travelttime of the compressional wave between transducers. The wave travels horizontally across the whole core and core liner. The total traveltime observed is composed of the following:

t_{delay} = time delay related to transducer faces and electronic circuitry,
 t_{pulse} = delay related to the peak detection procedure,
 t_{liner} = transit time through the core liner, and
 t_{core} = travelttime through the rock.

The system is calibrated using a core liner filled with distilled water, which provides control for t_{delay} , t_{pulse} , and t_{liner} . With these calibrations, core velocity (V_p) can be calculated on whole-round specimens in core liners as follows:

$$V_p = (d_{\text{cl}} - 2d_{\text{liner}})/(t_0 - t_{\text{pulse}} - t_{\text{delay}} - 2t_{\text{liner}}), \quad (15)$$

where

d_{cl} = measured diameter of core and liner,
 d_{liner} = liner wall thickness, and
 t_0 = measured total travelttime.

Equation 15 assumes that the core completely fills the core liner.

The V_p measurement system on the MSCL-W measures d and t_0 every 4 cm with a 500 kHz P-wave transmitter and receiver (Phase 1) or 230 kHz transmitter (Phase 2).

Noncontact electrical resistivity

Within limits, electrical resistivity may be useful for estimating physical properties like porosity, tortuosity, permeability, and thermal conductivity. Bulk electrical resistivity is controlled by solid grain resistivity, interstitial water resistivity, pore space distribution, and pore connectivity. Electrical resistivity

(R) is defined by the electrical resistance and geometry of the core measured:

$$\rho = R(A/L), \quad (16)$$

where

R = electrical resistance,
 L = length of measurement, and
 A = cross-sectional area of the core.

The NCR sensor on the MSCL-W system induces a high-frequency magnetic field in the core with a transmitter coil. This generates an electrical current in the bulk rock that is inversely proportional to its resistivity. The rock magnetic field generated by this induced electrical current is measured by a receiver coil. To measure this smaller magnetic field accurately, a differencing technique has been developed that compares readings from the sample core to readings from an identical set of coils operating in air. Electrical resistivity data were obtained at 4 cm intervals on the MSCL-W.

Half-round multisensor core logging

Color reflectance

The color spectrophotometer mounted on the MSCL-C frame (Konica-Minolta, CM2600d) has an xyz-type aluminum frame that can accommodate up to 7 core sections on the tray. The sensor unit, including the spectrophotometer and small laser distance measuring sensor, moves over each section, stopping at each measurement point to measure the color spectrum of the split surface of the archive half of the core.

Light reflected from the sample surface is collected in the color spectrophotometer's integration sphere. The instrument's structure allows for the specular component to be included (SCI setting) or excluded (SCE setting). The SCI setting is influenced by the surface condition and its data are closer to the actual color than those of the SCE setting. Data from the SCE setting are closer to the visual observation than those of the SCI setting. The SCE setting is the IODP recommended mode of operation to exclude glare, but the SCI setting was used during this expedition for the rough and dry condition on the cut surface of the OmanDP cores. The light is then divided into wavelengths at a 10 nm pitch (400–700 nm), and the spectral sensors in the sphere convert the light to electrical currents proportional to the intensity of the light. Next, the color spectrum from the sample is normalized by the source light of the reflectance. The obtained spectrum is calibrated with the measurement of a pure white standard, which has a high reflectance true value at visible wavelengths and is measured by the vendor, and a black box (zero calibration).

Color reflectance is categorized as an IODP standard measurement, and the measured color spectrum is normally converted to L^* , a^* , and b^* parameters, in which L^* is lightness (greater value = lighter) in the range between 0 (black) and 100 (white), a^* is the red-green value (greater value = redder) in the range between -60 (green) and 60 (red), and b^* is the yellow-blue value (greater value = yellower) in the range between -60 (blue) and 60 (yellow). L^* , a^* , and b^* provide relative changes in the composition of the bulk material and are widely used to correlate sections from core to core or hole to hole and to analyze the characteristics of lithologic changes. Color reflectance measurements were taken at 2 cm intervals.

Point magnetic susceptibility

MSP is measured using a Bartington MS2EI contact probe with a flat 15 mm diameter sensor operating at a frequency of 0.580 kHz. The sensor takes and averages 3 measurements at 1 s intervals to an accuracy of 5%. The area of response of the MS2E sensor is 3.8 mm × 10.5 mm, with a depth response of 50% at 1 mm and 10% at 3.5 mm, providing higher resolution measurements than the whole-round magnetic susceptibility instrument on the MSCL-W (Bartington Instruments, 2017). Measurements are reported in instrument units. The MSP meter was calibrated by the manufacturer before installation on the ship. The probe is zeroed in air before each measurement point, and a background magnetic field is measured and removed from the data before output. MSP measurements were taken at 2 cm intervals.

Discrete sample measurements

Thermal conductivity was measured on pieces from the working halves of the split core sections, where suitable material was available. Discrete samples (2 cm × 2 cm × 2 cm cubes) were taken from working section halves for P -wave velocity and MAD measurements, which are used to determine bulk density, grain density, and porosity. Most of these samples were the same as those used for paleomagnetic measurements, except when the latter were used for thermal demagnetization, in which case a separate cube was sampled. Shipboard samples were preferentially located close to where shipboard geochemistry samples, thin sections, and many of the paleomagnetism cubes were taken. A comprehensive discussion of the MAD and P -wave velocity methodologies and calculations used in the *JOIDES Resolution* physical properties laboratory, is presented in Blum (1997), and similar processes have been adopted for the ChikyuOman core logging.

Density and moisture

Mass and volume (MAD) measurements on discrete samples were made to determine bulk, dry, and grain

density. IODP shipboard Method C (Blum, 1997) apparatus was used for hard rock samples, which consists of a vacuum water saturator, a dual balance system, and a pentapycnometer. The volume of a specimen can be measured in three ways:

- Method A: wet bulk volume measured with a special volume sampler,
- Method B: wet bulk volume measured by gas pycnometer, and
- Method C: dry volume measured by gas pycnometer.

Method A is the least standardized method. Methods B and C use the same gas pycnometer. Gas pycnometry works with pressure ratios of an ideal gas (helium), which are sensitive to contamination with partial pressures of other fluids. The material to be measured should therefore be dry. The ODP/IODP database contains thousands of examples from specimens measured using both Methods B and C. A systematic error is clearly discernible in comparing calculated results, with bulk densities 1%–5% too high and grain densities about 5%–10% too high for Method B. It is therefore recommended that only Method C be used (Blum, 1997).

Vacuum water saturator

A vacuum pump system is used to ensure water saturation of discrete samples. For Phase 1, the system consisted of a plastic chamber and plastic vials filled with pure water (18 M-Ω Millipore water). For Phase 2, the vials were filled with 0.35% NaCl solution (3.5 g salt/L Millipore water; resistivity ~ 1.5 Ω·m; hereafter called salt water). The vacuum pump removes air from the chamber, essentially sucking air from connected pore spaces. Samples were kept under vacuum for at least 24 h. During this time, pressure in the chamber is monitored periodically, via a gauge attached to the vacuum pump, to ensure a stable vacuum. After removal from the saturator, cubes were stored in sample containers filled with pure or salt water to maintain saturation.

Dual balance system

The OHTI dual balance system was used to measure both wet and dry masses. Two analytical balances (Shimazu, Uni Block) compensate for ship motion; one acts as reference and the other measures the sample. A standard mass of similar value to that of the sample is placed on the reference balance to increase accuracy. A reference mass within ~10% of the sample and glass beaker mass (40.0000 g in total with two 20.0000 g weights) was used during ChikyuOman. The dual balance system was calibrated every 12 h using two 20.0000 g weights. This is performed by taring the balance before each calibration and checking that the total weight mass is within 0.005 g (0.01% accuracy).

After wet mass determinations and P-wave measurements (see [Seismic velocity](#), below) and prior to determination of dry masses, samples were placed in an oven at $105^\circ \pm 5^\circ\text{C}$ (Holes GT1A, GT2A, and GT3A and Phase 2) or $70^\circ \pm 5^\circ\text{C}$ (Hole BT1B) for 24 h to completely dry and then allowed to cool in a desiccator for a minimum of 1 h.

Pentapycnometer system

Two pentapycnometers were used to measure the grain volume of 20 mm cube discrete samples. These instruments (Quantachrome, PPYC-KU) are each capable of measuring the grain volumes of 5 discrete samples at once. The system measures dry sample volume with a normal precision of $\pm 0.01\%$, using pressurized helium-filled chambers. At the start of ChikyuOman and whenever the helium gas tank is changed, shipboard technicians perform a calibration using stainless steel spheres of known volume. For each measurement series, we ran 4 cells that contained unknowns and 1 cell that contained a stainless steel calibration sphere with the volume of 28.9583 cm^3 for each pentapycnometer. Calibration spheres were cycled through the cells to identify any systematic error and/or instrument drift. Spheres are assumed to be known to within 1% of their total volume. Individual volume measurements were preceded by 3 purges of the sample chambers with research grade (99.995% or better) helium heated to 28°C , followed by 3 data acquisition cycles.

For density calculations, both mass and volume are first corrected for the salt content of the pore fluid:

$$M_s = [S(M_w - M_d)] / (1 - S), \quad (17)$$

where,

S = pore water salinity,

M_s = mass of salt,

M_d = dry mass of the sample, and

M_w = wet mass of the sample.

During ChikyuOman Phase 1, the samples were saturated in pure water. In this case, the salt content of the pore fluid is 0.

Grain density (ρ_g) is determined from the dry mass (M_d) and dry volume (V_d) measurements:

$$\rho_g = (M_d - M_s) / [(V_d - M_s / \rho_s)], \quad (18)$$

where ρ_s = density of salt (2.20 g/cm^3 ; Blum, 1997).

The salt-corrected mass of pore water (M_{pw}) is calculated as follows:

$$M_{pw} = (M_w - M_d) / (1 - S). \quad (19)$$

Then, the volume of pore water (V_{pw}) is

$$V_{pw} = M_{pw} / \rho_{pw} = (M_w - M_d) / [(1 - S)\rho_{pw}], \quad (20)$$

where we assume the density of the pore fluid (ρ_{pw}) for Phase 1 is 0.9962 g/cm^3 (pure water) and for Phase 2 is 1.0017 g/cm^3 (0.35% salinity).

To calculate sample bulk density (ρ_b), first bulk volume is computed:

$$V_b = V_d + V_{pw}. \quad (21)$$

Then,

$$\rho_b = M_w / V_b. \quad (22)$$

Porosity (ϕ) is then is calculated from the two volume parameters obtained from the MAD measurements and resulting bulk and pore water volume calculations:

$$\phi = V_{pw} / V_b. \quad (23)$$

The propagated error on the porosity measurement by MAD analysis is within 0.03%, although there are some inevitable bias or problems, such as sampling biases and the short saturation time with water. Consequently, during ChikyuOman, a wide variety and quantity of samples were measured to account for the variability in the natural sample suite, with a minimum of, at least one sample per core.

Seismic velocity

P-wave velocity measurements on discrete samples (PWV-D) were performed on the same discrete cube samples that were used for MAD and many of the paleomagnetic determinations. For Phase 1, measurements were performed on pure water-saturated samples immediately before wet mass determinations were made. For Phase 2, measurements were performed on 0.35% salt water-saturated samples after wet mass determinations were made. The P-wave velocity measurement is taken by PWV-D onboard *Chikyu* (GEOTEK, MSCL-DPW). PWV-D consists of P-wave transducers, a thickness sensor, a temperature sensor, and an electronic console. The operation software *Discrete P-wave* controls measurement sequence and data processing. The peak of the first arrival was identified automatically by the software and the waveform is stored with the data. Regular shipboard visual checks confirmed that the automatic picks were satisfactory. System calibration runs with standards were conducted every day using a series of acrylic and glass cylinders of different thicknesses (4.2 mm and 4.0 mm, respectively) and known P-wave velocities of 2731–2757 m/s and 5382–5572 m/s, respectively, so system and transducer delay time settings were current.

The measurement protocol used for OmanChikyu Phase 1 and 2 core description campaigns were similar to that used on hard rock expeditions aboard the *JOIDES Resolution*. Samples were oriented following

the CRF of the OmanDP, which follows standard IODP conventions (see Fig. F5). Measurements were made in the x -, y -, and z -directions of each cube. Eight successive measurements were obtained along each of the three x -, y - and z -directions for each cube sample. Each of these measurements was taken for a different position of the sample (4 measurements around a given direction with a 90° rotation between each measurement, followed by the same combination of 4 measurements after flipping the sample 180°). The variability between individual measurements was sufficiently high that documenting the average and associated standard errors is required. The 8-part series average typically provided low standard errors of ~25 m/s on average and ~ 100 m/s maximum (~1.5% or less of the determined acoustic velocity).

The apparent anisotropy was approximated from the mean velocity along the 3 directions:

$$V_p \text{ anisotropy} = (V_{p\max} - V_{p\min})/V_{p\text{mean}}, \quad (24)$$

where $V_{p\max}$ and $V_{p\min}$ were the largest and smallest velocity, respectively, measured in one of the x , y , or z sample directions.

Electrical resistivity analysis (impedance analyzer)

The complex impedance, or equivalent resistivity, was measured by using an Agilent 4294A Procession impedance analyzer with a set of two stainless steel electrodes usually used for consolidated sedimentary rocks. Two paper filters soaked in salt water (practical salinity = 0.35%) are placed between steel electrodes and the sample cube on the top and bottom sides to allow better contact for sample measurements. The magnitude ($|Z|$) and phase angle (θ) of the complex impedance were measured at 25 kHz across the array while the measurement taking between 40 Hz and 10 MHz with the accuracy of $\pm 0.08\%$. Electrical resistivity on the x -axis, R_x , is defined follows:

$$R_x = (|Z_x| \cos\theta - |Z_f| \cos\theta_f) \times L_y \times L_z / L_x / 100, \quad (25)$$

where

$|Z_x| \cos\theta$ = measured resistance,

$|Z_f| \cos\theta_f$ = resistance of paper filter, and

L_x , L_y , and L_z = lengths of the triaxial directions.

The other resistivity values on the y - and z -axes (R_y , R_z) are described in the same manner. The mean value of triaxial resistivity, R_{bulk} , is described as

$$R_{\text{bulk}} = (R_x^2 + R_y^2 + R_z^2)^{1/2}. \quad (26)$$

Thermal conductivity

Thermal conductivity (k , in W/m·K) is a measure of the rate at which heat is transported through a mate-

rial by conduction. At steady state, it is the coefficient of heat transfer (q) across a steady-state temperature difference over a distance: $q = k(dT/dx)$. Thermal conductivities of rocks depend on many factors, including temperature, pressure, porosity, type of saturating fluid, and the composition, distribution, and alignment of mineral phases.

Thermal conductivity was measured on split-core pieces under ambient conditions using the Teka TK04 system described in Blum (1997). All measurements were made at room temperature and pressure, and measurements were not corrected to in situ conditions. This system measures thermal conductivity by transient heating of the sample with a known heating power and geometry. Changes in temperature with time during heating are recorded and used to calculate thermal conductivity. Ideally, the heating power should be adjusted for each sample. For Phase 1, as a rule of thumb, heating power in watts per meter was set to be ~2× the expected thermal conductivity in watts per meter degree K. For Phase 2, a heating power of 2.7–3.0 W/m was set for all measurements because the expected thermal conductivity for the cores from Holes CM1A and CM2B was in the range 2.2–4.1 W/m·K. The applied heating power for samples from Hole BA1B was 2.7 W/m because results were expected in the range 1.9–3.8 W/m·K. The temperature of the superconductive needle probe has a quasi-linear relationship with the natural logarithm of the time after the initiation of heating (Blum, 1997). The TeKa TK04 device uses a “special approximation method” (SAM) to calculate conductivity and to assess the fit of the heating curve. This method fits discrete windows of the heating curve to the theoretical temperature (T) with time (t) function:

$$T(t) = A_1 + A_2 \ln(t) + A_3 [\ln(t)/t] + (A_4/t), \quad (27)$$

where A_{1-4} are constants that are calculated by linear regression. A_1 is the initial temperature, whereas A_2 , A_3 , and A_4 are related to geometry and material properties surrounding the needle probe. Having defined these constants (and how well they fit the data), the apparent conductivity (k_a) for the fitted curve is time dependent and given by:

$$k_a(t) = q/4\pi \{A_2 + A_3[1 - \ln(t)/t] - (A_4/t)\}, \quad (28)$$

where q is the input heat flux. The maximum value of k_a and the time, t_{\max} , at which it occurs on the fitted curve are used to assess the validity of that time window for calculating the thermal conductivity. The best solutions are those where t_{\max} is greatest, and these solutions are selected for output. Fits are considered good if k_a has a maximum value, t_{\max} is large, and the standard deviation of the least-squares

fit is low. For each heating cycle, several output values can be used to assess the quality of the data, including LET (natural logarithm of extreme time t_{\max}), which should be large, the number of solutions (N), which should also be large, and the contact value, which assesses contact resistance between the probe and the sample and should be small, and uniform for repeat measurements.

Half-space determinations of thermal conductivity were made with a needle probe embedded in the bottom of a Plexiglas block with a thermal conductivity of 0.184 W/m·K. Heat is assumed to be transferred through the sample, and the TK04 documentation indicates that heat flow through the Plexiglas block itself is only significant for sample thermal conductivities <1 W/m·K. Good thermal contact with the heating needle is required, so the split face of the samples was polished with 240-gauge silicon carbide powder for Phase 1 or 220-gauge silicon carbide powder for Phase 2.

Standard measurements were conducted with both a certified MACOR ceramic standard ($k = 1.652$ W/m·K $\pm 2\%$) to evaluate the reproducibility of results. The 7.3 cm and 4.0 cm needles were used for measurements with the needle aligned with the axis core pieces. The quality of measurements completed with the large needle probe was assessed using LET and N (number of solutions); only a few measured values were rejected; our measurement protocol, with a series of 6 measurements, provided consistent analyses within analytical error $<2\%$.

Core pieces were saturated and left to equilibrate to room temperature in a pure water vacuum saturator for ≥ 12 h, and then the piece and sensor needle were equilibrated at room temperature in an isolated pure water bath ($k = \sim 0.6$ W/m·K) for at least 15 min (Phase 1) or 10 min (Phase 2) prior to measurement. Pure water was used to improve the needle/sample contact; silicone thermal contact gel was avoided in light of potential contamination of the core. Isolation of the piece and sensor needle eliminated the effect of small but rapid temperature changes introduced by air currents in the laboratory, as well as the ship's motion. The instrument internally measures temperature drift and does not begin a heating run until sufficient thermal equilibrium is attained.

Core pieces from the archive half were measured at irregular intervals downhole depending on the availability of homogeneous and relatively vein/crack-free pieces long enough (>5 cm for Phase 1; >10 cm for Phase 2) to avoid the edge reflection effects. The probe was regularly checked using the MACOR ceramic standard.

Core scratch analysis

The scratch test was developed in the late 1990s at the University of Minnesota as a simple, nondestructive,

fast, and robust rock testing technique that provides a direct measure of the rock strength equivalent to the uniaxial compressive strength (UCS) (Noufel et al., 2015). It produces a centimeter-resolution profile of strength (with centimeter steps), revealing the distributions of small heterogeneity length scales along tested core samples.

The scratch test is performed by tracing a groove of constant depth d on the surface of a rock sample with a cutting tool while imposing a constant cutting velocity v . The amplitude and orientation of the force acting on the cutting blade are recorded at high sampling frequency and high precision. Results from a series of successive passes performed on the same sample are interpreted to provide the intrinsic specific energy (ISE), which for suitable sets of operating parameters (depth of cut, cutter geometry, and inclination) is equivalent to the uniaxial compressive strength (UCS) of the material (Fig. F73A) (Germa et al., 2015). The Wombat is a state of the art semiautomated apparatus designed to perform scratch tests on core samples up to 3 ft long and from $\frac{1}{2}$ to 6 inches in diameter (Fig. F74). An experienced operator could test and analyze on average 2 m (6 ft) of core per hour with the Wombat. Results of the scratch test are highly repeatable continuous profiles of rock strength along core samples with a spatial resolution of the order of a centimeter (Fig. F75).

In addition, Epslog has recently developed a complement to its scratch test protocol with a continuous profile of the ultrasonic P -wave velocity V_p along tested core samples. The ultrasonic test measures the times pressure and shear waves take to travel between two ultrasonic probes. From these traveltimes, the compressional and shear wave velocity (V_p and V_s ; m/s or ft/s) can be derived. The apparatus (Fig. F73B) is used to make an indirect measurement of the pressure and shear wave velocities in the 1 cm wide groove left by the scratch test. The probes are 5 cm apart, and a measurement is taken every 2 cm (the resolution of the ultrasonic log is thus 5 cm). Also, when necessary, the apparatus can be used to take measurements on a slabbed face before any scratching. In that case, the orientation of the probes can be chosen; this is particularly interesting when dealing with inclined wells, as the test can be performed parallel or perpendicular to the bedding.

For the first time in the history of scientific drilling, core scratch measurements were made on selected cores across crust–mantle transition from Site CM1 at the JAMSTEC laboratory by the EPSLog engineer.

Imaging spectroscopy

Imaging spectrometers have made fundamental advances on orbital and airborne platforms on Earth and other planets in our solar system (e.g., Goetz et al., 1985; Bibring et al., 2006; Pieters et al., 2009),

and recent advances have miniaturized these systems for use in laboratories. Overtones and combination tones of absorption features in hydrated minerals, carbonates, sulfates, and other mineral groups (e.g., Clark et al., 1990) and electronic transitions and charge transfer absorptions of transition metals (Burns, 1993) in visible-shortwave-infrared reflectance spectra provide rapid mineral identifications at high spatial resolution.

Phase 1

Imaging spectrometers are not currently available in the nominal instrument suite aboard the *Chikyu* or *JOIDES Resolution*, but the OmanDP utilized an imaging spectrometer provided by California Institute of Technology to scan the cut faces of the archive half of the entire Phase 1 drill core (Holes GT1A, GT2A, GT3A, and BT1B). This section describes these measurements and their calibration in detail.

Instrument description and setup

The imaging spectrometer used here was custom-built for California Institute of Technology by Headwall Photonics, Inc. (Fitchburg, MA, USA) and contains one visible-near infrared (VNIR; 0.4–1.0 μm) and one shortwave infrared (SWIR; 0.97–2.60 μm) sensor co-boresighted on an optical bench. The VNIR sensor is a 2560×2160 pixel (1600 spatial and 372 spectral channels used) complementary metal-oxide semiconductor (CMOS) detector with 5 nm spectral resolution (VNIR) and a 1.625 nm spectral sampling interval. The SWIR sensor has a 640×512 pixel Stirling-cooled mercury cadmium telluride (MCT) detector (640 spatial and 285 spectral channels used) with 6 nm spectral resolution (FWHM) and 6 nm spectral sampling interval. A dichroic beam splitter, also mounted on the optical bench, splits light by wavelength to the two detectors. Each detector has its own lens that must be focused. The instrument also has an onboard compact data processing unit with 8 GB RAM and a 1 TB solid-state hard drive (SSD).

This instrument is a pushbroom imaging spectrometer, which means that it simultaneously acquires spatial and spectral measurements of a single line in the cross-track direction. Moving either the sample under the instrument or the instrument above the sample while continuously acquiring lines of data builds a 3-D image cube. In this case, we used the Geotek track aboard the *Chikyu* and described in [Physical properties](#). Using a rack built over the track, the imaging spectrometer was mounted looking vertically downward with the slit perpendicular to the track (Fig. F76). Also mounted on the rack was a halogen light source from the Headwall Photonics, Inc. Starter Kit that focuses light into a slit. The angle of the light was adjusted to provide maximum illumina-

tion directly under the slit. The entire setup was covered with black felt purchased at a craft store with a reflectance of <3% at all wavelengths sampled by the imager to block overhead lights.

Image acquisition and calibration

The instrument was focused for the average height of the cores. The VNIR and SWIR sensors each have their own lenses, which are focused separately. The focus was adjusted when switching between scanning HQ and NQ cores, since the different diameters of the core lead to a difference in the height of the cores. Because of time constraints, the instrument was not refocused between core sections of the same diameter, though precise heights varied slightly. The effective spatial resolutions on the core were $\sim 87 \mu\text{m}/\text{pixel}$ (VNIR) and $250 \mu\text{m}/\text{pixel}$ (SWIR) for HQ core and $89 \mu\text{m}/\text{pixel}$ (VNIR) and $260 \mu\text{m}/\text{pixel}$ (SWIR) for NQ core, which was slightly further from the sensor. The Geotek track moves core at $\sim 1 \text{ cm/s}$, and precise frame periods were determined to match the instrument's instantaneous field of view, which is angular, with the distance traveled by the core during one frame to ensure that pixels are square (i.e., no smearing or oversampling). Those frame periods were 9.197 ms (VNIR) and 26.25 ms (SWIR) for the larger diameter HQ cores and 9.31 ms (VNIR) and 27.37 ms (SWIR) for smaller diameter NQ cores. Exposure times, which are less than or equal to the frame periods, were selected to maximize signal without saturating the detector on the brightest surfaces and were 7–9 ms (VNIR) and 4–5 ms (SWIR), depending on fluctuations in intensity of the light source, which decreased 10%–20% over the month during which the measurements were completed, likely due to the life-cycle of the lamp. Using the same scan parameters, all of the thin section billets from the onboard sampling were imaged. These were lined up on top of a core liner filled with a half-core sized Styrofoam. The instrument was focused for an intermediate thickness of billet. Some of the thinnest and thickest billets may be out of focus, but time constraints prevented changing the focus based on the thickness of individual billets. The billets from Hole BT1B were thicker than those from other holes, and the instrument was refocused before imaging those billets.

The output of the measurements are raw image cubes of .img format with values in digital number (DN) for the intensity of light measured at each spatial pixel as a function of wavelength. For calibration, dark current measurements were taken periodically as single line images averaging 100 frames with the lens cap on. The SWIR sensor has an internal shutter that also blocks all outside light during this measurement, but the VNIR does not. Images of a 99% reflectance Spectralon target (Labsphere) with

known spectral properties traceable to National Institute of Standards (NIST) were also acquired periodically for calibration. As is standard in processing of spectral data to reflectance, pixel-by-pixel corrections were done to subtract the dark signal and ratio to the Spectralon target, correcting the final spectra for the absolute reflectance properties of Spectralon. These corrections remove both instrumental effects and differential lighting effects across the sample. In addition, an Avian Technologies calibration target with eight 1 cm × 1 cm squares of different reflectances was also imaged within each image cube of a section of core, providing a check on the calibration. Using the dark and white reference images and the known spectrum of Spectralon, calibration to reflectance is straightforward. An example of an image cube is shown in Figure F77.

Additional image processing to produce preliminary mineral maps has been done thus far on a limited number of images using calculation of spectral parameters mapping specific absorption features within the spectra (Clark and Roush, 1984; Pelkey et al., 2007) and mineral indicator parameters that combine spectral parameters looking for the presence or absence of specific absorption features diagnostic of minerals of interest (Greenberger et al., 2015). Further data processing on all image cubes and more robust mineral mapping will be completed at California Institute of Technology, and the maps will be made available to the OmanDP Science Team and eventually the broader scientific community. Image cubes will likely be available at that point upon request; the total volume of processed data is likely to exceed 30 TB.

Challenges

A few challenges arose during the measurements and are described in more detail here, as complete understanding is necessary for further data processing. Highly fractured sections, particularly for the NQ cores that were in liners sized for larger diameter core, would at times separate with different pieces falling to the side, putting the surfaces of the core section at varying heights and angles. Some sections were also cut such that the cut surface had variable heights. The imaging spectrometer's focus is sensitive, and differences in height resulted in less than ideal focus for portions of the core. Similarly, loose rocks would often be out of focus owing to their topography and variable heights. Because of time constraints, images of single core sections could not be acquired at multiple focuses to allow for later construction of a single image with every element in focus; nevertheless, spectra of out-of-focus regions will still provide compositional information with average spectra of the region. Another challenge that merits mention is the presence of other materials among

the core sections, including the hard plastic liner, the flexible plastic enclosure (cut along with the core), small pieces of sponges used to wet the core surface to assist the core description teams, smears from the saw blade used to cut the core, Styrofoam, and rare instances of tape residue. For all but the blade, these materials exhibit spectra of organic materials that will allow them to be filtered and removed from the data set before additional processing. Saw marks on the cut surfaces of the core should not affect mineral maps so long as no saw material was left on the surfaces, though textural changes resulting from cutting may change the depths of absorption features in places by increasing or decreasing volume scattering of light interacting with the samples. Finally, whereas most measurements were completed while docked at Shimizu port, we encountered difficulties scanning while transiting and at sea because of ship vibration. These vibrations shook the entire structure on which the spectrometer was mounted, thereby moving the spectrometer. The high spatial resolution of the imaging spectrometer combined with exposure times of <10 ms per line meant that visible shaking of the instrument resulted in noticeable artifacts within the image cubes. For future use of these instruments, we recommend looking into using vibration-damping optical tables and mounts.

Phase 2

Imaging spectroscopy measures the light reflected from a surface at many contiguous wavelengths (e.g., Goetz et al., 1985). Because different materials reflect and absorb light differently as a function of wavelength, imaging spectroscopy can be used to measure mineralogy rapidly and nondestructively. Continuing the imaging spectroscopy measurements from Phase 1 of the OmanDP, the Caltech imaging spectrometer was used to scan the entire archive half of the Phase 2 drill core. These measurements will provide the mineralogy of the entire core at a spatial resolution of ~87 µm/pixel at wavelengths 0.4–1.0 µm and ~250 µm/pixel at wavelengths 1.0–2.6 µm.

Instrument description and setup

The instrument and halogen light source are the same Caltech imaging spectrometer system as that used to measure the OmanDP Phase 1 core. Measurements again sampled wavelengths 0.4–2.6 µm. The general setup is the same, with the instrument mounted above the core as the core moves at a constant speed. The only change from the Phase 1 setup was the use of a conveyor belt instead of the GeoTek MSCL track because the track was not available (Fig. F78). The conveyor belt used was manufactured by Maruyasu Kikai Co., Ltd. with a DC variable speed

motor with part number Oriental Motor Model K1500-40A. The specific track model was MMX2-104-150-200-DC-75-0. Guides along the conveyor belt helped keep the core aligned, and a track with rollers was located at the end of the track. The full setup is shown in Figure F78.

Image acquisition and calibration

As with Phase 1, the lenses on the co-boresighted VNIR and SWIR sensors were focused for a split core surface of average height. Because more than 2000 core sections needed to be scanned within 3 weeks, the lenses could not be refocused for each core. This meant that core sections with loose material or pieces significantly higher or lower than the height of the split core may be slightly out of focus because the distance between the sensor and the surface of the target differed. Whereas most of the core was of HQ size, the last ~125 m of core from Hole CM1A was NQ size. The smaller core diameter meant that the height of the split core was ~8 mm lower. Wood boards were placed under the supports of the conveyor belt and roller track to raise the NQ core to the height of the HQ core. These boards were then removed before scanning the HQ core sections from the remaining holes.

Exposure times were set at 7–8.5 ms for the VNIR sensor and 4.5–5.4 ms for the SWIR sensor to maximize signal without saturating the sensor and were adjusted as necessary for fluctuations in the intensity of the light source. The frame periods were then selected as 9 ms for the VNIR sensor and 25.75 ms for the SWIR sensor. The VNIR frame period is just longer than the maximum exposure time, and the SWIR frame period was set based on the sensor's instantaneous field of view relative to that for the VNIR sensor, which has a narrower field of view. The speed of the conveyor belt was then selected based on the frame period to ensure that the cross-track pixel width viewed by the sensor was equal to the distance traveled by the core in one frame period. This speed was 220 (units are revolutions of a gear inside the motor).

Part or all of some sections from Holes BA1B, BA3A, and BA4A were sampled for microbiology studies during drilling. These sections were therefore not available for imaging spectroscopy measurements. There were 25 samples missing in their entirety, and the Styrofoam placeholder was not always scanned. Samples with part Styrofoam and part rock were

scanned, though the Styrofoam was not always scanned in its entirety.

Image calibration and processing methods are identical to Phase 1 with dark current and white reference (Spectralon) measurements between every ~4–6 core sections or 15 min. Preliminary data processing was performed on a few select images to check image quality, highlight the capability of the measurements, and in a few cases help the core description teams. Additional data processing to produce validated mineral maps will be completed at California Institute of Technology. These products will be made available to the OmanDP Phase 2 Science Party when completed and the general public after the project moratorium period. Imaging spectroscopy data cubes will be available at that point in an appropriate repository or by request; Phase 1 and 2 raw and processed data volumes will likely total ~100 TB.

Challenges

During Phase 1 measurements, there were some challenges and data quality issues from ship movement and motors shaking the structure on which the instrument was mounted while *Chikyu* was at sea. As a result, Phase 2 measurements were completed while the ship was docked in port and more stable with the exception of 48 h in the bay during a typhoon. We minimized the effects of ship movement during these couple of days by scanning only when the ship was most stable and visually checked every image to ensure that there were no significant ship vibrations during scanning; when this was the case, the core section was rescanned.

The main challenge for Phase 2 measurements was keeping the core itself stable because the conveyor belt was flat and the core sometimes rolled slightly or shifted during measurements. These are apparent in the images as obvious lateral offsets in both the core and core liner. This problem mostly occurred when the core moved onto the roller track if it was not perfectly aligned or when the liner made contact or lost contact with guides that were spaced along the length of the track. The guides could not be tighter to avoid these problems because caps at the end of the liner were wider than the liner itself and either the guides would touch the caps and not the liner or the caps would cause the core to get stuck and stop moving. If necessary, offsets from lateral core movement could be manually aligned using the edges of the liner within images to fix lateral offsets.

Downhole logging/ hydrogeological testing

Downhole logs are used to determine physical, chemical, and structural properties of the formations penetrated by the borehole. The data are continuously collected as a function of depth, and measurements are taken at closely spaced depth intervals (at vertical sampling intervals ranging 0.5–45 cm) and are measured in situ. Subsequently, these data can be interpreted in terms of stratigraphy, lithology, porosity, fluid content, fluid composition, geochemical composition, and structure of the formation. Where core recovery is incomplete, log data may provide the only way to characterize the geological formation. Where core recovery is high, log and core data are complementary and may be interpreted jointly.

Downhole logs measure formation properties on intermediate scale between laboratory measurements on core samples and surface geophysical surveys. They are useful in calibrating the interpretation of geophysical survey data (e.g. synthetic seismograms) and provide a necessary link for the integrated understanding of physical properties on all scales.

Two separate wireline logging operations were conducted from OmanDP during two campaigns in 2017 and 2018. All OmanDP holes were logged using a slimline wireline logging system. In addition, advanced downhole logging measurements were acquired by Schlumberger Oil Services, using oilfield-type logging tools in Holes CM1B and CM2A.

Slimline wireline logging

Operations, system, tools, and measurements

Slimline measurements were performed in open borehole conditions (no casing). The recovery and overall quality of the downhole logging data are generally excellent, with the exception of the inclined boreholes (GT2A, BT1B, and CM1A), where inclination of the borehole resulted in decline of the overall log quality, especially for the borehole wall image logs. Because of collapsed borehole conditions, only partial or no logs were collected in Holes GT3A, BT1B, CM1B, CM2A, CM2B, BA2A, and BA1C.

The following downhole measurements were acquired for OmanDP using the slimline system in 2017 and 2018: spectral and total gamma radiation, sonic velocity, acoustic and optical borehole images, electrical resistivity, spontaneous potential, magnetic susceptibility, caliper, borehole fluid parameters (pH, electrical conductivity, temperature, pressure, oxidation-reduction [redox] potential, dissolved oxygen), and flowmeter (spinner, heat-pulse) (Table T54.) Logs were recorded using either standalone tools or with stackable tools that were lowered into the holes

after completion of drilling operations over a given interval.

Two custom-made logging trucks from the Ministry of Regional Municipalities and Water Resources were used to conduct the wireline logging (Figs. F79, F80). The smaller Toyota truck (Fig. F79) is equipped with a Robertson Geo winch with ~600 m of 4-conductor wireline cable, whereas the larger GM truck (Fig. F80) is equipped with a GeoVista GV530 winch with 1000 m of single-conductor wireline cable.

Logging procedure, acquisition chain, and data recording

During each logging session, slimline tools were logged either on an individual string or combined into a tool string. A logging run commenced with zeroing the tool to a reference point (loggers zero). The zero reference is chosen at the top of the pipe for each of the holes and 46 cm above the GO-head make-up of each tool.

All the logs were subsequently adjusted to the ground reference using following equation:

$$\text{depth}_{\text{ground}} = \text{depth}_{\text{logging}} + 46 \text{ cm} + \text{offset}_{\text{pipe}}. \quad (29)$$

Note that $\text{offset}_{\text{pipe}}$ is always counted as positive downward from ground level zero reference.

After logging was completed, data were processed. Each logging pass was recorded and stored digitally. During data acquisition, the data flow was monitored in real time by the logging scientist for quality control and security using the Advanced Logging Technology (ALT) acquisition box and ALT Logger software. Tables T55 and T56 summarize the operations and acquisition parameters for each tool and borehole. Tools were raised at speeds that ranged from a minimum of 1.6 m/min for acoustic and optical borehole image logs to a maximum of 25 m/min for the Dual Laterolog (DLL) resistivity logs (Tables T55, T56). Generally, both up- and downlogs were recorded. After each logging run, the instrument was re-zeroed at the top of the borehole casing to ensure that no depth discrepancies occurred during data acquisition. The ALT WellCAD software package was used for data visualization, processing, and preliminary plotting of data.

Logged properties and tool measurement principles

The logged physical and chemical properties and information about the tools used to measure them are briefly described here. The type of logs are listed in Table T54. Technical details for individual tools are shown in Figure F81. More detailed information on individual tools and their geological applications may be found in Schlumberger (1989), Goldberg

(1997), and Ellis and Singer (2007). Additional information may be found at the manufacturers' websites (<http://www.alt.lu>, <http://www.geovista.co.uk>, and <https://mountsopris.com>).

Dual Laterolog resistivity probe (DDL3)

The DLL3 probe (Fig. F81) measures electrical resistivity within the formation at different depths of investigation (deep: >1 m and shallow: <0.5 m). Electrical resistivity reflects primarily lithology (composition and texture), porosity, saturation, and interstitial fluid properties. The probe has a central electrode, A0, from which a measured current is sent. The current is focused by means of a bucking current that flows from 4 guard electrodes. The potential of the guard electrodes is held equal to the potential of the measure electrode A0 in order to force the electrical current to be perpendicular to the tool axis and to flow a larger distance into the formation. The probe's measured current is proportional to the formation resistivity. The tool's output includes deep (LLD) and shallow (LLS) resistivities in ohm-meters ($\Omega\cdot\text{m}$). The vertical measurement interval is 0.05 m.

Spectral gamma ray (QL40-SGR512)

The QL40-SGR (Fig. F81) probe records total gamma ray emissions of the geological formation. It allows identification of the individual elements that emit gamma rays. Naturally occurring elements such as K, U, and Th emit gamma rays with characteristic energies. K decays into stable isotopes (Ar, Ca), and U and Th decay into unstable daughter elements. The most prominent gamma rays in the U and Th series originate from the decay of ^{214}Bi and ^{208}Tl , respectively. By counting gamma rays from ^{214}Bi and ^{208}Tl , it is possible to compute the concentration of parent ^{238}U and ^{232}Th . The probe's gamma ray detector is a bismuth germanium oxide scintillation crystal optically coupled to a photomultiplier. As the sonde moves up the borehole, gamma rays are sorted according to their emitted energy spectrum, and number of counts in each of the three preselected energy intervals, which are centered on the peak values of ^{40}K , ^{214}Bi , and ^{208}Tl , is recorded. The output includes K, U, and Th in Becquerel per kilogram and total gamma ray counts in API units. The vertical measurement interval is 0.05 m, and the vertical resolution of the tool is ~15 cm.

Magnetic susceptibility (QL40-MGS)

The QL40-MGS borehole magnetic susceptibility tool (Fig. F81) measures the apparent formation magnetic susceptibility in SI units. The probe includes a 2-coil system, and its electronic circuits reside in a high-strength nonmagnetic enclosure. The operating frequency (~2 kHz) is chosen to be low to avoid interference from rock conductivities. In addition, the cir-

cuitry is temperature compensated to minimize thermally induced drift. The tool's output is used to quantitatively determine the magnetic components in the rock and to estimate thicknesses of layers (stratigraphy). The measurement window ranges from 10^{-5} to 2 SI units. The vertical measurement interval is 0.05 m.

Full-wave sonic (QL40-FWS)

The QL40-FWS full waveform sonic tool (Fig. F81) can detect compressional (P), shear (S), Stoneley, and Tube wave arrivals depending on suitable borehole conditions. This tool implements a high-energy source generated by a ceramic-piezoelectric transducer that excites the geologic formation in such a way that waves of different frequencies are developed and propagated. Real-time analysis and processing of the full waveform are performed by the tool to enhance the picking of the different wave propagation modes (wave arrival times). When the lithology and bulk density are known, elastic properties (bulk and shear moduli) and porosity estimates can be derived from sonic measurements. The QL40-FWS probe can only operate in fluid-filled boreholes. The downhole measurement interval is 0.05 m.

Acoustic Borehole Imager (QL40-ABI)

The QL40-ABI (Fig. F81) produces millimeter- to centimeter-scale high-resolution, 360° unwrapped and 3-D acoustic images of the borehole wall. The images can be used for lithologic and structural interpretation (fracture detection and evaluation, breakout analysis, bedding dip), evaluate borehole deformation (stress field analysis), and core-log integration. A 3-component fluxgate magnetometer and 3 accelerometers allow orientation of the images to a global reference and determination of the borehole's azimuth and inclination. A voltage is applied in a piezoelectric ceramic to produce an acoustic wave generated at 1.2 Hz. On hitting a focalizing mirror, the wave is deflected perpendicularly toward the borehole wall. The probe records both the amplitude and the two-way traveltime of its echo from the borehole wall. To obtain a 360° image of the borehole wall, the mirror pivots on a central axis. The resolution is user defined and depends on numbers of measurements made in one mirror rotation and logging speed. The probe produces two images of the borehole wall: acoustic impedance and a traveltime image. The impedance image is derived from the reflected wave amplitude. The amplitude ratio between the emitted and the reflected wave provides information about absorption. The traveltime image is obtained from the reflected-wave traveltime from the transducer to the borehole wall, which is directly proportional to the distance between the borehole

wall and the probe. Traveltime data are used to compute acoustic caliper and to determine borehole size and shape. For each of the two images, a set of false colors is assigned and a virtual image of the borehole wall is produced.

Optical Borehole Imager (QL40-OB)

The OL40-OB borehole imager (Fig. F81) produces millimeter-scale, 360° unwrapped, high-resolution optical images of the borehole wall. It implements a high-resolution CMOS digital image sensor combined with a fisheye lens. The light source is provided by a LED light ring assembly located in the optical head. The images are oriented to a global reference using a 3-axis magnetometer and 3-axis accelerometer. This allows determination of the borehole's azimuth and inclination. The tool is designed for logs in air or clear water. Thus, the image quality degrades with hole diameter larger than 15 cm (6 inches) and with the presence of mudcake or murky water. The images are used to obtain detailed and oriented structural information, fracture detection and evaluation, breakout analysis, determination of bedding dip, and lithologic and mineralogic characterization.

Water quality probe (QL40 ALT, Robertson Geo probe)

Three different water quality probes, the QL40-MUSET and the QL40-Ocean, both from ALT, and a similar one from Robertson Geo (IDRO-ROB) were used to characterize borehole fluids (Fig. F81). All probes are equipped with 6–7 sensors (Ocean Seven 303 CTD multiparameter probe, Idronaut, Italy). The ALT tools are equipped with pressure, temperature, conductivity, dissolved oxygen, pH, and redox potential sensors. The QL40-MUSET is combined with a nonpolarizable spontaneous electrical potential probe. The Robertson tool is equipped with the same sensors as QL40-Ocean with an additional nitrate sensor. The temperature sensor consists of a low-time-response platinum resistance thermometer. The conductivity sensor is a flow-through cell with 7 platinum ring electrodes. The pH sensor has a titanium body and a pH sensitive glass tip. It is combined with a reference sensor (silver/silver chloride cell in saturated KCl solid gel [Ag/AgCl; KCl sat]). The head of the sensor is made of titanium. The redox sensor consists of a platinum wire that ends at the tip of the glass body. It makes use of the same reference sensor as the pH electrode. The measured potential is not representative of a true Eh value but is only the electric/magnetic field of an electrochemical cell. Such cell difference potentials measured in natural environments are still often referred to the hydrogen scale and expressed as redox potentials or Eh. In the water quality probe, the potential of the reference electrode (Ag/AgCl; KCl sat) is +202 mV at 20°C, which is added to the measured value. Thus,

the positive potential of the reference electrode with respect to hydrogen must be always added to the value measured by the probe. The dissolved oxygen sensor is a polarographic sensor consisting of two half-cells (anode and cathode). The anode is a silver tube inside the sensor, which encircles a glass body where a platinum wire forms the cathode. A special membrane cap with a gas-permeable membrane screws onto the sensor. The inside of the cap is filled with a special electrolyte. By applying a polarizing voltage to the half-cells, the sensor develops a current proportional to the concentration of oxygen in the sample. During the OmanDP logging campaign, the recorded dissolved oxygen data are not reliable because of a malfunction of the sensor. The data should therefore be used with care. The pressure sensor is a high-quality strain gauge mounted in the center of the probe. The nitrate sensor on the IDRO-ROB probe is a liquid membrane ion-selective electrode. The active membrane consists of an organic solvent that contains the ion exchanger. The nitrate sensor is used in conjunction with the Ag/AgCl reference sensor.

Caliper (QL40-CAL)

The QL40-CAL (Fig. F81) is a 3-arm caliper measuring borehole diameter. In OmanDP, the caliper tool was not run in every borehole because of its limited use. The 3 arms are mechanically linked together and open only by the same amount, which makes its measurements in tilted or asymmetric boreholes unreliable. The acoustic caliper, derived from the acoustic borehole imager, should be used instead.

Spinner flowmeter (QL40-SFM)

The QL40-SFM spinner flowmeter probe (Fig. F81) measures impeller rotation caused by groundwater flow in the borehole. The tool uses a magnetically coupled pick-up, which drives a low-friction, high-resolution encoder. The encoder produces 256 pulses per shaft rotation. Quadrature sensing electronics detect flow direction changes. Spinner flowmeter measurements are used to identify hydrostratigraphic units to determine interval-specific flow rates and to detect transmissive zones in open holes.

Heat-pulse flowmeter (HFM-2293)

The HFM-2293 heat-pulse flowmeter (Fig. F81) measures low flow rates in the borehole. It also provides the vertical direction of fluid flow. Measurements are made while the probe is stationary at different depths within the borehole. A heat grid in the tool is activated to heat a packet of water at a specific depth in the borehole. In case there is vertical flow in the borehole, the heated water packet moves with the flow toward the upper or lower sensor in the tool. The difference in temperature between the sensors is

monitored. The probe records the time from when the heat grid was first activated to the moment when the greatest temperature change is detected by one of the sensors. This information is then used to calculate the flow rate and direction of flow at the specific depth in the borehole and time. The HFM can measure flow of 0.04–5.5 L/min.

Data processing, quality control, and delivery

Slimline logging data were processed using the WellCAD software package. If necessary, logs were depth-adjusted and invalid values were replaced by a null value of –99999.00 in the case of the following:

- Approaching the metallic borehole casing in the open borehole (DLL, QL40MGS, QL40SGR, some channels of the QL40ABI and QL40OBI, QL40-MUSET, QL40Ocean, and QL40-FWS);
- The lowermost data points are affected by the termination of the measurement; and
- Gaps in data recordings resulting from halts.

Data quality was assessed by the responsible petrophysicist in terms of reasonable values for the logged formation, repeatability between different passes of the same tool (up and down logs), and correlation between logs of the same formation. The overall wireline logging data quality is very good, with the exception of some logs in boreholes with challenging conditions (e.g., inclination, drilling grease/oil). Inclination of hole resulted in tool centralization problems, whereas leftovers of grease from drill pipes in the borehole affected the image quality of the optical borehole wall imager (e.g., Holes GT1A, CM1A, CM2B). Furthermore, the total gamma ray and the spectral components (K, U, and Th) should be used with care, especially those from the boreholes in serpentinized dunite and harzburgite (CM and BA holes). The total counts and the concentrations of U, Th, and K (Bq/L) are very low in these formations. With regard to the QL40-MUSET, QL40-Ocean, and IDRO_ROB, logs that were run shortly after drilling may still be affected by the drilling. The quality of these logs is best when they are conducted once the borehole fluid has reached equilibrium with the formation. Thus, repeated logs after 12 months equilibrium period are available for the BA multiborehole test site holes. With regard to the full-wave sonic logs, all waveforms from the sonic tool were filtered and processed through a slowness-time coherence (STC) analysis to measure the compressional and shear velocity (V_p and V_s) in the formation from the acoustic waves generated by the tool's transducers. At each depth, the method searches through reasonable values of arrival times and velocity the highest semblance across the receivers. The bandpass filters were adjusted for each tool and each well to enhance the compressional and shear waves and mask other waves traveling in the boreholes. The improvement

provided by this semblance-based analysis over the original threshold picking procedure was more significant for the tools configured with three or more receivers.

Processed and raw data from all downhole logs are available in **Supplementary material > L_Wireline logging** and in the ICDP Oman Drilling Project online data repository (<http://oman.icdp-online.org>). Please note that access to the ICDP data repository during the moratorium period is restricted to the Science Party. Processed wireline data are available in ASCII and WellCAD format. QL40-ABI and QL40-OBI borehole image files are available in WellCAD format and as PDF files.

Advanced wireline logging–Schlumberger Oil Services

During the OmanDP, advanced logging measurements were made in Holes CM1B and CM2A with special contributions and cooperation from Schlumberger Oil Services. The survey included total and spectral gamma ray, density, neutron porosity, photoelectric factor (PEF), resistivity borehole images, laterolog resistivity, sonic velocity (P - and S -wave), and geochemical elements. The wireline logging tools were lowered into the open hole on a multiple-conductor contra helically armored wireline, and measurements were taken from the bottom of the hole upward. For depth correlation purposes, we tried to maintain steady cable tension. A total of five logging runs were conducted at two different times, the first four runs in January 2018 and a fifth run (LithoScanner) was successful in its second attempt in March 2018. The tool strings used and shown in Figure F82, include the following runs:

1. Platform Express (PEX)–high-resolution laterolog array (HRLA)–gamma ray (total enhanced digital telemetry cartridge [EDTC] and spectral hostile-environment natural gamma ray sonde [HNGS]), and PEX: compensated neutron log (CNL)–highly integrated gamma ray neutron sonde (HGNS)–high-resolution mechanical sonde (HRMS).
2. Dipole shear sonic imager (DSI)–gamma ray (EDTC).
3. Fullbore Formation MicroImager (FMI-HD)–gamma ray (EDTC).
4. Elemental capture spectroscopy (ECS)–gamma ray (EDTC).
5. LithoScanner (NEXT)–gamma ray (EDTC).

Operations, system, tools, and measurements

Logs are recorded with a variety of tools combined into several tool strings, which are run down the hole after completion of drilling operations. Each tool string deployment is a logging “run,” starting with the assembly of the tool string and the neces-

sary calibrations. The tool string is sent down to the bottom of the hole while recording a partial set of data and then pulled up at a constant speed, precision mode of ~120 m/h, to record the main data. During each run, the tool string can be lowered down and pulled up the hole several times for quality control or to try to increase the circumferential coverage of the imaging tools. Each lowering or hauling-up of the tool string while collecting data constitutes a “pass.” During each pass, incoming data are recorded and monitored in real time on the surface using Schlumberger’s multitask acquisition and imaging system (MAXIS). A logging run is complete once the tool string has been brought to the rig floor and disassembled.

In general, wireline depth is more precise than drilling depth, which is affected by the stretch of the borehole assembly, and is measured accurately during logging operations with an integrated depth wheel. This device uses tension measurement for the correction of cable stretch and provides calibrated absolute depth values. Data from each wireline logging tool were recorded in the data logger within the tool and were available for real-time display via MAXIS.

Logged properties and tool measurement principles

The Schlumberger logging measurement specifications are listed in Table T57. More detailed information on individual tools and their geological applications may be found in Goldberg (1997), Rider (1996), Schlumberger (1989), and Serra (1984, 1986), as well as a complete online list of acronyms at glossary.oil-field.slb.com and software product mnemonics at <https://www.apps.slb.com/cmd/>.

Hostile environment natural gamma ray sonde (HNGS)

The HNGS tool (Fig. F82A) uses spectroscopic analysis and two bismuth germanate scintillation detectors to determine the concentration of radioactive isotopes. The measurements focus on three common decay chain reactions of radioactive isotopes that are common in natural formations (K, Th, and U), each emitting photons at different energies. The HNGS measures gamma radiation from each decay that is converted to concentrations of K, Th, and U.

The radius of investigation depends on several factors: hole size, mud density, formation bulk density (denser formations display a slightly lower radioactivity), and the energy of the gamma rays (a higher energy gamma ray can reach the detector from deeper in the formation). This tool has a 24 cm depth of investigation and can also be used inside casing.

Electrical resistivity

The High-Resolution Laterolog Array (HRLA) tool (Fig. F82A) provides 6 resistivity measurements at different depths of investigation (including the borehole or mud resistivity, and 5 measurements of formation resistivity with increasing penetration into the formation). The sonde sends a focused current into the formation and measures the intensity necessary to maintain a constant drop in voltage across a fixed interval, providing direct resistivity measurement. The array has 1 central source electrode and 6 electrodes above and below it, which serve alternatively as focusing and returning current electrodes. By rapidly changing the role of these electrodes, a simultaneous resistivity measurement at 6 penetration depths is achieved. The tool is designed to ensure that all signals are measured at exactly the same time and same tool position and to reduce the sensitivity to “shoulder bed” effects when crossing sharp beds thinner than the electrode spacing. Typically, igneous minerals found in crustal rocks are electrical insulators, whereas sulfide and oxide minerals as well as ionic solutions like pore water are conductors. In most rocks, electrical conduction occurs primarily by ion transport through pore fluids and thus is strongly dependent on porosity. Electrical resistivity, therefore, can be used to evaluate alteration, porosity, and fluid salinity.

Microresistivity formation imaging/High-Definition Formation Microlmager (FMI-HD)

The FMI tool (Fig. F82C) provides real-time microresistivity formation images and dip data in water-based mud. The tool has 80% borehole coverage in 8 inch boreholes and 100% coverage in 6 inch boreholes with 0.2 inch image resolution in the vertical and azimuthal directions (Schlumberger, 2013). The FMI provides an electrical borehole image and dip information generated from up to 192 microresistivity measurements. The 4 electrode flaps attached to the 4 pads are applied to the borehole wall using caliper arms (Fig. F82B). The combination of measuring button diameter, pad design, and high-speed telemetry system produces a vertical and azimuthal resolution of 0.51 cm. This means that the dimensions of a feature larger than this resolution can be identified in the image. The size of features <0.51 cm is estimated by quantifying the current flow to the electrode. The azimuthal coverage of the borehole image is ~100% in the 6 inch hole. The general purpose inclinometry tool (GPIT), which integrates both a 3-axis inclinometer and a 3-axis magnetometer, is associated with the FMI to determine the orientation and acceleration of its image. It can also provide the geometry of the borehole path.

Acoustic velocity

The dipole sonic imager (DSI) (Fig. F82B) generates acoustic pulses from monopole and crossed-dipole transmitters and records the full waveforms with an array of 8 receivers. The waveforms are then used to calculate the sonic velocity in the formation. The omnidirectional monopole transmitter emits high-frequency (5–15 kHz) pulses to extract the compressional velocity (V_p) of the formation, as well as the shear velocity (V_s) when it is faster than the sound velocity in the borehole fluid. The tool is made up of three sections (acquisition cartridge, receiver section, and transmitter section). An isolation joint is placed between the transmitter and receiver sections to prevent direct flexural wave transmission through the tool body. The transmitter section contains a piezoelectric monopole transmitter and 2 electrodynamic dipole transmitters perpendicular to each other. To the monopole transmitter, an electric pulse at sonic frequencies is applied to excite compressional and shear wave propagation in the formation. The 2 dipole transmitters obtain azimuthal shear wave anisotropy and are also driven at low frequency to excite the flexural wave around the borehole. The same transmitter can be fired in alternance at a lower frequency (0.5–1 kHz) to generate Stoneley waves that are sensitive to fractures and variations in permeability (Hornby et al., 1989). The DSI also has 2 orthogonal dipole transmitters (0.5–3.5 kHz) that allow measurement of shear wave velocity in “slow” formations, where V_s is slower than the velocity in the borehole fluid. In hard rock formations, V_s can be measured from the monopole waveforms. These higher frequency waveforms usually provide a sharper shear arrival and more accurate estimate of V_s than either of the dipole sources. The array of 8 receiver stations are spaced 15.24 cm apart, which confines the vertical resolution of this tool and provides spatial samples of the propagating wave field for full waveform analysis.

High-definition elemental capture spectroscopy/LithoScanner

Geochemical logging tools were first introduced in the 1970s for cased-hole evaluation of saturation using carbon:oxygen ratios and qualitative evaluation of lithology based on Si, Ca, and Fe (Culver et al., 1974; Hertzog, 1980). Over the next two decades, focus on elemental spectroscopy logging expanded to include open-hole formation evaluation where technological advances led to new tools to measure elemental concentrations and interpret formation mineralogy and nuclear properties (e.g., Herron and Herron, 1996; Radtke et al., 2012).

The elemental capture spectroscopy (ECS) tool (Fig. F82D) was the first commercial service designed for

open-hole formation evaluation. It uses a radionuclide source to bombard the formation with neutrons that are captured by nuclei of specific atoms, which emit γ -rays of characteristic energy that are measured and interpreted in terms of formation composition. More modern tools (LithoScanner) (Pemper et al., 2009; Radtke et al., 2012) use pulsed neutron generator (PNG) sources that allow simultaneous acquisition of the capture γ -ray spectrum and a spectrum of γ -rays produced by inelastic scattering reactions, which allows measurement of formation carbon and computation of total organic carbon (TOC). Modern neutron-induced γ -ray spectroscopy or elemental spectroscopy logging tools yield concentration logs of important rock-forming elements. Among few tools in service, the LithoScanner reports concentrations of the major elements Si, Ca, Fe, Mg, S, K, Al, Na, and C as well as some minor or trace elements, such as Mn, Ti, and Gd (Radtke et al., 2012; Aboud et al., 2014). Elemental concentration logs can be used to describe TOC, lithology, or mineralogy and matrix properties.

The LithoScanner (Fig. F82E) combines the advantages of inelastic and capture gamma ray spectroscopy, opening new avenues for detailed description of complex reservoirs. The new service provides higher precision and improved accuracy for analysis of key elements in rock formations and simultaneously offers a standalone quantitative determination of TOC. The measurements are offered at faster logging speed, eliminating the americium beryllium ($^{241}\text{AmBe}$) radioisotopic source makes combination with traditional measurements a much more attractive and viable logging option for both conventional and unconventional markets (Radtke et al., 2012).

The neutrons emitted by the PNG of the LithoScanner tool induce the emission of gamma rays from the formation via two primary interactions: inelastic scattering and thermal neutron capture. Each of these interactions produces gamma rays with a specific set of characteristic energies. The LithoScanner tool's LaBr₃:Ce detector is coupled to a high-temperature spectroscopy photomultiplier, producing signals that are integrated, digitized, and processed by a high-performance pulse-height analyzer. The analyzer determines the pulse height (proportional to energy) of each detected gamma ray and accumulates pulse-height histograms (spectra) that tally counts vs. pulse height. Spectra are acquired during and after each neutron burst, which enables separation of the inelastic and capture gamma rays. Each spectrum is decomposed into a linear combination of standard spectra from individual elements. This step involves correction for some environmental and electronic factors. The coefficients of the linear combination of the standard spectra are converted to elemental weight fractions via a modified geochemical

oxides closure model or by using an inversion approach. Two methods are available to generate mineralogy and lithologic fractions from the elemental concentration logs. One is sequential SpectroLith processing, which is based on the derivation of empirical relationships between elemental concentrations and mineral concentrations. The other is by using an iterative inversion technique, such as the Techlog Quanti multicomponent inversion ELAN module.

Logging data acquisition, quality control, and log depth scales

For the best quality of the logs and cooperation from Schlumberger, every run was made in slowest possible speed and repeat runs to the full length of the hole as Schlumberger's complimentary service. Data for each wireline logging run were monitored in real time and recorded using Schlumberger's MAXIS. The wireline logging data were stored in MAXIS, and an initial data quality check was conducted by field engineers and the Japan Agency for Marine-Earth Science and Technology (JAMSTEC) logging scientists at the well site. The data were received from Schlumberger after checking by their domain specialists in Oman. Using Schlumberger SIS's TechLog software, data were processed at JAMSTEC for (1) depth-shifting all logs to the seafloor, (2) environmental corrections specific to individual tools and depth matching, and (3) logging data quality control comparing repeated sections. The FMI data processing steps included data format conversion, inclinometry quality check, speed correction and equalization, resistivity calibration, and normalization.

References

- Abily, B., and Ceuleneer, G., 2013. The dunitic mantle-crust transition zone in the Oman ophiolite: residue of melt-rock interaction, cumulates from high-MgO melts, or both? *Geology*, 41(1):67-70.
- Aboud, M., Badry, R., Grau, J., Herron, S., Hamichi, F., Horowitz, J., Hemingway, J., et al., 2014. High-definition spectroscopy-determining mineralogic complexity. *Oil-field Review*, 26/1, Schlumberger.
- Arason, P., and Levi, S., 2010. Maximum likelihood solution for inclination-only data in paleomagnetism. *Geophys. J. Int.*, 182(2):753-771. <https://doi.org/10.1111/j.1365-246X.2010.04671.x>
- Barnes, I., and O'Neil, J.R., 1969. The Relationship between Fluids in Some Fresh Alpine-Type Ultramafics and Possible Modern Serpentinization, Western United States. *GSA Bull.*, 80:1947-1960.
- Barrat, J.A., Zanda, B., Moynier, F., Bollinger, C., Liorzou, C., and Bayon, G., 2012. Geochemistry of CI chondrites: Major and trace elements, and Cu and Zn isotopes. *Geochimica et Cosmochimica Acta*, 83:79-92.
- Bartington Instruments, 2017. Operation Manual for MS2 Magnetic Susceptibility System: Oxford, United Kingdom. https://www.bartington.com/wp-content/uploads/pdfs/operation_manuals/MS2_OM0408.pdf
- Bernasconi, S.M., Müller, I.A., Bergmann, K.D., Breitenbach, S.F.M., Fernandez, A., Hodel, D.A., Jaggi, M., et al., 2018. Reducing uncertainties in carbonate clumped isotope analysis through consistent carbonate-based standardization. *Geochem., Geophys., Geosyst.*, 19(9):2895-2914.
- Bibring, J.-P., Langevin, Y., Mustard, J.F., Poulet, F., Arvidson, R., Gendrin, A., Gondet, B., Mangold, N., Pinet, P., Forget, F., and the OMEGA Team, 2006. Global Mineralogical and Aqueous Mars History Derived from OMEGA/Mars Express Data. *Science*, 312:400-404. <https://doi.org/10.1126/science.1122659>.
- Blackman, D.K., Ildefonse, B., John, B.E., Ohara, Y., Miller, D.J., MacLeod, C.J., and the Expedition 304/305 Scientists, 2006. Proc IODP, 304/305: College Station, TX (Integrated Ocean Drilling Program Management International, Inc.). <https://doi.org/10.2204/iodp.proc.304305.2006>
- Blum, P., 1997. Physical properties handbook: a guide to the shipboard measurement of physical properties of deep-sea cores. ODP Tech. Note, 26. <https://doi.org/10.2973/odp.tn.26.1997>
- Braman, R.S., and Hendrix, S.A., 1989. Nanogram nitrite and nitrate determination in environmental and biological materials by vanadium(III) reduction with chemiluminescence detection. *Analytical Chemistry*, 61(24):2715-2718.
- Breitenbach, S.F.M., and Bernasconi, S.M., 2011. Carbon and oxygen isotope analysis of small carbonate samples (20 to 100 µg) with a GasBench II preparation device. *Rapid Communications in Mass Spectrometry*, 25(13):1910-1914.
- Burns, R.G., 1993. Mineralogical Applications of Crystal Field Theory (2nd ed.): Cambridge (Cambridge Univ. Press).
- Canfield, D.E., and Raisewell, R., 1999. The evolution of the sulfur cycle. *Am. J. Sci.*, 299:697-723.
- Canfield, D.E., Raiswell, R., Westrich, J., Reaves, C., Berner, R., 1986. The use of chromium reduction in the analysis of reduced inorganic sulfur in sediments and shales *Chemical Geology*, 54: 149-155. [https://doi.org/10.1016/0009-2541\(86\)90078-1](https://doi.org/10.1016/0009-2541(86)90078-1)
- Clark, R.N., King, T.V.V., Klejwa, M., Swayze, G.A., and Vergo, N., 1990. High Spectral Resolution Reflectance Spectroscopy of Minerals: *Journal of Geophysical Research*, 95:12653-12680. <https://doi.org/10.1029/JB095iB08p12653>
- Clark, R.N., and Roush, T.L., 1984. Reflectance spectroscopy: Quantitative analysis techniques for remote sensing applications. *Journal of Geophysical Research, Solid Earth*, 89:6329-6340. <https://doi.org/10.1029/JB089iB07p06329>
- Clark, R.N., Swayze, G.A., Wise, R., Livo, E., Hoefen, T., Kokaly, R., and Sutley, S.J., 2007. USGS Digital Spectral Library 06: U.S. Geological Survey, Digital Data Series, 231. <http://speclab.cr.usgs.gov/spectral.lib06/>
- Cordier, C., Clément, J.-P., Caroff, M., Hémond, C., Blais, S., Cotten, J., Bollinger, C., Launeau, P., and Guille, G., 2005. Petrogenesis of coarse-grained intrusives from Tahiti Nui and Raiatea (Society Islands, French Polynesia).

- sia). *J. Petrol.*, 46(11):2281–2312. <https://doi.org/10.1093/petrology/egi055>
- Culver, R.B., Hopkinson, E.C., and Youmans, A.H., 1974. Carbon/oxygen (C/O) logging instrumentation. *SPE Journal*, 14(5):463–470.
- Davis, G.H., Reynolds, S.J., and Kluth, C., 2011. *Structural Geology of Rocks and Regions* (3rd ed.): New York (John Wiley & Sons, Inc.)
- Dulski, P., 2001. Reference materials for geochemical studies: New analytical data by ICP-MS and critical discussion of reference values. *Geostand. Newslett.* 25:87–125.
- Eberl, D.D., 2003. User Guide to RockJock - A Program for Determining Quantitative Mineralogy from X-Ray Diffraction Data., U.S. Geological Survey. Available at: <http://pubs.er.usgs.gov/publication/ofr200378> [Accessed 15 August 2018].
- Ellis, D.V., and Singer, J.M., 2007. *Well Logging for Earth Scientists* (2nd ed.): Dordrecht, The Netherlands (Springer).
- Erdman, M.E., Lee, C.-T.A., Yang, W., and Ingram, L., 2014. Sulfur Concentration in Geochemical Reference Materials by Solution Inductively Coupled Plasma-Mass Spectrometry. *Geostand. Geoanal. Res.*, 38:51–60. <https://doi.org/10.1111/j.1751-908X.2013.00226.x>
- Expedition 304/305 Scientists, 2006. Methods. In Blackman, D.K., Ildefonse, B., John, B.E., Ohara, Y., Miller, D.J., MacLeod, C.J., and the Expedition 304/305 Scientists, *Proc. IODP, 304/305: College Station, TX (Integrated Ocean Drilling Program Management International, Inc.)*. <https://doi.org/10.2204/iodp.proc.304305.102.2006>
- Expedition 309/312 Scientists, 2006. Methods. In Teagle, D.A.H., Alt, J.C., Umino, S., Miyashita, S., Banerjee, N.R., Wilson, D.S., and the Expedition 309/312 Scientists, *Proc. IODP, 309/312: Washington, DC (Integrated Ocean Drilling Program Management International, Inc.)*. <https://doi.org/10.2204/iodp.proc.309312.102.2006>
- Expedition 322 Scientists, 2010. Methods. In Saito, S., Underwood, M.B., Kubo, Y., and the Expedition 322 Scientists, *Proc. IODP, 322: Tokyo (Integrated Ocean Drilling Program Management International, Inc.)*. <https://doi.org/10.2204/iodp.proc.322.102.2010>
- Expedition 335 Scientists, 2012b. Site 1256. In Teagle, D.A.H., Ildefonse, B., Blum, P., and the Expedition 335 Scientists, *Proc. IODP, 335: Tokyo (Integrated Ocean Drilling Program Management International, Inc.)*. <https://doi.org/10.2204/iodp.proc.335.103.2012>
- Expedition 343/343T Scientists, 2013. Methods. In Chester, F.M., Mori, J., Eguchi, N., Toczko, S., and the Expedition 343 Scientists, *Proc. IODP, 343/343T: Tokyo (Integrated Ocean Drilling Program Management International, Inc.)*. <https://doi.org/10.2204/iodp.proc.343343T.102.2013>
- Falk, E.S., and Kelemen, P.B., 2015. Geochemistry and petrology of listvenite in the Samail ophiolite, Sultanate of Oman: complete carbonation of peridotite during ophiolite emplacement. *Geochim. et Cosmochim. Acta*, 160:70–90.
- Fernandez, A., Müller, I.A., Rodríguez-Sanz, L., van Dijk, J., Looser, N., Bernasconi, S.M., 2017. A reassessment of the precision of carbonate clumped isotope measurements: implications for calibrations and paleoclimate reconstructions. *Geochem., Geophys., Geosyst.*, 18:4375–4386.
- Fossen, H., 2010. *Structural Geology*: Cambridge (Cambridge Univ. Press).
- French, K.L., Hallmann, C., Hope, J.M., Schoon, P.L., Zumberge, J.A., Hoshino, Y., Peters, C.A., et al., 2015. Reappraisal of hydrocarbon biomarkers in Archean rocks. *Proc. Natl. Acad. Sci.*, 112(19):5915–5920.
- Friese, A., Kallmeyer, J., Kitte, J., Montaña Martínez, I., Bijaksana, S., Wagner, D., 2017. A simple and inexpensive technique for assessing contamination during drilling operations. *Limnol. Oceanog.: Meth.*, 15. <https://doi.org/10.1002/lom3.10159>
- Früh-Green, G.L., Orcutt, B.N., Green, S.L., Cotterill, C., Morgan, S., Akizawa, N., Bayrakci, G., et al., 2017. Expedition 357 methods. In Früh-Green, G.L., Orcutt, B.N., Green, S.L., Cotterill, C., and the Expedition 357 Scientists, *Atlantis Massif Serpentinization and Life. Proceedings of the International Ocean Discovery Program, 357: College Station, TX (International Ocean Discovery Program)*. <https://doi.org/10.14379/iodp.proc.357.102.2017>
- García-Robledo, E., Corzo, A., Papaspyrou, S., 2014. A fast and direct spectrophotometric method for the sequential determination of nitrate and nitrite at low concentrations in small volumes. *Mar. Chem.*, 163:30–36.
- GE Healthcare, 2013. *Discovery CT750 Service Method rev.15*.
- GE Healthcare, 2013. *Discovery CT750 User Manual rev.1*.
- GE Healthcare, 2013. *Technical Reference Manual rev.1*.
- Germay, C., Richard, T., Mappanyompa, E., Lindsay, C., Kitching, D., and Khaksar, A., 2015. The continuous-scratch profile: A high-resolution strength log for Geomechanical and Petrophysical characterization of rocks. *SPE 174086 Reservoir Evaluation & Engineering*.
- Gillis, K.M., Snow, J.E., Klaus, A., Guerin, G., Abe, N., Akizawa, N., Ceuleneer, G., et al., 2014. Methods. In Gillis, K.M., Snow, J.E., Klaus, A., and the Expedition 345 Scientists, *Proceedings of the Integrated Ocean Drilling Program, 345: College Station, TX (Integrated Ocean Drilling Program)*. <https://doi.org/10.2204/iodp.proc.345.102.2014>
- Glombitza, C., Adhikari, R.R., Riedinger, N., Gilhooly III, W.P., Hinrichs, K.-U., and Inagaki, F., 2016. Microbial sulfate reduction potential in coal-bearing sediments down to ~2.5 km below the seafloor off Shimokita Peninsula, Japan. *Front. Microbiol.*, 7:1576.
- Govindaraju, K., 1994. 1994 compilation of working values and sample description for 383 geostandards. *Geostandards Newsletter 18: Special Issue*.
- Goetz, A.F.H., Vane, G., Solomon, J.E., and Rock, B.N., 1985. Imaging Spectrometry for Earth Remote Sensing. *Science*, 228:1147–1153. <https://doi.org/10.1126/science.228.4704.1147>.
- Goldberg, D., 1997. The role of downhole measurements in marine geology and geophysics. *Rev. Geophys.*, 35(3):315–342. <https://doi.org/10.1029/97RG00221>
- Greenberger, R.N., Mustard, J.F., Cloutis, E.A., Mann, P., Wilson, J.H., Flemming, R.L., Robertson, K.M., Salvatore, M.R., and Edwards, C.S., 2015. Hydrothermal alteration and diagenesis of terrestrial lacustrine pillow basalts: Coordination of hyperspectral imaging with laboratory measurements. *Geochimica et Cosmochim.*

- ica Acta, 171:174–200. <https://doi.org/10.1016/j.gca.2015.08.024>
- Herron, S., and Herron, M., 1996. Quantitative lithology: An application for open and cased hole spectroscopy. SPWLA 37th annual logging symposium.
- Hertzog, 1980. Laboratory and field evaluation of an inelastic neutron scattering and capture gamma ray spectrometry tool. SPE Journal, 20/5.
- Hornby, B.E., Johnson, D.L., Winkler, K.W., and Plumb, R.A., 1989. Fracture evaluation using reflected Stoneley-wave arrivals. Geophysics, 54(10):1274–1288. <https://doi.org/10.1190/1.1442587>
- Hu, B., Radke, J., Schlüter, H.-J., Heine, F.T., Zhou, L., Bernasconi, S.M., 2014. A modified procedure for gas-source isotope ratio mass spectrometry: the long-integration dual-inlet (LIDI) methodology and implications for clumped isotope measurements. Rapid Communications in Mass Spectrometry, 28(13):1413–1425.
- Imai N., Terashima S., Itoh S., Ando A., 1999. 1998 Compilation of analytical data for five GSJ geochemical reference samples: The “Instrumental Analysis Series” Geostandards Newsletter: The Journal of Geostandards and Geoanalysis, 23(2):223–250. <https://doi.org/10.1111/j.1751-908X.1999.tb00576.x>
- Jahn, U., Summons, R., Sturt, J., Grosjean, E., Huber, H., 2004. Composition of the lipids of Nanoarchaeum equitans and their origin from its host Ignicoccus sp. strain KIN4/I. Arch. Microbiol., 182:404–413.
- Jelínek, V., 1981. Characterization of the magnetic fabric of rocks. Tectonophysics, 79:63–67.
- Jochum, K.P., Weis, U., Stoll, B., Kuzmin, D., Yang, Q., Raczek, I., et al., 2011. Determination of reference values for NIST SRM 610–617 glasses following ISO guidelines. Geostandards and Geoanalytical Research, 35(4): 397–429.
- Jousselin, D., Nicolas, A., Boudier, F., 1998. Detailed mapping of a mantle diapir below a paleo-spreading center in the Oman ophiolite. J. Geophys. Res., 10(B8):18153–18170.
- Kallmeyer, J., Ferdelman, T.G., Weber, A., Fossing, H., and Jørgensen, B.B., 2004. A cold chromium distillation procedure for radiolabeled sulfide applied to sulfate reduction measurements. Limnol. Oceanogr. Methods, 2:171–180.
- Kelemen, P.B., Kikawa, E., Miller, D.J., et al., 2004. Proc. ODP, Init. Repts., 209: College Station, TX (Ocean Drilling Program). <https://doi.org/10.2973/odp.proc.ir.209.2004>
- Kelemen, P.B., Matter, J., Teagle, D.A.H., Abed, R., Ali Al Rajhi, A., Arai, S., et al., 2014. *Scientific Drilling in the Samail Ophiolite, Sultanate of Oman*. Proposal to the International Continental Scientific Drilling Program. [https://www.ldeo.columbia.edu/sites/default/files/uploaded/image/2014%20ICDP%20Oman%20Drilling%20Proposal\(1\).pdf](https://www.ldeo.columbia.edu/sites/default/files/uploaded/image/2014%20ICDP%20Oman%20Drilling%20Proposal(1).pdf)
- Kelemen, P.B., Rajhi, A.A., Godard, M., Ildefonse, B., Koepke, J., Macleod, C.J., Manning, C., Michibayashi, K., Nasir, S., Shock, E., Takazawa, E., and Teagle, D.A.H., 2013. Scientific drilling and related research in the Samail ophiolite, Sultanate of Oman. Scientific Drilling, 15:64–71. <https://doi.org/10.2204/iodp.sd.15.10.2013>
- Kirschvink, J.L., 1980. The least-squares line and plane and the analysis of palaeomagnetic data. Geophys. J. R. Astron. Soc., 62(3):699–718. <https://doi.org/10.1111/j.1365-246X.1980.tb02601.x>
- Krause, E.A., Beeler, S.R., Mors, R.A., Floyd, J.G., et al., 2018. Microscale biosignatures and abiotic mineral authigenesis in Little Hot Creek, California. Front. Microbiol., 9:997.
- Kubota, R., 2009. Simultaneous Determination of Total Carbon, Nitrogen, Hydrogen and Sulfur in Twenty-seven Geological Reference Materials by Elemental Analyser. Journal of Geostandards and Geoanalysis, 33(2):271–283.
- Lafuente, B., Downs, R.T., Yang, H., Stone, N., 2016. The power of databases: the RRUFF project. In Armbruster, T., and Danisi, R.M. (Eds.), Highlights in Mineralogical Crystallography: Berlin (Walter de Gruyter), 1–29.
- Le Maitre, R.W., 1989. A Classification of Igneous Rocks and Glossary of Terms: Oxford (IUGS, Blackwell).
- Le Maitre, R.W., Streckeisen, A., Zanettin, B., Le Bas, M.J., Bonin, B., Bateman, P., Bellieni, G., Dudek, A., Efremova, S., Keller, J., Lameyre, J., Sabine, P.A., Schmid, R., Sorensen, H., and Woolley, A.R. (Eds.), 2002. Igneous Rocks: A Classification and Glossary of Terms: Recommendations of the International Union of Geological Sciences Subcommittee on the Systematics of Igneous Rocks: Cambridge (Cambridge Univ. Press).
- Lever, M.A., Alpern, M., Engelen, B., Inagaki, F., Nakagawa, S., Steinsbu, B.O., and Teske, A., 2006. Trends in basalt and sediment core contamination during IODP Expedition 301. Geomicrobiology Journal, 23(7):517–530. <https://doi.org/10.1080/01490450600897245>
- Lever, M.A., Torti, A., Eickenbusch, P., Michaud, A.B., Santl-Temkiv, T., and Jørgensen, B.B., 2015. A modular method for the extraction of DNA and RNA, and the separation of DNA pools from diverse environmental sample types. Frontiers in Microbiology, 6:476. <https://doi.org/10.3389/fmicb.2015.00476>
- Lurcock, P.C., and Wilson, G.S., 2012. PuffinPlot: A versatile, user-friendly program for paleomagnetic analysis. Geochemistry, Geophysics, Geosystems, 13(Q06Z45).
- Luyendyk, B.P., and Day, R., 1982. Paleomagnetism of the Samail ophiolite, Oman 2. The Wadi Kadir gabbro section. J. Geophys. Res., 87:10903–10917.
- Luyendyk, B.P., Laws, B.R., Day, R., Collinson, T., 1982. Paleomagnetism of the Samail ophiolite, Oman 1. The sheeted dike complex at Ibra. J. Geophys. Res., 87:10883–10902.
- MacLeod, C.J., Dick, H.J.B., Blum, P., and the Expedition 360 Scientists, 2017a. Southwest Indian Ridge Lower Crust and Moho. Proceedings of the International Ocean Discovery Program, 360: College Station, TX (International Ocean Discovery Program). <https://doi.org/10.14379/iodp.proc.360.2017>
- MacLeod, C.J., Dick, H.J.B., Blum, P., Abe, N., Blackman, D.K., Bowles, J.A., Cheadle, M.J., et al., 2017b. Expedition 360 methods. In MacLeod, C.J., Dick, H.J.B., Blum, P., and the Expedition 360 Scientists, Southwest Indian Ridge Lower Crust and Moho. Proceedings of the International Ocean Discovery Program, 360: College Station, TX (International Ocean Discovery Program). <https://doi.org/10.14379/iodp.proc.360.102.2017>
- Martel, S.J., 1999. Analysis of fracture orientation data from boreholes. Environmental and Engineering Geoscience, 5(0):213–233.

- McDonough, W.F., and Sun, S.S., 1995. The composition of the Earth. *Chemical Geology*, 120(3-4):223-253.
- Meckler, A.N., Ziegler, M., Millán, M.I., Breitenbach, S.F., Bernasconi, S.M., 2014. Long-term performance of the Kiel carbonate device with a new correction scheme for clumped isotope measurements *Rapid Communications in Mass Spectrometry*, 28(15):1705-1715.
- Mees, F., Swennen, R., Van Geet, M., Jacobs, P., 2003. Application of X-ray computed tomography in the geoscience. *Geol. Soc. London, Spec. Publ.*, 215:7-22.
- Morris, A., Meyer, M., Anderson, M.W., MacLeod, C.J., 2016. Clockwise rotation of the entire Oman ophiolite occurred in a suprasubduction zone setting. *Geology*, 44(12):1055-1058.
- Müller, I.A., Fernandez, A., Radke, J., van Dijk, J., Bowen, D., Schwieters, J., Bernasconi, S.M., 2017. Carbonate clumped isotope analyses with the long-integration dual-inlet (LIDI) workflow: scratching at the lower sample weight boundaries. *Rapid Communications in Mass Spectrometry*, 31(2):1057-1066.
- Nakano, T., Nakashima, Y., Nakamura, K., Ikeda, S., 2000. Observation and analysis of internal structure of rock using X-ray CT. *Jour. Soc. Japan*, 106(5):363-378.
- Newmark, R.L., Anderson, R.N., Moos, D., and Zoback, M.D., 1985. Sonic and ultrasonic logging of Hole 504B and its implications for the structure, porosity and stress regime of the upper 1 km of the oceanic crust. In Anderson, R.N., Honnorez, J., Becker, K., et al., *Init. Repts. DSDP, 83: Washington (U.S. Govt. Printing Office)*, 479-510.
- Nicolas, A., Boudier, F., and Ildefonse, B., 1996. Variable crustal thickness in the Oman ophiolite: implication for oceanic crust. *Geophys. Res.*, 101(B8):17941-17950. <https://doi.org/10.1029/96JB00195>
- Nicolas, A., Boudier, F., Ildefonse, B., Balle, E., 2000. Accretion of Oman and United Arab Emirates ophiolite—discussion of a new structural map. *Mar. Geophys. Res.*, 21(3-4):147-179.
- Norrish, K., and Hutton, J.T., 1969. An accurate X-ray spectrographic method for analysis of a wide range of geological materials. *Geochem. Cosmochim. Acta*, 33:431-453.
- Noufel, A., Gernay, C., Lhomme, T., Hegazy, G., and Richard, T., 2015. Enhanced core analysis workflow for the geomechanical characterization of reservoirs in a giant offshore field, Abu Dhabi. *SPE 177520412-MS*.
- Pallister, J.S., Hopson, C.A., 1981. Samail Ophiolite plutonic suite: Field relations, phase variation, cryptic variation and layering, and a model of a spreading ridge magma chamber. *J. Geophys. Res.*, 86:2593-2644.
- Parada, A., Needham, D.M., Fuhrman, J.A., 2016. Every base matters: assessing small subunit rRNA primers for marine microbiomes with mock communities, time-series and global field samples. *Environ. Microbiol.* 18:1403-1414.
- Passchier, C.W., and Trouw, R.A.J., 1996. *Microtectonics*: Berlin (Springer-Verlag).
- Passchier, C.W., and Trouw, R.A.J., 2005. *Microtectonics* (2nd ed.): Berlin (Springer).
- Pelkey, S.M., Mustard, J.F., Murchie, S., Clancy, R.T., Wolff, M., Smith, M., Milliken, R., Bibring, J.-P., Gendrin, A., Poulet, F., Langevin, Y., and Gondet, B., 2007. CRISM multispectral summary products: parameterizing mineral diversity on Mars from reflectance. *J. Geophys. Res.*, 112(18).
- Pemper, R.R., Han, X., Mendez, F.E., Jacobi, D., LeCompte, B., Bratovich, M., Feuerbacher, F., Gruner, M., Bliven, S., 2009. The direct measurement of carbon in wells containing oil and natural gas using a pulsed neutron mineralogy tool. *SPE ATCE 1242334*.
- Peters, D., and Pettke, T., 2017. Evaluation of Major to Ultra Trace Element Bulk Rock Chemical Analysis of Nanoparticulate Pressed Powder Pellets by LA-ICP-MS. *Geostandards and Geoanalytical Research*, 41(1):5-28.
- Pieters, C.M., Goswami, J.N., Clark, R.N., Annadurai, M., Boardman, J., Buratti, B., Combe, J.-P., Dyar, M.D., Green, R., Head, J.W., Hibbitts, C., Hicks, M., Isaacson, P., Klima, R., et al., 2009. Character and spatial distribution of OH/H₂O on the surface of the Moon seen by M3 on Chandrayaan-1. *Science*, 326:568-572. <https://doi.org/10.1126/science.1178658>.
- Radtke, R.J., Lorente, M., and Aldolph, B., 2012. A new capture and inelastic spectroscopy tool takes geochemical logging to the next level. *SPWLA 53rd annual logging symposium*.
- Ramsay, J.G., and Huber, M.I., 1987. *The Techniques of Modern Structural Geology (Vol. 2): Folds and Fractures*: New York (Academic Press).
- Rempfert, K.R., Miller, H.M., Bompard, N., Nothaft, D., Matter, J.M., Kelemen, P., Fierer, N., and Templeton, A.S., 2017. Geological and Geochemical Controls on Subsurface Microbial Life in the Samail Ophiolite, Oman. *Front. Microbiol.*, 8. <https://www.frontiersin.org/articles/10.3389/fmicb.2017.00056/full> [Accessed 8 August 2018].
- Reynolds, R.C., 1963. Matrix corrections in trace elements by X-ray fluorescence estimation of mass absorption coefficient by Compton scattering. *Am. Min.*, 48:1133-1143.
- Richter, T.O., van der Gaast, S., Koster, B., Vaars, A., Gieles, R., de Stigter, H.C., De Haas, H., van Weering, T.C.E., 2006. The Avaatech XRF Core Scanner: technical description and applications to NE Atlantic sediments. In Rothwell, R.G. (Ed.), *New Techniques in Sediment Core Analysis*. *Geol. Soc. (Lond.) Spec. Publ.*, 267(1):39-50. <https://doi.org/10.1144/GSL.SP.2006.267.01.03>
- Rickard, D., and Morse, J.W., 2005. Acid volatile sulfide (AVS). *Marine Chemistry*, 97(3-4):141-197.
- Rider, M.H., 1996. *The Geological Interpretation of Well Logs* (2nd ed.): Caithness (Whittles Publ.).
- Rospabé, M., Benoit, M., and Candaudap, F., 2018. Determination of Trace Element Mass Fractions in Ultramafic Rocks by HR-ICP-MS: A Combined Approach Using a Direct Digestion/Dilution Method and Preconcentration by Coprecipitation. *Geostandards and Geoanalytical Research*, 42(1):115-129.
- Røy, H., Weber, H.S., Tarpgaard, I.H., Ferdelman, T.G., and Jørgensen, B.B., 2014. Determination of dissimilatory sulfate reduction rates in marine sediment via radioactive ³⁵S tracer. *Limnol. Oceanogr. Methods*, 12:196-211.
- Sakamoto, T., Kuroki, K., Sugawara, T., Aoike, K., Iijima, K., and Sugisaki, S., 2006. Non-destructive X-ray fluores-

- cence (XRF) core-imaging scanner, TATSCAN-F2. *Sci. Drill.*, 2:37–39.
- Schlumberger, 1989. Log Interpretation Principles/Applications: Houston (Schlumberger Educ. Serv.), SMP-7017.
- Schlumberger, 2013. FMI-HD: High-definition formation microimager. 13-FE-0025.
- Schubotz, F., Hays, L.E., Meyer-Dombard, D.R., Gillespie, A., Sock, E.L., Summons, R.E., 2015. Stable isotope labeling confirms mixotrophic nature of streamer biofilm communities at alkaline hot springs. *Front. Microbiol.*, 6:42.
- Schwarzenbach, E.M., Früh-Green, G., Bernasconi, S.M., Alt, J.C., Plasa, A., 2013. Serpentinization and carbon sequestration: a study of two ancient peridotite-hosted hydrothermal systems. *Chemical Geology*, 351:115–133.
- Senda, R., Kimura, J.-I., and Chang, Q., 2014. Evaluation of a rapid, effective sample digestion method for trace element analysis of granitoid samples containing acid-resistant minerals: Alkali fusion after acid digestion. *Geochem. J.*, 48(1):99–103.
- Serra, O., 1984. Fundamentals of Well-Log Interpretation (Vol. 1): The Acquisition of Logging Data: Amsterdam (Elsevier).
- Serra, O., 1986. Fundamentals of Well-Log Interpretation (Vol. 2): The Interpretation of Logging Data. Amsterdam (Elsevier).
- Shipboard Scientific Party, 1989. Introduction and explanatory notes. In Robinson, P.T., Von Herzen, R., et al., *Proc. ODP, Init. Repts.*, 118: College Station, TX (Ocean Drilling Program), 3–23. <https://doi.org/10.2973/odp.proc.ir.118.101.1989>
- Shipboard Scientific Party, 1991. Explanatory notes. In Taira, A., Hill, I., Firth, J.V., et al., *Proc. ODP, Init. Repts.*, 131: College Station, TX (Ocean Drilling Program), 25–60. <https://doi.org/10.2973/odp.proc.ir.131.104.1991>
- Shipboard Scientific Party, 1992a. Explanatory notes. In Behrmann, J.H., Lewis, S.D., Musgrave, R.J., et al., *Proc. ODP, Init. Repts.*, 141: College Station, TX (Ocean Drilling Program), 37–71. <https://doi.org/10.2973/odp.proc.ir.141.105.1992>
- Shipboard Scientific Party, 1992b. Explanatory notes. In Dick, H.J.B., Erzinger, J., Stokking, L.B., et al., *Proc. ODP, Init. Repts.*, 140: College Station, TX (Ocean Drilling Program), 5–33. <https://doi.org/10.2973/odp.proc.ir.140.101.1992>
- Shipboard Scientific Party, 1992c. Explanatory notes. In Parson, L., Hawkins, J., Allan, J., et al., *Proc. ODP, Init. Repts.*, 135: College Station, TX (Ocean Drilling Program), 49–79. <https://doi.org/10.2973/odp.proc.ir.135.102.1992>
- Shipboard Scientific Party, 1993a. Explanatory notes. In Alt, J.C., Kinoshita, H., Stokking, L.B., et al., *Proc. ODP, Init. Repts.*, 148: College Station, TX (Ocean Drilling Program), 5–24. <https://doi.org/10.2973/odp.proc.ir.148.101.1993>
- Shipboard Scientific Party, 1993b. Explanatory notes. In Gillis, K., Mével, C., Allan, J., et al., *Proc. ODP, Init. Repts.*, 147: College Station, TX (Ocean Drilling Program), 15–42. <https://doi.org/10.2973/odp.proc.ir.147.102.1993>
- Shipboard Scientific Party, 1995. Explanatory notes. In Cannat, M., Karson, J.A., Miller, D.J., et al., *Proc. ODP, Init. Repts.*, 153: College Station, TX (Ocean Drilling Program), 15–42. <https://doi.org/10.2973/odp.proc.ir.153.10X.1995>
- Shipboard Scientific Party, 1999. Site 735. In Dick, H.J.B., Natland, J.H., Miller, D.J., et al., *Proc. ODP, Init. Repts.*, 176: College Station, TX (Ocean Drilling Program), 1–314. <https://doi.org/10.2973/odp.proc.ir.176.103.1999>
- Shipboard Scientific Party, 2003. Explanatory notes. In Wilson, D.S., Teagle, D.A.H., Acton, G.D., *Proc. ODP, Init. Repts.*, 206: College Station, TX (Ocean Drilling Program), 1–94. <https://doi.org/10.2973/odp.proc.ir.206.102.2003>
- Shipboard Scientific Party, 2004. Explanatory notes. In Kelemen, P.B., Kikawa, E., Miller, D.J., et al., *Proc. ODP, Init. Repts.*, 209: College Station, TX (Ocean Drilling Program), 1–75. <https://doi.org/10.2973/odp.proc.ir.209.102.2004>
- Sibson, R.H., 1977. Fault rocks and fault mechanisms. *Journal of the Geological Society*, 133:191–213. <https://doi.org/10.1144/gsjgs.133.3.0191>
- Siivola, J., and Schmid, R., 2007. List of mineral abbreviations: Cambridge (Cambridge Univ. Press).
- Streckeisen, A., 1974. Classification and nomenclature of plutonic rocks recommendations of the IUGS subcommission on the systematics of igneous rocks. *Geol. Rundsch.*, 63(2):773–786. <https://doi.org/10.1007/BF01820841>
- Streit, E., Kelemen, P., Eiler, J., 2012. Coexisting serpentine and quartz from carbonate-bearing serpentinized peridotite in the Samail ophiolite, Oman. *Contrib. Mineral. Petrol.*, 164(5):821–837.
- Teagle, D.A.H., Alt, J.C., Umino, S., Miyashita, S., Banerjee, N.R., Wilson, D.S., and Expedition 309/312 Scientists, 2006. *Proc. IODP, 309/312*: Washington, DC (Integrated Ocean Drilling Program Management International, Inc.). <https://doi.org/10.2204/iodp.proc.309312.2006>
- Teagle, D.A.H., Ildefonse, B., Blum, P., and the Expedition 335 Scientists, 2012. *Proc. IODP, 335*: Tokyo (Integrated Ocean Drilling Program Management International, Inc.). <https://doi.org/10.2204/iodp.proc.335.2012>
- Terashima, S., Taniguchi, M., Mikoshiba, M., Imai, N., 1998. Preparation of two new GSJ geochemical reference materials: Basalt JB-1b and coal fly ash JCFA-1. *Geostandards Newsletter: The Journal of Geostandards and Geoanalysis*, 22(1):113–117. <https://doi.org/10.1111/j.1751-908X.1998.tb00550.x>
- Twiss, R.J., and Moores, E.M., 1992. *Structural Geology*: New York (Freeman).
- Vance, D., Little, S.H., Archer, C., Cameron, V., Anderson, M.B., Rijkenberg, M.J.A., Lyons, T.W., 2016. The oceanic budgets of nickel and zinc isotopes: the importance of sulfidic environments as illustrated by the Black Sea. *Phil. Trans. Royal Soc. A: Mathematical, Physical, and Engineering Sciences*, 374(2081).

- Weatherburn, M.W., 1967. Urease-Berthelot colorimetric method for in vitro determination of urea. *Analytical Chemistry*, 39:971-974.
- Weigand, M.A., Foriel, J., Barnett, B., Oleynik, S., Sigman, D.M., 2016. Updates to instrumentation and protocols for isotopic analysis of nitrate by the denitrifier method. *Rapid Communications in Mass Spectrometry*, 30(12):1365-1383.
- Weiler, P.D., 2000. Differential rotations in the Oman Ophiolite: Paleomagnetic evidence from the southern massifs. *Marine Geophysical Researches*, 21:195-210.
- Welander, P.V., Doughty, D.M., Wu, C.H., Mehay, S., Summons, R.E., Newman, D.K., 2012. Identification and characterization of *Rhodopseudomonas palustris* TIE-1 hopanoid biosynthesis mutants. *Geobiol.*, 10:163-177.
- Whitney, D.L., and Evans, B.W., 2010. Abbreviations for names of rock-forming minerals. *American Mineralogist*, 95:185–187.
- Wormer, L., Lipp, J.S., Hinrichs, K.U., 2015. Comprehensive analysis of microbial lipids in environmental samples through HPLC-MS protocols. In McGenity, T., Timmis, K., Nogales, B. (Eds.), *Hydrocarbon and Lipid Microbiology Protocols*: Berlin (Springer).

Figure F1. Diagram illustrating curation concepts for cores and sections for the Oman Drilling Project.

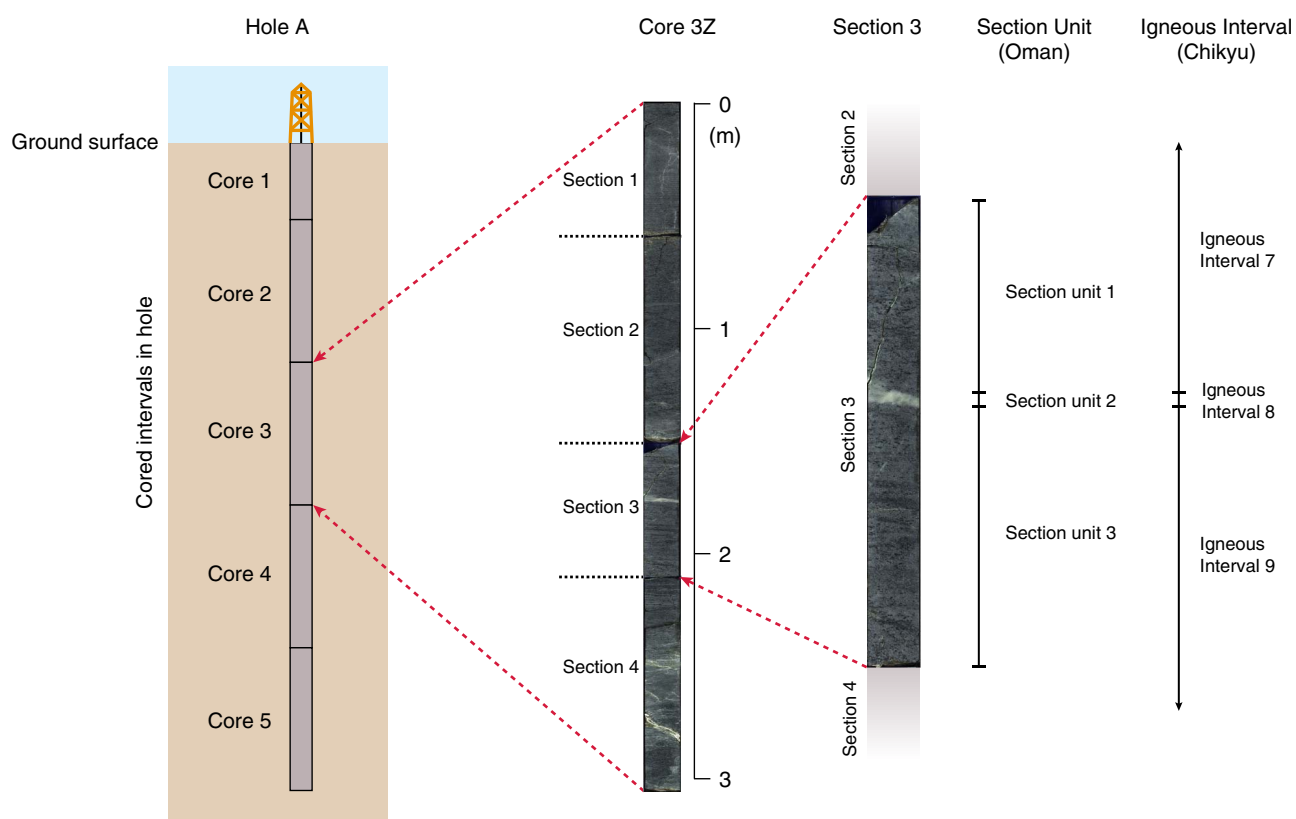


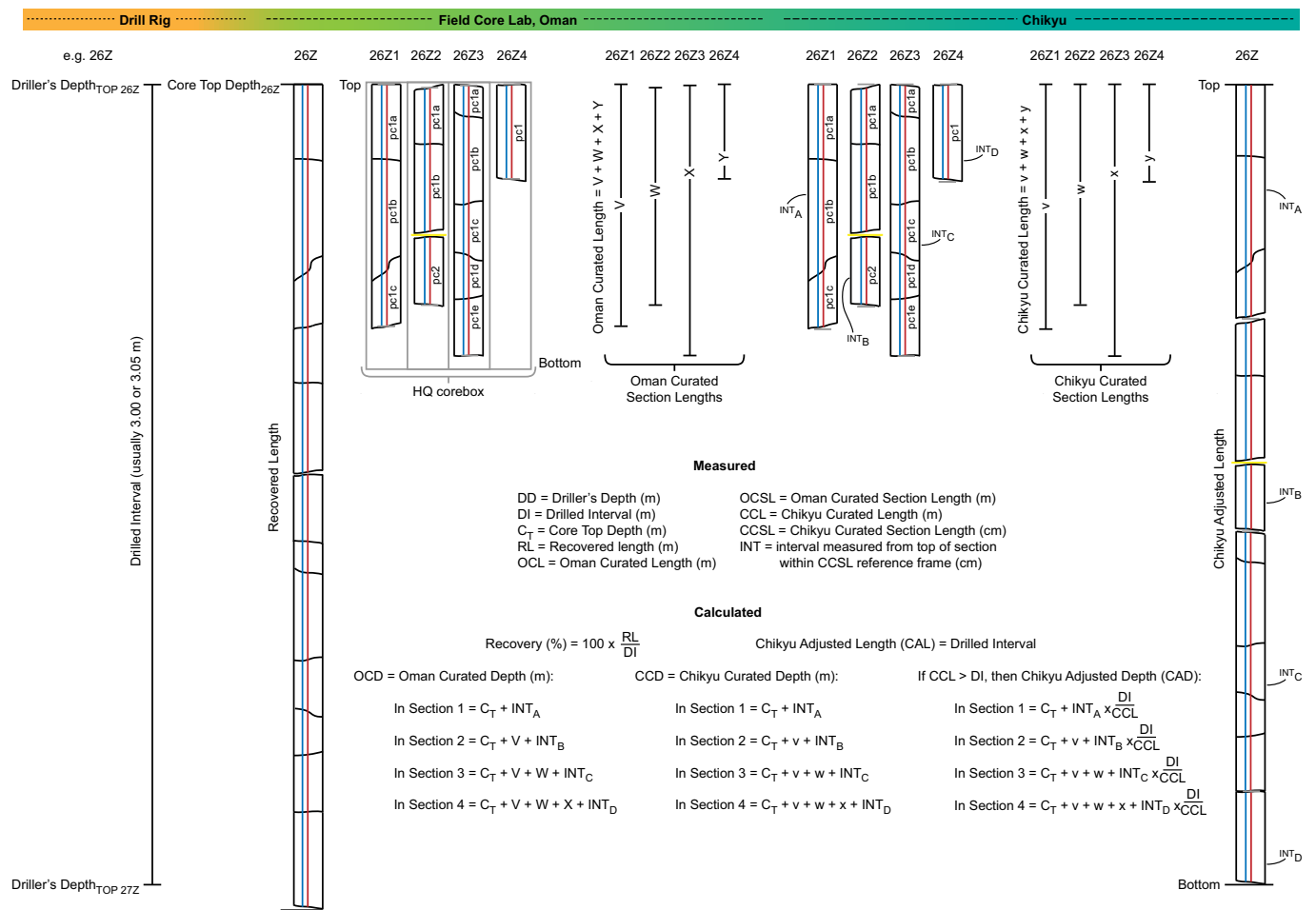
Figure F2. Definition of Oman Drilling Project and ChikyuOman curatorial core length scales (see [Depth computations](#)).

Figure F3. Examples of (A) core and (B) section curation interfaces, (C) Section_Unit rock type description, and (D) sample interface of the ICDP DIS curation system used on the OmanDP Phase 1 diamond coring drill sites.

A CORE SECTION

Expedition: OmanDP Site: 2 Hole: A [recalculate depths of sections](#) [DIS](#) **CORE - Input**

Core: 144 Core Type: Advanced Diamond Core B Top Depth (m): 383.70 Drilled Length (m): 3.05
 Section Count: 4 Core Catcher?: no Curator: SM Core On Deck: dd-mm-yyyy hh:mm 17-Jan-2017 08:11
 Core Recovery (m): 3.08 Core Recovery (%): 100.98 Bottom Depth (m): 386.75 MCD Offset [m]: 0.00 Top MCD: 383.70
 Core Oriented?: no Diameter (mm): 47.6 Comments: cont. 143-4 to 144-1
 IGSN: ICDP5057EC35001

Core	T-Depth	B-Depth	Recovery	Rec.PC	D-Length	Sections	CC	Curator	Oriented	Temp.	Remarks
1432	380.65	383.7	3.08	100.98	3.05	4	no	SM	no		cont. 142-4 to 143-1
1442	383.7	386.75	3.08	100.98	3.05	4	no	SM	no		cont. 143-4 to 144-1
1452	386.75	389.8	3.06	100.33	3.05	4	no	SM	no		cont. 144-4 to 145-1
1462	389.8	392.05	2.94	96.39	3.05	4	no	SM	no		cont. 145-4 to 146-1
1472	392.05	395.9	3.23	105.9	3.05	4	no	SM	no		cont. 146-4 to 147-1
1482	395.9	398.95	3.07	100.66	3.05	4	no	SM	no		
1492	398.95	402	3.08	100.98	3.05	4	no	SM	no		
1502	402	404.3	1.91	83.04	2.3	3	no	SM	no		
1512	404.3	406.6	2.43	105.65	2.3	3	no	SM	no		

B CORE SECTION

Expedition: OmanDP Site: 2 Hole: A Core: 144 Type: Z [recalculate depths of sections](#) [DIS](#) **SECTION - Input**

Section: 3 Sec. Length (m): 0.8 Curator: SM Core Catcher: no
 Core Box: 114 Slot: 2 Position in Box: M Number of Pieces: 1
 Curated Length (m): 0.8 Top Depth (m): 385.04 Bottom Depth (m): 385.84 Top MCD: 385.04
 Comments: cont. 144-4. pc1a-d, b in bag IGSN: ICDP5057ES06IU2
[open cores / sections report](#)

Core	Section	T-Depth	B-Depth	Sec. Length	Cur. Length	Operator	Remarks
1442	1	383.7	384.37	0.67	0.67	SM	cont. 144-2. pc1a-d
1442	2	384.37	385.04	0.67	0.67	SM	cont. 144-3. pc1
1442	3	385.04	385.84	0.8	0.8	SM	cont. 144-4. pc1a-d, b in bag
1442	4	385.84	386.78	0.94	0.94	SM	cont. 145-1. pc1a-e

C SECTION UNIT

Expedition: OmanDP Site: 1 Hole: A Core: 156 Section: 2 **SECTION UNIT - DESCRIPTION**

Geologist 1: Michelle Harris Geologist 2: Gretchen Fruh-Green Geologist 3:
 Section Unit: 1 Top Of Unit In Section (cm): 0 Top Depth (m): 402.5 Top (mcd): 402.5 # of Pieces:
 Rock Class: OPHIO Rock Type: Gabbro Descriptor: Layered VCD-File: [Open](#) [Link](#)
 Rock Type Comments: 2.4mm grain size, oliv bearing, variable distribution, more oliv rich at base
 Top Contact Type: Grain size or modal Bottom Contact Type:
 Alteration Intensity: High / extensive Alteration Intensity: Pinkish grey green bkgd altn, oliv altered black, plag variably altered grey green, milky white in halos
 Vein Intensity (veins > 1mm): <1mm discontinuous chlorite veins, Network of subparallel grey green veins at 3-10cm giving banded appearance, 1mm thick milky white veins, variably oriented, Comments: <99.25%
 Structural Features: Moderately dipping foliation defined by plagioclase
 Composite Description for NN

Core	Sec.	Unit	Top	Unit Class	Unit Type	Foliation	Colo...	Colo...	Grai...	Grai...	Dist...	Disc...	Text...	Co
155	3	1	400.52	OPHIO	Gabbro								Lay...	
155	4	1	401.11	OPHIO	Gabbro								Lay...	
155	4	2	401.58	OPHIO	Olivine gabbro								Lay...	
156	1	1	401.9	OPHIO	Olivine gabbro								Lay...	
156	2	1	402.5	OPHIO	Gabbro								Lay...	

D SAMPLE SUB SAMPLES

Expedition: OmanDP Site: 1 Hole: A [Report](#) **SAMPLE - Input**

Repository: Request: Part: Type: Series: Which Sample Observer: Core: Section: Half: Section Depth Top (cm): Bot (cm): Vol (cc):
 DRI OMAN0001 A R_TS Undefined core NB 156 2 W 30 35 80

Comments: Top (m): 402.6 Top MCD (m): 402.6 IGSN: ICDP5057EXL270

Sample	Request	Part	Code	Exp.	Site	Hole	Mat...	La...	H...	Top	Bottom	Vol.	Curator
9179	OMAN0001	A	R_TS	5057	1	A	CO	11...	W	63	68	80	MH
9180	OMAN0001	A	R_TS	5057	1	A	CO	12...	W	68	72	80	MH
9181	OMAN0001	A	R_TS	5057	1	A	CO	12...	W	15.5	20.5	80	MH
9182	OMAN0001	A	R_TS	5057	1	A	CO	13...	W	5	10	80	JC
9183	OMAN0001	A	R_TS	5057	1	A	CO	14...	W	53	58	80	NB
9184	OMAN0001	A	R_TS	5057	1	A	CO	14...	W	46	51	80	NB
9185	OMAN0001	A	R_TS	5057	1	A	CO	15...	W	30	35	80	NB

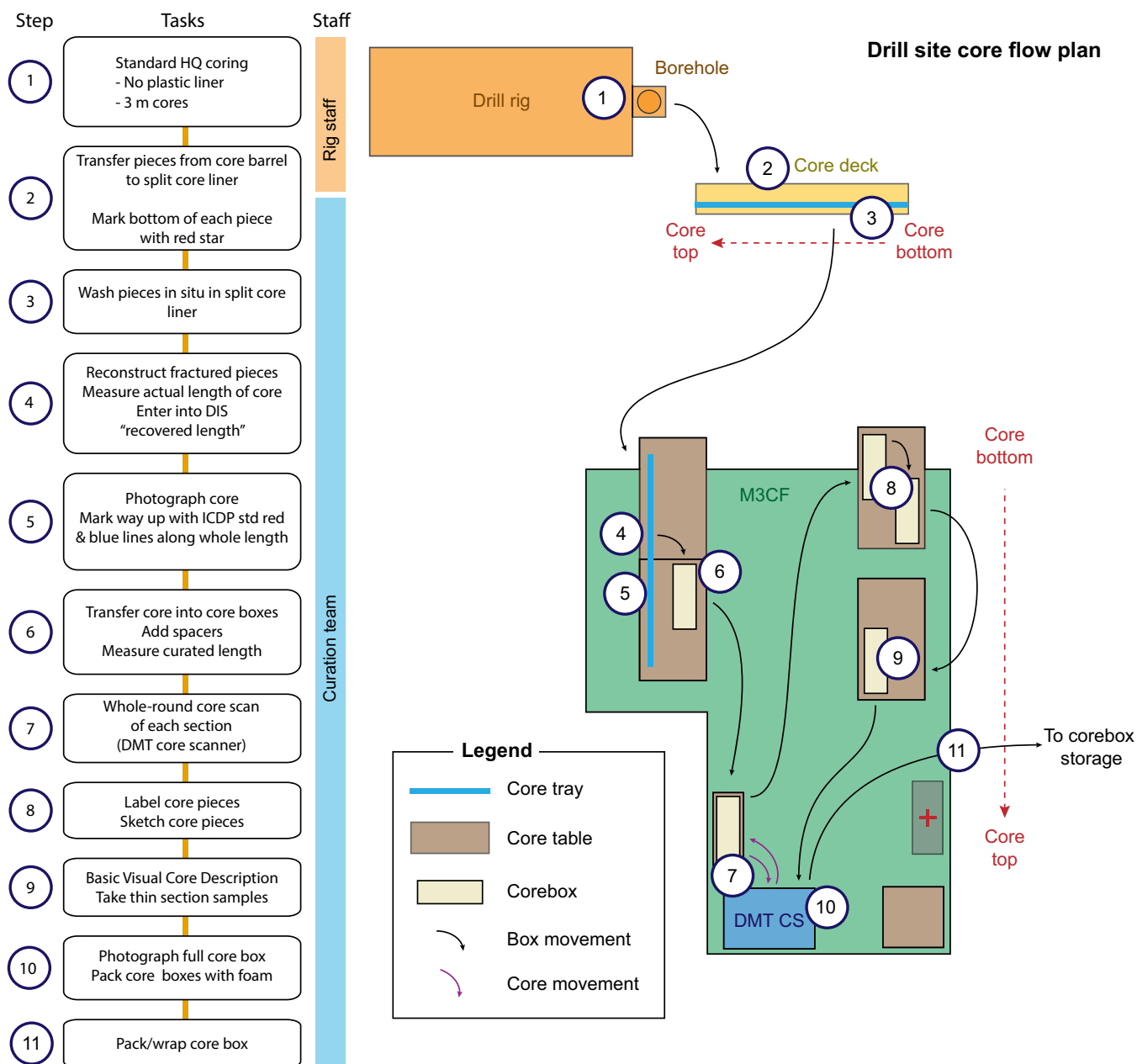
Figure F4. Drill site core flow for the diamond coring sites of Phase 1 of the OmanDP.

Figure F5. Core reference frame for structural and paleomagnetic orientation measurements used during the OmanDP ChikyUOman core description campaign (modified from Expedition 335 Scientists, 2012b, and MacLeod et al., 2017b). **A.** Primary orientation of each core piece is up and down along the core axis. **B.** Coordinates in both archive and working section halves. **C.** Conventions for labeling samples and thin sections taken from working section half.

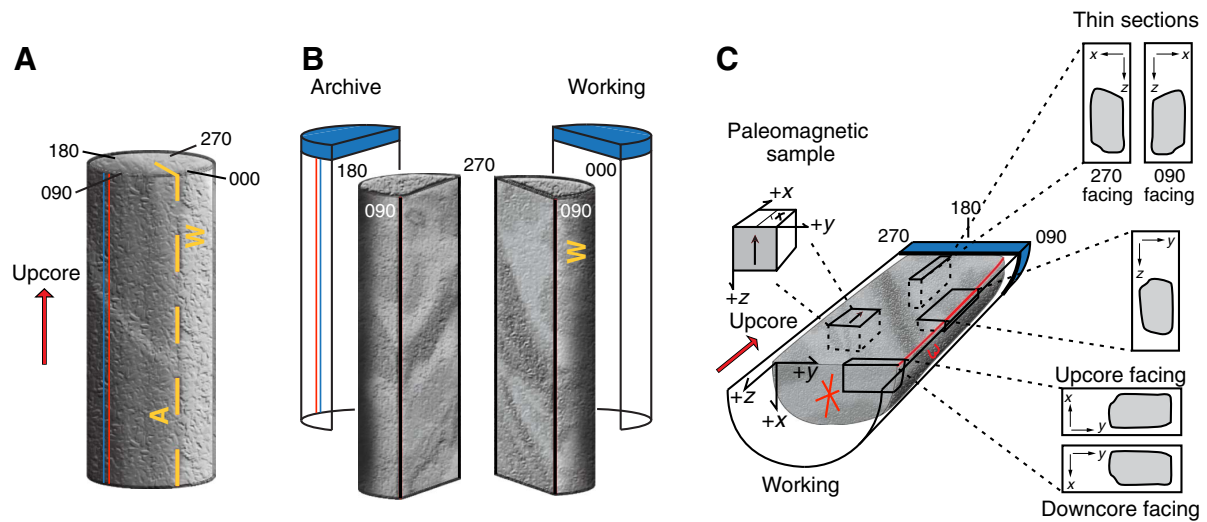


Figure F6. (A) DMT360 TM core scanner used for the OmanDP, (B) 360° unrolled image of nice core, and (C) image of core box with color balance chart.

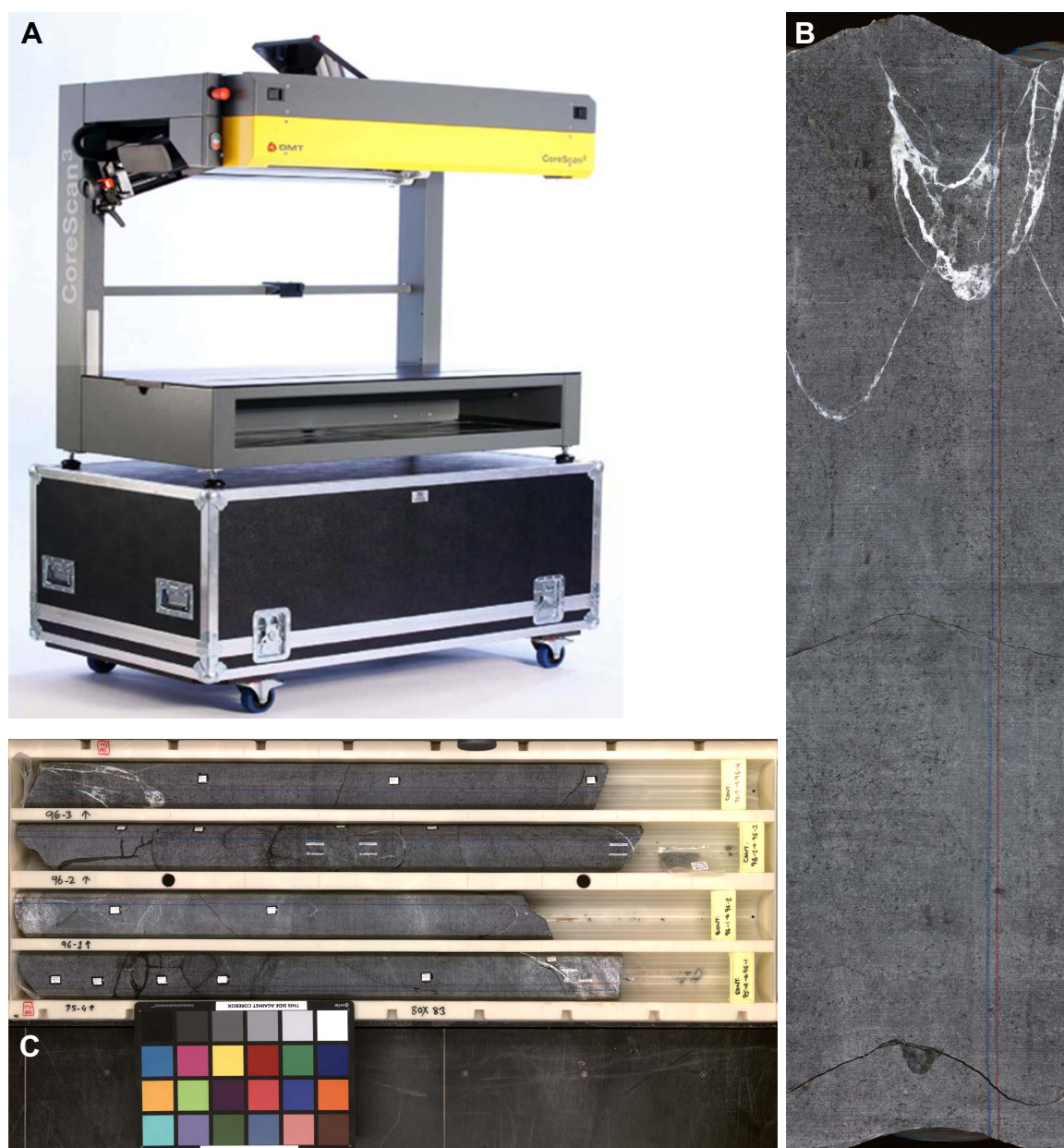


Figure F7. Example for the IGSN assignment for holes, core runs, core sections, and core samples by the ICDP DIS. Due to the relational data model in DIS the derived naming convention guarantees the uniqueness of each object within an ICDP expedition. Beginning with hole, any type of sample material can be assigned an IGSN using the following structure. ICDP is a registered IGSN name space, and 5057 is the expedition identifier for the OmanDP, E is the default report prefix, and the object tag (H = hole, C = core, S = section, X = sample) indicates the type of sample material followed by a unique 5-character coded pattern.

Regional data model in DIS	Data values	Naming convention	IGSN
<pre> graph BT PROGRAM -- "1 to n" --> EXPEDITION EXPEDITION -- "1 to n" --> SITE SITE -- "1 to n" --> HOLE HOLE -- "1 to n" --> CORE CORE -- "1 to n" --> SECTION SECTION -- "1 to n" --> SAMPLE </pre>	ICDP		
	5057	5057	
	1	5057_1	
	A	5057_1_A	ICDP5057EH62001
	149 Z	5057_1_A_149_Z	ICDP5057ECP9001
	4	5057_1_A_149_Z_4	ICDP5057ES84JU2
	46-51	5057_1_A_149_Z_4,46-51	ICDP5057EXK270

Figure F8. Photograph of rack of core cuttings from Hole BA1.



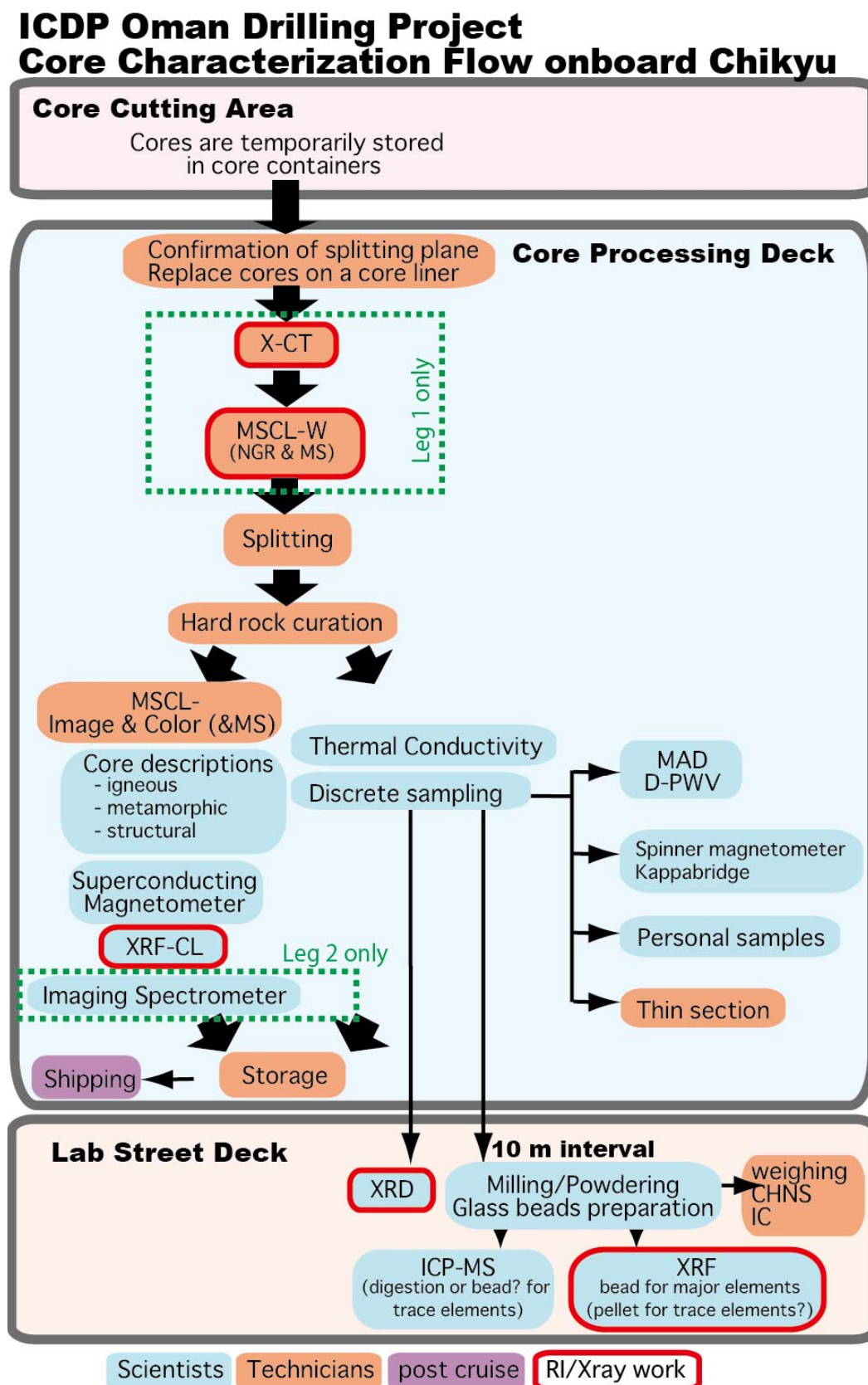
Figure F9. Core flow aboard *Chikyu* during the Oman Drilling Project.

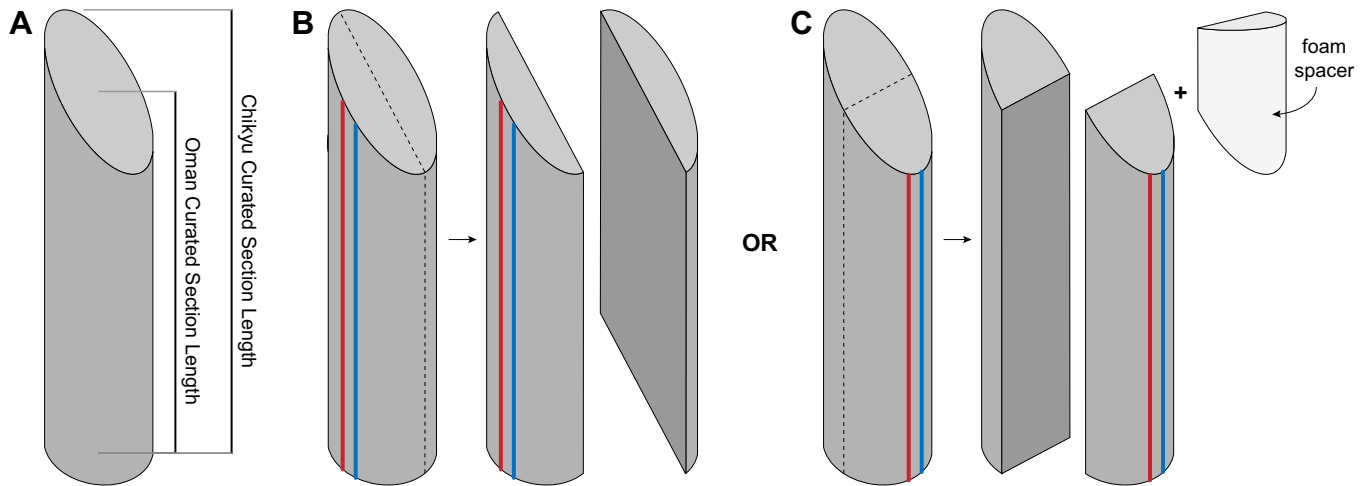
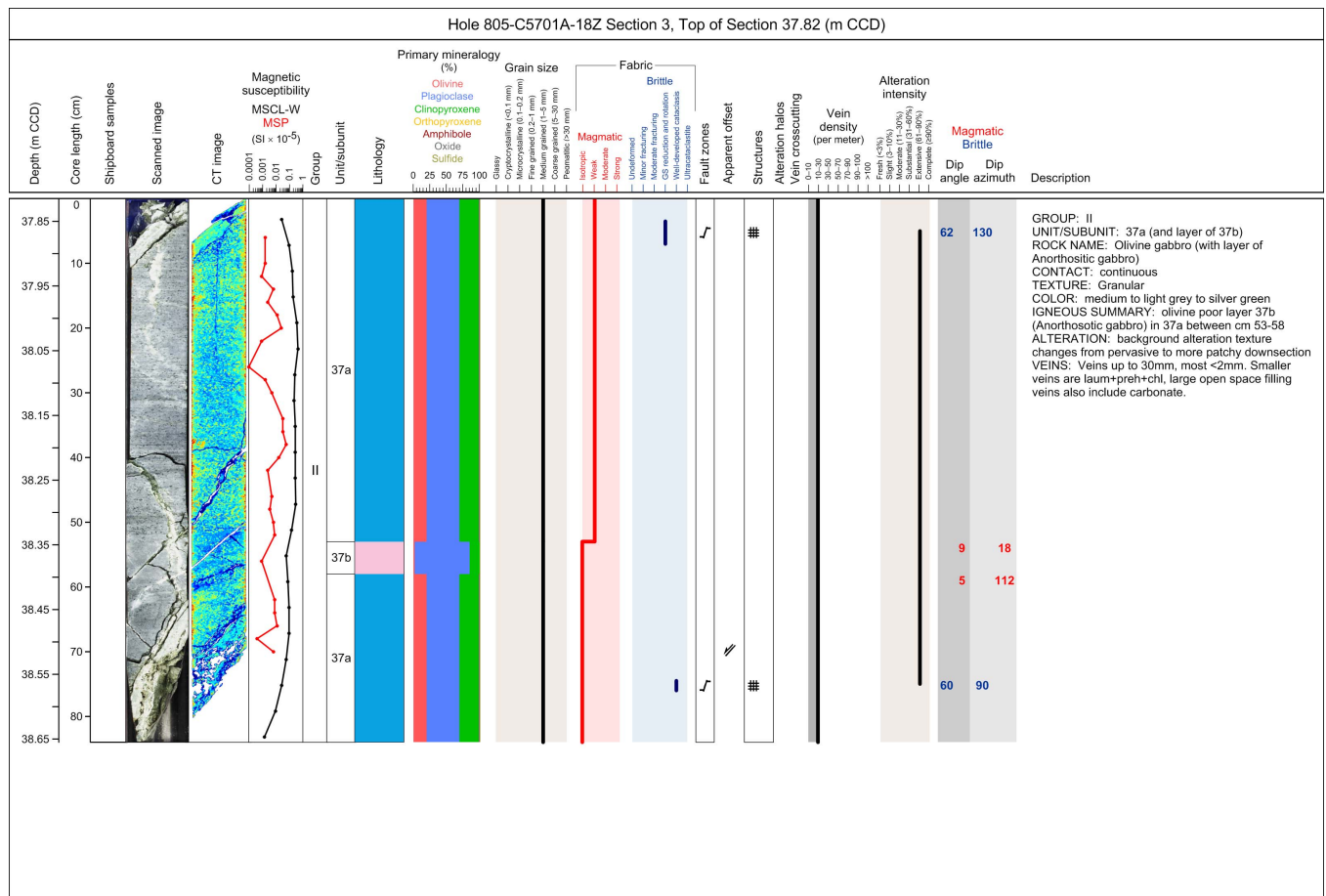
Figure F10. A–C. Use of foam core spacer to indicate gap in a section.**Figure F11.** Example of core section graphic summary (VCD) for the Gabbro-Traverse drill sites of the Oman Drilling Project.

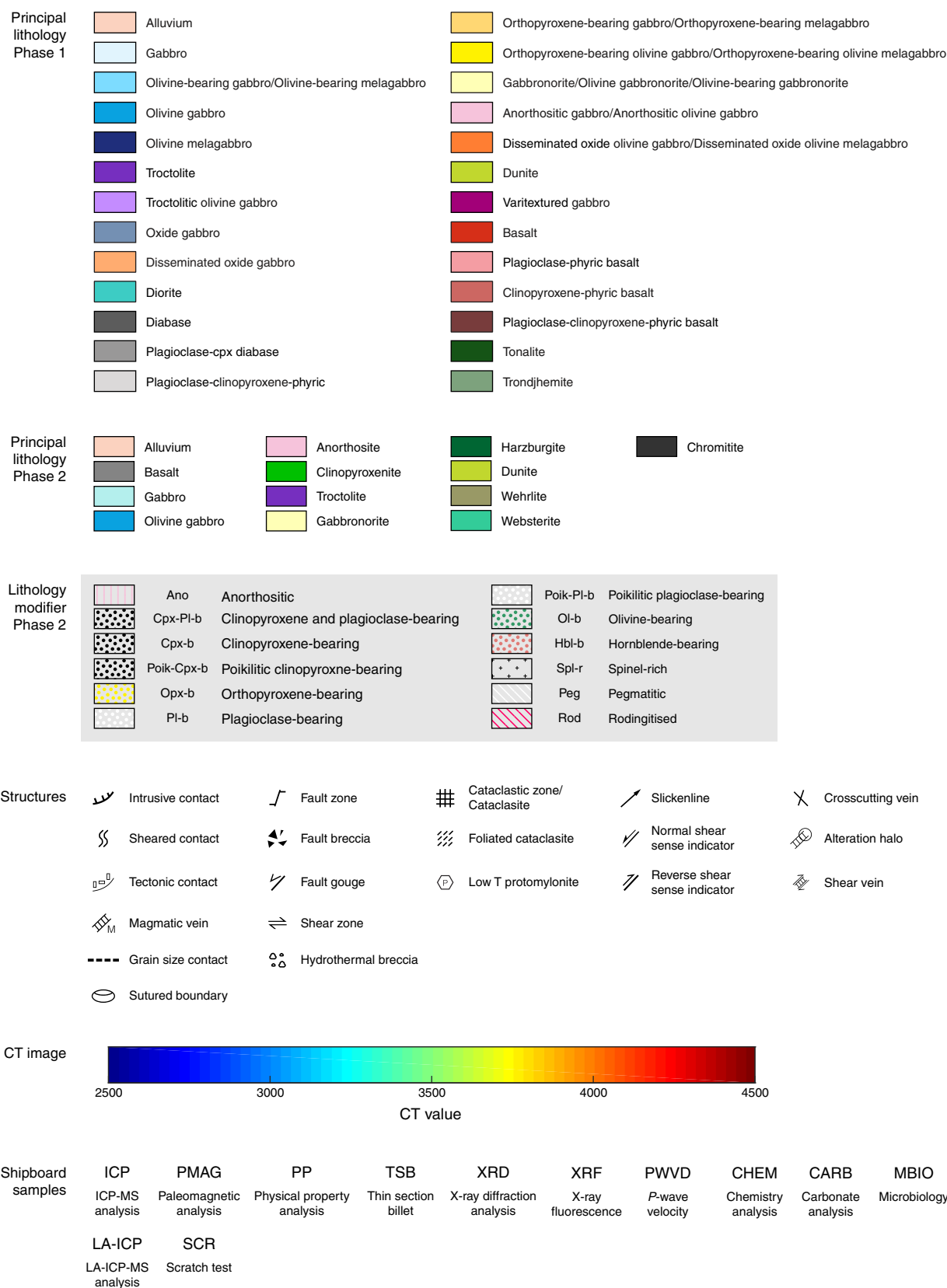
Figure F12. Symbols and abbreviations used in the graphical section summaries (VCD) during OmanDP ChikyuOman Phase 1 and Phase 2 detailed core description.

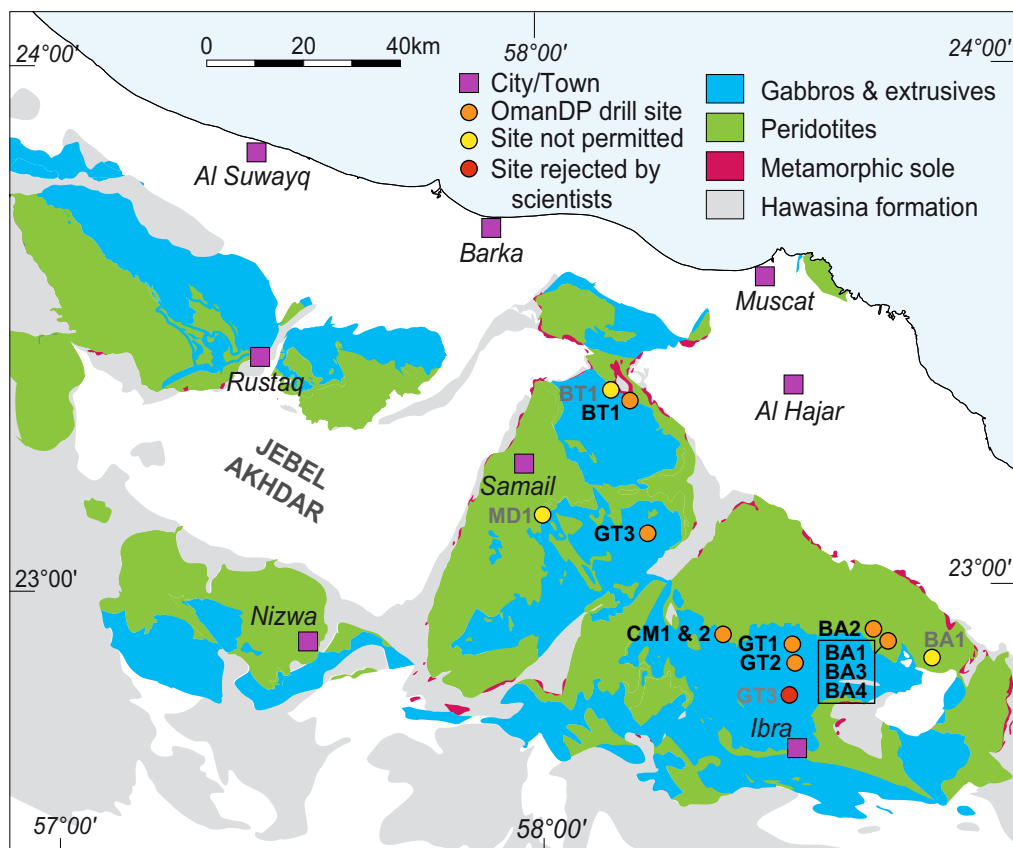
Figure F13. Map of Oman Drilling Project sites. (Geological map after Nicolas et al., 2000.)

Figure F14. Modal classification scheme for mafic-ultramafic plutonic igneous rocks used during OmanDP Phase 1 detailed core description (after Streckeisen, 1974).

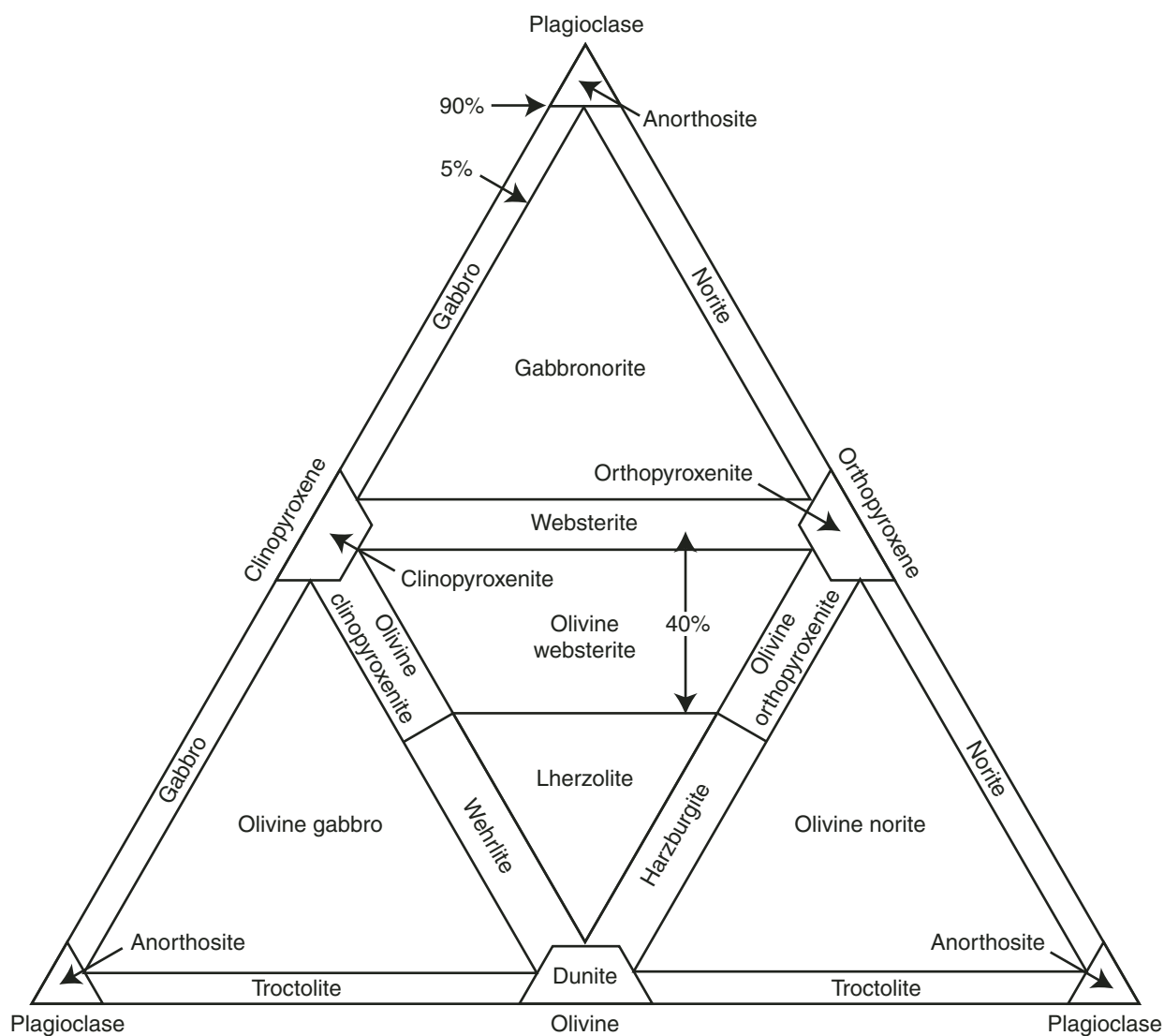


Figure F15. Quartz-alkali feldspar-plagioclase (QAP) modal classification scheme for plutonic igneous rocks used during OmanDP Phase 1 detailed core description (from Le Maitre et al., 2002).

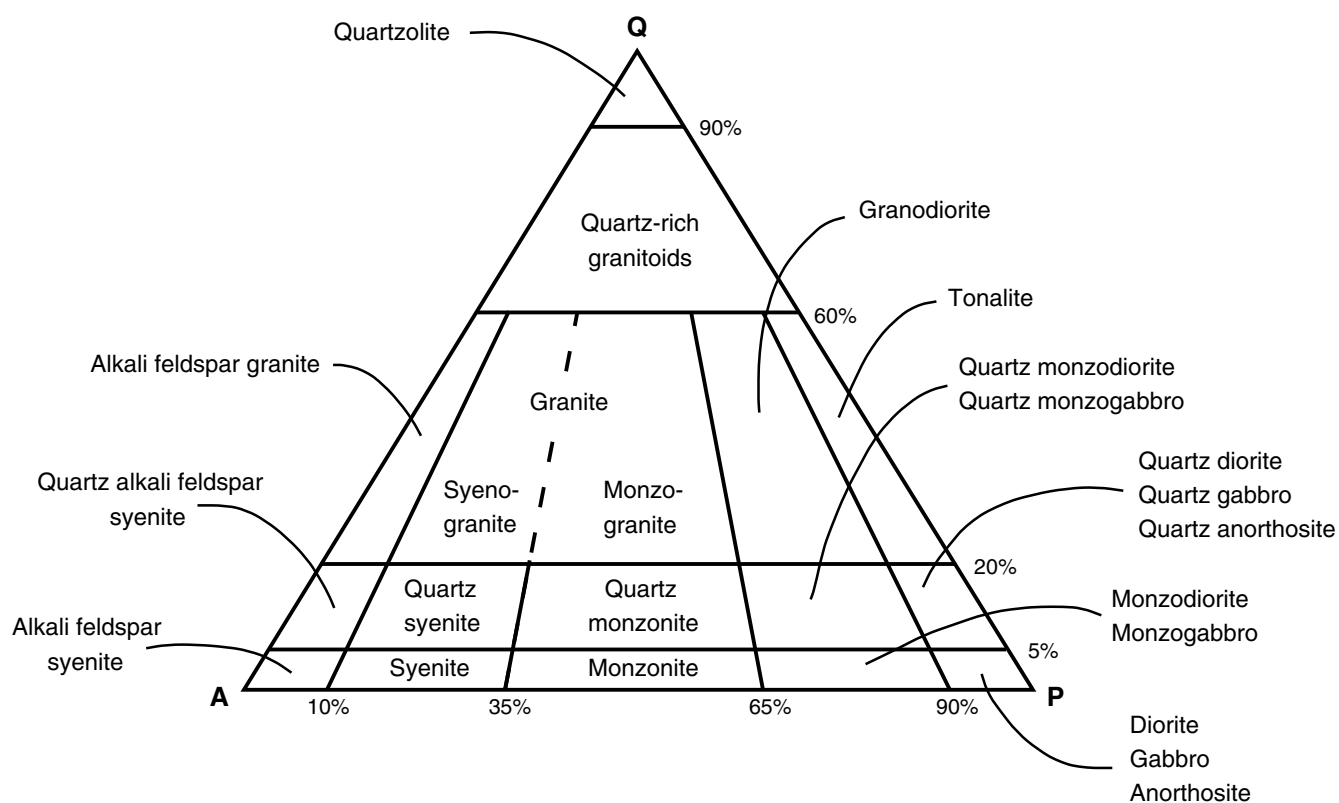


Figure F16. Textural classification for igneous rocks used during OmanDP Phase 1 detailed core description (modified from Cordier et al., 2005).

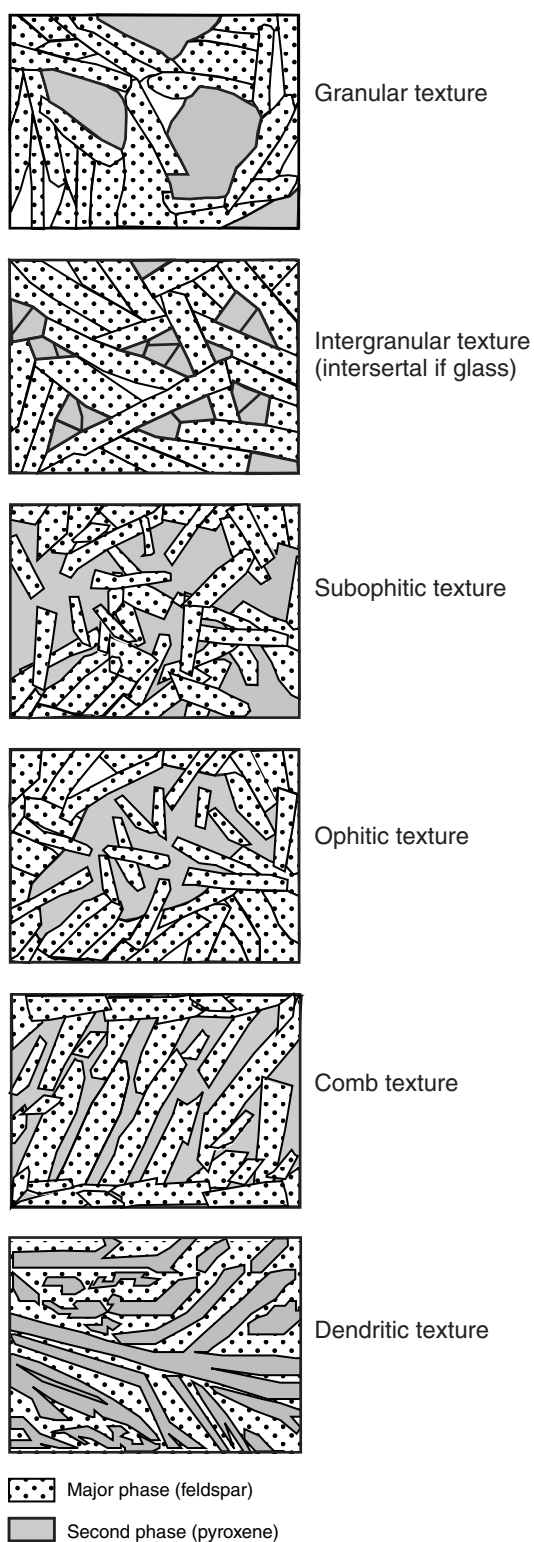
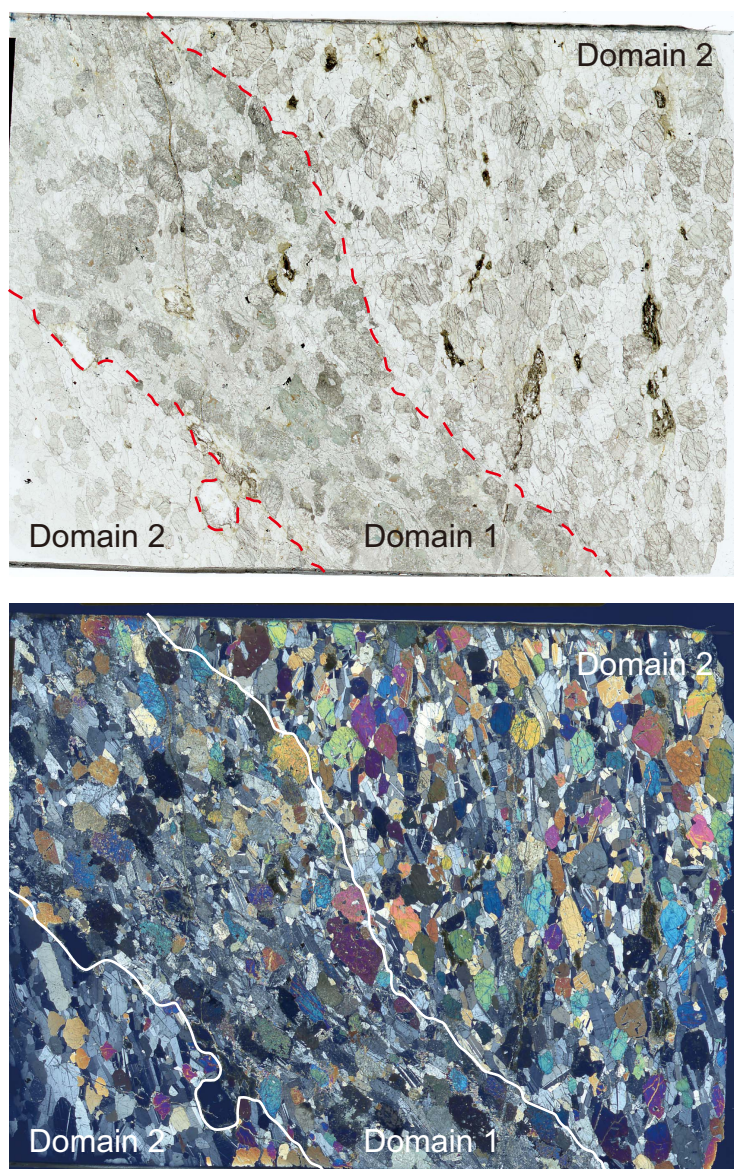


Figure F17. Example of full thin section photomicrographs under plane-polarized (top) and cross-polarized (bottom) light in which multiple domains were defined.



Sample GT1A_5Z4_35-39 cm (Thin section 2)

Figure 1 consists of four photographs labeled A, B, C, and D, each showing a different texture of the mineral sample. A ruler is placed vertically to the left of each photograph for scale. Photograph A shows a dark, fine-grained texture. Photograph B shows a dark, fine-grained texture with a prominent diagonal crack. Photograph C shows a light-colored, fibrous texture with a prominent diagonal crack. Photograph D shows a light-colored, fibrous texture with a prominent diagonal crack.

	A	B	C	D	E	F	G	H	I	J	K	L	M	N	O	P	Q	R	S	T	U	V	W	X	Y	Z	AA	AB	AC	AD	AE	AF	AG	AH	AI	AJ	AK	AL	AM	AN	AO	AP	AQ	AR	AS	AT	AU	AV	AW	AX	AY	AZ	BA	BB	BC	BD	BE	BF	BG	BH	BI	BJ	BK	BL	BM	BN	BO	BP	BQ	BR	BS	BT	BU	BV	BW	BX	BY	BZ	CA	CB	CC	CD	CE	CF	CG	CH	CI	CJ	CK	CL	CM	CN	CO	CP	CQ	CR	CS	CT	CU	CV	CW	CX	CY	CA	CB	CC	CD	CE	CF	CG	CH	CI	CJ	CK	CL	CM	CN	CO	CP	CQ	CR	CS	CT	CU	CV	CW	CX	CA	CB	CC	CD	CE	CF	CG	CH	CI	CJ	CK	CL	CM	CN	CO	CP	CQ	CR	CS	CT	CU	CV	CW	CX	CA	CB	CC	CD	CE	CF	CG	CH	CI	CJ	CK	CL	CM	CN	CO	CP	CQ	CR	CS	CT	CU	CV	CW	CX	CA	CB	CC	CD	CE	CF	CG	CH	CI	CJ	CK	CL	CM	CN	CO	CP	CQ	CR	CS	CT	CU	CV	CW	CX	CA	CB	CC	CD	CE	CF	CG	CH	CI	CJ	CK	CL	CM	CN	CO	CP	CQ	CR	CS	CT	CU	CV	CW	CX	CA	CB	CC	CD	CE	CF	CG	CH	CI	CJ	CK	CL	CM	CN	CO	CP	CQ	CR	CS	CT	CU	CV	CW	CX	CA	CB	CC	CD	CE	CF	CG	CH	CI	CJ	CK	CL	CM	CN	CO	CP	CQ	CR	CS	CT	CU	CV	CW	CX	CA	CB	CC	CD	CE	CF	CG	CH	CI	CJ	CK	CL	CM	CN	CO	CP	CQ	CR	CS	CT	CU	CV	CW	CX	CA	CB	CC	CD	CE	CF	CG	CH	CI	CJ	CK	CL	CM	CN	CO	CP	CQ	CR	CS	CT	CU	CV	CW	CX	CA	CB	CC	CD	CE	CF	CG	CH	CI	CJ	CK	CL	CM	CN	CO	CP	CQ	CR	CS	CT	CU	CV	CW	CX	CA	CB	CC	CD	CE	CF	CG	CH	CI	CJ	CK	CL	CM	CN	CO	CP	CQ	CR	CS	CT	CU	CV	CW	CX	CA	CB	CC	CD	CE	CF	CG	CH	CI	CJ	CK	CL	CM	CN	CO	CP	CQ	CR	CS	CT	CU	CV	CW	CX	CA	CB	CC	CD	CE	CF	CG	CH	CI	CJ	CK	CL	CM	CN	CO	CP	CQ	CR	CS	CT	CU	CV	CW	CX	CA	CB	CC	CD	CE	CF	CG	CH	CI	CJ	CK	CL	CM	CN	CO	CP	CQ	CR	CS	CT	CU	CV	CW	CX	CA	CB	CC	CD	CE	CF	CG	CH	CI	CJ	CK	CL	CM	CN	CO	CP	CQ	CR	CS	CT	CU	CV	CW	CX	CA	CB	CC	CD	CE	CF	CG	CH	CI	CJ	CK	CL	CM	CN	CO	CP	CQ	CR	CS	CT	CU	CV	CW	CX	CA	CB	CC	CD	CE	CF	CG	CH	CI	CJ	CK	CL	CM	CN	CO	CP	CQ	CR	CS	CT	CU	CV	CW	CX	CA	CB	CC	CD	CE	CF	CG	CH	CI	CJ	CK	CL	CM	CN	CO	CP	CQ	CR	CS	CT	CU	CV	CW	CX	CA	CB	CC	CD	CE	CF	CG	CH	CI	CJ	CK	CL	CM	CN	CO	CP	CQ	CR	CS	CT	CU	CV	CW	CX	CA	CB	CC	CD	CE	CF	CG	CH	CI	CJ	CK	CL	CM	CN	CO	CP	CQ	CR	CS	CT	CU	CV	CW	CX	CA	CB	CC	CD	CE	CF	CG	CH	CI	CJ	CK	CL	CM	CN	CO	CP	CQ	CR	CS	CT	CU	CV	CW	CX	CA	CB	CC	CD	CE	CF	CG	CH	CI	CJ	CK	CL	CM	CN	CO	CP	CQ	CR	CS	CT	CU	CV	CW	CX	CA	CB	CC	CD	CE	CF	CG	CH	CI	CJ	CK	CL	CM	CN	CO	CP	CQ	CR	CS	CT	CU	CV	CW	CX	CA	CB	CC	CD	CE	CF	CG	CH	CI	CJ	CK	CL	CM	CN	CO	CP	CQ	CR	CS	CT	CU	CV	CW	CX	CA	CB	CC	CD	CE</
--	---	---	---	---	---	---	---	---	---	---	---	---	---	---	---	---	---	---	---	---	---	---	---	---	---	---	----	----	----	----	----	----	----	----	----	----	----	----	----	----	----	----	----	----	----	----	----	----	----	----	----	----	----	----	----	----	----	----	----	----	----	----	----	----	----	----	----	----	----	----	----	----	----	----	----	----	----	----	----	----	----	----	----	----	----	----	----	----	----	----	----	----	----	----	----	----	----	----	----	----	----	----	----	----	----	----	----	----	----	----	----	----	----	----	----	----	----	----	----	----	----	----	----	----	----	----	----	----	----	----	----	----	----	----	----	----	----	----	----	----	----	----	----	----	----	----	----	----	----	----	----	----	----	----	----	----	----	----	----	----	----	----	----	----	----	----	----	----	----	----	----	----	----	----	----	----	----	----	----	----	----	----	----	----	----	----	----	----	----	----	----	----	----	----	----	----	----	----	----	----	----	----	----	----	----	----	----	----	----	----	----	----	----	----	----	----	----	----	----	----	----	----	----	----	----	----	----	----	----	----	----	----	----	----	----	----	----	----	----	----	----	----	----	----	----	----	----	----	----	----	----	----	----	----	----	----	----	----	----	----	----	----	----	----	----	----	----	----	----	----	----	----	----	----	----	----	----	----	----	----	----	----	----	----	----	----	----	----	----	----	----	----	----	----	----	----	----	----	----	----	----	----	----	----	----	----	----	----	----	----	----	----	----	----	----	----	----	----	----	----	----	----	----	----	----	----	----	----	----	----	----	----	----	----	----	----	----	----	----	----	----	----	----	----	----	----	----	----	----	----	----	----	----	----	----	----	----	----	----	----	----	----	----	----	----	----	----	----	----	----	----	----	----	----	----	----	----	----	----	----	----	----	----	----	----	----	----	----	----	----	----	----	----	----	----	----	----	----	----	----	----	----	----	----	----	----	----	----	----	----	----	----	----	----	----	----	----	----	----	----	----	----	----	----	----	----	----	----	----	----	----	----	----	----	----	----	----	----	----	----	----	----	----	----	----	----	----	----	----	----	----	----	----	----	----	----	----	----	----	----	----	----	----	----	----	----	----	----	----	----	----	----	----	----	----	----	----	----	----	----	----	----	----	----	----	----	----	----	----	----	----	----	----	----	----	----	----	----	----	----	----	----	----	----	----	----	----	----	----	----	----	----	----	----	----	----	----	----	----	----	----	----	----	----	----	----	----	----	----	----	----	----	----	----	----	----	----	----	----	----	----	----	----	----	----	----	----	----	----	----	----	----	----	----	----	----	----	----	----	----	----	----	----	----	----	----	----	----	----	----	----	----	----	----	----	----	----	----	----	----	----	----	----	----	----	----	----	----	----	----	----	----	----	----	----	----	----	----	----	----	----	----	----	----	----	----	----	----	----	----	----	----	----	----	----	----	----	----	----	----	----	----	----	----	----	----	----	----	----	----	----	----	----	----	----	----	----	----	----	----	----	----	----	----	----	----	----	----	----	----	----	----	----	----	----	----	----	----	----	----	----	----	----	----	----	----	----	----	----	----	----	----	----	----	----	----	----	----	----	----	----	----	----	------

Figure F20. Headers of Vein spreadsheet.

[illegible]

Figure F21. Sketch showing convention used by the alteration team for measuring vein lengths and widths if the vein crosses the centerline for use in the vein log.

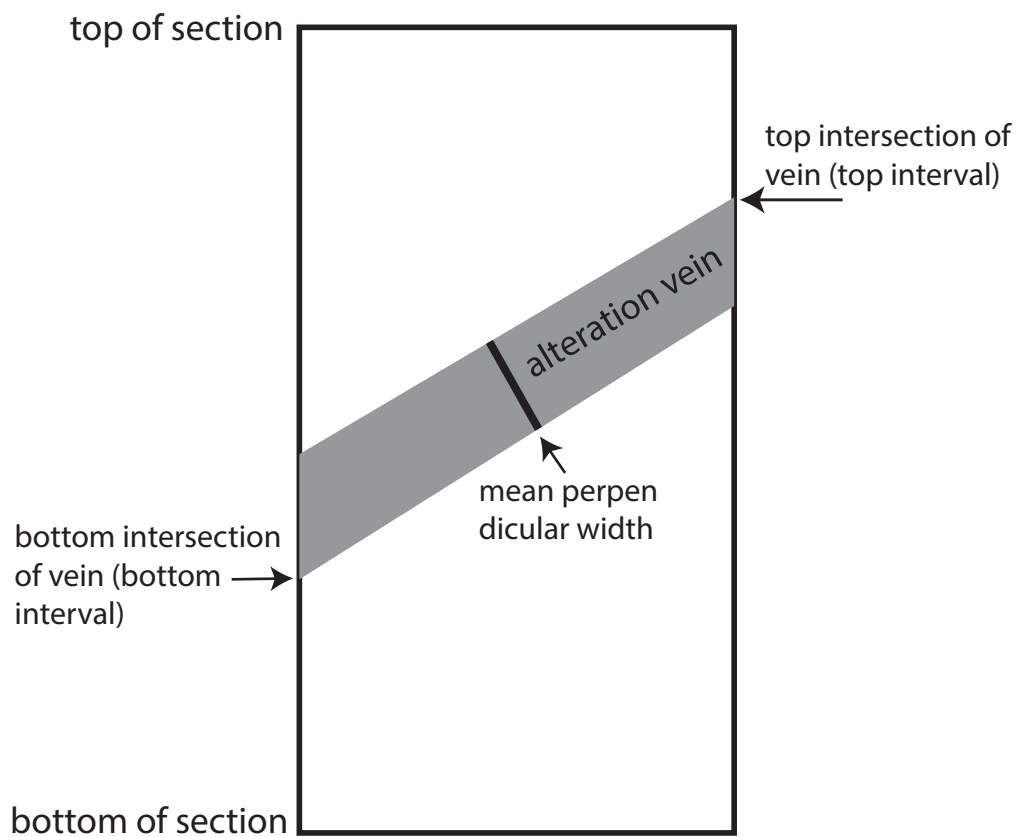


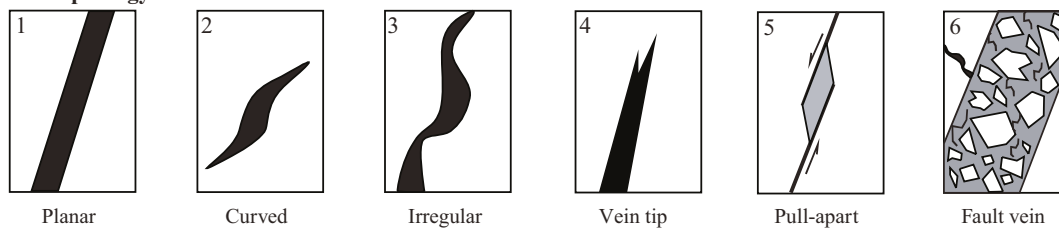
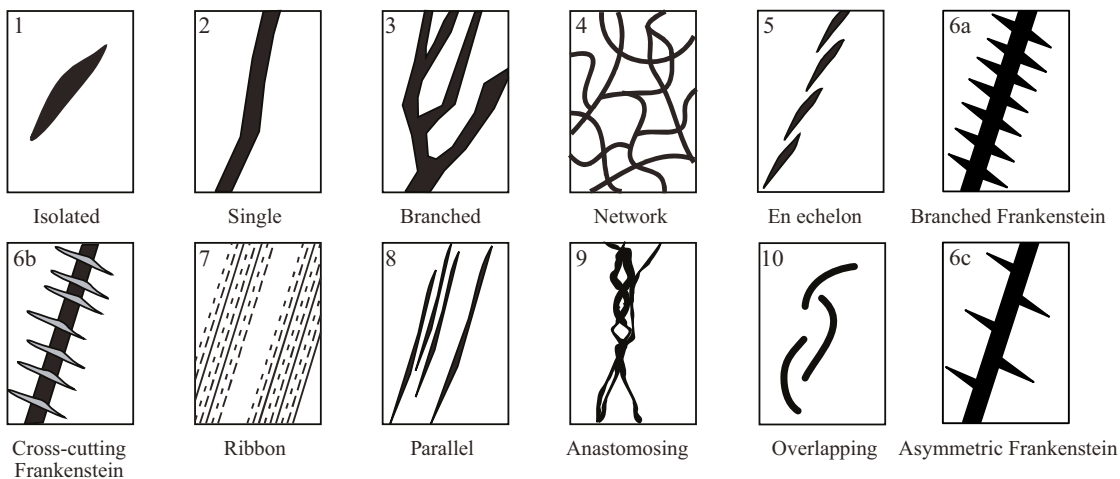
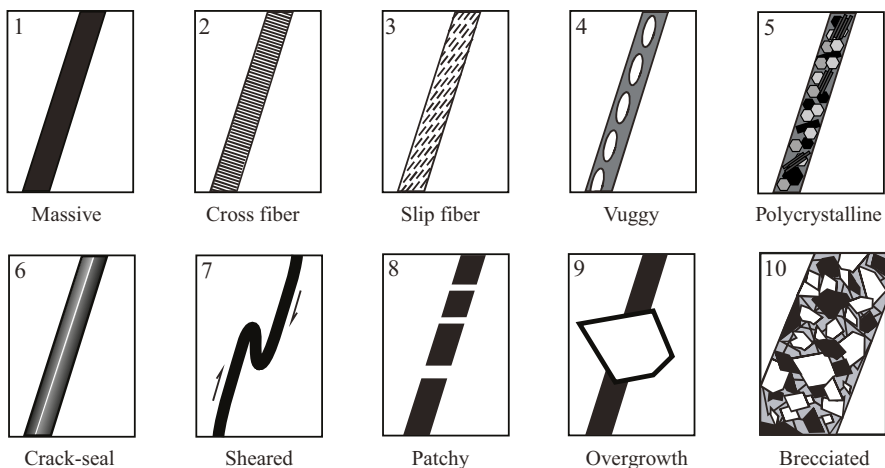
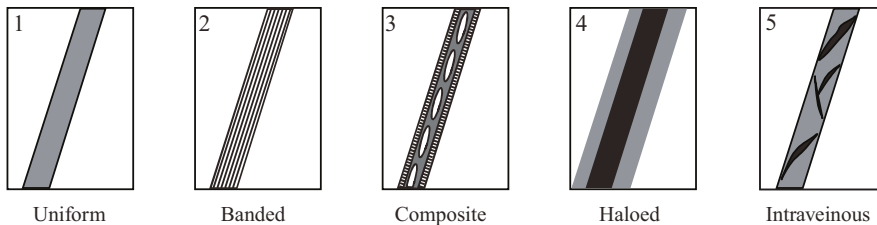
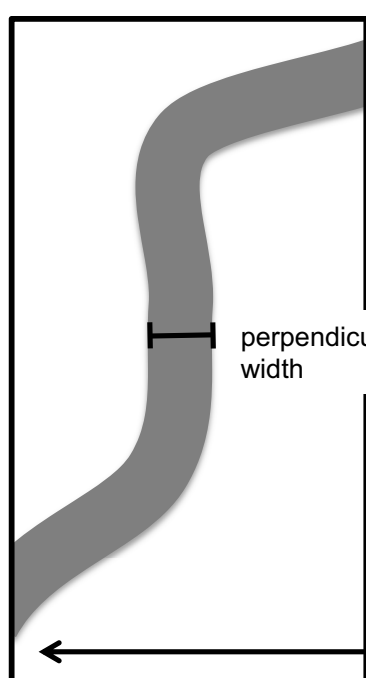
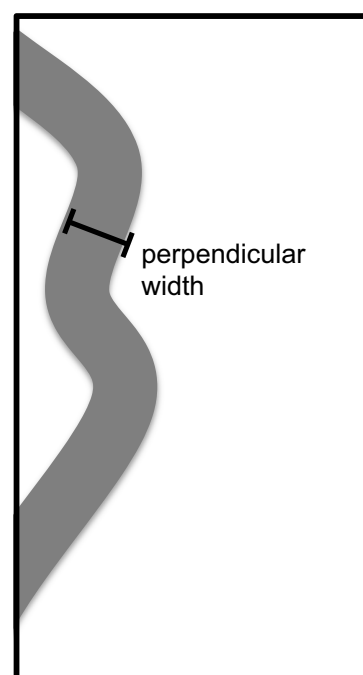
Figure F22. Vein characteristics and classifications used in the vein log (adapted from MacLeod et al., 2017b).**Vein morphology****Vein connectivity****Vein texture****Vein structure**

Figure F23. Convention used for measuring vein length and width if vein does not cross the core centerline for use in vein log.

veins with vertical width at center
>> perpendicular width



veins that do not cross the center line



happy, friendly veins
with good behavior

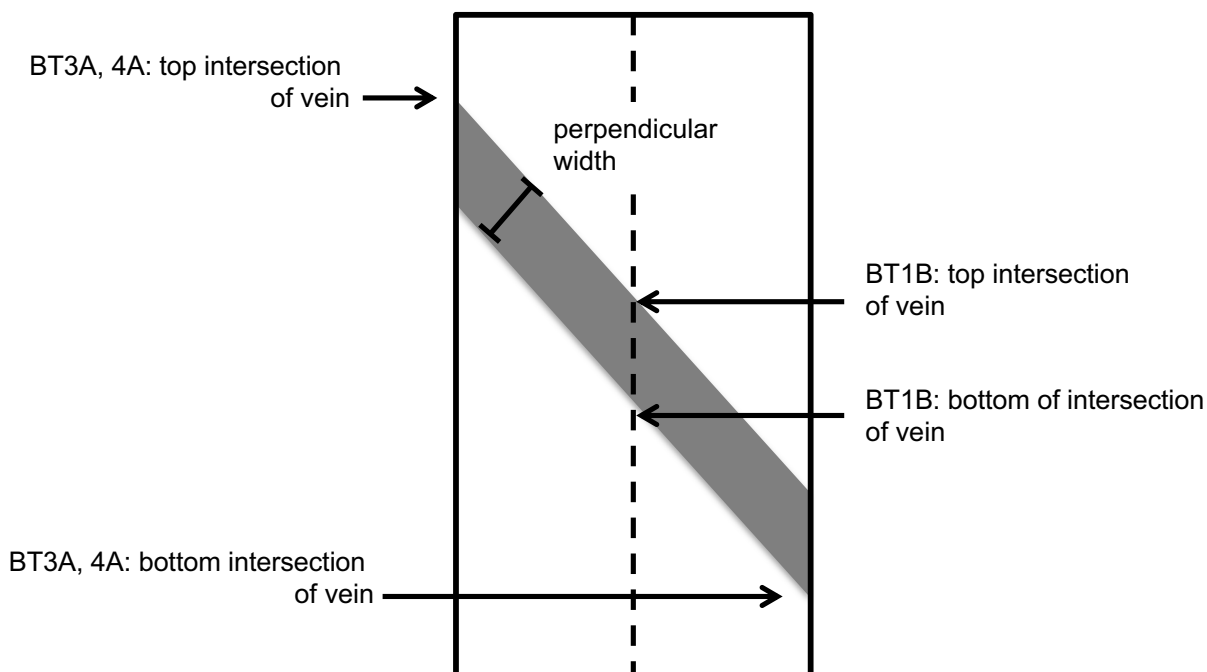


Figure F24. Schematic illustration of how structures were logged. Top and bottom offsets from top of section of a structure are logged where structure intersects center line of section half surface. **A.** Magmatic fabric is logged for the interval over which it occurs and for its perpendicular thickness. **B.** If structural features do not cross center line of core (e.g., magmatic veins or fractures), then their center point is logged as its interval. If structural feature is a fracture network, the interval over which the network occurs is logged.

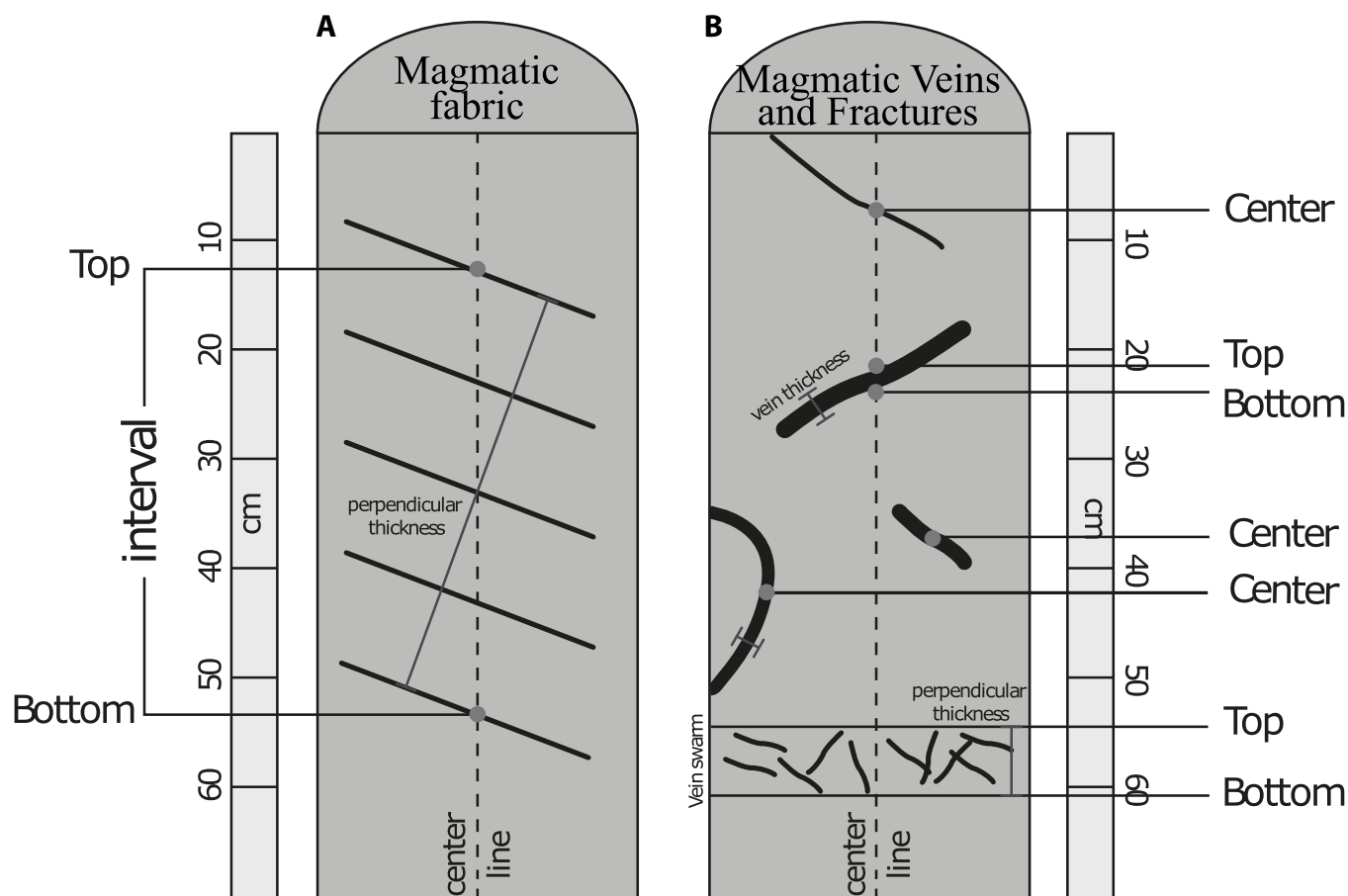


Figure F25. A–C. Reference frame and method of measuring the orientation of a planar feature. If a piece is cut perpendicular to strike of a structural feature, dip/dip azimuth can be measured directly. If a structural feature is oblique to cut face, two measurements must be made.

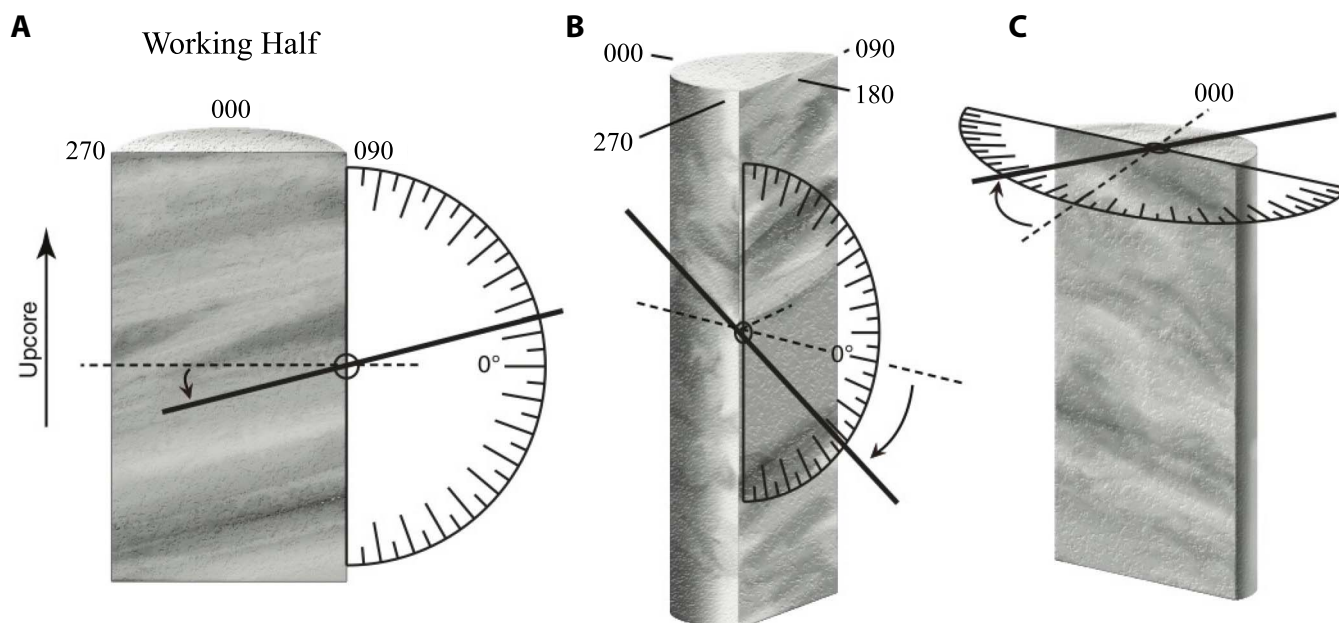


Figure F26. Predicted distribution of a random set of planar features sampled within a borehole. Curve I (Equation 1) shows effect of spherical geometry on true dip data. Curve II (Equation 3) shows bias effect introduced by sampling with a borehole. Curve III (Equation 4) combines the two effects and shows predicted distribution of a random set of planes in a vertical borehole. See text for discussion.

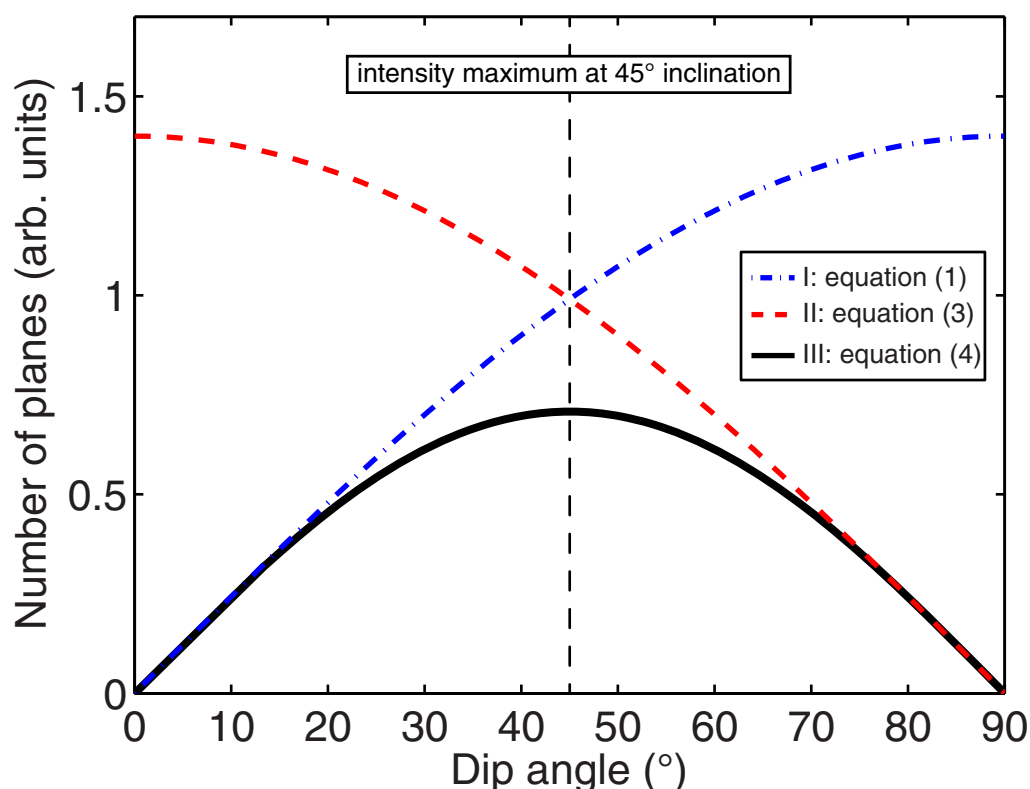


Figure F27. Intensity ranks used to describe macroscopic and microscopic observations for magmatic foliation, crystal-plastic deformation, fault rock fabrics (following McLeod et al., 2017).

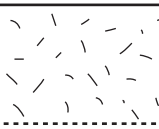
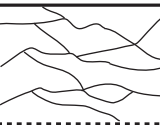
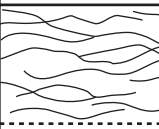
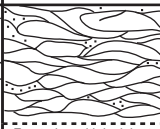
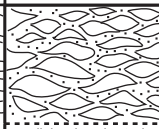
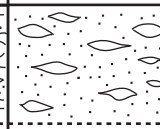
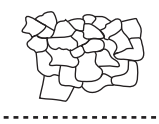
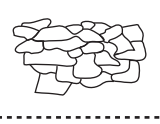
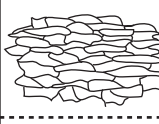
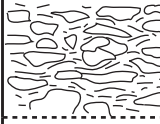
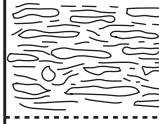
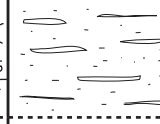
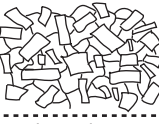
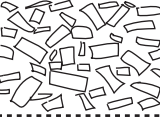
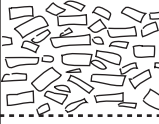
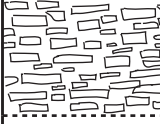
Feature	0	1	2	3	4	5
Fault Rock Deformation	 Undeformed	 Minor fracturing No sig. grain size reduction	 Moderate fracturing No sig. grain size reduction	 Fracturing with incipient grain reduction and clast rotation (<50% Matrix)	 well developed cataclasis Cataclasis (50% - 90% Matrix)	 Ultracataclasis (>90% Matrix)
Gabbro Crystal Plastic Deformation	 Isotropic	 Weakly foliated	 Moderately foliated	 Protomylonite (Porphyroclastic)	 Mylonite	 Ultramylonite
Magmatic Fabric	 Isotropic: no shape fabric	 Weak shape fabric	 Moderate shape fabric	 Strong shape fabric		

Figure F28. Structure intensity ranks, Leg 3.

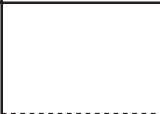
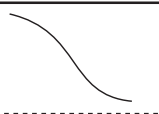
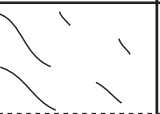
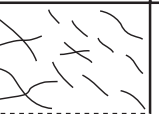






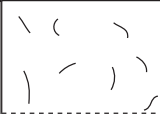



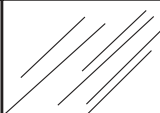


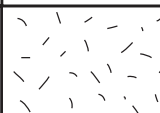
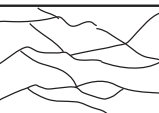
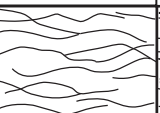

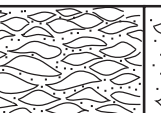
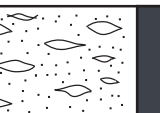


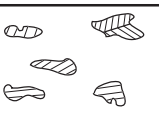
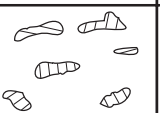

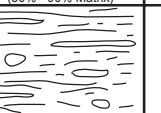


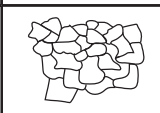
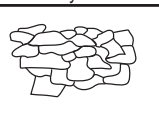
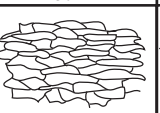


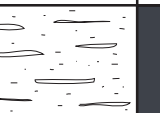

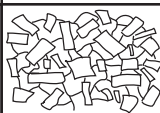



Feature	0	1	2	3	4	5	
Joints or Open Fractures	 No Open Fractures	 <1 per 10 cm	 1-5 per 10cm	 >5 per 10 cm			
Veins	 No Veins	 <1 per 10 cm	 1-5 per 10cm	 5-10 per 10 cm	 10-20 per 10 cm	 >20 per 10 cm	
Schistose & Network Fabrics	 Random	 Weakly Oriented	 Moderately Oriented	 Strongly Oriented			
Structure Geometry	 Planar	 Anastomosing/ facoidal	 S-C				
Cataclastic Deformation	 Undeformed	 Minor fracturing No sig. grain size reduction	 Moderate fracturing No sig. grain size reduction	 Dense anastomosing fracturing and incipient breccia (<50% Matrix)	 Well-developed cataclasis Cataclasite (50% - 90% Matrix)	 Ultrataclasite (>90% Matrix)	
Peridotite Crystal Plastic Deformation	 Undeformed Protogranular	 Porphyroclastic Weakly foliated	 Porphyroclastic Strongly foliated	 Porphyroclastic (Protomylonite)	 Mylonite	 Ultramylonite	
Gabbro Crystal Plastic Deformation	 Undeformed	 Weakly foliated	 Strongly foliated	 Porphyroclastic (Protomylonite)	 Mylonite	 Ultramylonite	
Magmatic Foliation	 Isotropic: no shape fabric	 Weak shape fabric	 Moderate shape fabric	 Strong shape fabric			

Figure F29. Classification of fracture and fracture network morphologies used in the worksheets (following MacLeod et al., 2017b).

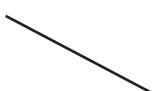


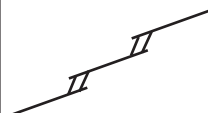


Fracture Morphology				
	No open fractures	Planar	Curved	Irregular
Fracture morphology/network				
	Stepped	Splayed	Anastomosing	

Figure F30. Structural intensity rankings for metamorphic rocks.


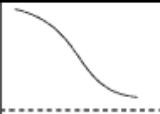


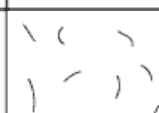

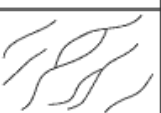


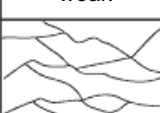
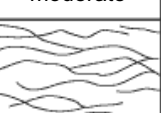
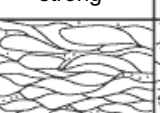
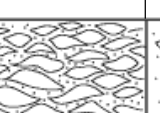
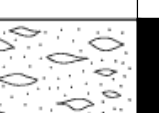


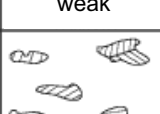
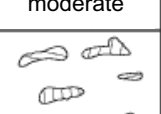
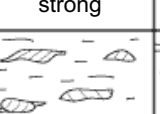
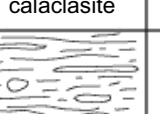
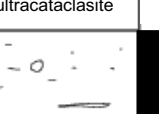
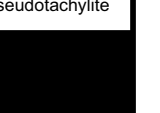

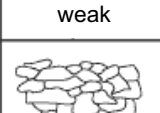
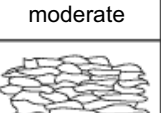
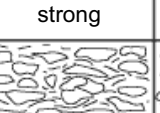
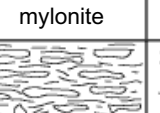
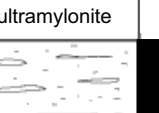

intensity	0	1	2	3	4	5	6
joints, veins, fractures	 none	 <1 per 10 cm	 1-5 per 10 cm	 >5 per 10 cm			
foliation & banding	 none	 weak	 moderate	 strong			
cataclastic deformation	 none	 weak	 moderate	 strong	 calacclasite	 ultracataclasite	 pseudotachylite
crystal-plastic deformation	 none	 weak	 moderate	 strong	 mylonite	 ultramylonite	 pseudotachylite
	 none	 weak	 moderate	 strong	 mylonite	 ultramylonite	 pseudotachylite

Figure F31. Fracture and vein rankings for metamorphic rocks, based on IODP Expedition 360 methods.


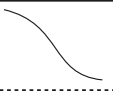
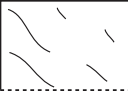
















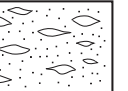







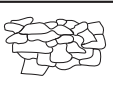
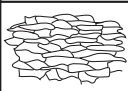


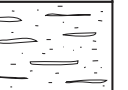



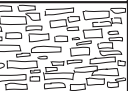
Feature	0	1	2	3	4	5
Open fracture density	 No open fractures	 <1/10 cm	 (1-5)/10 cm	 >5/10 cm		
Vein density	 No veins	 <1/10 cm	 (1-5)/10 cm	 (5-10)/10 cm	 (10-20)/10 cm	 >20/10 cm
Serpentine network orientation	 Isotropic	 Weakly oriented	 Moderately oriented	 Strongly oriented		
Fault rock deformation	 Undeformed	 Minor fracturing No sig. grain size reduction	 Moderate fracturing No sig. grain size reduction	 Dense anastomosing fracturing and incipient breccia (<20% matrix)	 Well-developed fault brecciation; clast rotation (20%-70% matrix)	 Cataclasite (>70% matrix)
Peridotite crystal-plastic deformation	 Undeformed protogranular	 Porphyroclastic weakly foliated	 Porphyroclastic strongly foliated	 Porphyroclastic (protomylonite)	 Mylonite	 Ultramylonite
Gabbro crystal-plastic deformation	 Isotropic	 Weakly foliated	 Strongly foliated	 Porphyroclastic (protomylonite)	 Mylonite	 Ultramylonite
Magmatic fabric	 Isotropic: no shape fabric	 Weak shape fabric	 Moderate shape fabric	 Strong shape fabric		

Figure F32. Deformation intensity classification for metamorphic rocks (after Sibson, 1977).

		Random - Fabric	Foliated
Incohesive		Fault Breccia (visible fragments > 30% of rock mass)	?
		Fault Gouge (visible fragments < 30% of rock mass)	?
Cohesive	Glass/ Devitrified glass	Pseudotachlyte	?
	Nature of Matrix Tectonic reduction in grain size dominates grain growth by recrystallization and neomineralization	Crush breccia (fragments > 0.5 cm) Fine crush breccia (0.1 cm < frags, < 0.5 cm) Crush microbreccia (fragments < 0.1 cm)	0-10%
		Protocataclasite	10-50%
		Cataclasite	50-90%
		Ultracataclasite	90-100%
		?	Blastomylonite

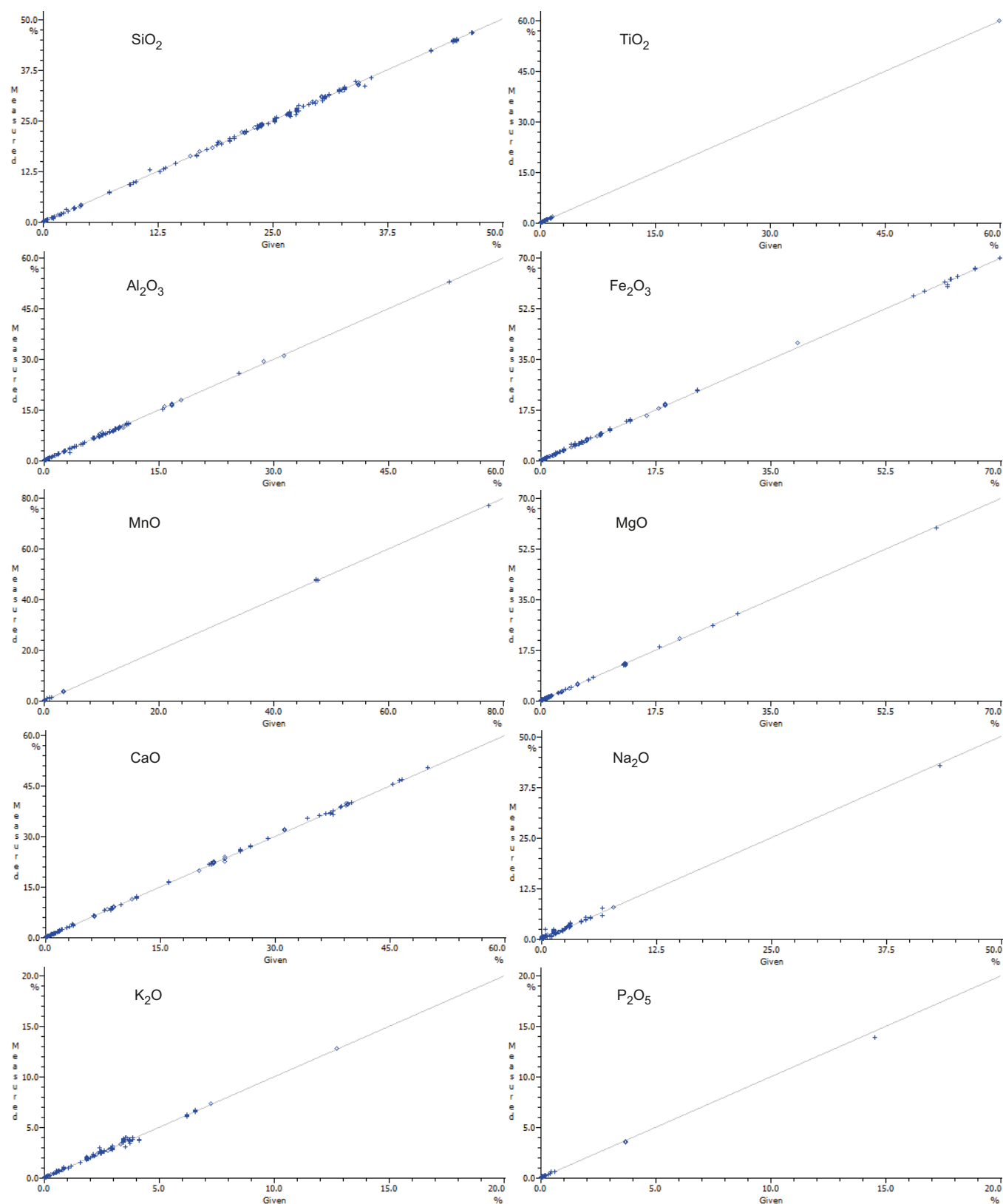
Figure F33. Calibration curves for XRF analyses of major elements determined at the University of St. Andrews.

Figure F34. A. Calibration curves for XRF analyses of trace elements determined at the University of St. Andrews. (Continued on next page.)

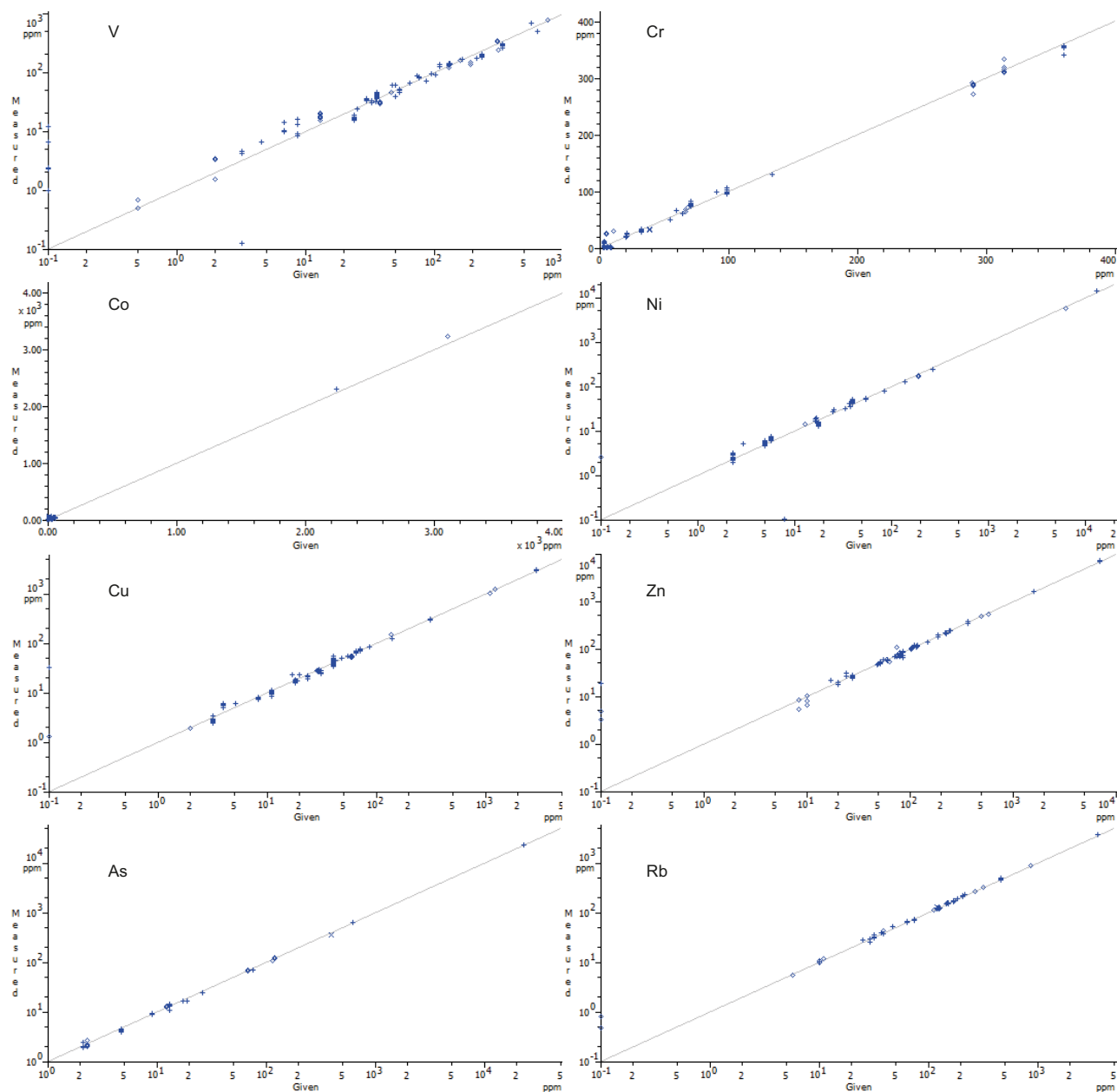


Figure F_F34 (continued). B. Calibration curves for XRF analyses of trace elements determined at the University of St. Andrews.

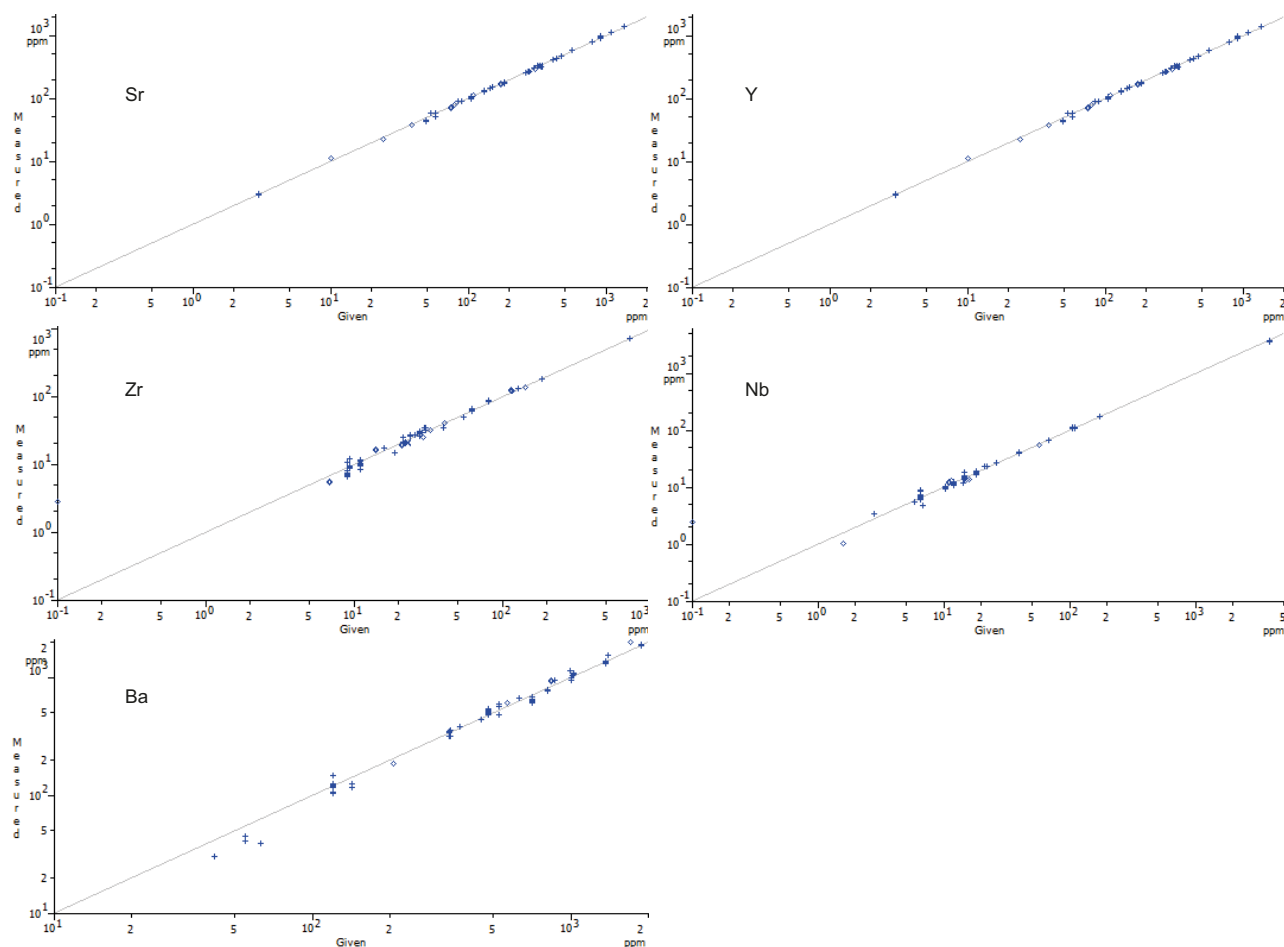


Figure F35. Calibration curves for XRF analyses of major elements in Geological Survey Japan geological SRMs JA-1, JA-2, JB-2, JB-3, JF-1, JF-2, JG-1a, JG-2, JGb-1, JGb-2, JH-1, JP-1, JR-2, JR-3, and JSy-1 and JG-1 determined onboard *Chikyu*. The red bar represents the expected range in concentration of samples.

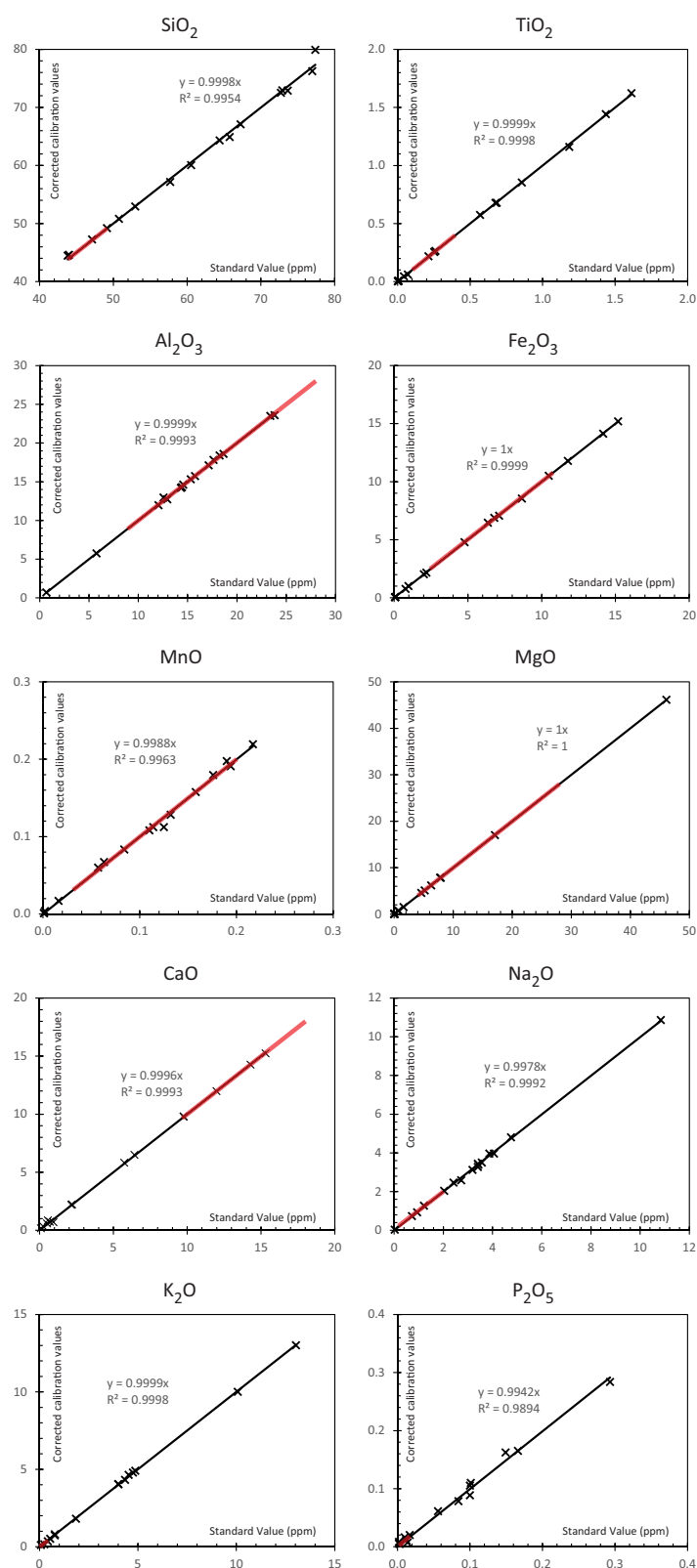


Figure F36. Calibration curves for XRF analyses of trace elements in Geological Survey Japan geological SRMs JA-1, JA-2, JB-2, JB-3, JF-1, JF-2, JG-1a, JG-2, JGb-1, JGb-2, JH-1, JP-1, JR-2, JR-3, JSy-1, and a 3:1 mix of JGb-2 and JP-1 determined onboard *Chikyū*. The red bar represents the expected range in concentration of samples.

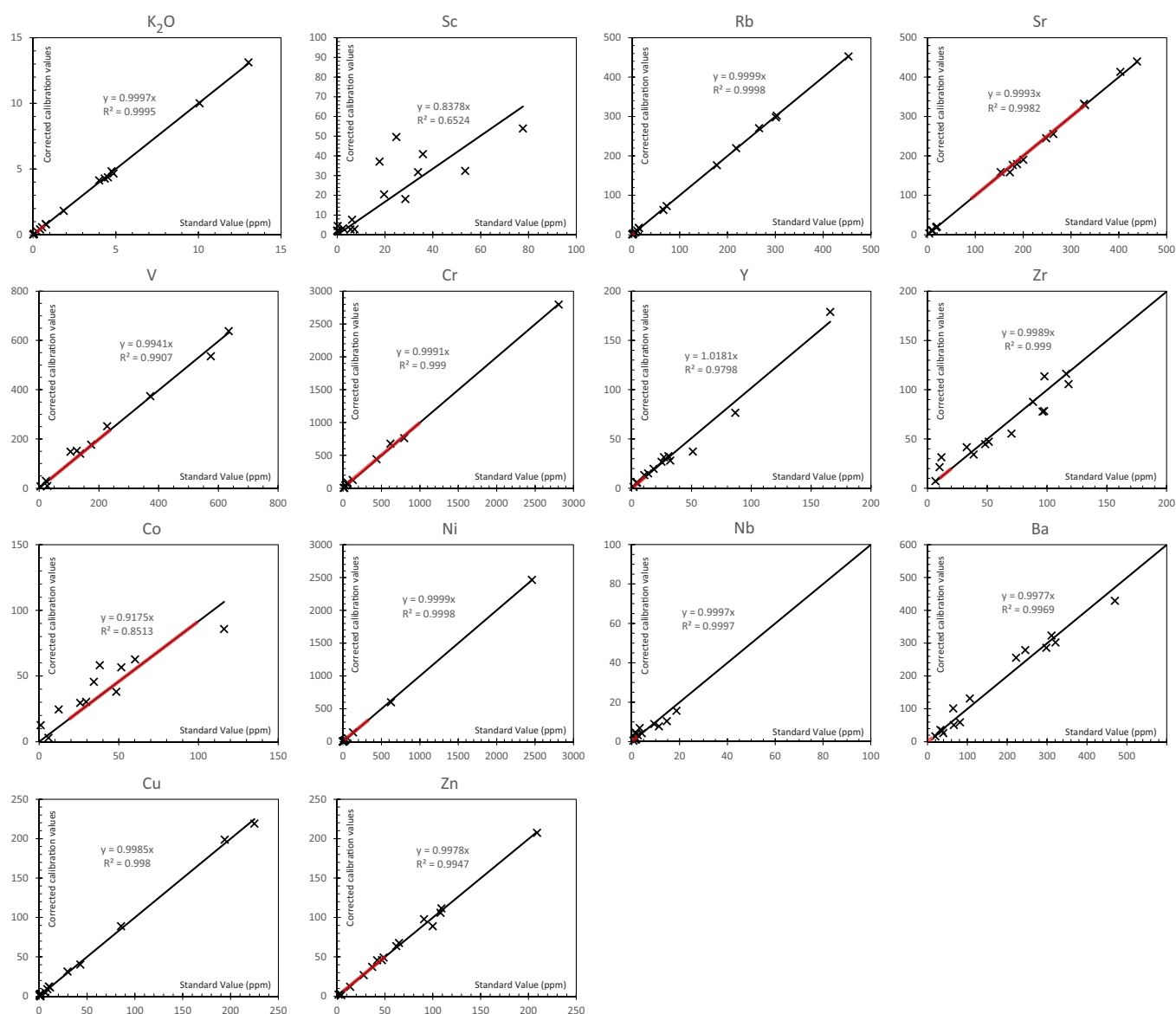


Figure F37. Calibration curves for XRF analyses of major elements determined onboard *Chikyu* during Leg 2 showing the ranges of concentration for samples from Holes GT3A (red) and BT1B (green) compared to Holes GT1A and GT2A. Where relevant, listvenite and metamorphic sole ranges are indicated separately.

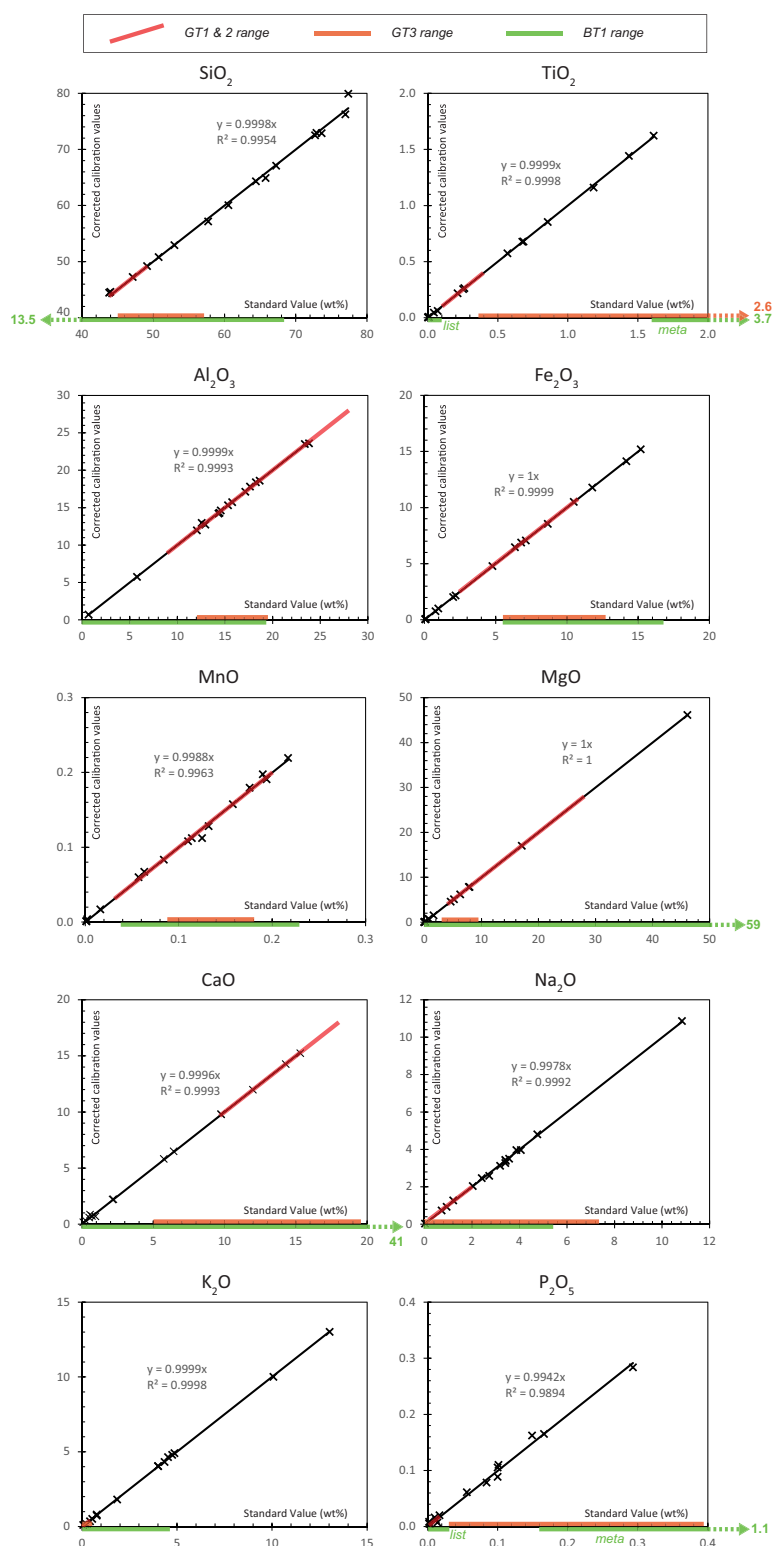


Figure F38. Calibration curves for XRF analyses of trace elements determined onboard *Chikyu* showing the ranges of measured concentrations for samples from Holes GT3 (red) and BT1 (green) compared to Holes GT1 and GT2. Where relevant, listvenite and metamorphic sole ranges are indicated separately.

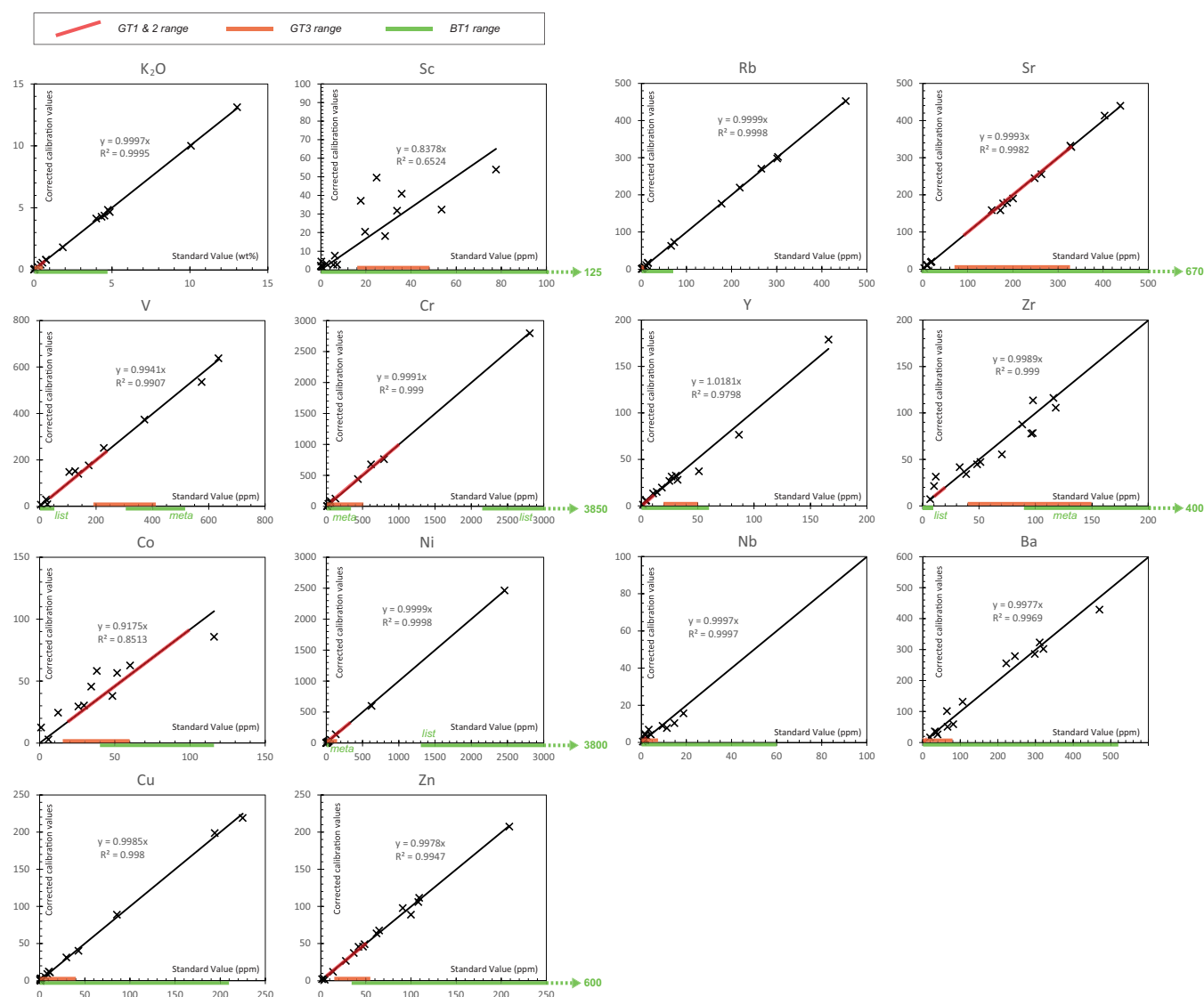


Figure F39. Comparison of XRF major element data measured on selected samples from Holes GT1A and GT2A between the University of St. Andrews and *Chikyu* laboratories.

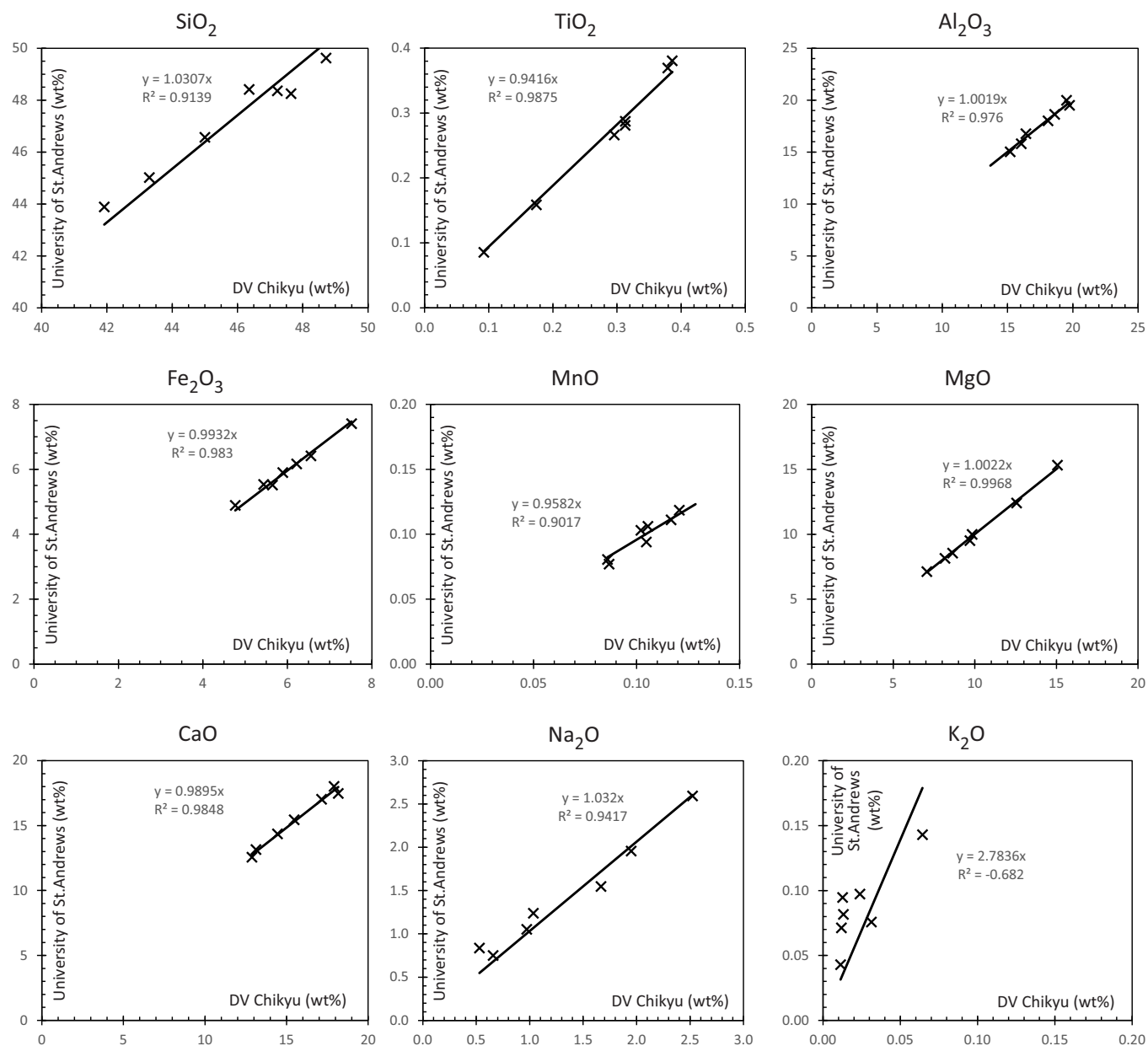


Figure F40. Comparison of XRF trace element data between The University of St. Andrews and *Chikyu* laboratories and also K_2O measured on powder pellets on the *Chikyu* due to low concentrations in samples.

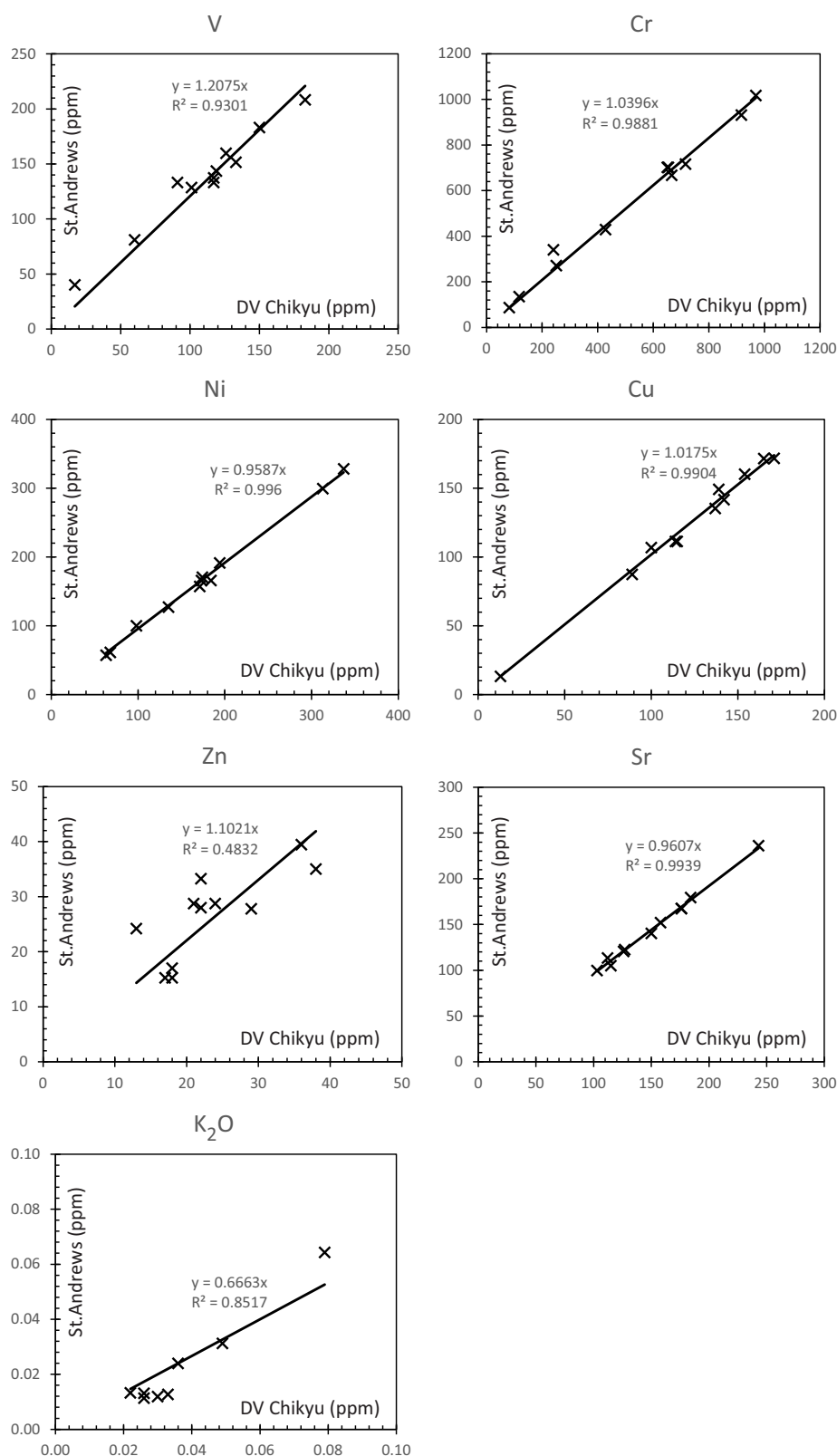


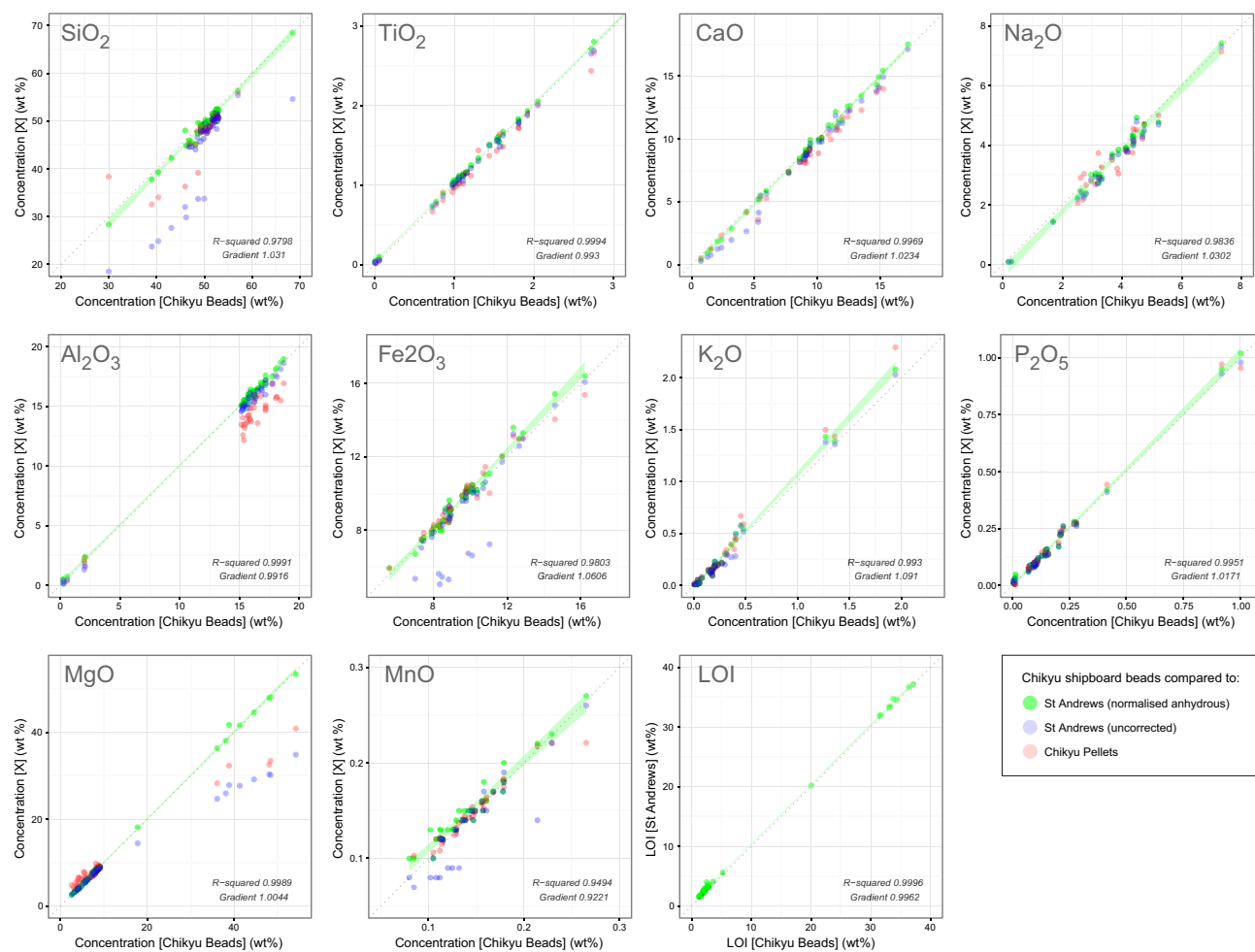
Figure F41. Comparison of XRF major element data between The University of St. Andrews and *Chikyu* laboratories for on-site samples from Holes BT1B and GT3A.

Figure F42. Comparison of XRF trace element data between The University of St. Andrews and *Chikyu* laboratories during Leg 2. Note: K_2O was measured on powder pellets on the *Chikyu* due to low concentrations in samples for on-site samples from Holes BT1B and GT3A.

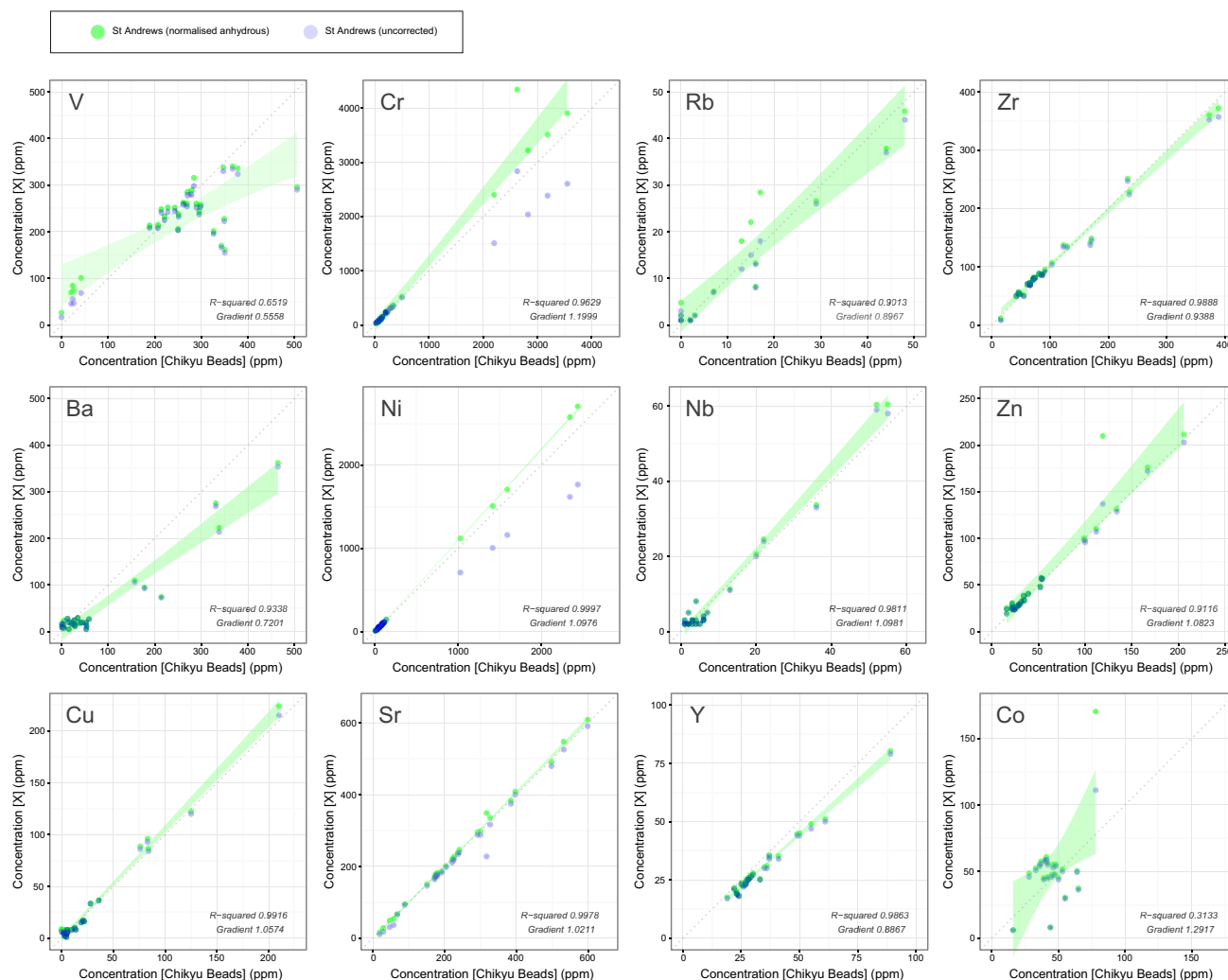


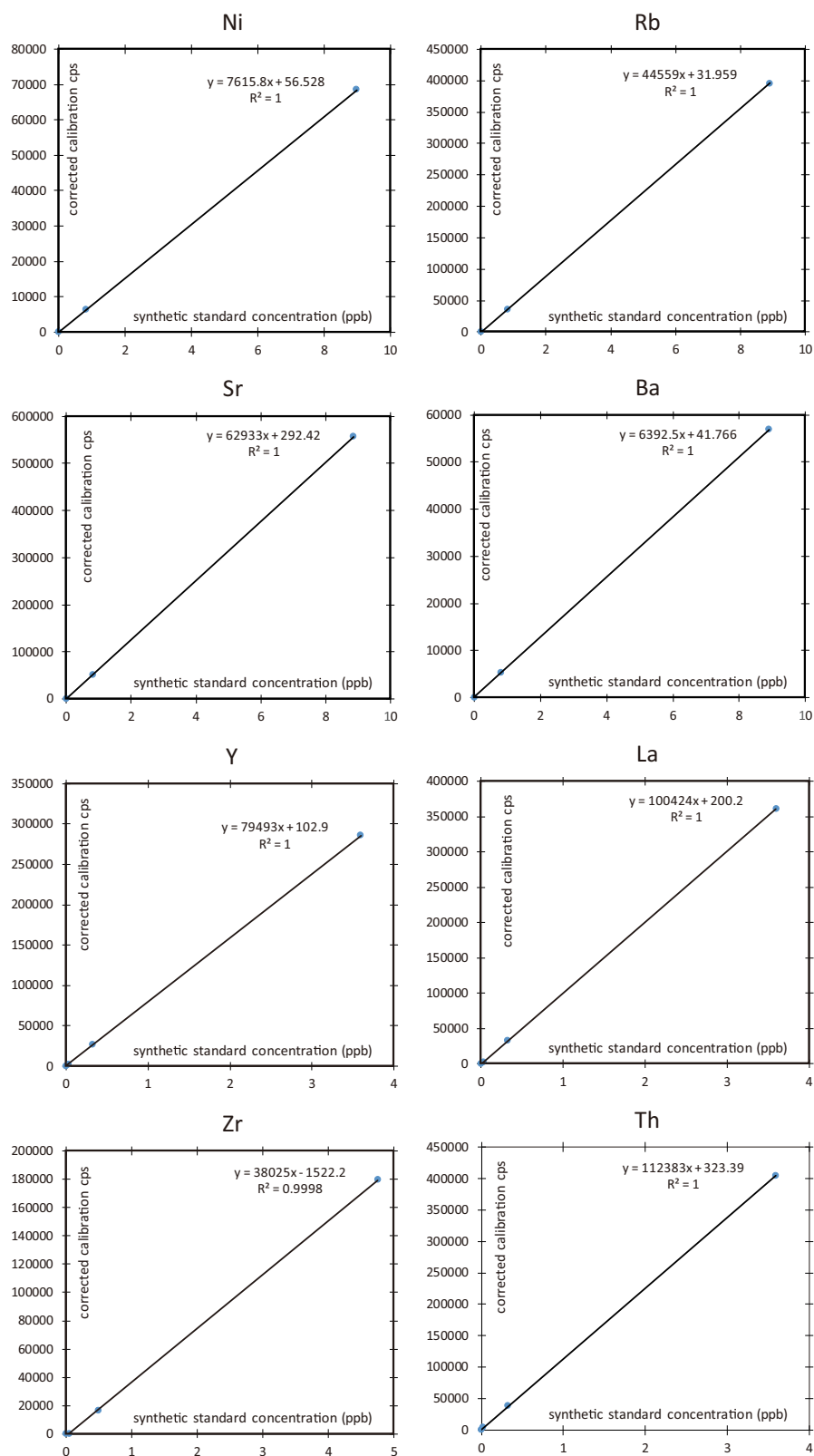
Figure F43. Calibration curves for ICP-MS analyses of trace and rare earth elements.

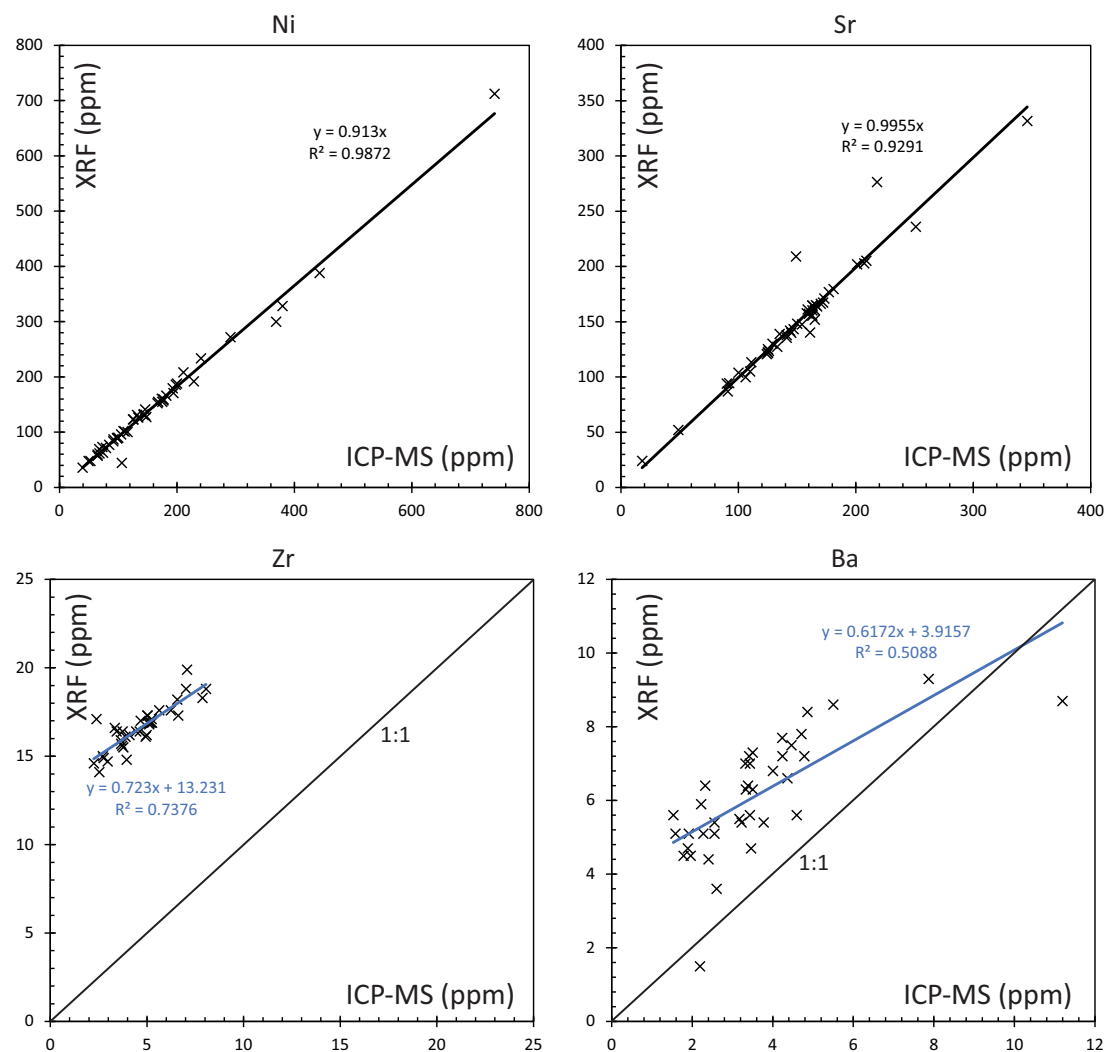
Figure F44. Comparison of trace element quantification by ICP-MS and XRF.

Figure F45. Calibration curves obtained for measurement of total carbon, hydrogen, nitrogen, and sulfur. Calibrations were made using both rock standards (JSI-1 for C, N, S and JGb-1 for H) and sulphanilamide to cover the range in concentration expected in samples. Calibrations between these different standard types are linear with R^2 no worse than 0.09939.

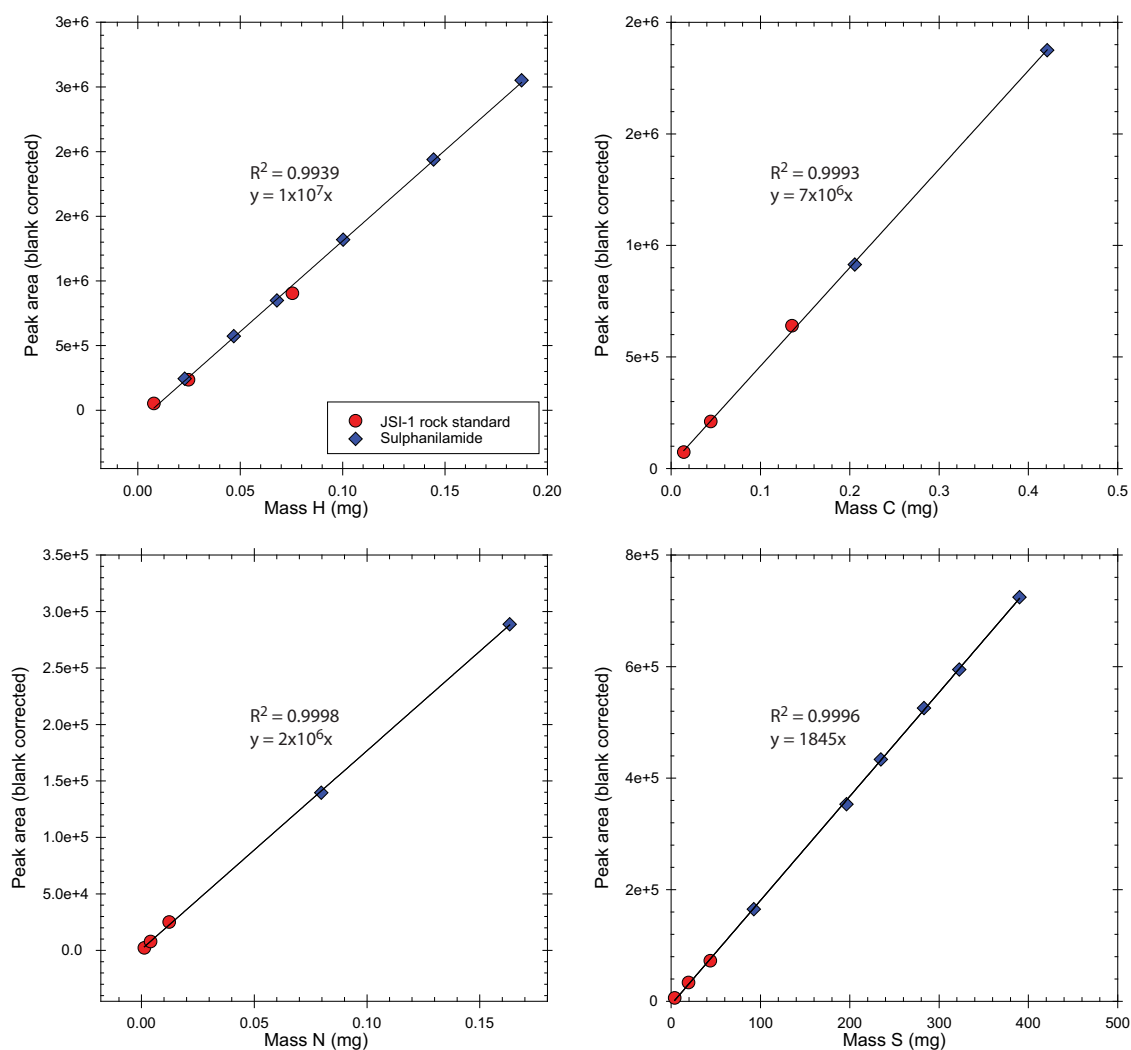


Figure F46. Calibration curves for XRF analyses of major elements determined using glass beads during ChikyuOman 2018 Leg 3, showing the ranges of measured concentrations for CM1A (pink) and CM2B (blue).

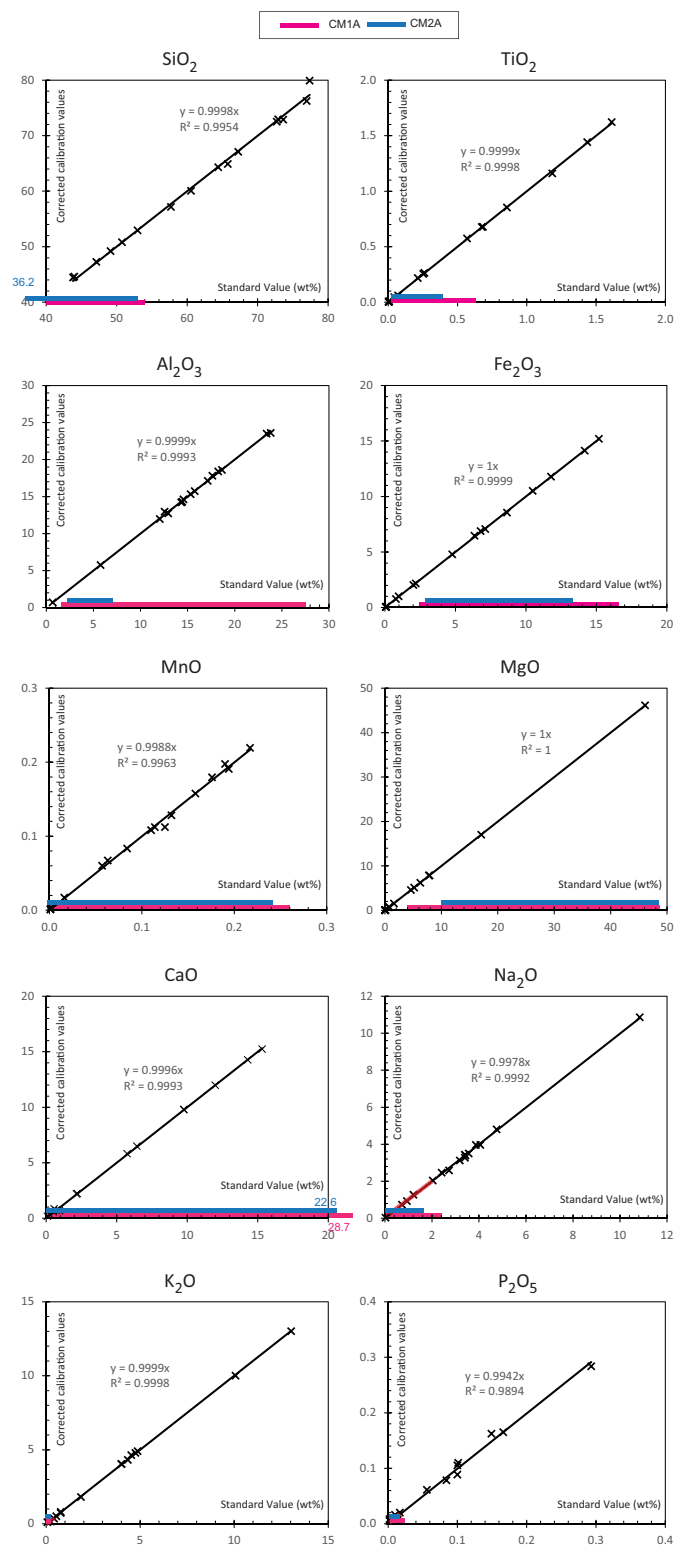


Figure F47. Calibration curves for XRF analyses of trace elements determined onboard *Chikyu*, showing the ranges of measured concentrations for CM1A (pink) and CM2B (blue).

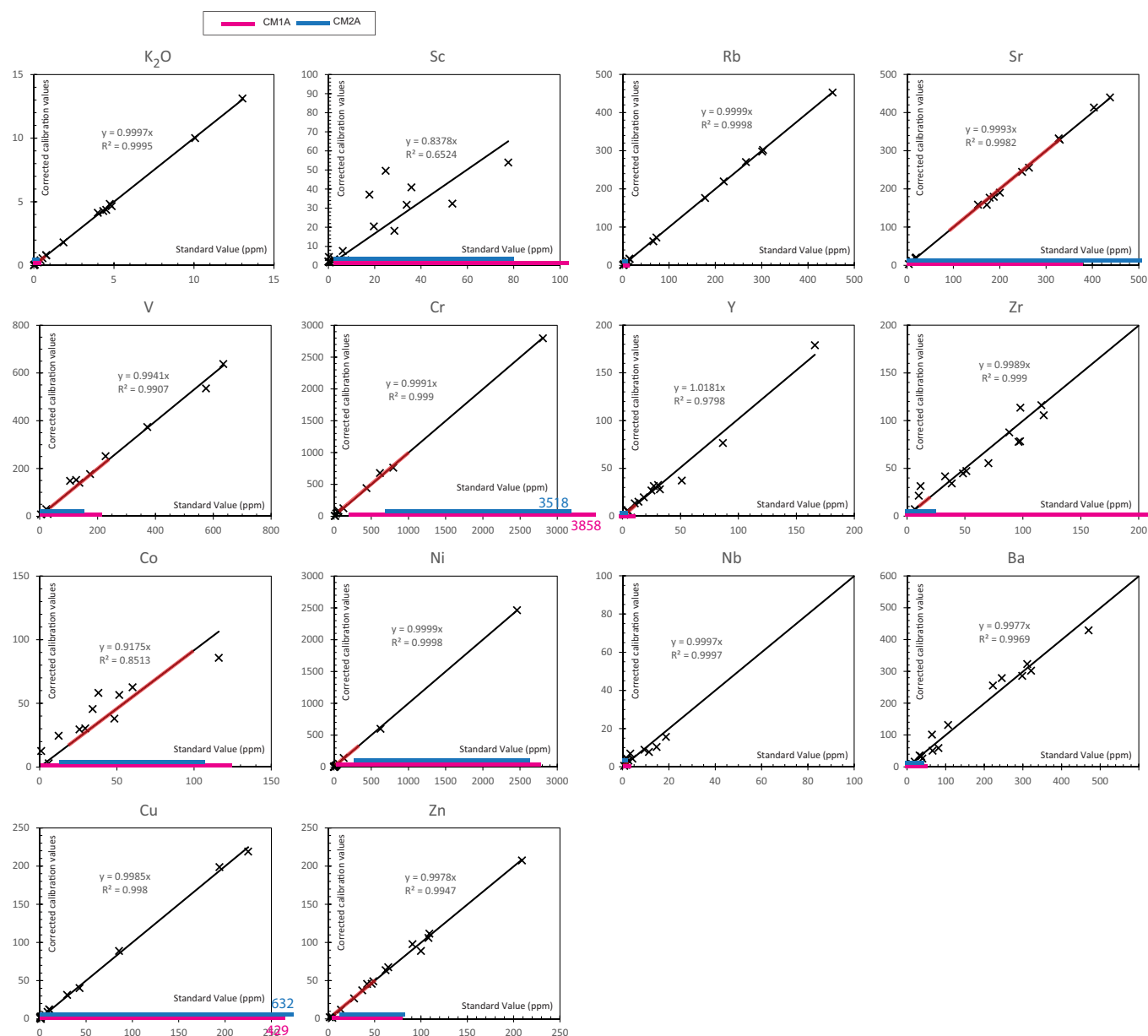
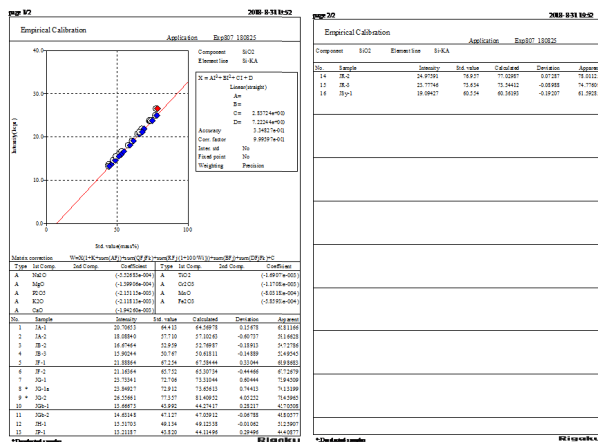
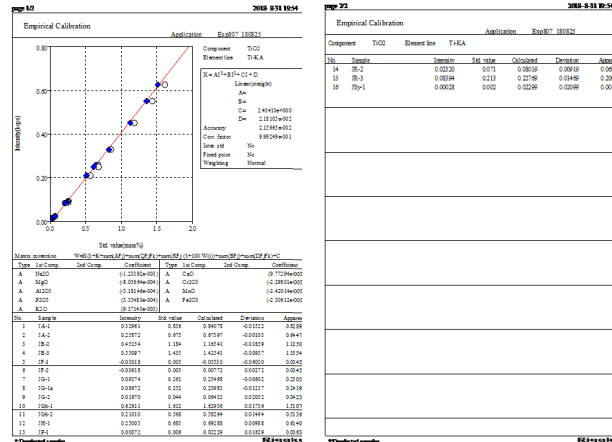
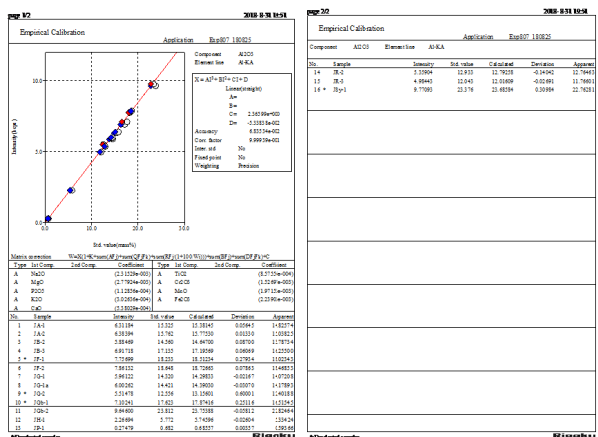
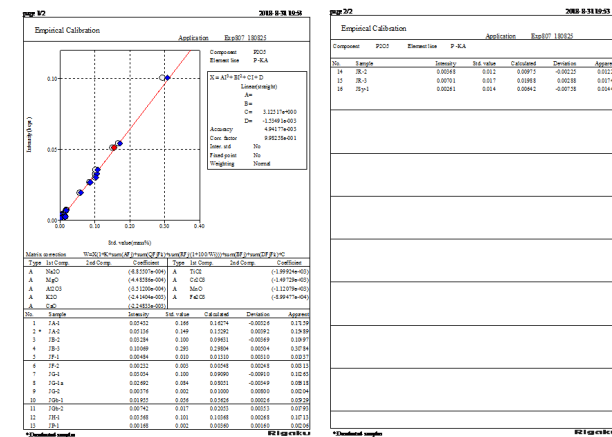


Figure F48. Calibration curves for XRF bead analyses of major elements determined on board *Chikyu*. **A.** SiO₂, TiO₂, Al₂O₃, P₂O₅. **B.** MgO, MnO, CaO, Na₂O. **C.** K₂O, Fe₂O₃, Cr₂O₃. (Continued on next 2 pages.)

SiO₂TiO₂Al₂O₃P₂O₅

MnO

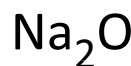


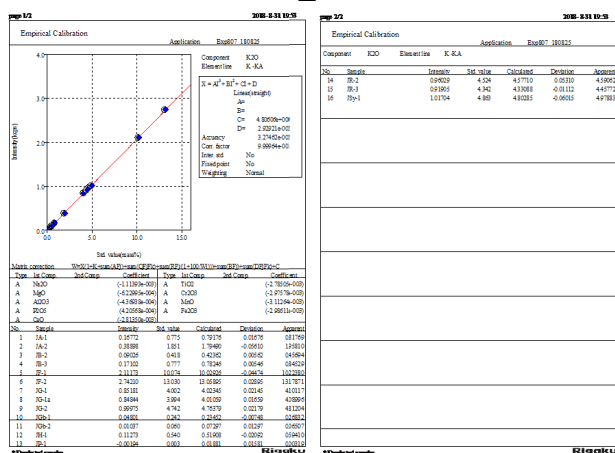
Figure F48 (continued). Calibration curves for XRF bead analyses of major elements determined on board *Chikyu*. A. SiO₂, TiO₂, Al₂O₃, P₂O₅. B. MgO, MnO, CaO, Na₂O. C. K₂O, Fe₂O₃, Cr₂O₃.K₂OFe₂O₃

Figure F49. Schematic diagram showing the calibration applied to shipboard XRF data using shore-based XRF analyses of drill site samples.

For each element / oxide:

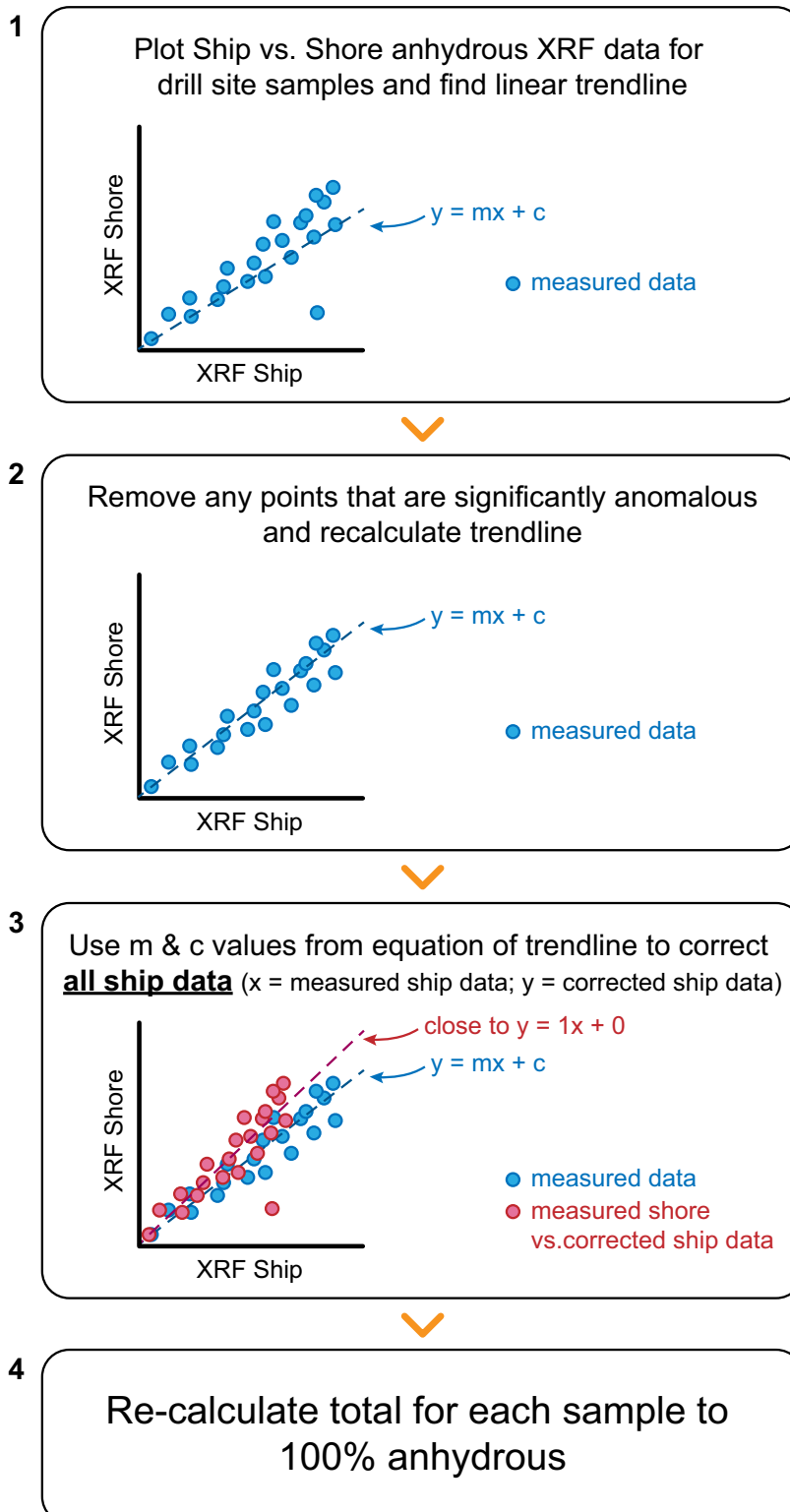


Figure F50. Photograph of the two types of pressed powder pellets prepared for trace element determination by laser ablation ICP-MS.



Figure F51. Polished grain mounts embedded in epoxy resin prepared for trace element measurement by LA-ICPMS.

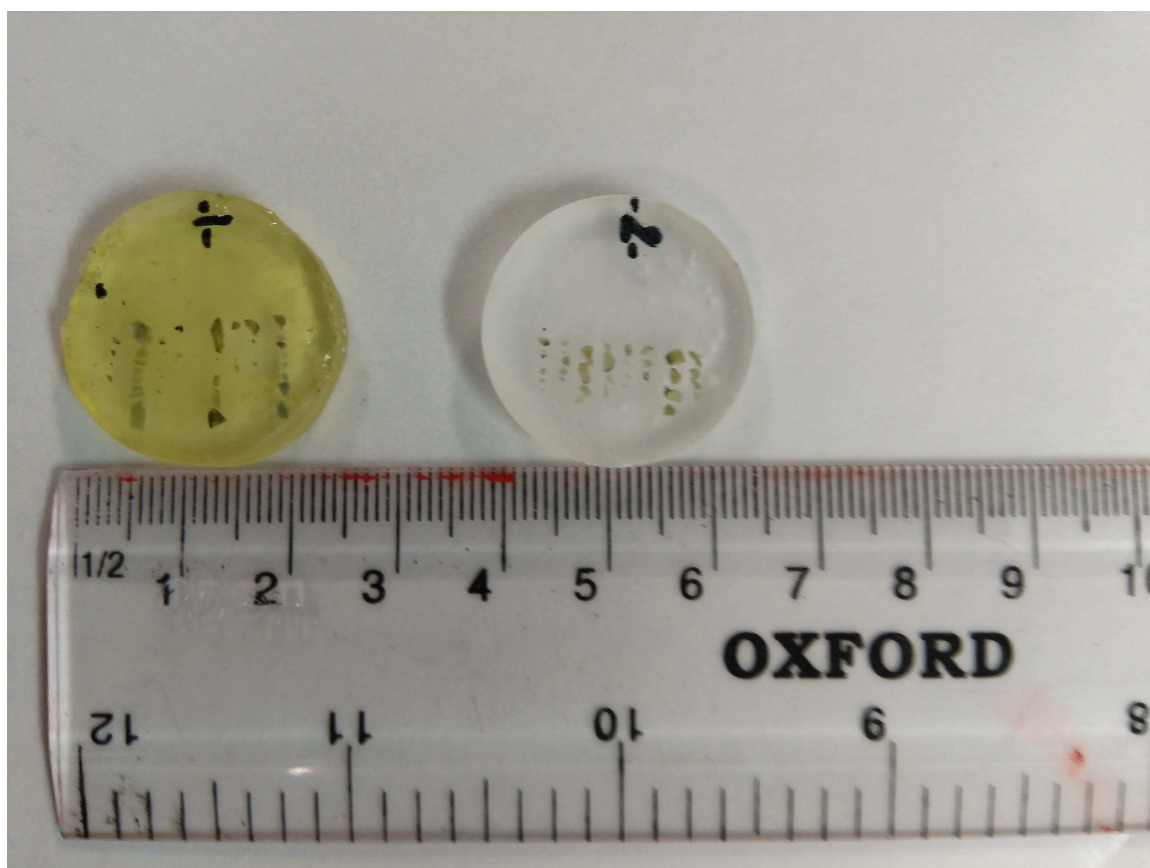
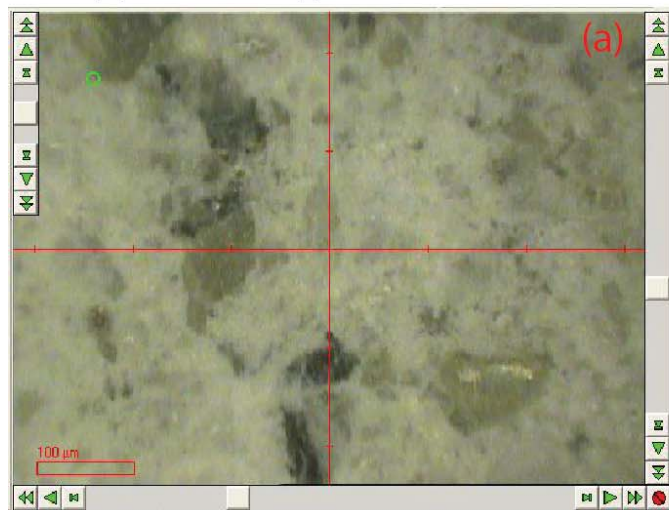


Figure F52. Pressed powder pellet before (left) and after (right) the second step milling for one sample from the Hole CM1A (top) and for the reference material BIR (bottom).

CM1A_Gabbro 6Z2_12-17



CM1A_Gabbro 6Z2_12-17



BIR-1a



BIR-1a



Figure F53. Chondrite-normalized REE patterns for (A) reference materials BHVO-2, BIR-1a, and JP-1 and (B) primitive mantle-normalized multielement patterns measured on board *Chikyu* by LA-ICP-MS using pressed powder pellets (green lines). They are compared to reference or preferred values (blue lines) from Barrat et al. (2012) for BHVO-2, from GeoREM (<http://georem.mpch-mainz.gwdg.de>) for BIR-1a, and from Rospabé et al. (2018) for JP-1. Normalizing chondrite and primitive mantle values are from Barrat et al. (2012) and McDonough and Sun (1995), respectively.

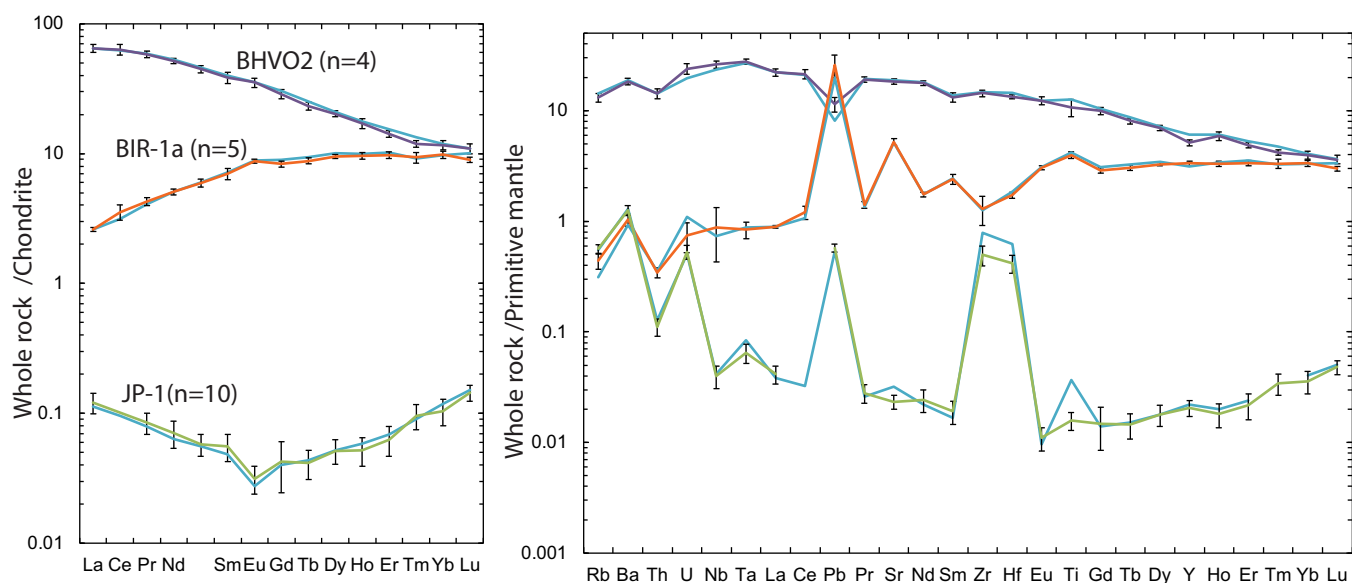


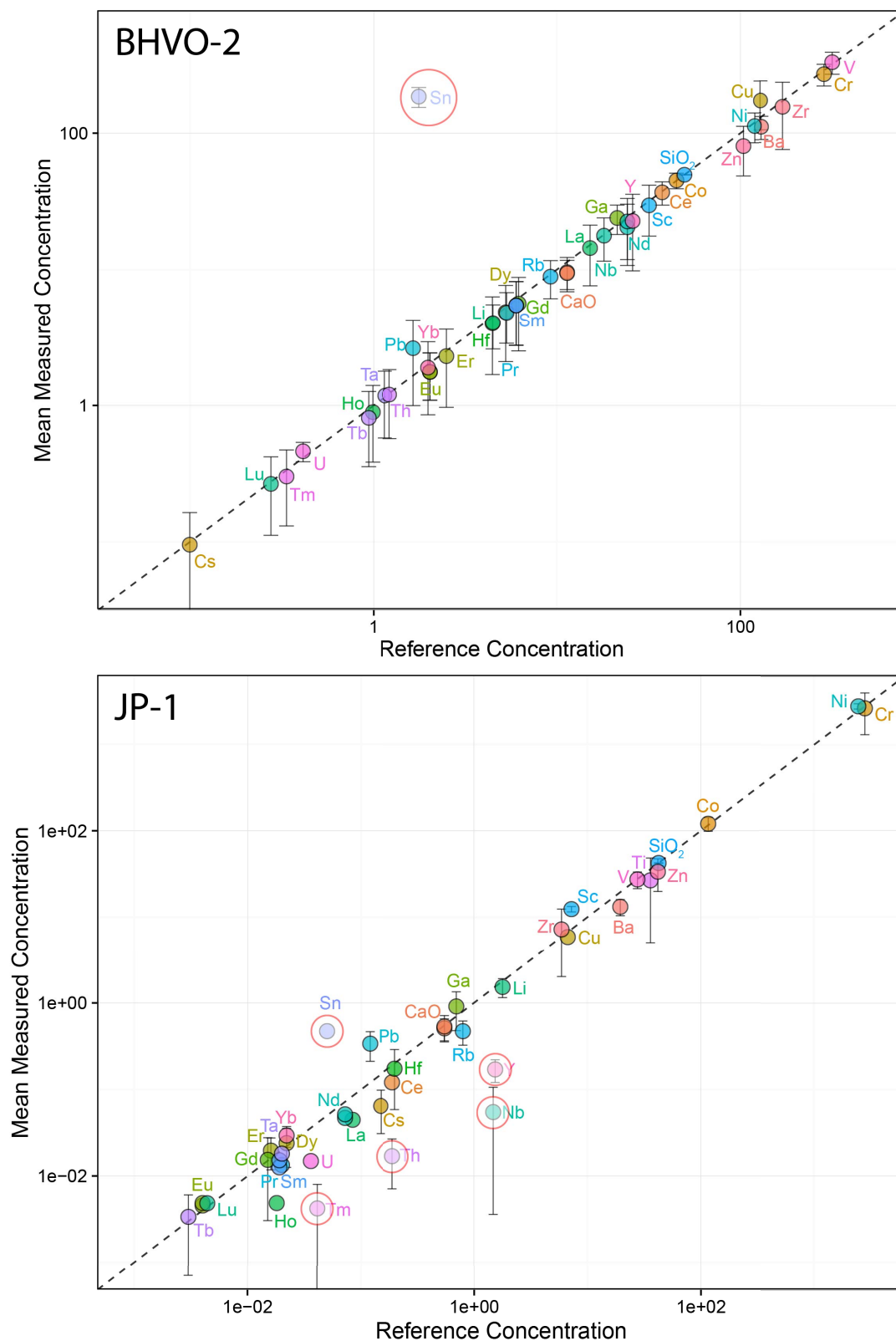
Figure F54. Secondary standard accuracy and repeatability for making count correction with LA-ICP-MS.

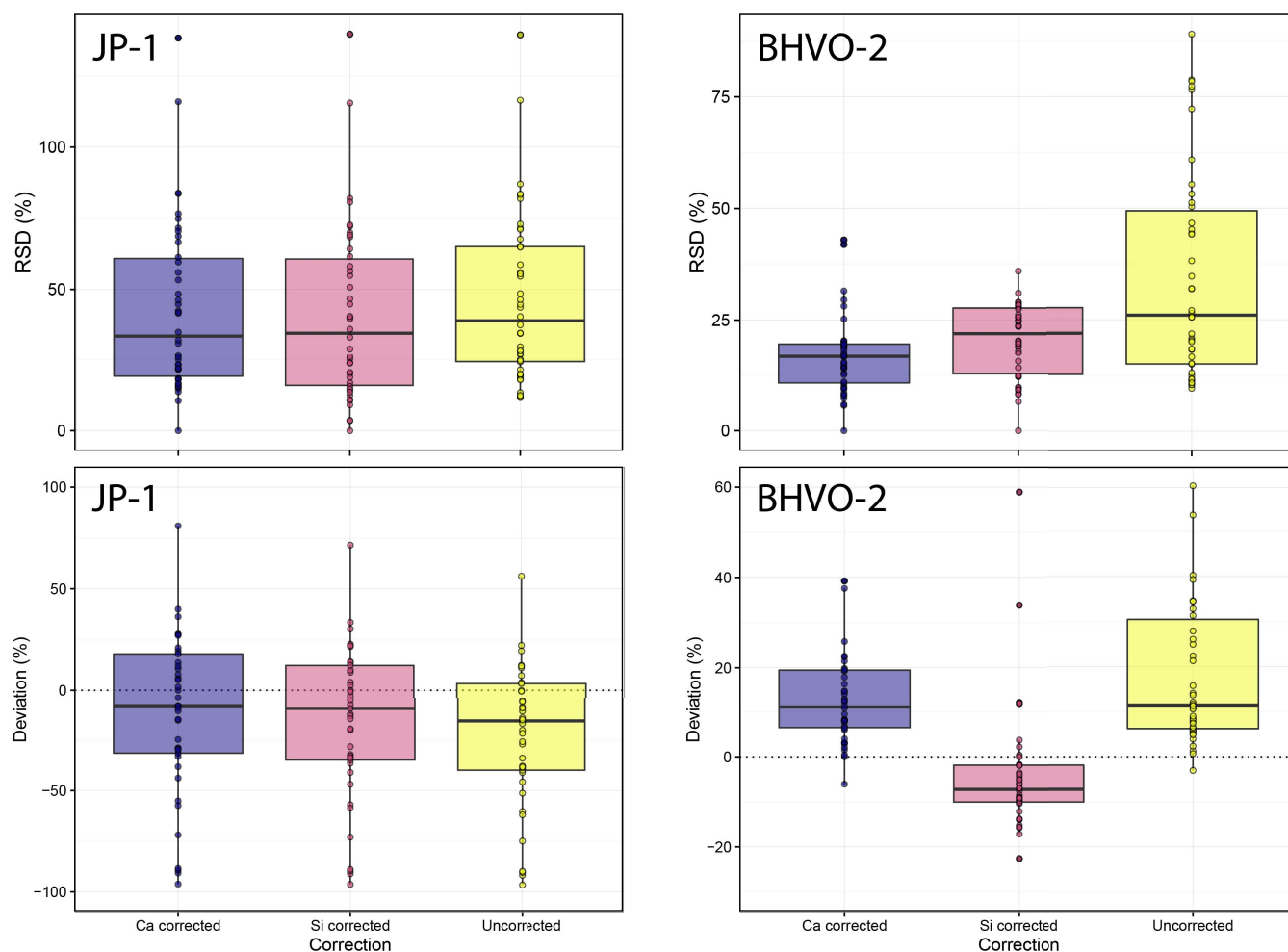
Figure F55. Accuracy for Si-standardized JP-1 and BHVO-2.

Figure F56. (A) Reference material chondrite-normalized REE and (B) primitive mantle-normalized multi-element patterns obtained on board *Chikyu* for glass plots. They are compared to reference or preferred values from Barrat et al. (2012) for BHVO-2 and from GeoREM (<http://georem.mpch-mainz.gwdg.de>) for BIR-1G. Normalizing chondrite and primitive mantle values are from Barrat et al. (2012) and McDonough and Sun (1995), respectively.

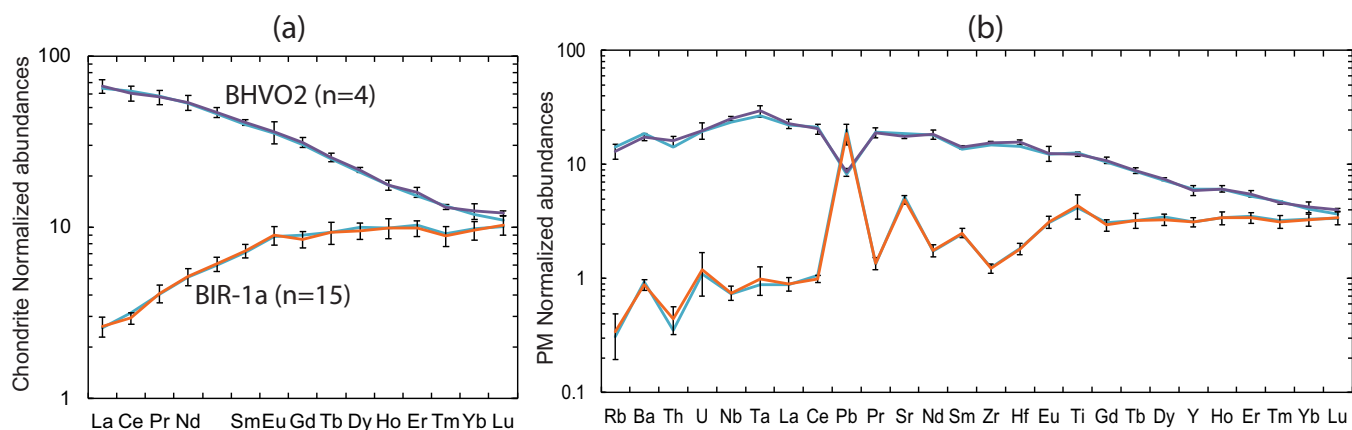


Figure F57. Comparison of Hole CM1A and CM2B whole rock trace element concentrations obtained by LA-ICP-MS (x-axis) and XRF (y-axis).

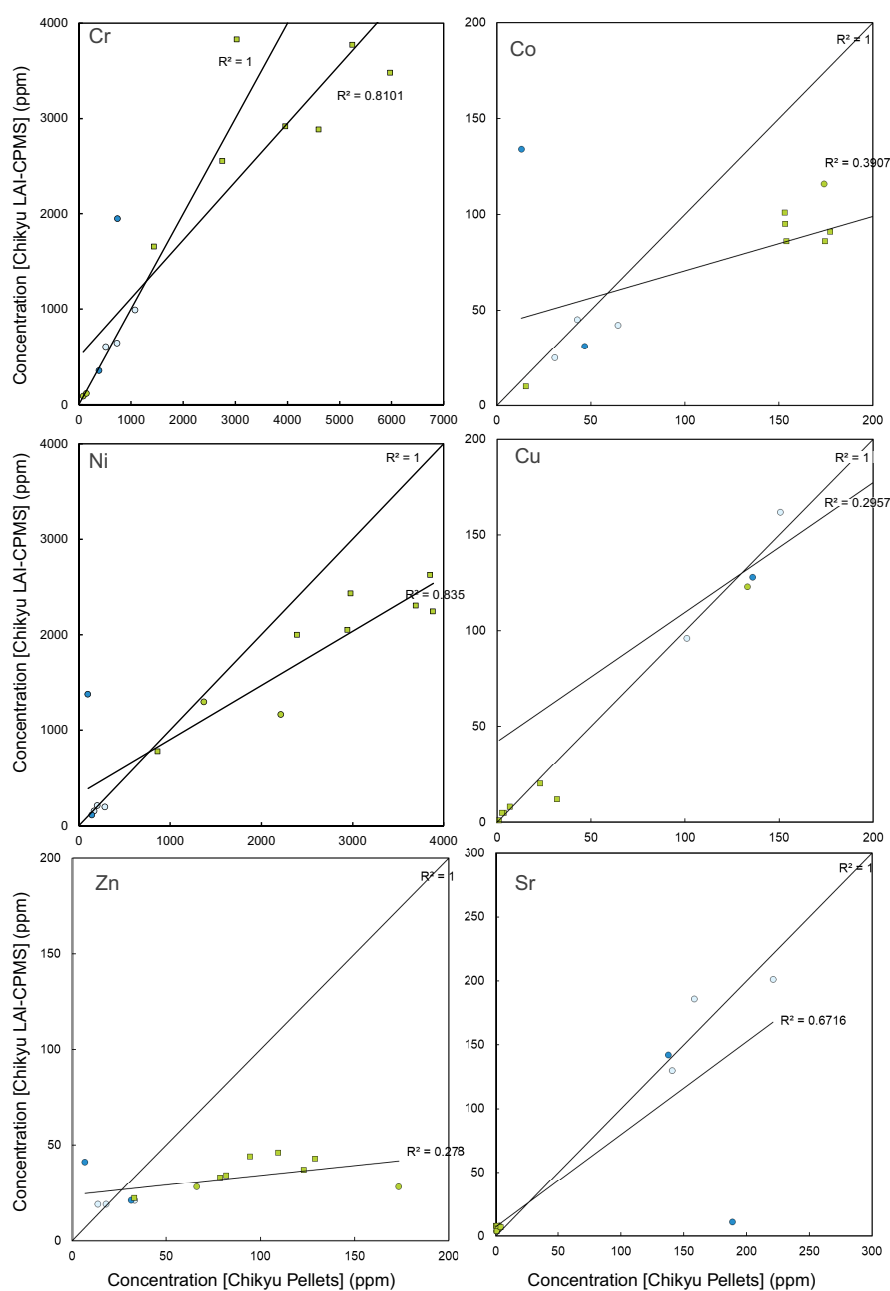


Figure F58. Calibration curves obtained for measurement of total carbon, hydrogen, nitrogen, and sulfur. Calibrations were made using NCS soil or sulfanilamide for C, sulfanilamide for H, NCS soil for N, and both standards JGb-1 and sulfanilamide for S to cover the range in concentration expected in samples. Calibrations between these different standard types are linear with R^2 no worse than 0.99978.

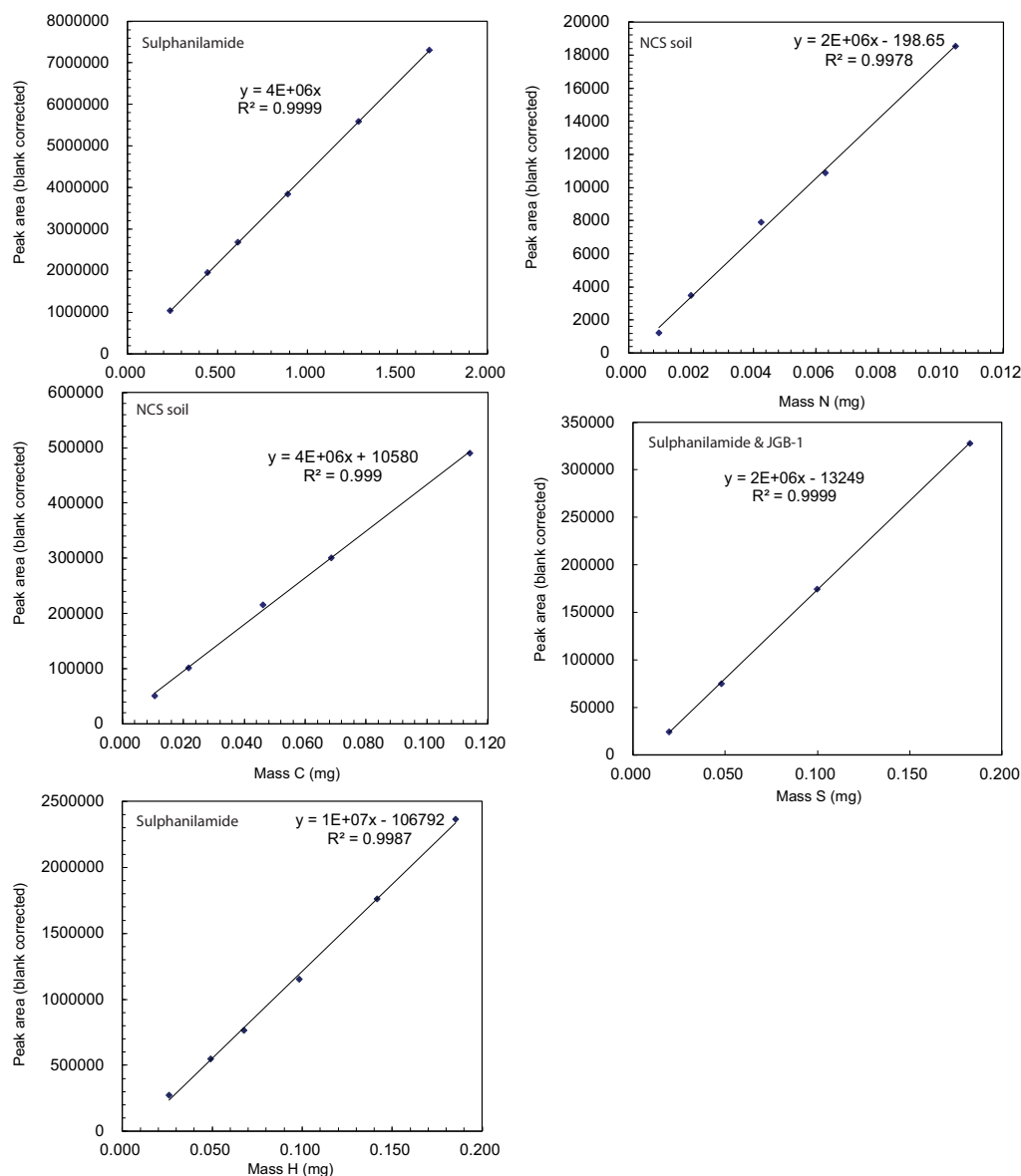


Figure F59. XRF instrument conditions.

Scan Program

Name: Revisions...

Description: ☐ Show also deleted

Last change: 7/22/2017 18:04:30
 Changed by: ADM

Diffractometer settings

☒ Use default setting View Default Settings

☐ Use other setting Diffractometer Settings...

Scan parameters

Scan type:

Scan mode:

	Actual values
Start angle ($^{\circ}2\theta$): <input type="text" value="2"/>	2.0000
End angle ($^{\circ}2\theta$): <input type="text" value="60"/>	60.0048
Step size ($^{\circ}2\theta$): <input type="text" value="0.01"/>	0.0050134
Time per step (s): <input type="text" value="20"/>	19.685
Scan speed ($^{\circ}2\theta/s$): <input type="text" value="0.0635"/>	0.032345
No. of steps: <input type="text" value="5800"/>	11570
Total time (hh:mm:ss): <input type="text" value="00:15:13"/>	00:31:12
Active length ($^{\circ}2\theta$): <input type="text" value="2.54"/>	2.5464

Delete Export... Print Save as... Save Close

Figure F60. Comparison of core-scanner XRF (CS-XRF) energy dispersive spectra (EDS) for SRM JB-1b for two beam currents and a range of counting times.

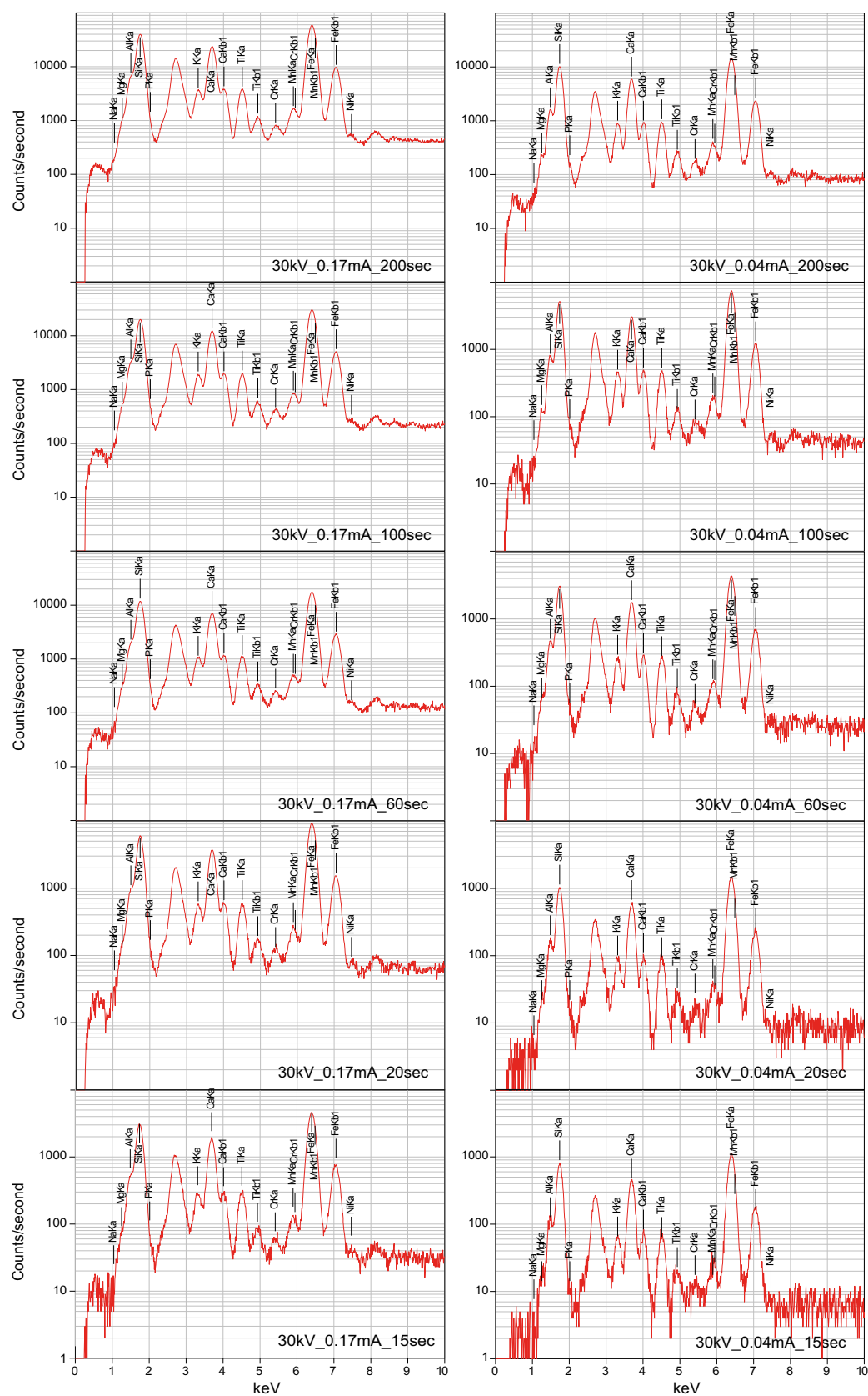


Figure F61. Calibration lines for selective elements by comparing the results of measurements by CS-XRF and by XRF at St. Andrews for 10 on-site selected samples.

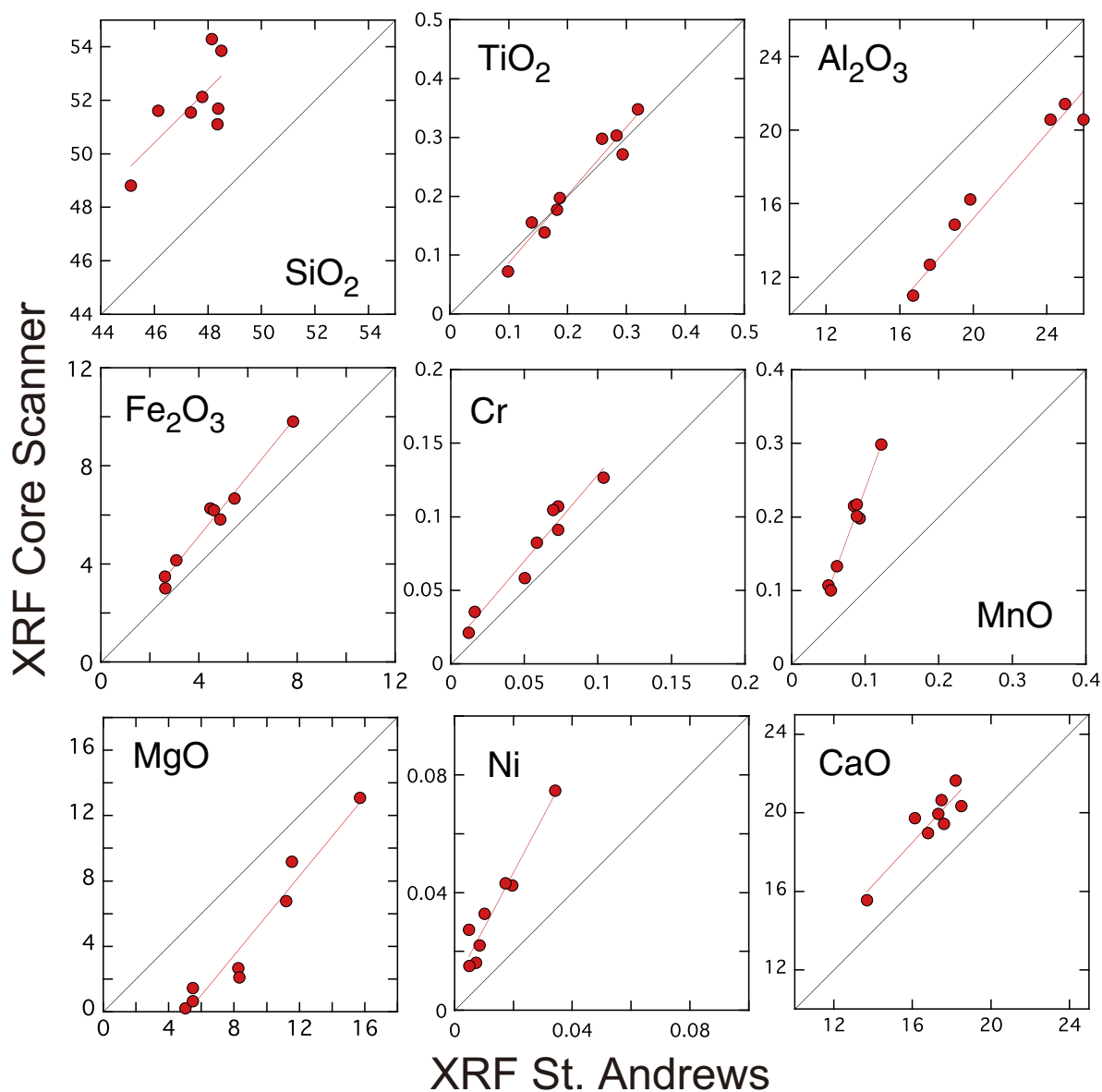


Figure F62. A–J. Major elements Cr and Ni vs. depth for interval GT1A-38Z-3, 13–40 cm. Small red spots indicate the compositions of individual spots, whereas blue spots indicate averaged compositions for each depth.

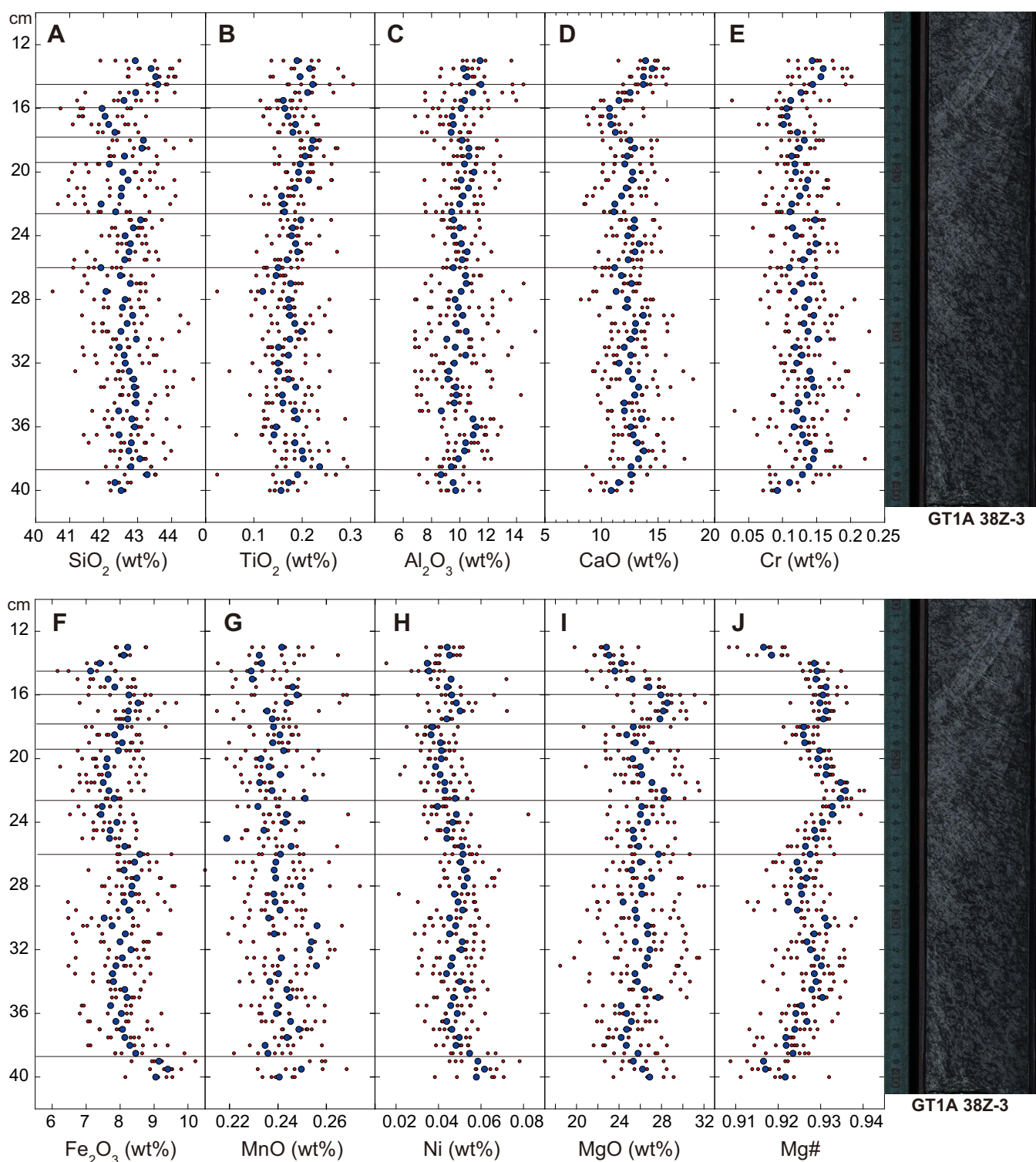


Figure F63. Element concentration maps collected by XRF-CL for Sample GT3A-52Z-3, 58–68 cm, showing an intrusion of tonalite (left side of interval) into a basalt/diabase host and cut by a later basalt dike (right side of interval).

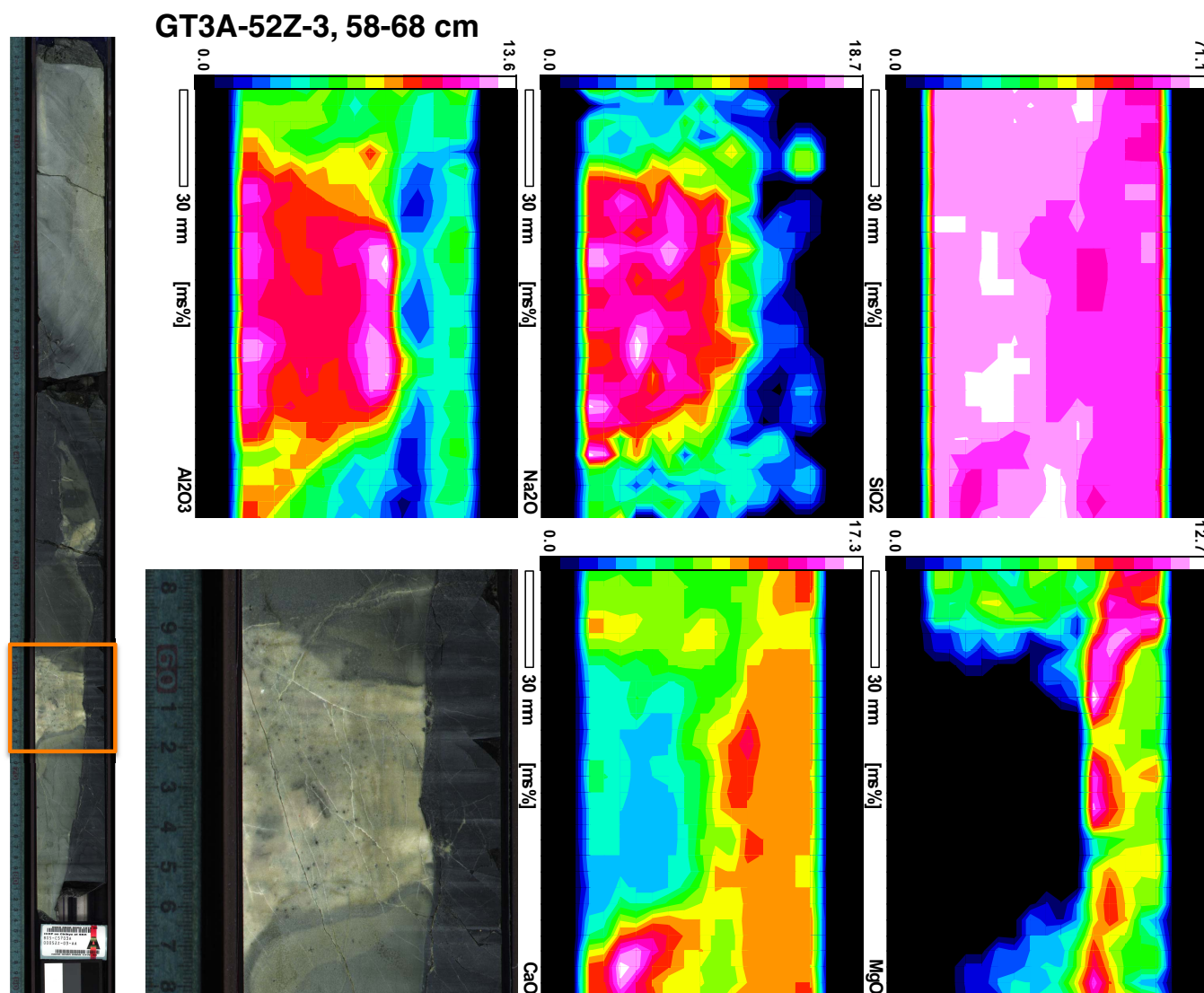


Figure F64. BIO sampling schema.

BIO SAMPLING SYSTEM

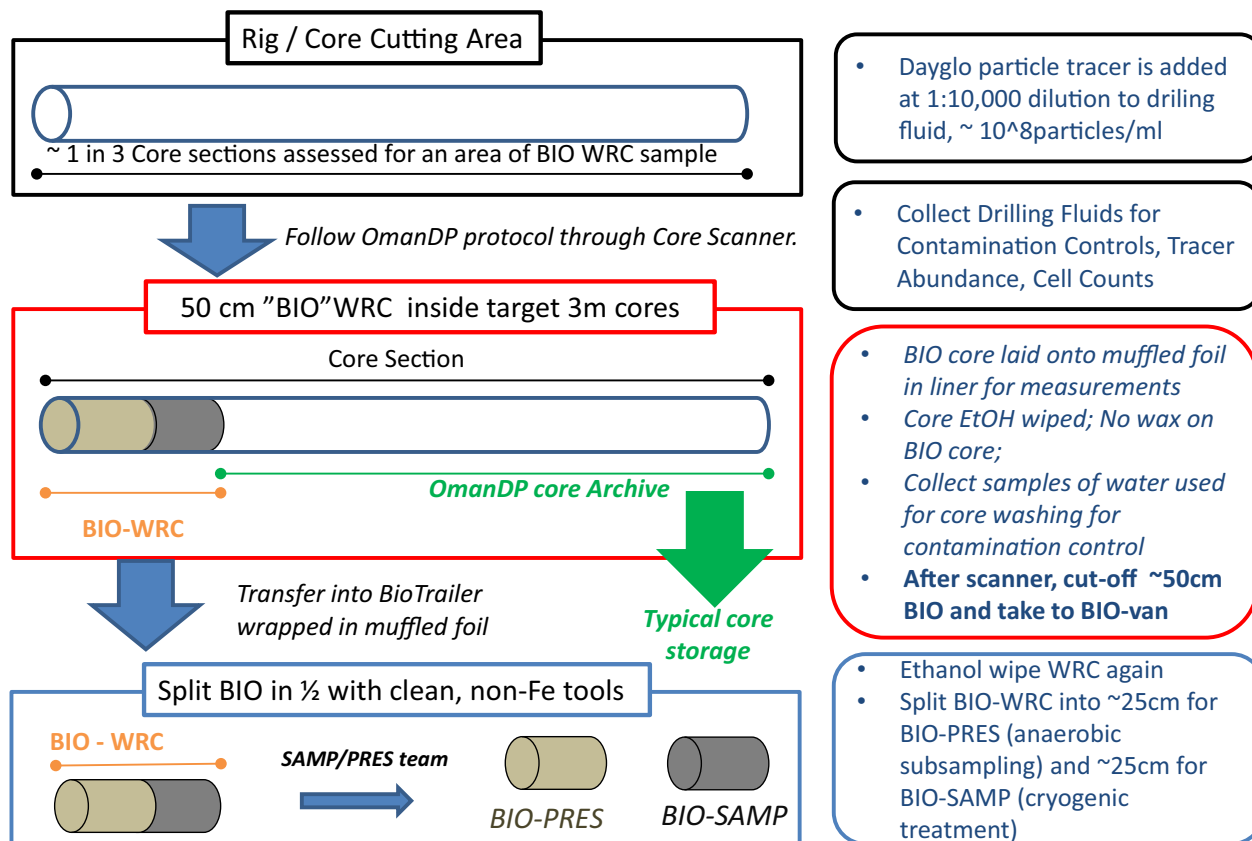


Figure F65. BIO-van where samples were prepared onsite.

BIOTRAILER ACTIVITIES

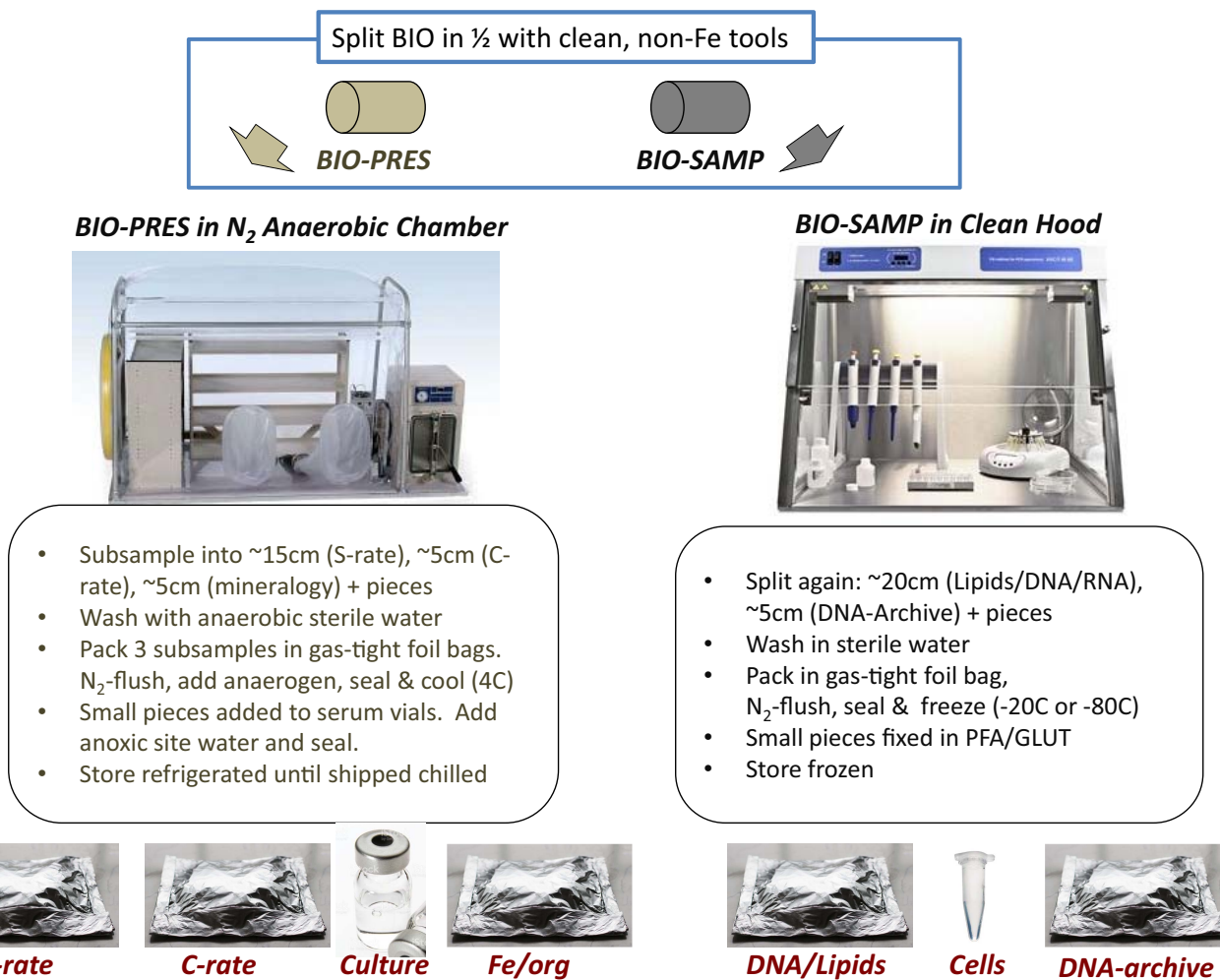


Figure F66. Photos of Dayglo tracer curve under UV light.

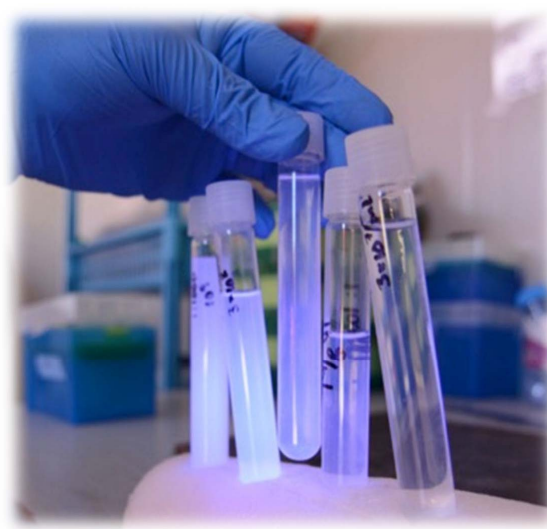


Figure F67. Fluorescence of DayGlo Blue paint in serpentinized core, under ultraviolet light.

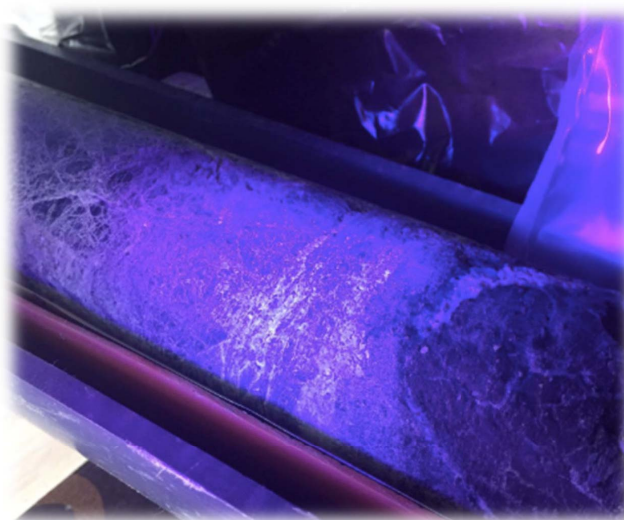


Figure F68. Normalized response functions for the SRM on the *Chikyu*.

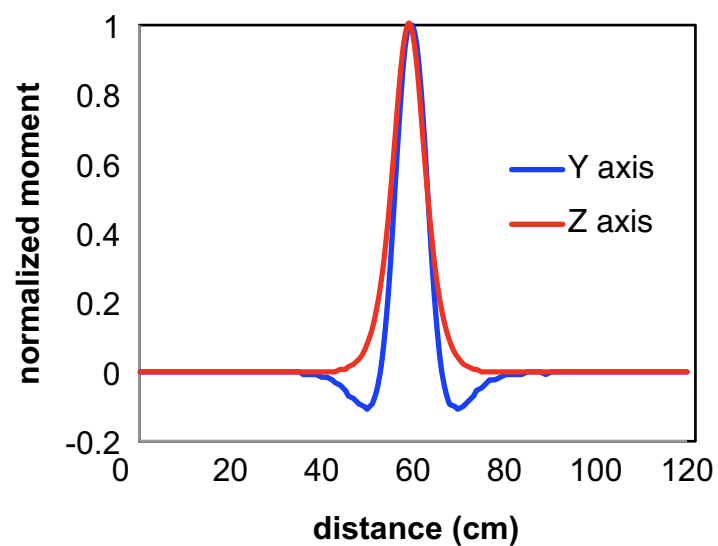


Figure F69. Schematic diagrams showing the relationship between the core axes and scanned sections. The left panel shows a 3-D voxel of 512×512 some numbers corresponding to the core length, including a red-colored cylindrical core: a large core is HQ, whereas a small core is NQ. A CT image is generated for a section parallel to the core-axis longitudinal plane (Y-Z plane) (right panel).

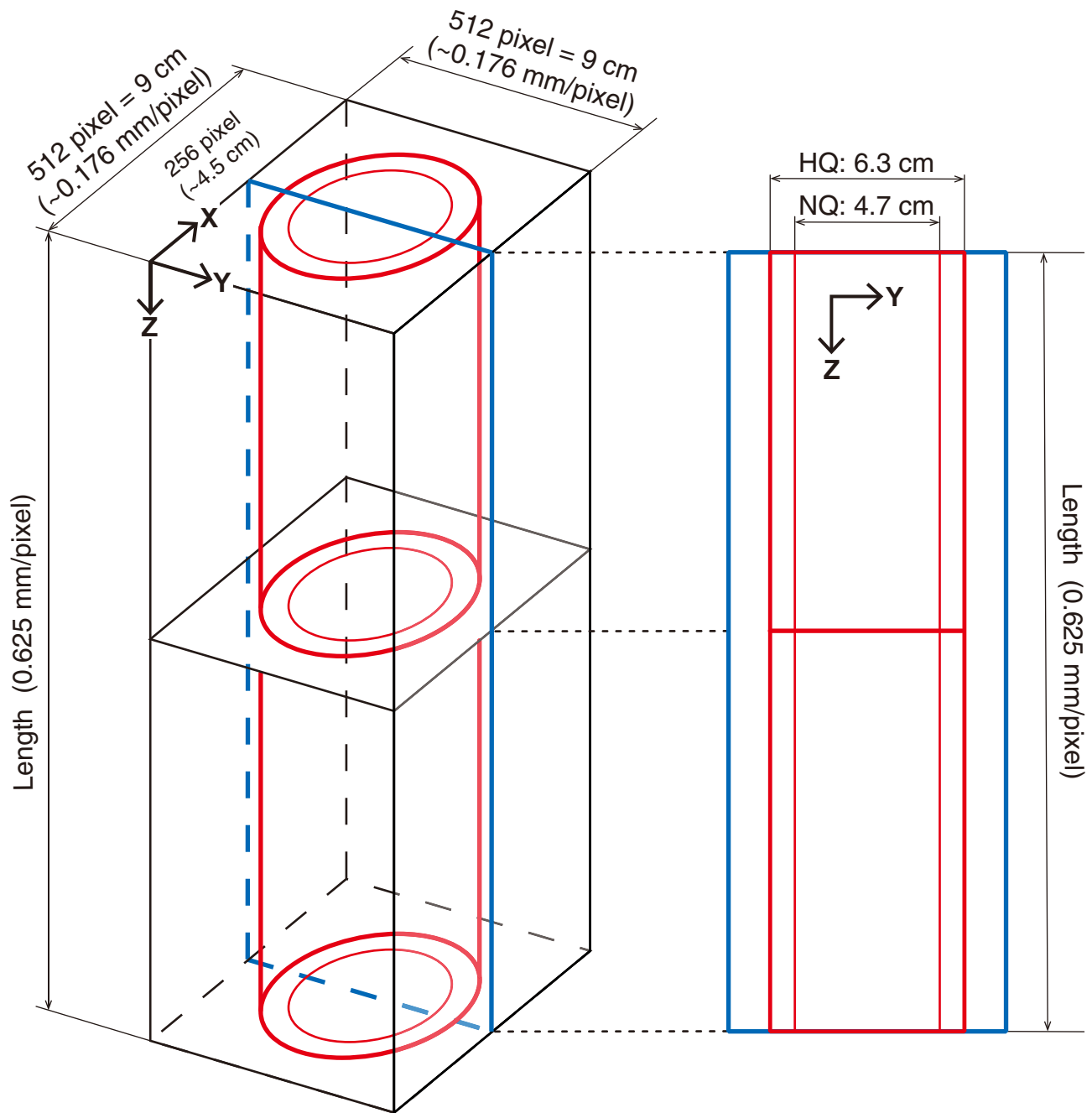


Figure F70. A. X-ray CT standards comprising three components: air, water, and a telescope-shaped aluminum cylinder with six steps (1–6 cm in diameter), and surrounding water. **B.** Slice X-ray CT images of each component of the standard piece.

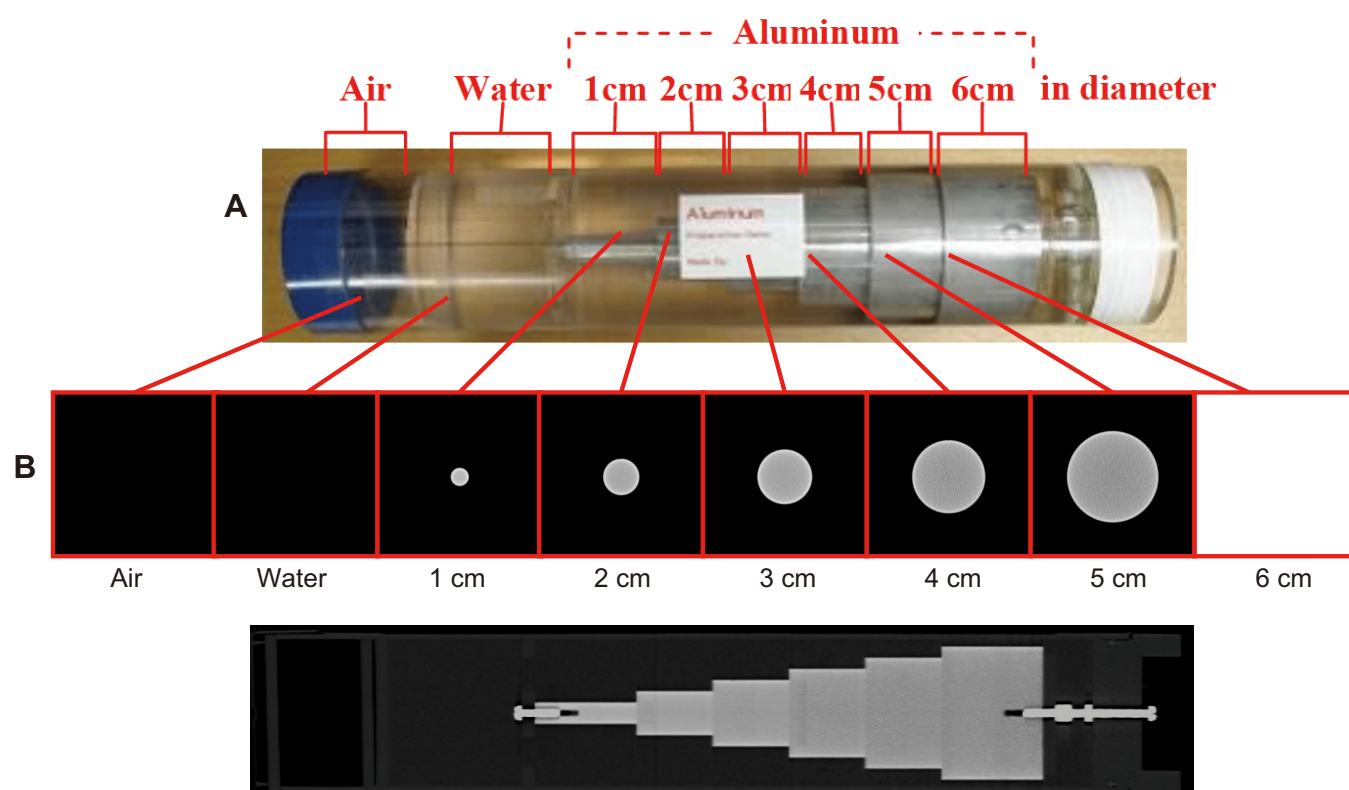


Figure F71. Information of data files and folders saved for X-ray attenuation values in DICOM format. Each data file corresponds to CT numbers with dimensions of 512×512 pixels in $9 \text{ cm} \times 9 \text{ cm}$ cross-section for a core-axis normal plane (X-Y plane). Numbers of data files depend on the actual length of a core, as a series of scan images are produced each 0.625 mm thick.

X-ray CT file format

Folder name:

000000000000111400.805C5703A001Z01.20170724T035831.zip

000000000000111400.805C5703A001Z01.20170724T035831

Chikyu# Hole# Core# Section#

File names:

1.2.840.113619.2.80.2543476764.4841.1500877677.2

a file for an image of the core section

1.2.840.113619.2.340.3.514592786.430.1500728562.572.1

the first data file

.....

1.2.840.113619.2.340.3.514592786.430.1500728562.572.10

.....

1.2.840.113619.2.340.3.514592786.430.1500728562.604.33

.....

1.2.840.113619.2.340.3.514592786.430.1500728562.988.448

1.2.840.113619.2.340.3.514592786.430.1500728563.20.449

.....

1.2.840.113619.2.340.3.514592786.430.1500728563.52.481

.....

1.2.840.113619.2.340.3.514592786.430.1500728563.564.1000

.....

1.2.840.113619.2.340.3.514592786.430.1500728563.788.1248

the last data file

For **MATLAB**, the file names may be modified as follows:

1.2.840.113619.2.340.3.514592786.430.1500728562.0572.0001 the first data file

.....

1.2.840.113619.2.340.3.514592786.430.1500728562.0988.0448

1.2.840.113619.2.340.3.514592786.430.1500728563.0020.0449

.....

1.2.840.113619.2.340.3.514592786.430.1500728563.0564.1000

.....

1.2.840.113619.2.340.3.514592786.430.1500728563.0788.1248 the last data file

Figure F72. An example image of the X-ray CT on the split surface and the optical image of the same section (Section GT1A-108Z-4).

Hole 805-C5701A-108Z Section 4

Core Photo

CT image

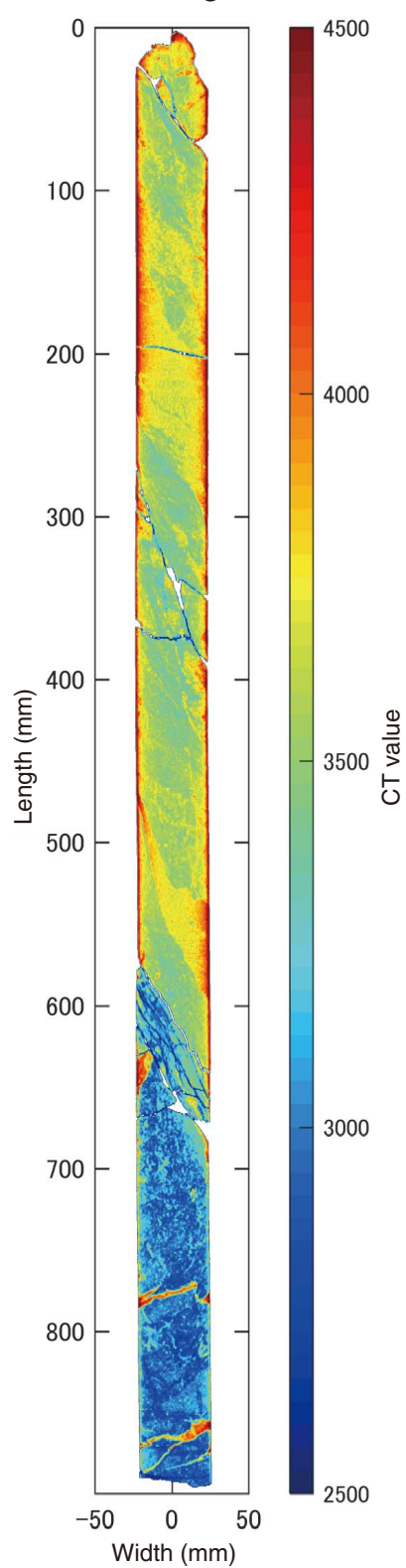


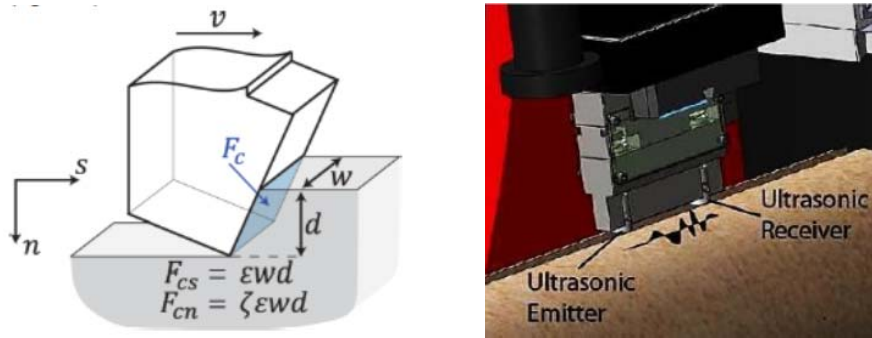
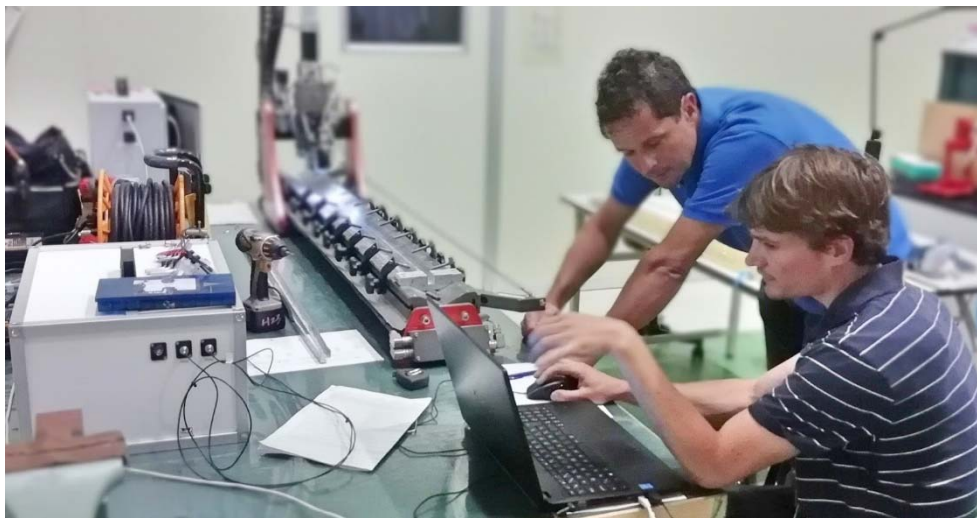
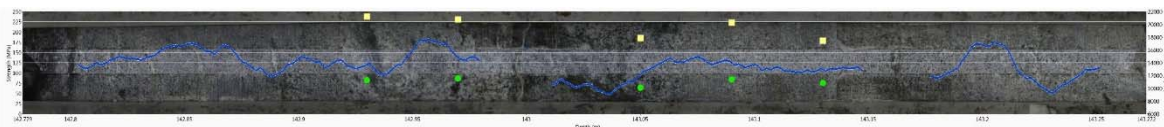
Figure F73. A. Forces acting on a sharp cutter. B. Ultrasonic V_p and V_s profiling.**Figure F74.** The last generation of the core scratcher, the wombat, in operation of selected Site CM1 cores at JAMSTEC.**Figure F75.** Measured specific energy (strength) log (blue), V_p (yellow dots), and V_s (green dots) along a core sample image.

Figure F76. Photograph of the setup of the imaging spectrometer system aboard the *Chikyu*. Before measurements began, black felt was added to block overhead lights.

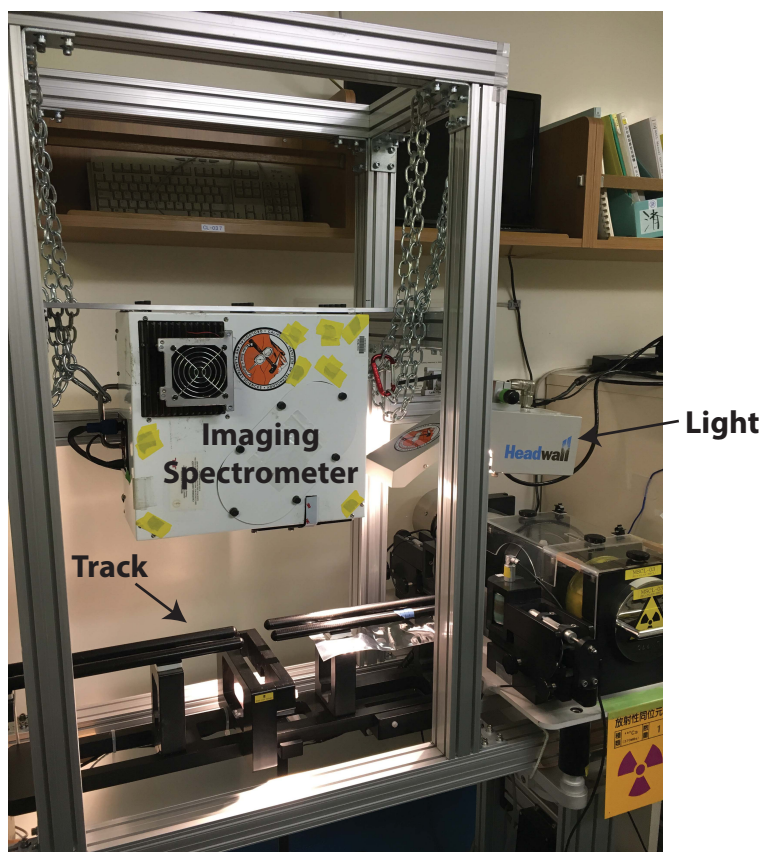


Figure F77. **A.** Image of the core section GT3A-72Z-2 with subset showing location of (B). **B.** Example 3-D image cube created using SWIR imaging spectroscopy measurements of the same core section. The spatial image is a false color infrared composite of a portion of the core with the reflectance at 2.31 μm in red, 1.58 μm in green, and 1.08 μm in blue. Color differences are related to compositional differences. The third dimension shows the intensity of reflected light as a function of wavelength for each pixel within the image, with black/purple/blue low and red high. **C.** Example spectra of different compositional units in the upper plot. Numbers correspond to points shown in (B). These spectra are likely mixtures of multiple minerals. The bottom plot contains spectra from the US Geological Survey spectral library (Clark et al., 2007). Hornblende is sample NMNH117329, epidote is GDS26.a (75–200 μm particle size), and chlorite is SMR-13.b (60–140 μm). Spectra in both plots are offset for clarity.

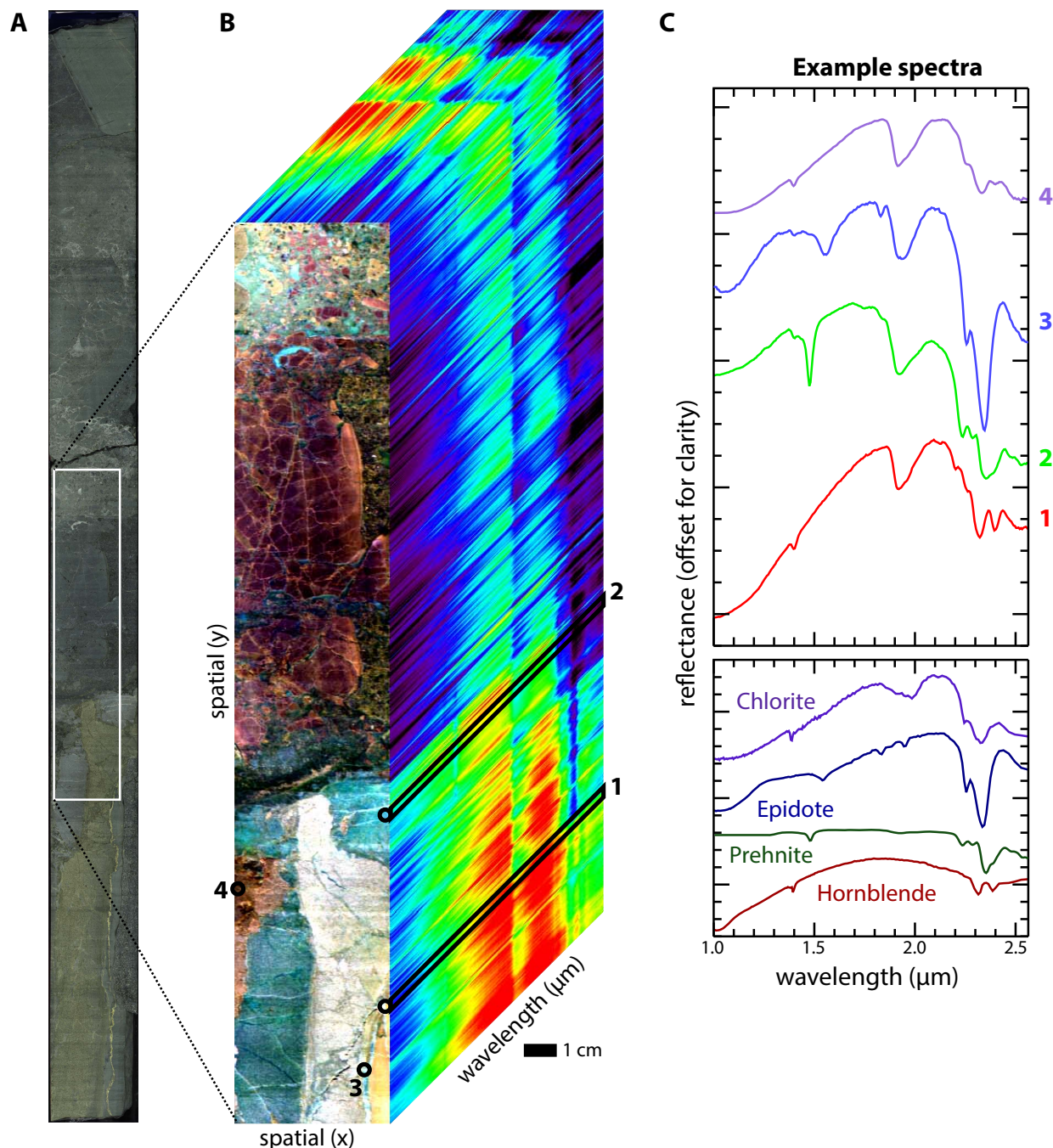


Figure F78. Photograph of the setup of the imaging spectrometer system aboard the *Chikyu*.

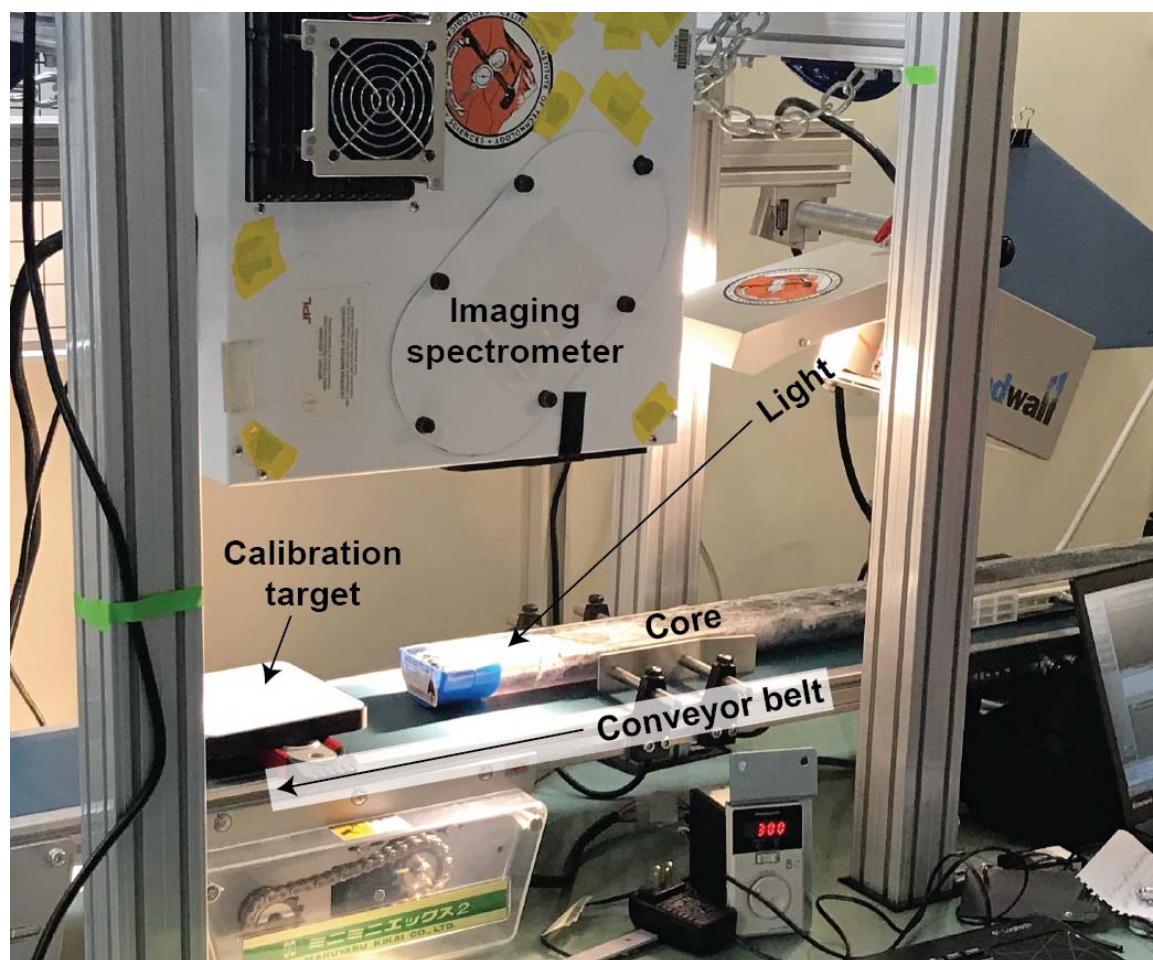


Figure F79. Ministry of Regional Municipalities and Water Resources Toyota wireline logging truck, equipped with a Robertson Geologging winch.



Figure F80. Ministry of Regional Municipalities and Water Resources GM wireline logging truck, equipped with a GeoVista winch.



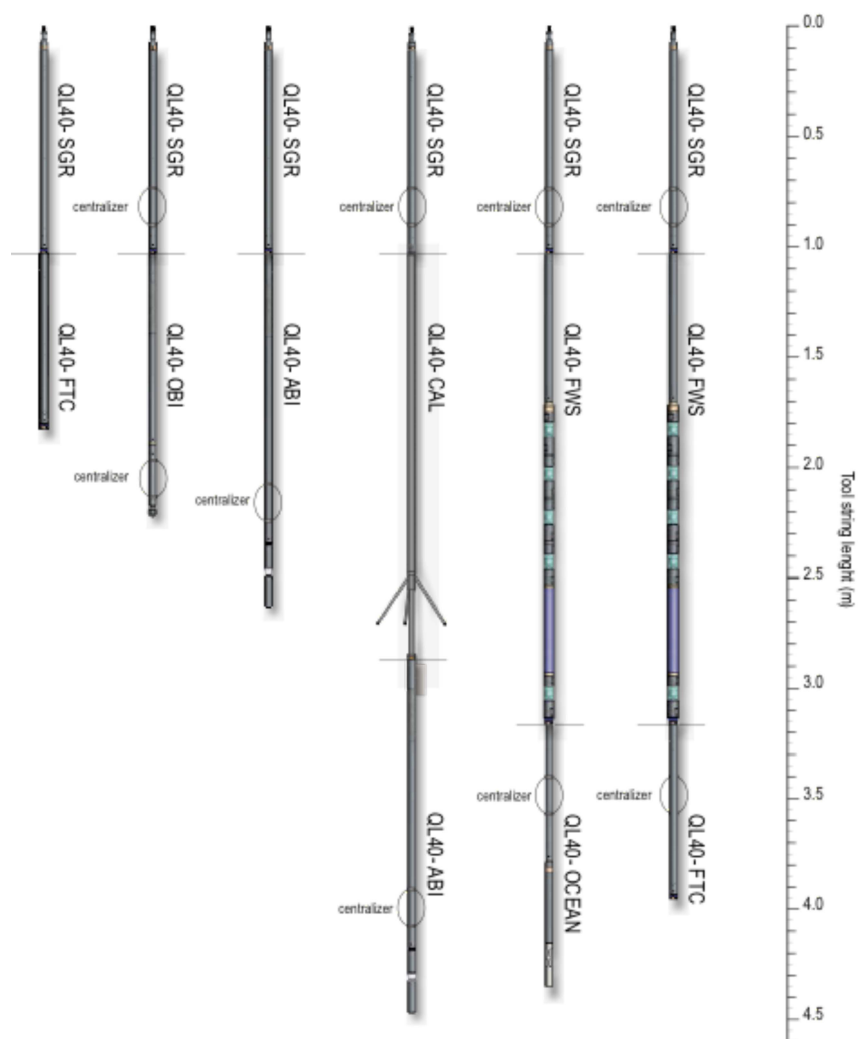
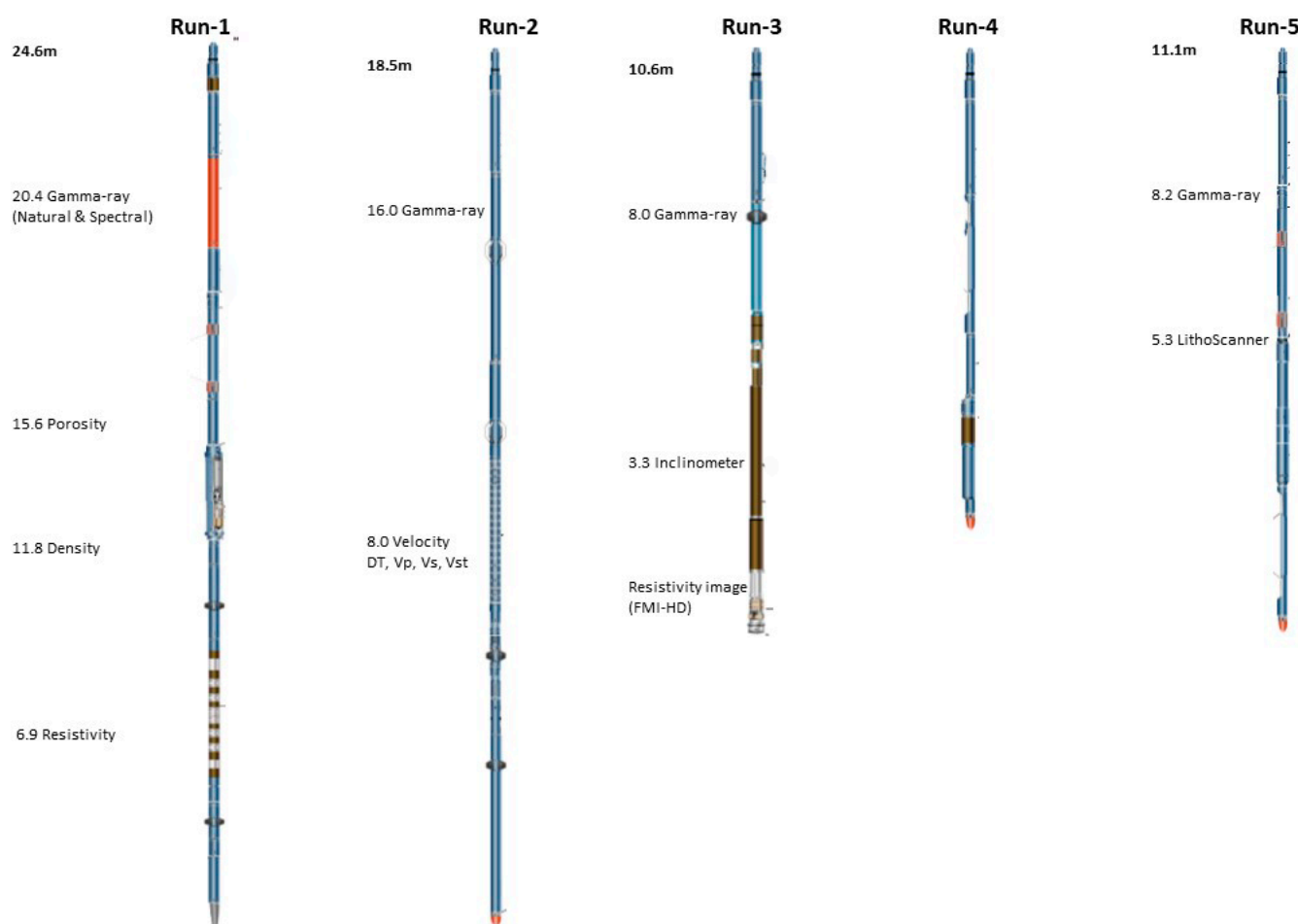
Figure F81. Slimline wireline tool strings (showing all ALT probes).

Figure F82. Schlumberger wireline tool strings for Sites CM1 and CM2. **A.** Run 1 PEX-HRLA-GR. **B.** DSI-GR. **C.** FMI-GR. **D.** ECS-GR. **E.** NEXT-GR. See Table T54 for tool acronyms and measurement specifications.



Tables

Table T1. Database designations for OmanDP cores/samples. [This table is available in Microsoft Excel format.](#)

Table T2. Database information for samples collected during OmanDP Phases 1 and 2. [This table is available in Microsoft Excel format.](#)

Table T3. Operations at all sites. [This table is available in Microsoft Excel format.](#)

Table T4. Alteration and metamorphic petrology glossary. [This table is available in Microsoft Excel format.](#)

Table T5. Mineral abbreviations for metamorphic petrology, Phase 1. [This table is available in Microsoft Excel format.](#)

Table T6. Alteration textures glossary. [This table is available in Microsoft Excel format.](#)

Table T7. Mineral abbreviations, Phase 2. [This table is available in Microsoft Excel format.](#)

Table T8. Minerals and chemical formulas for Site BT1. [This table is available in Microsoft Excel format.](#)

Table T9. Summary of major elements on beads, Legs 1–4. [This table is available in Microsoft Excel format.](#)

Table T10. Summary of trace elements on pellets, Legs 1–4. [This table is available in Microsoft Excel format.](#)

Table T11. Interlaboratory comparison of major elements by XRF, Leg 1. [This table is available in Microsoft Excel format.](#)

Table T12. Interlaboratory comparison of trace elements by XRF, Leg 1. [This table is available in Microsoft Excel format.](#)

Table T13. Interlaboratory comparison of trace elements by XRF, Leg 2. [This table is available in Microsoft Excel format.](#)

Table T14. Interlaboratory comparison of major elements by XRF, Leg 2. [This table is available in Microsoft Excel format.](#)

Table T15. Rock sample digestion and ICP-MS analyses. [This table is available in Microsoft Excel format.](#)

Table T16. ICP-MS operating parameters for trace elements, Phase 1. [This table is available in Microsoft Excel format.](#)

Table T17. Reproducibility and accuracy for AFAD/ICP-MS. [This table is available in Microsoft Excel format.](#)

Table T18. Procedure blanks for AFAD/ICP-MS. [This table is available in Microsoft Excel format.](#)

Table T19. Instrument blanks for AFAD/ICP-MS analysis. [This table is available in Microsoft Excel format.](#)

Table T20. Preferred methods for trace and REEs in Site GT and BT samples. [This table is available in Microsoft Excel format.](#)

Table T21. Interlaboratory comparison of methods for major and trace element analyses on SRM JB1-b. [This table is available in Microsoft Excel format.](#)

Table T22. Interlaboratory comparison of methods for major and trace element analyses on SRM JGb-1. [This table is available in Microsoft Excel format.](#)

Table T23. Interlaboratory comparison of methods for major and trace element analyses on SRM JGb-2. [This table is available in Microsoft Excel format.](#)

Table T24. CHNS QA/QC summary, Leg 1. [This table is available in Microsoft Excel format.](#)

Table T25. Inorganic C/carbonate QA/QC summary, Leg 1. [This table is available in Microsoft Excel format.](#)

Table T26. CHN calibration standards, Leg 1. [This table is available in Microsoft Excel format.](#)

Table T27. S calibration standards, Leg 1. [This table is available in Microsoft Excel format.](#)

Table T28. Inorganic C/carbonate QA/QC summary, Leg 2. [This table is available in Microsoft Excel format.](#)

Table T29. S calibration standards, Leg 2. [This table is available in Microsoft Excel format.](#)

Table T30. CHN calibration standards, Leg 2. [This table is available in Microsoft Excel format.](#)

Table T31. XRD hardware/software operation parameters. [This table is available in Microsoft Excel format.](#)

Table T32. Instruments used during OmanChikyu Phase 1. [This table is available in Microsoft Excel format.](#)

Table T33. Preferred methods for trace and REEs, Leg 3. [This table is available in Microsoft Excel format.](#)

Table T34. Trace element reproducibility and accuracy for glass bead and pellet SRMs by LA-ICP-MS, Leg 3. [This table is available in Microsoft Excel format.](#)

Table T35. LA-ICP-MS operating parameters, Leg 4. [This table is available in Microsoft Excel format.](#)

Table T36. Trace element reproducibility and accuracy for glass bead and pellet SRMs by LA-ICP-MS, Leg 4. [This table is available in Microsoft Excel format.](#)

Table T37. CHNS QA/QC summary, Leg 3. [This table is available in Microsoft Excel format.](#)

Table T38. Inorganic C/carbonate QA/QC summary, Leg 3. [This table is available in Microsoft Excel format.](#)

Table T39. CHN calibration standards, Leg 3. [This table is available in Microsoft Excel format.](#)

Table T40. S calibration standards, Leg 3. [This table is available in Microsoft Excel format.](#)

Table T41. CHN calibration standards, Leg 4. [This table is available in Microsoft Excel format.](#)

Table T42. S calibration standards, Leg 4. [This table is available in Microsoft Excel format.](#)

Table T43. Inorganic C/carbonate QA/QC summary, Leg 4. [This table is available in Microsoft Excel format.](#)

Table T44. Instruments used during OmanChikyu, Leg 4. [This table is available in Microsoft Excel format.](#)

Table T45. Instrument settings for CS-XRF for hard rock elemental analysis. [This table is available in Microsoft Excel format.](#)

Table T46. Best-fit line parameters for SRM analyzed by CS-XRF under a range of instrumental conditions. [This table is available in Microsoft Excel format.](#)

Table T47. Major element and Cr and Ni in SRM JB-1b compared to Expedition 343/343T and ChikyuOman analyses by CS-XRF. [This table is available in Microsoft Excel format.](#)

Table T48. Best-fit line parameters for archive-half samples analyzed by CS-XRF at beam current = 0.04 mA and count time = 60 s per spot. [This table is available in Microsoft Excel format.](#)

Table T49. Reproducibility of CS-XRF over 5 days. [This table is available in Microsoft Excel format.](#)

Table T50. Interlaboratory comparison of major elements, Cr, and Ni determined by CS-XRF compared to St. Andrews. [This table is available in Microsoft Excel format.](#)

Table T51. Microbiology subsampling scheme. [This table is available in Microsoft Excel format.](#)

Table T52. Sulfate reduction samples taken from BA holes. [This table is available in Microsoft Excel format.](#)

Table T53. Depths of samples taken for mineralogy/spectroscopy studies from BA holes. [This table is available in Microsoft Excel format.](#)

Table T54. Wireline slimline probes and measurement specifications. [This table is available in Microsoft Excel format.](#)

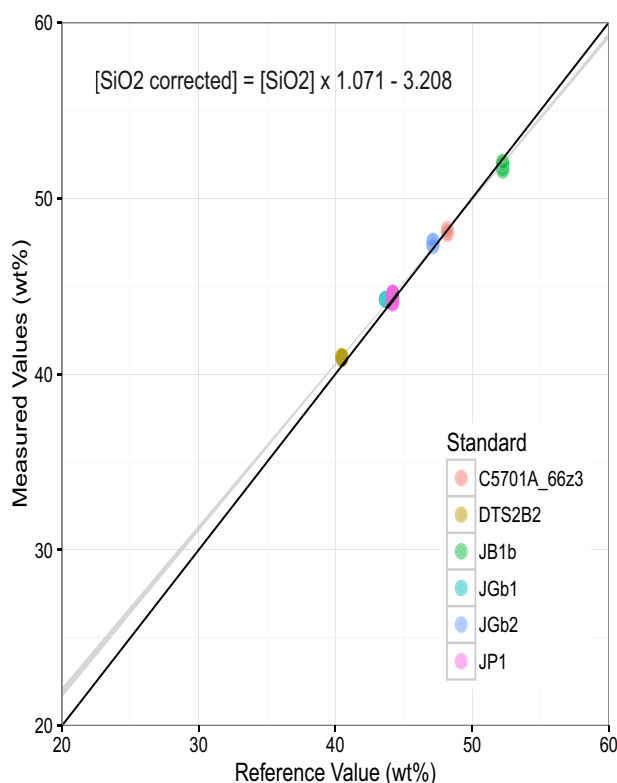
Table T55. Operations/acquisition during slimline wireline logging surveys, Phase 1. [This table is available in Microsoft Excel format.](#)

Table T56. Operations/acquisition during slimline wireline logging surveys, Phase 2. [This table is available in Microsoft Excel format.](#)

Table T57. Measurement specifications of the Schlumberger wireline logging tools. [This table is available in Microsoft Excel format.](#)

Appendix A

Linear correction for silica, Hole BT1B



Appendix B

Procedure for alkali fusion/acid digestion for ICP-MS

Precautions

Special care must be taken at all times to prevent contamination. Wash your hands with soap and rinse thoroughly before you start or return to experiments, so that you are free from contamination.

All the acids used are highly corrosive! Wear plastic gloves anytime you deal with them.

A. Weighing

1. Weigh sample 0.1000 ± 0.0005 g.
2. Weigh Na₂CO₃ (anhydrous) 0.5000 ± 0.0005 g (in separate, labeled weighing papers).

B. Acid digestion

1. Place sample powder in the bottom of the Pt crucible (don't touch the side walls).
2. Add 1 mL HClO₄ to the sample with a 1000 mL pipette, and ensure the sample is wet.
CAUTION: Add HClO₄ first. Direct addition of HF may cause an explosive reaction!
CAUTION: HClO₄ reacts explosively with carbon and organic matter. Be sure NO carbon or organic is present in the sample or crucible!
3. Add 1 mL 40% HF.
4. Place the crucible on a hot plate and gradually increase temperature (i.e., 5 min at 100°C, 5 min at 150°C, up to 200°C. Hold at 200°C until all acids have evaporated to dryness (this will take ~3 h).
 - Note: Use this time to weigh and wash the polyethylene bottles for Step D. Write [bottle weight (without lid)] and [sample number] on the bottle wall, then wash in Milli-Q water.

CAUTION: Ensure complete dryness; otherwise, acids will react explosively with alkali flux in the next step!

5. Remove crucible from hot plate and allow to cool (5 min) before the next step.

C. Alkali fusion

1. Add 0.5 g Na_2CO_3 to the sample and cover.
2. Place crucibles in the muffle furnace at 1050°C , using Pt-tipped tongs.
3. Hold at $>900^\circ\text{C}$ for 10 min, then remove.
4. Allow to cool before the next step.

CAUTION: Muffle furnace is very hot; use safety gloves and Pt tongs! Do not let the crucibles touch each other, and handle carefully (they are easily deformed at high T).

D. Acid digestion and recovery

1. Add 5 mL HNO_3 using a 5 mL pipette and several drops of HF using a 200 mL pipette to each crucible.
CAUTION: The fused alkali-sample mixture reacts explosively with acid. Add small amounts of acid dropwise in the beginning until the reaction ceases.
2. Heat crucible at 100°C until flux-sample mixture is partially dissolved (at least 10 min).
3. Add 10 mL Milli-Q water (deionized water). Add slowly to avoid excessive reaction and potential loss of sample aerosol.
4. Heat for 20 min.
5. Transfer solution from Pt crucible to polyethylene bottle quantitatively, rinsing with Milli-Q water in Teflon bottle. Take care to transfer all undissolved material, if present.
• NOTE: Polyethylene bottles should have been weighed and washed before this stage!
6. Add 10 mL HCl, several drops of HF, and 5 mL H_2O to the Pt crucibles.
7. Heat at 150°C until the residue is dissolved (if present).
8. Continue heating for 30 min.
9. Transfer solution quantitatively to polyethylene bottle rinsing with Milli-Q water repeatedly (at least 3 times), so that complete transfer is achieved.
• NOTE: Do not skip Steps 6–9 even if no residue exists after HNO_3 dissolution. This step is important for HFSE recovery.

E. Dilution

1. Place polyethylene bottle on the top-loading electric balance, and add Milli-Q water until ([solution] + [bottle]) weight in grams reaches ([100] + [bottle]) weight in grams.
2. Screw cap on firmly.
3. Solution should be kept at room temperature to prevent evaporation.

Appendix C

Brief Manual for Retsch BB50 Jaw Crusher

Geochemical samples were selected during the daily ChikyuOman Phase 2 sampling meetings in consultation with the core description teams. Shipboard samples were cut from the working half of the core as 5 cm (HQ) to 8 cm long (NQ) quarter-round core sections (HQ core: ~100 g; NQ core: 60 g). A diamond-impregnated continuous-rim edged lapidary rock slab saw blade was used to carefully cut rock samples and to remove alteration rinds. The samples were cut into thin slices to facilitate crushing to a <1 mm grit. Contamination from drilling and sawing was removed by grinding. The slices were ultrasonicated in Milli-Q deionized water (18.2 M Ω) for consecutive rounds until the Milli-Q water was clear with no turbidity. The cleaned pieces were then dried at 105°C for at least 8 h.

The first steps of the crushing procedure were modified for samples from Holes CM1A and CM2B. The new “Retsch BB50” jaw crusher was purchased by the Oman Drilling Project and used for crushing the OmanDP Phase 2 samples to a <1 mm grit. We used steel 1.1750 breaking jaws and wearing plates to avoid heavy metal contamination. This jaw crusher is well suited for gently crushing relatively small samples with large feed sizes and with minimal loss. This short document describes the operating procedures for the Retsch BB50 jaw crusher during ChikyuOman Phase 2 (2018).

How to use

The main switch can be found on the back of the machine. After turning the power ON, the display will show the gap width between the crushing plates and the stroke frequency. The machine is started by pressing the START button. Turn the hand wheel clockwise until a clicking sound comes from the contact of the crusher jaws. Press the RESET button. The display should now show 00.0/ for the current gap width. The grinding speed should be set at 550–950 strokes per minute. The stroke speed can be adjusted using the “plus” and “minus” buttons located just below the display.

Do not put any sample in the grinder chamber before starting the machine. After starting the crusher put small sample chunks in to the hopper through the sample window (6 cm). During ChikyUOman Phase 2, whole-rock samples were ground in four steps, starting with a 14 mm jaw gap, decreasing to 7 mm, 4 mm, and 1 mm in progressive steps. The crusher jaw-gap is increased by turning the handwheel in an anti-clockwise direction and decreased by rotating in the opposite direction. The crushed samples are collected in the sample receptacle. The receptacle should be pulled out, emptied, and put back into position between each crushing run, before decreasing the jaw-gap of the crusher. The process is repeated until the sample is reduced to the desired grain size (<1 mm).

Cleaning procedure

Every part of this crusher that comes into contact with samples can be separated for cleaning. Pull the release handle and fold back the fill hopper. Remove the grinding chamber cover by sliding forward. Remove the side bolt to detach frontal breaking jaw and pull that out. Clean all metal parts using laboratory ethanol because the jaw materials are not made of stainless steel and are consequently easily oxidized by cleaning water. Finally, pull out the sample receptacle, wash it first with water, then dry with paper towel and clean with ethanol. Reassemble the jaw crusher.

Appendix D

Brief manual for LOI and glass bead making

Loss on ignition

1. Calibrate the balance with the mass 20 g.
2. Take a porcelain crucible, check its number on the both parts, and enter it in the Excel file “LogSheet-Glassbead.”
3. Weigh the porcelain crucible and enter the measured weight into the Excel file.
4. Add ± 3 g of the sample in the porcelain crucible.
5. Weigh the porcelain crucible and enter the measured weight in the Excel file.
6. Place the porcelain crucible in the desiccator.
7. Repeat Steps 2–6 for the 8 next samples and the HSTD02 standard.
8. Place the 9 samples and the standard in the oven at 105°C for 6 h.
9. Place the porcelain crucibles in the desiccator for 40 min to cool.
10. Weigh each porcelain crucible and enter the measured weight in the Excel file.
11. Place the porcelain crucibles in the burn-out furnace for 10 h.
12. Take them out and place them in the desiccator for 40 min.
13. Weigh each porcelain crucible and enter the measured weight in the Excel file to obtain the LOI.

Glass bead

1. Tare a plastic tray on the balance.
2. Mill all the LOI sample powder in an agate mortar for 1 min.
3. Add 0.8950–0.9040 g of sample powder to the tray.
4. Weigh this powder and enter the measured weight in the Excel file.
5. Clean a plastic bottle.
6. Put the powder residue from the agate mortar in the plastic bottle and paste a label XRF-B(-D) on it.
7. Clean the agate mortar with ethanol.
8. Place the powder from the tray into the agate mortar.
9. Add the lithium metaborate powder from a glass dish stored in the desiccator.
10. Enter the number of the lithium metaborate glass dish in the Excel file.
11. Mill the powders together.

12. Transfer the powder to a Pt crucible and shake it gently to obtain a flat surface.
 13. Add 3 drop of LiI to the center of the crucible.
 14. Place the crucible in the Bead and Fuse-Sample device.
 15. Take out the sample and place it in the cooling area in a flat position (the light must blink; sometimes you have to move up and down the crucible).
 16. Return the crucible on a Kimwipe.
 17. Check that there is no bubble at the measurement surface of the glass bead (if there is a bubble, melt the sample again).
 18. Write the name of the sample on the glass bead.
- Store the glass bead in paper in a plastic bag in the desiccator.

Appendix E

Brief manual: Pressed powder pellet preparation for whole-rock trace elements by LA-ICP-MS

Stage 1

1. Grind the sample using the Jaw Crusher “Retsch BB50” flowing four step, starting from 14 mm gap, 7 mm, 4 mm, and 1 mm (see [Appendix C](#)).
2. Mill the resulting <1 mm crushate using a Fritsch Pulverisette 5 Planetary Mill with agate grinding bowls (500 mL) and agate balls (13 × 20 mm and 5 × 30 mm diameter).
3. Run grit samples at 200 rpm for 10 min and cool for five minutes four times,
4. Sieve the sample through 500 µm diameter and 250 µm sieves.
5. Return the large pieces (>500 µm) to grinding bowls for a further 10 min.

Once the whole sample is powdered, all sample material is returned to the grinding bowl and milled for 5 min to homogenize. The final powders are stored in ethyl alcohol cleaned, 100 mL screw-top polystyrene bottles.

Stage 2

1. Mill the resulting <250 µm crushate using a Fritsch Pulverisette 5 Planetary Mill with agate grinding bowls (80 mL) and agate balls (4 × 30 mm diameter).
2. Run grit samples at 400 rpm for 30 min and cool for 5 min 4 times.
3. Sieve the sample through 100 µm diameter and 60 µm sieves.
4. Return the large pieces (>100 µm) to grinding bowls for a further 10 min.

Once the whole sample is powdered (the result sample grain size should be <<60 µm), all sample is returned to the grinding bowl and milled for 5 min to homogenize. The final powders are stored in ethyl alcohol cleaned bottle, and stored.

Pressed pellet preparation

See figure below.

1. Load ~1 g of this fine-grained sample powder (grain size <<60 µm) into a 5 mm high sample holder cut from a 7 mm (OD) aluminum pipe and pressed into a tablet applying 10 tons for 20 s. Then gradually release the pressure over 66 s.
2. Remove the sample from the press, labeled it, and place it into a weigh paper envelope, seal it in a labeled Ziplock bag, and store it in a desiccator until analysis.

Appendix F

Brief manual: Preparing polished grain mounts embedded in epoxy resin for LA-ICP-MS

Mounting

1. Use a piece of two-sided tape (as thin as possible) and fix it on the stiff flat surface of the epoxy mount support.
2. Pick grains and mount them onto the tape within the circle.
3. Press the mount support ring firmly onto the sticky tape (there shouldn't be any gaps, as the epoxy may leak).

4. Once you are ready, pour the epoxy. The thickness of the epoxy layer MUST be exactly less than or equal to 5 mm.

Epoxy resins recommended:

- EpoxiCure
- EpoFix (this is the one we currently use)

Grinding

In order to have a flat surface and a good polishing, the mount needs grinding first.

Manual grinding and polishing should always be done in a figure-8 motion to avoid bulging of the mount surface.

Grinding manually with sandpaper

Start with grid size 800 and sequentially use the 1200 and finally 2000 grid size. Use with a thin layer of water and clean the samples carefully between each stage.

Polishing

Start with 15 μm , then 10 μm , followed by the 6 μm , 3 μm , and finally 1 μm diamond paste. Depending on the fragility of the grains, they may get damaged if polished or grinded for long. Progress should be checked with a reflected light microscope between each polishing stage.

If the sample contains soft material (carbonates, micas, etc.), you may have to finish the polishing stage using a 0.5 μm , or even a 0.25 μm diamond paste to avoid scratches on the surface of the grains.

Clean samples and the polishing device carefully between each polishing stage. We use an ultrasonic bath between each stage (30 s depending on the fragility of the grains, as they may get damaged if left too long in the ultrasonic bath). Progress should be checked with a reflected light microscope.

The back of the plug needs to be straight and reasonably flat as well. The drying of the epoxy, as well as surface attraction at the contact between the epoxy and the ring or mount support result in a concave structure at the back of the plug. You will have to remove that part with a saw so that the plug has parallel surfaces (back and front) or by manually grinding. The mount should be 3–5 mm thick.

Clean the polished plug using dry alcohol in an ultrasonic bath. From then, the plug should be handled with gloves. (See Fig. [F51](#).)